Arctic low vegetation cover properties assessment : coupled experimental and numerical approach

Simon Cazaurang

THÈSE

En vue de l'obtention du

DOCTORAT DE L'UNIVERSITÉ DE TOULOUSE

Délivré par :

Institut National Polytechnique de Toulouse (Toulouse INP)

Discipline ou spécialité :

Dynamique des Fluides

Présentée et soutenue par :

M. SIMON CAZAURANG

le lundi 18 décembre 2023

Titre :

Caractérisation des propriétés de transfert de la couverture végétale inférieure arctique - approche expérimentale et numérique couplée

---

École doctorale :

Mécanique, Energétique, Génie civil, Procédés (MEGeP)

Unité de recherche :

Institut de Mécanique des Fluides de Toulouse (IMFT)

Directeur(s) de Thèse :

M. MANUEL MARCOUX

M. LAURENT ORGOGOZO

Rapporteurs :

M. HOTAEK PARK, JAPAN AGENCY FOR MARINE EARTH

Membre(s) du jury :

M. LAURENT OXARANGO, UNIVERSITE GRENOBLE ALPES, Président

M. LAURENT ORGOGOZO, UNIVERSITE TOULOUSE 3, Membre

M. MANUEL MARCOUX, TOULOUSE INP, Membre

MME LAURE GANDOIS, TOULOUSE INP, Invitée

MME SOPHIE OPFERGELT, UNIVERSITE CATHOLIQUE DE LOUVAIN, Membre

M. MICHEL QUINTARD, TOULOUSE INP, Membre

M. OLEG POKROVSKY, CNRS TOULOUSE, Invitée

ARCTIC LOW VEGETATION COVER PROPERTIES ASSESSMENT - COUPLED EXPERIMENTAL AND NUMERICAL APPROACH

CARACTÉRISATION DES PROPRIÉTÉS DE TRANSFERT DE LA COUVERTURE VÉGÉTALE INFÉRIEURE ARCTIQUE - APPROCHE EXPÉRIMENTALE ET NUMÉRIQUE COUPLÉE

SIMON CAZAURANG

For the title of Doctor of Philosophy
National Higher School of Electrical Engineering, Electronics, IT, Hydraulics and Telecommunications (ENSEEIHT)
Toulouse Institute of Fluid Mechanics (IMFT)
Toulouse INP

December 18th 2023

ABSTRACT

Arctic environments are the regions that see the most significant climate warming of the Northern Hemisphere. These wetlands are widespread in Arctic ecosystems due to the large accumulation of organic matter (peat) produced by the organisms found there, *Sphagnum* mosses and lichens. The presence of large amounts of permanently frozen soil horizons (permafrost) makes these environments vulnerable. Numerous signals (increasing average annual temperatures, precipitation anomalies, changes in plant diversity) can already be observed. Climate projections for the year 2100 predict increases in temperature and precipitation in northernmost Arctic regions. These increases lead to the activation of climate feedback loops, which in return amplify climate change.

The aim of this thesis is to study the low vegetation cover of Arctic wetlands (*Sphagnum*, lichens, peat) by considering them as a porous medium. A set of experimental and numerical techniques for studying porous media will be applied to samples from several sites: Khanymey (Siberia) as first place, but also Abisko (Sweden). Some samples from Clarens (France) are collected to serve as test samples. The samples are digitally reconstructed using X-ray tomography. The digital reconstruction is then used to study the morphological (§I), hydraulic (§II) and thermal (§III) properties of this biological porous medium.

(§I) The morphological study shows a high porosity (sometimes more than 90%) for *Sphagnum*, lichen, and peat samples. High specific surface areas indicate a significant exchange and absorption potential for the study of element transfer. Representative Elementary Volumes (REV) may be defined for a majority of the samples.

(§II) The simulation of a single-phase flow is used to compute the effective permeability of the studied samples. Samples with a REV are studied by direct numerical simulation at the REV scale. For samples without REV, a pore network is generated from the sample reconstruction. In both cases, the obtained values of the effective permeability tensor show a high hydraulic conductivity. The results are similar to other experimental tests reported in the literature and make it possible to overcome the problem of sample compressibility.

(§III) The thermal properties are characterized using a coupled experimental and numerical approach. The experimental approach consists in studying the steady-state conductive heat transfer. The characterization of the effective thermal conductivity highlights the insulating property of the Arctic vegetation cover, with consistent values between each

type of sample. The value of the intrinsic thermal conductivity of the plant material is calculated by inverse modeling of the experiments.

Taken together, these transfer property studies provide a solid basis for generating an effective boundary condition for Arctic vegetation cover. However, further work is needed, in particular to quantify the influence of solar radiation flux on the energy balance of the Arctic vegetation cover. To this end, a preliminary work is presented that confirms the need for further information on the radiative transfer properties of this porous biological interface.

RÉSUMÉ

Les milieux arctiques sont les écosystèmes subissant la plus forte élévation de température moyenne annuelle liée au réchauffement climatique dans l'hémisphère nord. Les zones humides couvrent une grande partie des régions arctiques, avec notamment de vastes tourbières formées par l'accumulation importante de matière organique (tourbe) issue des organismes s'y trouvant : les Sphaignes et les lichens. Le changement climatique entraîne un dégel du pergélisol, horizon pédologique gelé en profondeur tout au long de l'année, présent sur 25 % des terres émergés de l'hémisphère nord, principalement aux hautes latitudes. La présence de grandes quantités de matières organiques gelées conservées dans le pergélisol pourrait entrainer des rétroactions positives non négligeables sur le changement climatique. De nombreux signaux (augmentation des températures moyennes annuelles, anomalies de précipitation, modification de la diversité végétale) peuvent déjà être observés. Les projections climatiques à l'horizon 2100 prévoient une augmentation de ces phénomènes sur l'ensemble des régions arctiques.

Cette thèse consiste à étudier la couverture végétale basse des zones humides arctiques (Sphaignes, lichen, tourbe) en les considérant comme des milieux poreux. Pour cela, un ensemble de techniques expérimentales et numériques est déclinée sur des échantillons prélevés sur plusieurs sites : principalement Khanymey (Sibérie), mais aussi Abisko (Suède). Des échantillons sont par ailleurs prélevés à Clarens (France) en guise d'échantillon-test. Les échantillons sont numériquement reconstruits grâce à la tomographie à rayons X. La reconstruction numérique permet ensuite d'étudier les propriétés

morphologiques (§I), hydrauliques (§II) et thermiques (§III) de ces milieux poreux biologiques.

(§I) L'étude morphologique indique une porosité importante (parfois supérieure à 90 %) pour les échantillons de Sphaignes, de lichen et de tourbe. La surface spécifique élevée montre des possibilités d'échange et d'absorption non négligeables dans l'étude des transferts d'éléments chimiques. Des Volumes Élémentaires Représentatifs (VER) ont pu être mis en évidence pour une majorité d'échantillon.

(§II) La simulation d'un écoulement monophasique permet d'établir la perméabilité effective des échantillons étudiés. Les échantillons possédant un VER sont étudiés au travers d'une simulation numérique directe à l'échelle du VER. Pour les échantillons ne présentant pas de VER, un réseau de pore est généré à partir de la reconstruction de l'échantillon. Dans les deux cas, les valeurs du tenseur de perméabilité effective obtenue montrent une conductivité hydraulique élevée. Les résultats sont similaires à d'autres essais expérimentaux présents dans la littérature et permettent de s'affranchir des effets de compressibilité des échantillons.

(§III) Les propriétés thermiques sont caractérisées au travers d'une approche expérimentale et numérique couplée. L'approche expérimentale consiste en l'observation d'un transfert de chaleur conductif à l'état stationnaire. La caractérisation de la conductivité thermique effective met en exergue le caractère isolant de la couverture végétale basse de l'arctique, avec une consistance des valeurs entre chaque type d'échantillon. La valeur de la conductivité thermique intrinsèque du matériel végétal est calculée par modélisation inverse des résultats expérimentaux. L'ensemble des études des propriétés de transfert permettent de fournir un ancrage solide dans la génération d'une condition limite effective de la couverture végétale arctique. Des travaux ultérieurs seront néanmoins nécessaires, notamment sur la quantification de l'influence du flux radiatif solaire dans l'équilibre énergétique de la couverture végétale arctique. À cette fin, quelques travaux préliminaires sont présentés affirmant la nécessité d'obtenir des informations complémentaires sur les propriétés de transfert radiatif de cette interface poreuse biologique.

Ei luulo ole tiedon vertainen.
Belief does not worth knowledge.

E. Lönnrot, *Suomalaisia sananlaskuja*, 1892

ACKNOWLEDGMENTS

Writing a thesis can be a solitary task, but the work produced is never done alone. I want to hereby thank and acknowledge the work of all the people involved, by near or by far (literally) to this project.

First, I would like to warmly thank my thesis supervisors, Manuel Marcoux and Laurent Orgogozo for all the help and time they have spent to guide my research and to help me understanding porous media sciences. More especially, I would like to thank them for their listening, the suggestions and ideas that they were brought through discussions and meetings. I remember the time when I was a Master student and asking Laurent "what modeling tools are used for hydrological monitoring ?".Manuel had the confidence while being an intern to hire me as a PhD student, even though porous media science was something new to me. With both Manuel and Laurent, I had the chance to learn various new skills in numerical processing and experimental work, linking both physics and geosciences. I am sincerely grateful for their help during these three years spent at Toulouse Fluid Mechanics Institute.

I would like to warmly thank Hotaek Park and Laurent Oxarango for their willing to review this thesis dissertation and be part of the defense jury. I sincerely acknowledge Sophie Opfergelt and Michel Quintard to have accepted to be examinators of this thesis defense. Finally, I want to thank Laure Gandois and Oleg Pokrovsky for their attendance of the thesis' defense panel.

The coupled approach developed in this thesis requires solid bases of experimental work and lab practice. I would like to thank Julien Lefort from the experimental engineering department, Sébastien Cazin and Hervé Ayrolles from signals and images department for their dedication and the late stays at the lab, helping on some experimental bench or just to discuss science in general. I also thank Christophe Escape from the PROMES laboratory for the measurements of infrared emissivity. I have learned a lot from you! As this thesis is a small brick of a bridge, I would like to thank all the HiPerBorea project members namely Yves Auda, Emmanuel Mouche, Claude Mugler, Liudmila Shirokova, Oleg Pokrovsky, Etienne Gondet, Eric Pohl for the interesting discussions and advices on this thesis, in meetings and in more informal discussions. A special thank for the eternal good mood of Thibault Xavier, postdoc in the HiPerBorea project, with whom I now

share the office. I am sincerely thankful for the support you provided me on the weeks before the defense.

During my thesis, I had the chance to make various trips outside the lab, at conferences or in the field work. Therefore, I would like to thank Laurie Boithias, Catherine Noiriel, Stéphane Audry, Carine Lézin, Jelmer Njip, Jonas Gustafsson, Emily Pickering Pedersen and Israel Cañamón who shared their ideas, giving to it new perspectives, and also for more informal talks about the career of a researcher.

Being either in front of a computer for hours waiting to find the last bug in your code or the last leakage in your water cooling system is not fun without others in the same (sinking) ship. I particularly want to thank post-docs, other PhD students and interns that I have met through these three years: Glad, Isaac, Térence, Jade, Emma, Edith, Elisa, Asma, Omar, Oumeima, Amal, Sarah, Klervia and David.

I would also like to thank the members of the Biological Porous Media team and permanent members for their help throughout the thesis: Paul Duru, Yohan Davit, Michel Quintard, Pauline Assémat, Olivier Liot, Nicolas Hengl and Rachid Ababou. Likewise, I also acknowledge the help of the administrative chapter of the Fluid Mechanics Institute, and particularly Suzy Bernard, Karine Defretin, Muriel Sabater-Boutic and Céline Perles-Picotto.

Furthermore, I would like to thank my parents, my late father Philip and my mother Heidi, who inspired me the curiosity and dedication I needed to make the most of my doctorate. I thank also my Finnish family for the numerous journeys in boreal forest where the will to study such environments was set.
And last by not least, I would like to thank the most important person in my life, Natacha, who has always been here to help me, to bring me happiness and always read my drafts.

Figure 0.0.1 – ... And thanks for the reindeers that we were able to see during the field trip to Abisko!

CONTENTS

LIST OF FIGURES

LIST OF TABLES

GENERAL INTRODUCTION

Since the early 1990's, many clues of warming arctic environments have been shown in literature (Biskaborn et al., 2019; Hinzman and Kane, 1992). Arctic region's mean annual temperature increase have been assessed as the Northern Hemisphere's most significant warming at the beginning of the 21st century. Extreme events (droughts, floods, wildfires, thunderstorms) are more recurrent and more especially since the beginning of the 2020's (massive wildfires in Siberia, Kim et al., 2020, massive fires in Canada in 2023), threatening the arctic ecosystems.

Arctic soils contain high concentration of organic matter horizons, making them significant carbon stocks. Arctic soils are considered to contain more carbon than all the carbon present in the atmosphere ($1.7.10^{18}$ g carbon, Tarnocai et al., 2009; E. A. G Schuur et al., 2015). This organic carbon is mainly stored in Arctic wetlands which cover about 25% of the Northern Hemisphere's surface, with 99% of the wetlands surface have at least one cryotic soil horizon permanently frozen throughout the year (permafrost, Kåresdotter et al., 2021). A biologically active interface connects climatological phenomena in the atmosphere and pedogeomorphological phenomena in the geosphere: the Arctic vegetation cover.

This Arctic vegetation cover can be subdivided into several biocenoses, mainly determined by latitude. There are numerous studies about the potential influence of permafrost thaw in the global climate change dynamics (Edward A. G Schuur et al., 2008; Walvoord and Kurylyk, 2016; Hofmeister et al., 2021) however, the role of arctic low vegetation cover in climate change effects mitigation is still poorly quantified (Porada et al., 2016; Park, Launiainen, et al., 2018). Moss and lichen cover has been assess to drive significantly the thermal dynamics of the low arctic vegetation cover (Blok et al., 2011) where most of the energy exchanges occurs via evapotranspiration (Launiainen et al., 2015). Most of the visible ecohydrological changes occurring in the Arctic regions are driven by changes in evapotranspiration (Karlsson et al., 2015), or snow cover change at continental-scale (Park, Fedorov, Zheleznyak, et al., 2015; Ishikawa, 2003; Berteaux et al., 2017). Therefore, a mechanistic approach to the low vegetation cover is compulsory in order to make an adequate permafrost dynamics model at a watershed scale. More accurately, an effective boundary condition has to be defined for this biological cover, accounting for an interface between the atmosphere and the geosphere. This boundary condition could further be implemented in an Earth-System Model after having done some upscaling. Thereby, the main focus of this thesis is the morphological description of the bog vegetation

cover and the characterization of its hydraulic and heat transfer properties. To this end, the approach adopted during this research work is to assimilate the Arctic peatland vegetation cover to a porous cover. The application of porous media study methodologies (representative elementary volume quantification, volume averaging) used as standards is thus performed through various experimental and numerical methods. This thesis is part of a project about the quantification of the impacts of climate change on boreal regions at a centennial timescale (the HiPerBorea[1] project, founded by the French national research agency). In this way, quantifying the transfer properties of arctic vegetation cover will contribute to inform catchment scale permafrost simulations at centennial timescale for the experimental watersheds under study in HiPerBorea. The main focus for the experimental and numerical work presented in this thesis is done on Khanymey Research Station and on Abisko Scientific Research Station, taking into account the vegetation cover variability.

The work done in this thesis articulates on 12 samples of *Sphagnum*, lichen, and peat collected at Khanymey Research Station in order to quantify their transfer properties (*e. g.* hydraulic conductivity, thermal conductivity) using a numerical reconstruction of the samples done through X-ray tomography. To do so, this thesis is divided into four main parts as shown:

- The first part consists in a literature review on cryogenic environments, the challenges of climate change in Arctic regions and the sustainability of permafrost. This part also includes a few elements of porous media analysis for the sake of accessibility.
- The second part deals with sample collection and digital reconstruction using X-ray tomography. This section also presents the HiPerBorea study sites that are considered in this thesis.
- The third part deals with the assessments of the transfer properties of the considered samples. Morphological and hydraulic properties are presented as published in Cazaurang et al. (2023) in *Hydrology and Earth System Sciences*. Thermal properties are also studied in a separate chapter of Part III.
- The fourth part presents the additional lines of inquiry that have emerged in the course of this research project, as well as the most recent results. There is also a brief presentation of future work and long-term perspectives.

Some clues about the research perspectives emerging from this thesis project are then shown to conclude this work on arctic low vegetation cover transfer properties.

1 High Performance Computing for quantifying climate change impacts on boreal areas. More information about this project available on https://hiperborea.omp.eu/

Part I

LITERATURE REVIEW

1

ARCTIC VEGETATION COVER AND CLIMATE CHANGE

Historically, global climate phenomena have been approached through the prism of meteorological data, leading to the formulation of climate models. However, some recent research acknowledged the potential of arctic low vegetation cover in climate forcings estimations (Oehri et al., 2022). Therefore, the properties of arctic ecosystems need to be precisely characterized in order to obtain more accurate models of the exchange phenomena between the geosphere and the atmosphere. The aim of this chapter is to give a brief overview of Arctic ecosystems, the plant populations that live there and the impacts of climate change on these fragile ecosystems.

1.1 TAIGA, TUNDRA AND PERMAFROST

Two biomes covers the great majority of arctic landscapes: taiga and tundra. About 30% of Earth's continental surfaces are covered by arctic ecoregions, of which 17% consists of taiga ecosystems and 13% of tundra ecoregions. Note that taiga and tundra environments can be found in the Southern Hemisphere although most of tundra ecosystems are located in the Northern Hemisphere. A general overview of these two biomes is available in Fig. 1.1.1.

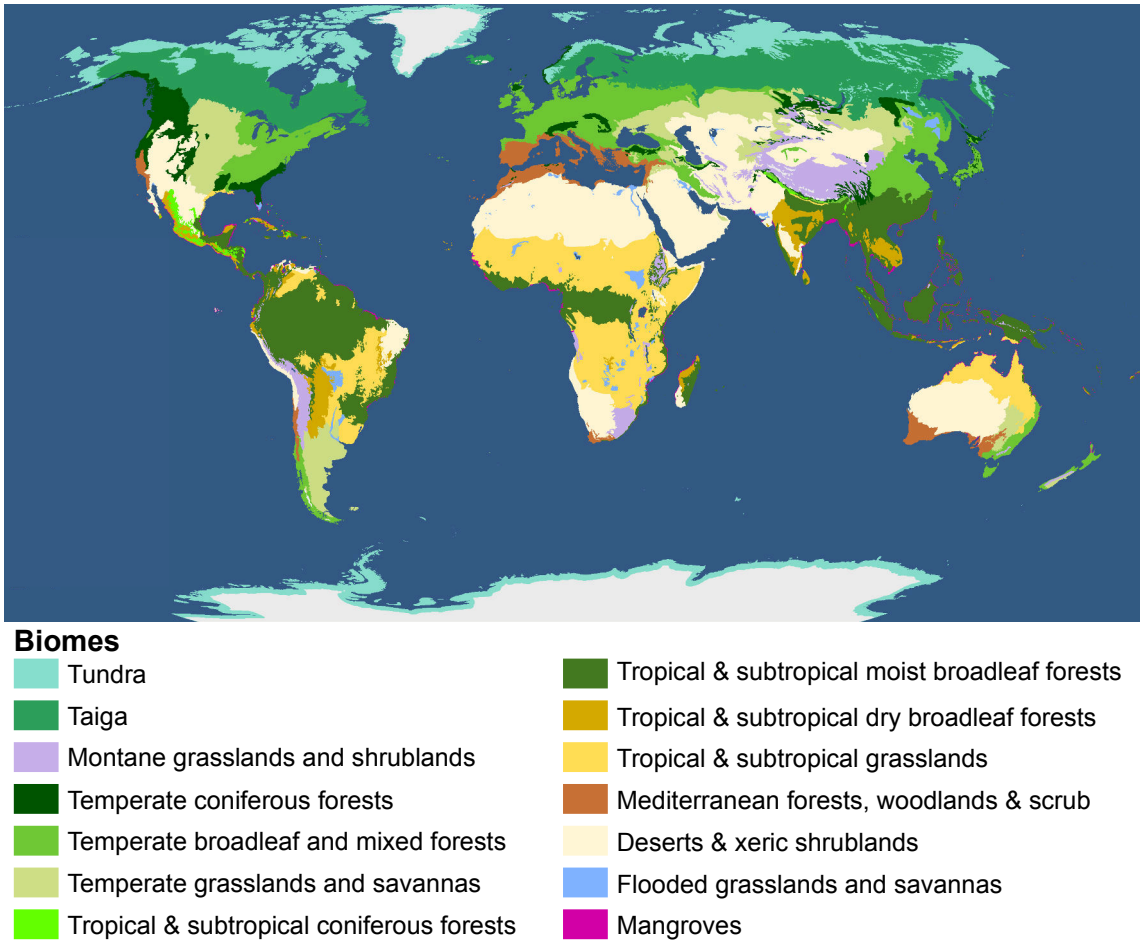

Figure 1.1.1 – Ecoregions map with taiga and tundra extension over the Northern Hemisphere. *Licensed under CC-BY-SA 3.0 to Terpsichores.*

These two biomes are found in areas strongly affected by fluvioglacial erosion following the melting of the Pleistocene ice sheet (-11,600 years, Tanguy et al., 2023). These two biomes can be characterized by important thermal amplitudes. As a first approximation, we can give a synthetic definition of these two biomes:

- Taiga is defined by a mean annual temperature between -5 °C and +5 °C, the presence of a boreal forest (consisting of pine, spruce and birch) and a significant lake network. Summers are short (from June to early September) but with high temperatures (temperatures around 30 °C can often be measured in taiga biomes). Winters are significantly longer than summers and can be cold (from -10 °C to -40 °C). Intermediate seasons are of short duration and marked by significant precipitation and freeze/thaw cycles in the case of frozen soils.
- Tundra is defined by the predominance of low vegetation and the presence of large bog areas. The vegetation is mainly composed of grasses, dwarf trees, shrubs, and mosses. The vegetation is strongly constrained by the presence of snow most of the year and an asymmetric sunlight amount during the year (short daytime in winter,

midnight sun during summer). Tundra ecoregions offers ground for lots of lichens species, most of them being adapted to these abrupt changes throughout the year. Winters are extensive and harsh (from -30 °C to -40 °C). Summers are short (about a month and a half between the end of June and mid-August). The intermediate seasons are little marked, the transition between winter and summer being rapid on the scale of a seasonal cycle.

Although tundra and taiga ecoregions share common characteristics, it is possible to differentiate both ecoregions with annual average temperatures (Huntley and Cramer, 1997). Annual precipitations can also be linked, as shown in the Whittaker diagram (Fig. 1.1.2). The thesis will mainly emphasize on the Eurasian arctic ecoregions, gathered under the term palearctic. Fig. 1.1.2 and Fig. 1.1.3 both show that the main climatic drivers for biomes differentiation at a global scale is annual precipitation on one hand and potential evapotranspiration ratio on the other hand.

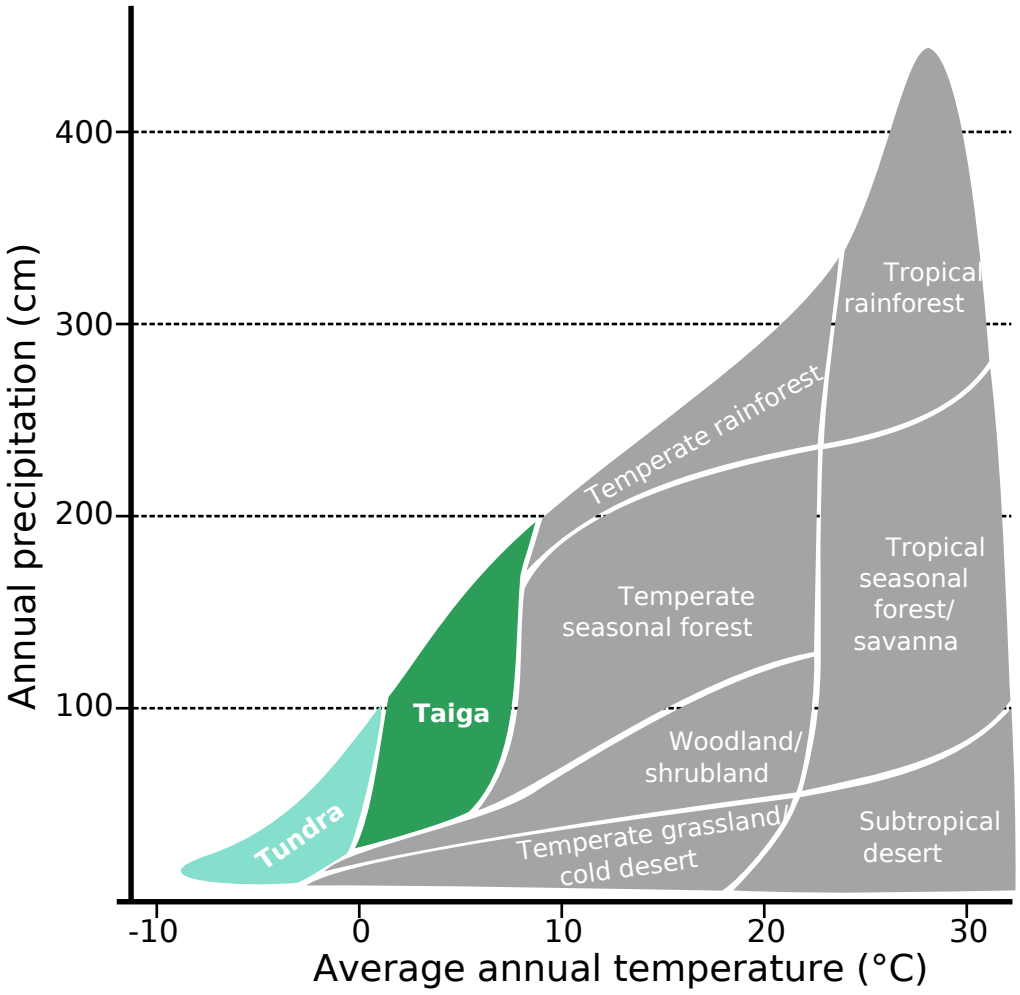

Figure 1.1.2 – Average annual temperature - average rainfall diagram (adapted from Whittaker, 1975).

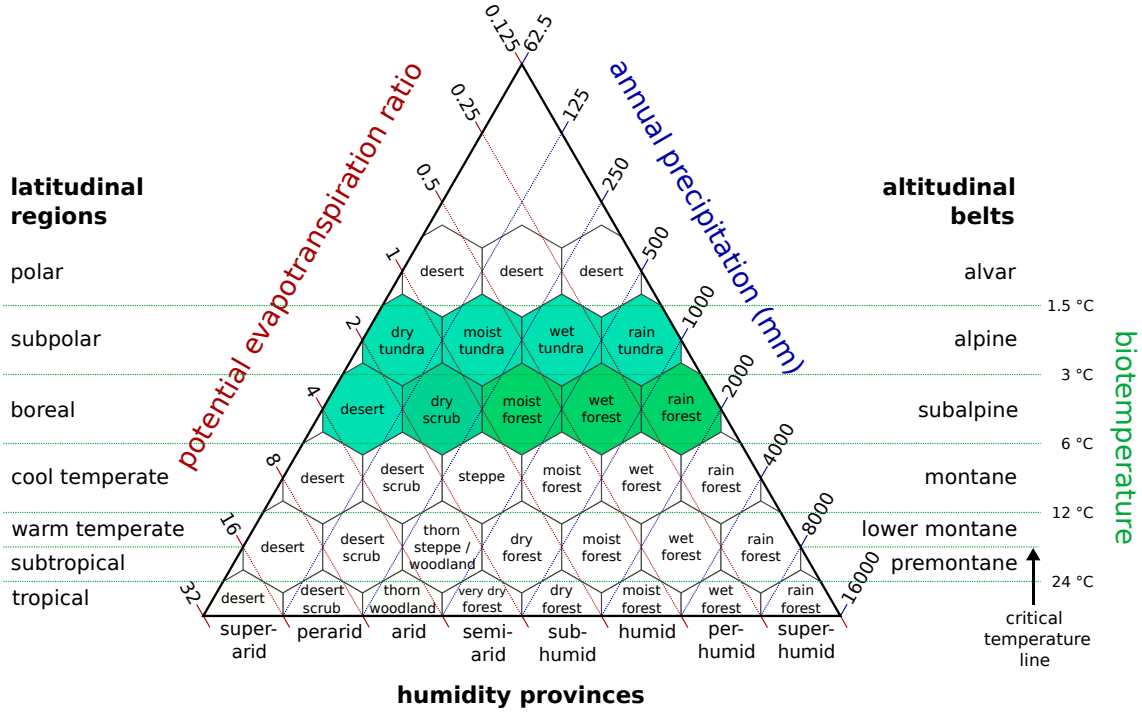

Figure 1.1.3 – Holdridge diagram (Holdridge, 1947) showing the relationships between potential evapotranspiration ratios, humidity and average annual air temperature. *Licensed under CC BY-SA 2.5 to Peter Halasz.*

Potential evapotranspiration ratio is the maximum amount of water vapor that can be evaporated by plants if their water source would be unlimited. High temperature combined with low annual precipitation gives high potential water evapotranspiration. On the contrary, high precipitation or low temperature lead to poor potential evapotranspiration. Tundra ecoregions can be likened to arid ecoregions, in the same way as a hot desert. The difference between these two ecoregions is based on potential evapotranspiration, which is very high in hot desert environments and low in cold desert environments. The Arctic regions feature extensive watersheds, with rivers of major hydrological and economic importance, especially for Siberian communities (Dvina, Ob, Yenisei, Lena, Kolyma). These watersheds have large, gently sloping areas, conducive to the presence of large-scale wetlands. Arctic wetlands are presented in detail in section 1.2.2.

1.2 COLD ENVIRONMENT DYNAMICS: A BIOGEOMECHANICAL PERSPECTIVE

Unlike other terrestrial domains, the polar domain, and more specifically the Arctic domain, is peculiar in the fact that it can hold water in all three of its physical states simultaneously. The dynamics of cold environments in the broadest sense encompasses a variety of biogeochemical and geophysical processes specific to these environments. This section looks at cold environments from a geodynamic angle. A general presentation of

permafrost is given in section 1.2.1, followed by a description of the active layer and its dynamics at plot and watershed scales. Section 1.3 then discusses the impacts of climate change on cold climate ecosystems from hydro-ecological (section 1.3.2), geotechnical (section 1.3.3) and anthropogenic (section 1.3.4) perspectives.

1.2.1 *Cryosoils and permafrost*

Subzero annual mean temperature is a characteristic feature of Arctic environments, resulting in frozen soils. In the World Reference Base for Soil Resources (International Union of Soil Sciences, 2022), the Gelisol family includes all soils with at least one soil horizon containing ice. According to the International Union of Soil Sciences (2022), the main characteristics that define a cryic soil horizon are:

- visible ice crystals in the cryic soil horizon;
- a soil temperature below 0 °C;
- a soil horizon thickness of more than five centimeters.

Thus, a cryic soil horizon is usually present in location where the mean annual temperature is below 0 °C, which is the case for polar regions in general and high-altitude mountain soils. On the other hand, permafrost, a contraction of permanent frost, is a characteristic feature of soil horizons containing frozen water (cryosoils). A cryosoil is generally considered to be affected by permafrost if at least one of the soil horizons is cryic for two consecutive years (International Permafrost Association, 2015) and summer warming does not allow all soil horizons to thaw completely. Permafrost can vary in thickness from a few centimeters to several hundred meters. Obu et al. (2019) estimates that permafrost covers about 25% of the land surface of the northern hemisphere. The pedological nature of permafrost and cryosoils in general is diverse. Permafrost can consist of sedimentary deposits (sand, silt, clay), accumulations of organic matter (peat, discussed in detail in section 1.2.2.2), or bedrock in the absence of a distinct pedological horizon.

Permafrost cryosoils may have a continuous spatial extent (with no permanently thawed zone). This is known as continuous permafrost. This type of permafrost is often found in the northernmost regions of the Arctic, particularly in the northern Siberian plains, the Canadian territory of Nunavut, or the northern part of Alaska. A map showing the spatial extent of permafrost can be found in Fig. 1.2.1.

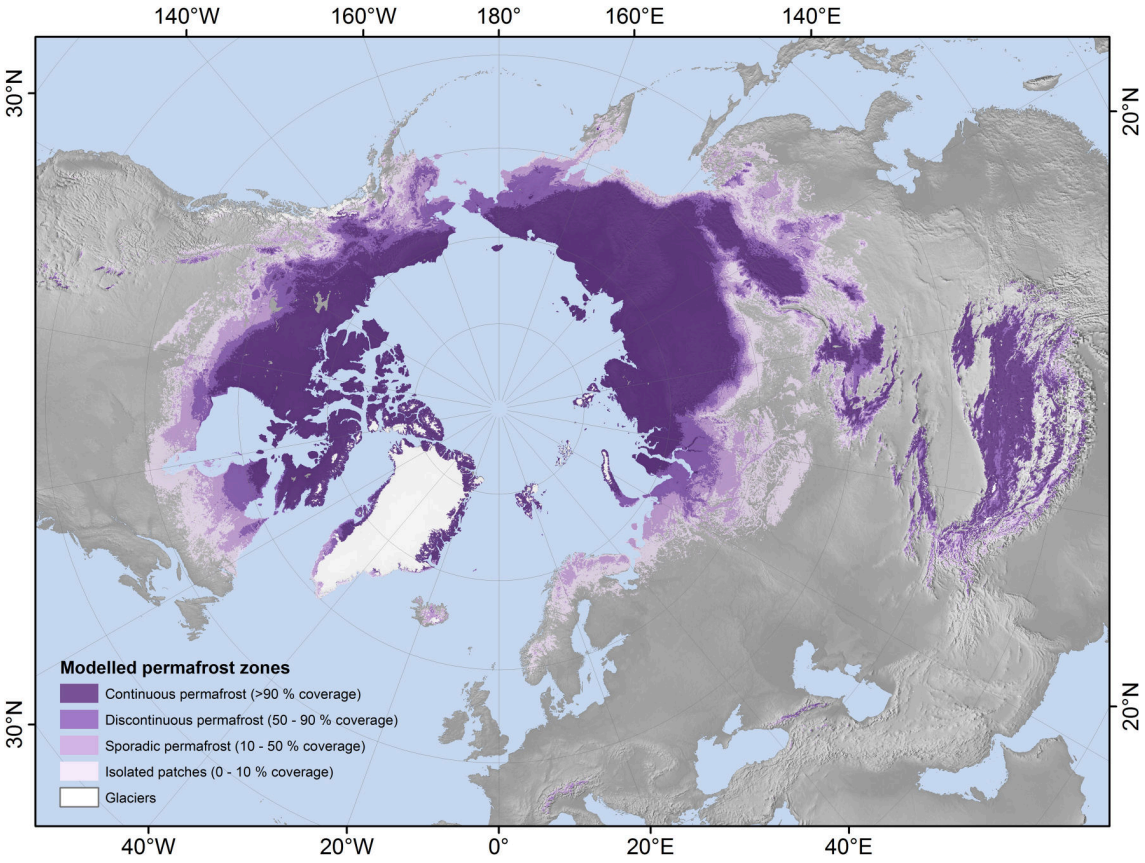

Figure 1.2.1 – Map of permafrost spatial extension (from Obu et al., 2019).

Fig. 1.2.1 also shows that permafrost also occurs in regions outside the Arctic Circle, such as the Tibetan high plateau, the Alps and Caucasus. Permafrost is also found in the southern hemisphere, and more precisely in Antarctica but is out of the scope of this thesis.

1.2.2 *Arctic wetlands and peatlands*

1.2.2.1 *A definition of wetlands*

A wetland can be defined as an area saturated with water, either permanently (as for bogs or swamps) or periodically, due to maritime inputs for instance. Wetlands are often located in the lowest zones of a watershed, which can be near of its outlet (near the sea) or in flat topography plains (such as the Western Siberian lowlands). Wetlands are found in most terrestrial biomes. Depending on the ecoregion in which the wetland is located, different terms are used (marsh in temperate zone, swamp in subtropical zone, mangrove in equatorial zone). Wetlands are the prime areas for the accumulation of organic matter, as they are generally located downstream of watersheds. This accumulation is generally the result of a matter balance that favors photosynthesis of organic matter over its decomposition. In tropical biomes, wetlands are generally due to the abundance of

precipitation. For Arctic regions, even though precipitations are low, a lot of wetlands persists due to low potential evapotranspiration. The accumulation of organic matter is generally the result of a matter balance that favors photosynthesis of organic matter over its decomposition. In the case of low mean annual temperatures combined with high water saturation, organic matter degradation is less active, leading to the accumulation of organic matter in an unconsolidated form known as peat.

1.2.2.2 *Peat formation in wetlands*

Peatland is assumed to cover about 4% of total Earth's continental surface (Adon et al., 2013). Arctic peatlands cover vast surfaces across the Northern Hemisphere, both in taiga and tundra ecoregions. Peat is a ground formation consisting of decayed vegetation, which is often found in closed basin geomorphological structures. The accumulation of partially decomposed organic matter is the main factor in the formation of peat. This accumulation requires a topographical depression and local geomorphological stability, which allows it to accumulate over long periods of time (generally several thousand years). Peat material is the main component of a peat bog. Peat can have different origins, depending on the climate and the type of vegetation present, and are spanning in different biomes on Earth. Three stages of decomposition can be distinguished:

- Sapric peat (or "black" peat) corresponds to the most advanced stage of decomposition. It is difficult to distinguish the original organic material. Due to its state of decomposition, sapric peat is the richest in carbon.
- Fibrous peat (or "blond" peat) represents an early stage of peat formation. Traces of the plant material are easily visible. Unlike sapric peat, fibric peat is the least carbon-rich type of peat. It is also less dense than sapric peat.
- Mesic peat (or "brown" peat) is an intermediate state between sapric peat and fibrous peat.

A picture of *Sphagnum* peat as well as a scanning electronic microscope image of peat is available in Fig1.2.2.

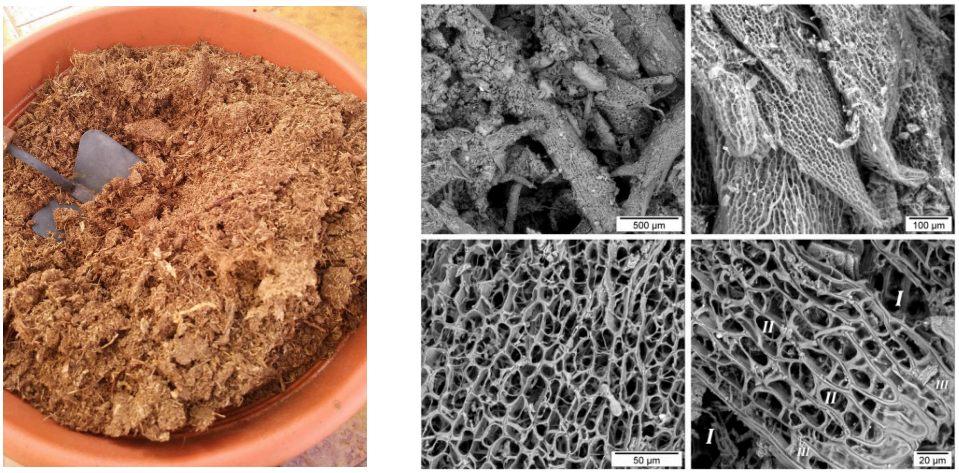

(a) **(b)**

Figure 1.2.2 – (a): *Sphagnum* peat in a bucket, (b): Peat observed under Scanning Electron Microscope (SEM) at 10 kV (adapted from Fereidoun Rezanezhad et al., 2016).

The decaying status of peat and the local climate accounts for peat acidity. There are two main types of peat bogs:

- A minerotrophic peatland (fen) corresponds to a peat bog whose water and mineral inputs are mainly provided by groundwater or surface water (including rivers);

- An ombrotrophic bog is fed exclusively by meteoric and eolian sediments, has a low pH and a low concentration of minerals available to vegetation.

Peat is also distinguished according to its acidity and the dominant hydrological phenomenon of the peat bog in which it occurs. Thus,

A majority of Arctic peat bogs are ombrotrophic. Bryophytes and lichens are abundant in these environments, which generally do not support larger plants due to low pH and water saturation. The acidity and the continuous growth of the bryophytes allows a significant accumulation of moss and lichen material. When such material is slowly buried and removed from sunlight exposure, this material starts to decay. The acidity, combined with polyphenols contained in moss sprigs and cold temperatures slows this decomposition, which leads to organic matter accumulation. Therefore, the growing and living upper part of this vegetation layer is named acrotelm whereas the non-photosynthetically active decaying layer is called catotelm. Acrotelm is about 5 to 20 cm thick depending on the living *Sphagnum species*. Some other material can also be found in peat formations such as pine spikes, pine cones, lichen fragments or vertebrates' bones.

Arctic peatlands consists in a specific type of peatland due to permafrost occurrence. These peculiar peatlands are presented in Minayeva et al. (2016) as mires that are sea-

sonally frozen due to the negative mean annual temperatures occurring in these regions. Sites studied during the thesis are mostly located in arctic and subarctic ecoregions. Details on these sites are described in section 3. It should be noted that these ecoregions cover large areas ($3.5.10^6$ km^2, approx 25% of Arctic total landmass, Kåresdotter et al., 2021). Therefore, some local microclimate effects can be found, mainly depending local hydrology regime.
Peat properties have been studied since the early 20^{th} century. Historically, many peatlands have been drained and dried because local population believed peatlands where unsafe and carried diseases. Due to this, and due to the fact that peat is rich in organic matter and therefore rich in carbon, peat have been used and is still sporadically used as a household fuel. Hydraulic properties of peat are the properties that have seen the subject of many publications in the early 20^{th} century. One of the first paper mentioning such work is Malmström (1925) studying the implications of peatland drainage in Sweden. The first consistent studies about peat hydraulic properties can be found in scientific reports made on Finnish peatlands (Heikurainen, 1963; Sarasto, 1963; Virta, 1962) in the United-States (Boelter, 1968) or also in Irish peatlands (Galvin, 1976). The results shown in such works show that the hydraulic properties of peat are variable and depends heavily on the local hydrology. These work work are also confirmed by recent studies made on peat (Fereidoun Rezanezhad et al., 2016; Hamamoto et al., 2016) also linking hydraulic properties to freeze/thaw dynamics (Nagare et al., 2012).

1.2.3 *Arctic cryptogamic cover*

A low biological strata forms an interface between the atmosphere and the geosphere. This low vegetation cover composition is diverse (*Sphagnum* moss, Fungi, lichen, peat) and forms a complex patchwork with some heterogeneity at decimeter-scale. It might be useful to recall at this stage that lichen cannot be considered as vegetation, as it is a heterotrophic organism. Therefore, *Sphagnum* moss and lichen can be classified under the term cryptogamic gathering all species that shares hidden reproductive apparatus. This triptych configuration is found over millions of square kilometers, especially in Siberian wetlands (Soudzilovskaia et al., 2013).

In this section, an overview of the three main types of cover found in arctic peatlands will be presented (moss, lichen, and peat). Some clues of climate change impacts on this cryptogamic cover will be discussed further in section 1.3.

1.2.3.1 *Moss (Bryophytes)*

The Bryophyte or *Bryophyta* (*s. l.*) vegetation reign can be considered as a paraphyletic or a monophyletic group regrouping all non-vascularized dwarf plants (Troitsky et al., 2007). Bryophyte (*s. l.*) gathers around 20.000 species that were classified by Schimper in 1880 (Bryophyta, 1880). At the time, *Bryophyta* (*s.l.*) reign has been identified as a

monophyletic group, with other studies converging to this assumption (Goremykin and Hellwig, 2005). Yet, the monophyly is nowadays the main consensus and evidences showing the monophyly of *Bryophyta* (*s. l.*) are numerous (Harris et al., 2020; Sousa et al., 2019).

In a palaebiologic definition, the *Bryophyta* (*s.l.*) reign is assumed to be derived of *Charophytae*, a branch of algae widely present during the Cambrian era (522-478 My BP). The divergence happened in the early stage of the hypothetical embryophyte, the first terrestrial plant. Therefore, *Bryophyta* (*s. l.*) shares some characteristics of algae (sexual reproduction via spores) and some characteristics of most of the angiosperms (terrestrial plants, Delwiche and Timme (2011)). A phylogenetic tree representing *Bryophyta* (*s. l.*) taxonomic diversity is presented in Fig. 1.2.3.

Figure 1.2.3 – Cladogram of the Bryophyta (s. l.) reign. Adapted from Záveská Drábková et al. (2015). *Licensed under CC-SA 4.0.*

The metabolic similarity between green algae and Bryophytes can also be seen in their reproductive cycle, shown in Fig. 1.2.4. The main living structure in the life cycle of a sprig of *Sphagnum* is the gametophyte. This gametophyte can produce female gametes called archegones or male gametes called antheridia. Fertilization of the gametes produces apical cellular structures called sporophytes, the terminal sac of which is called the sporangium. When the sporophytes reach maturity, the capsule opens and the spores are released, sometimes under the strong pneumatic pressure accumulated in the sporangium.

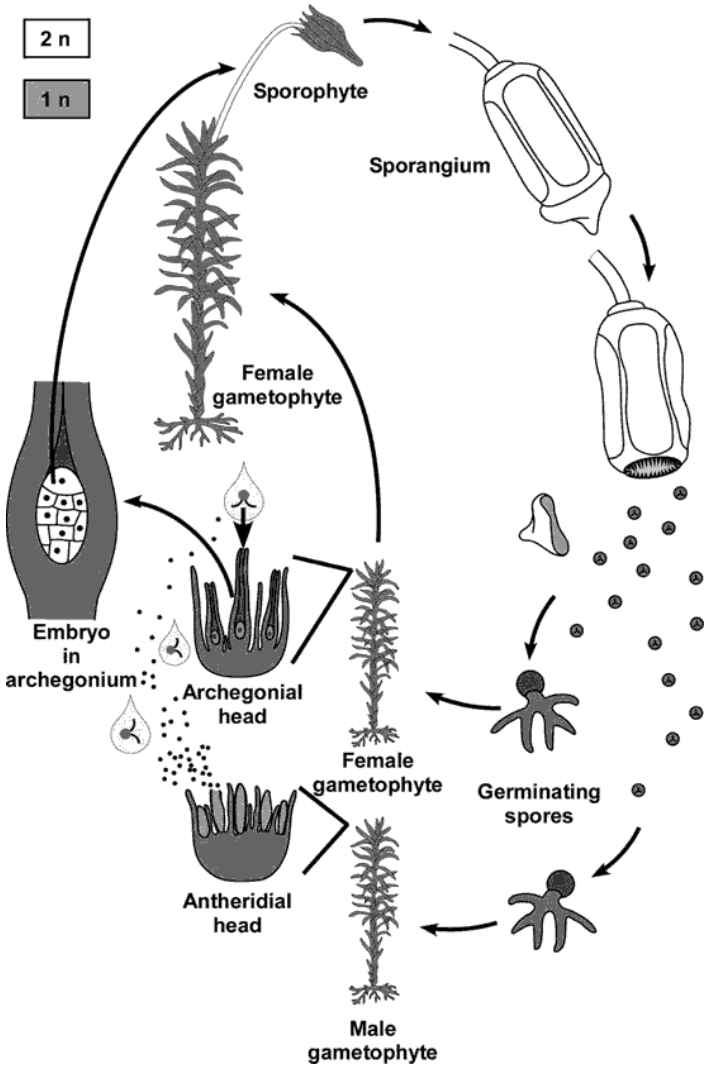

Figure 1.2.4 – Life cycle and schematic representation of a Bryophyta plant individual (adapted from Gerrienne et al., 2020).

In the contemporary definition, the *Bryophyta* (*s.l.*) reign gathers three main families:

- *Marchantiophytae* (liverworts)
- *Anthocerotophytae* (hornworts)
- *Bryophyta* (s. s.) (mosses)

Although the families of Bryophytes below are grouped together in the same class, the morphological variability of species can be considerable. Nevertheless, Bryophytes share a number of common characteristics, such as the absence of internal cellular structures for the vertical transport of nutrients. Thus, Bryophytes, and more specifically *Sphagnum* species only rely on capillary force to fulfill their water supply. A picture of a *Sphagnum* colony and an extracted *Sphagnum* individuals are shown in Fig. 1.2.5.

(a) *Sphagnum* colony

(b) *Sphagnum* gametophytes of different species.

Figure 1.2.5 – An example of *Sphagnum* mire (Clarens, France).

A synthetic description of a schematic *Sphagnum* plant is presented in Fig. 1.2.6. One can find that the descriptive vocabulary is very similar to the one used to describe green *Algae*. Indeed, the complex arrangement of each *Sphagnum* strand in a colony forms a fibrous structure Then, capillary force variations are occurring based on the variation of space between each strand, and therefore on the pore space. The vertical support of *Sphagnum* is achieved solely by the turgidity of the plant cells making up a *Sphagnum* strand. The absence of plant support structures (wood, bark) or sap conduction systems limits the height of *Sphagnum* to around ten centimeters. This non-vascularization gives *Sphagnum* mosses a similar cellular shape to what is found for green Algae. However, adversely to Algae, water and nutrients are kept in inert macrocells called hyaline cells, visible in Fig. 1.2.6.

The hyaline cell does not contain any nucleus and only consists of a single pore through which water can flow. Thus the follicular system of *Sphagnum* does not consist of leaves *stricto sensu*. It is only a regular structure of hyaline cells and chlorophyll cells in the same pattern as on the thallus. *Sphagnum* mosses survive in their natural environment if there is a sufficient number of individuals to form a colony. Thus, a single individual dries fast comparatively with a colony. This is usually not the case for the other *Bryophyta* species, which have developed stomata in their phylogenetic history. In the present work, the focus is put on one peculiar *Bryophyta* (*s.s.*) family, *Sphagnacae*. This family gathers all *Sphagnum* species encountered in Arctic biomes. *Sphagnum* mosses are one of the most representative cryptogamic covers found in Arctic peatlands and especially in Western Siberia (Soudzilovskaia et al., 2013). The dominant visible structure (*i.e.*, the visible *Sphagnum* individual) is the gametophyte. The gametophyte grows from their apical structure called capitulum. The growing pattern follows a fractal structure, which

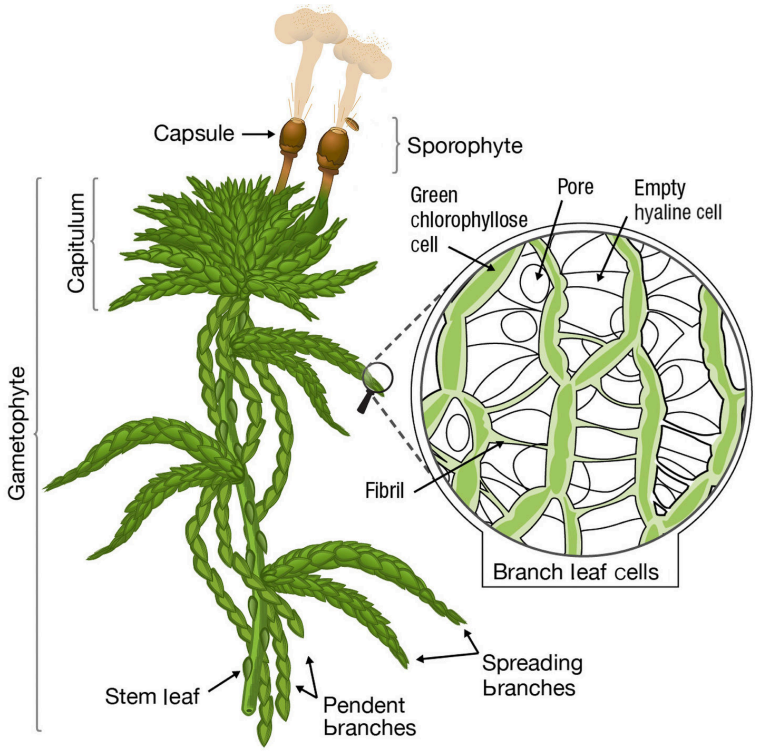

Figure 1.2.6 – General description of a *Sphagnum* gametophyte and microscopic cell structure of *Sphagnum* pseudoleaf (from Weston et al., 2015).

is called in botanic sciences an indeterminate growth. This means that the growth is never ending if the water and nutrient needs are fulfilled.
One of the main characteristic of *Sphagnum* species is their high resilience capabilities, tolerating extreme water conditions (droughts to flooding) and extreme temperature ranges (from -40 °C to +40 °C). The relative structural simplicity of *Sphagnum* metabolism and the low degree of cell specialization mean that these plants do not require large quantities of nutrients. This characteristic allows them to grow extensively in Arctic wetlands, where water is generally very poorly mineralized and acidic due to the large amount of adsorbent organic matter. It is also important to note that maximum photosynthetic activity is identified not in full sunlight, but in diffuse light, due to CO_2 diffusion (Marschall and Proctor, 2004).

1.2.3.2 *Lichen*

Lichen is a composite organism distinct from peat mosses that cannot be considered as vegetation. Lichen worldwide coverage is estimated to be around 8% (Lutzoni and Miadlikowska, 2009). Lichens can be found in almost every ecosystems and more especially in arctic environments. Lichen is a symbiotic association (or symbiosis) between two heteromorphic species. Here, a lichen is an association of heterotrophic fungi named mycobiont and an autrotrophic algae (usually green algae or cyanobacteria) called photobiont. Lichens' shape and texture are very variable, and so is their phylogeny. There are

mostly nine types of lichens on Earth, which are mainly determined upon their growth form:

- byssoid (very fibrous)
- crustose (forms a crust on a surface, solidly fixed to the surface)
- foliose (forms flat pseudoleafs)
- filamentous
- fruticose (forms a sort of a dwarf schrub or bush)
- gelatinous
- leprose (forms a sort of powdery shape)
- squamulose (very close to crustose but forms a multishaped structure)
- without any structure

In the present work, the emphasis will be put on the fruticose and foliose lichen types, and precisely the 560 species gathered under the division of the *Cladoniacae* reign. An example of a lichen organism and a slice observed under the optic microscope is visible in Fig. 1.2.7.

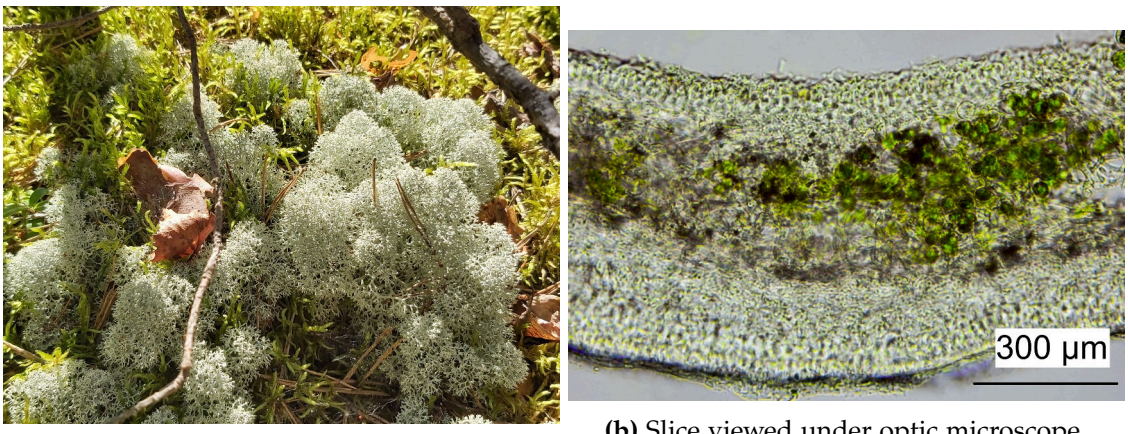

(a) Field picture.

(b) Slice viewed under optic microscope.

Figure 1.2.7 – *Cladonia stellaris* thallus longitudinal cut observed under the optic microscope. Green middle cells corresponds to green Algae cells and the surrounding enclosure is formed by *Fungus* mycorrhiza (adapted from Piskova and Sacha, 2023).

The symbiotic association between a green Algae and a Fungi gives the ability to this composite organism to survive extreme drought and flooding. Energy and and nutriments are supplied by the photosynthetic organism (in this case, the green Algae) while the mycobiont gives shelter and ensure water exchanges between the two symbiotic organisms. Lichen can also survive under the snow for the whole. Lichen constitute the main food for reindeer and is the main predator of it in Arctic environments.

1.2.4 *Permafrost dynamics*

1.2.4.1 *Active layer*

The presence of ice in the porous soil matrix leads to significant structural changes in the mechanical behavior of Arctic soils. The seasonal dynamics of permafrost are marked by summer thawing and autumn freezing of the upper layer of permafrost known as the active layer. This critical interface between permafrost and the atmosphere can be represented using the annual thermal envelope as a function of depth shown in Fig. 1.2.8.

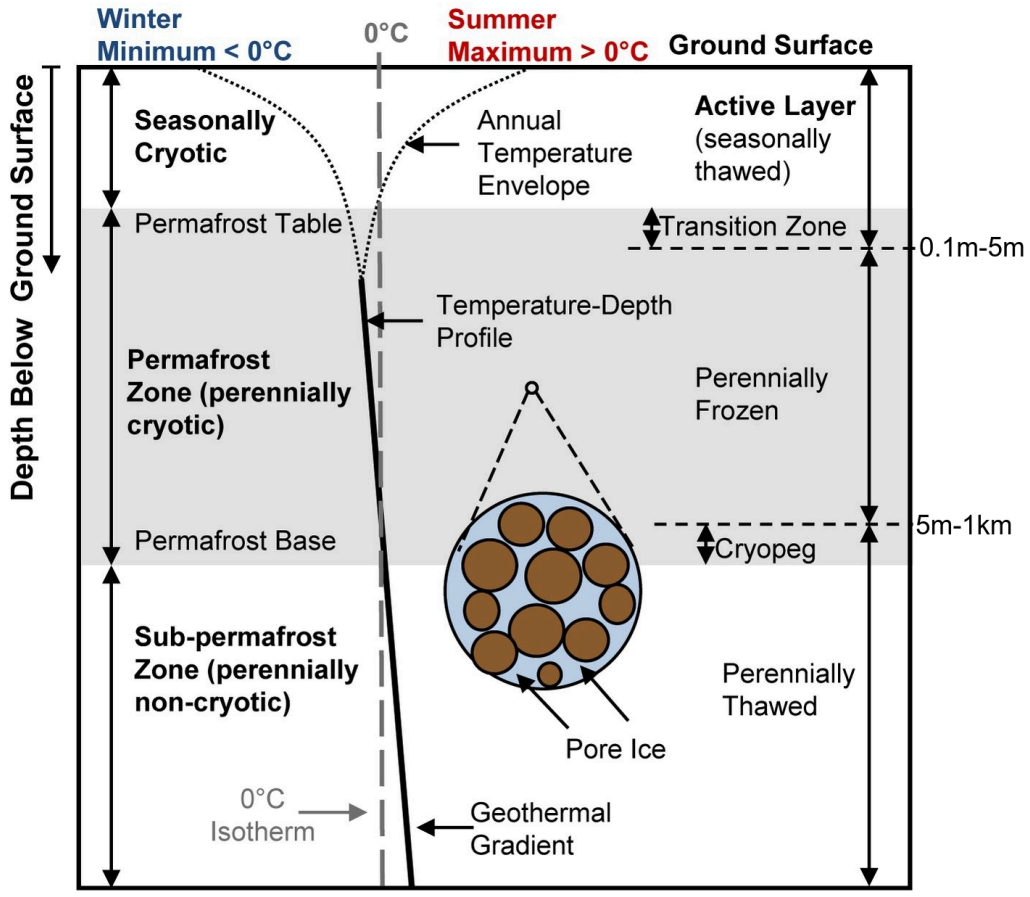

Figure 1.2.8 – Permafrost thermal profiles showing the evolution of the active layer (Walvoord and Kurylyk, 2016, adapted from Woo, 2012).

The presence of ice in the porous soil matrix leads to significant changes in the mechanical behavior of Arctic soils. From the thermal envelope as a function of depth, we can distinguish three main domains, independent of the geological nature of the soil horizons concerned. The active layer, the interface between the atmosphere and the geosphere, has the greatest annual thermal amplitude between winter and summer maxima. With temperatures above the melting point of water, this layer thaws and behaves in summer similarly to non-cryogenic soil. For example, the dynamics of a thawed histosol horizon

in a peat bog will be mainly governed by the dynamics of the histosol itself during the summer. The presence of a large quantity of organic matter and liquid water make this layer particularly active from a bacteriological and plant point of view. The nature of the substrate and the maximum thickness of the active layer determine the type of vegetation that can grow on the surface. In return, the presence of roots in the soil tend to modify the active layer thickness (Orgogozo, Prokushkin, et al., 2019). Freeze-thaw cycles cause the formation of characteristic structures known as cryoturbation patterns.
The main cryoturbation phenomenon that can be observed in soils with low gradients (particularly the flood plains of Arctic watersheds) is the formation of polygons (ice-wedge). This polygonation of the soil occurs as a result of recurrent freezing and thawing cycles of the active layer and the local maintenance of ice flakes intersected by cryodessication cracks. Other types of cryoturbation patterns include pingos which corresponds to a subsidence around an ice wedge, resulting in the formation of a conic-shaped hill. An example of polygonal soil formation (pingo) can be seen in Fig. 1.2.9.

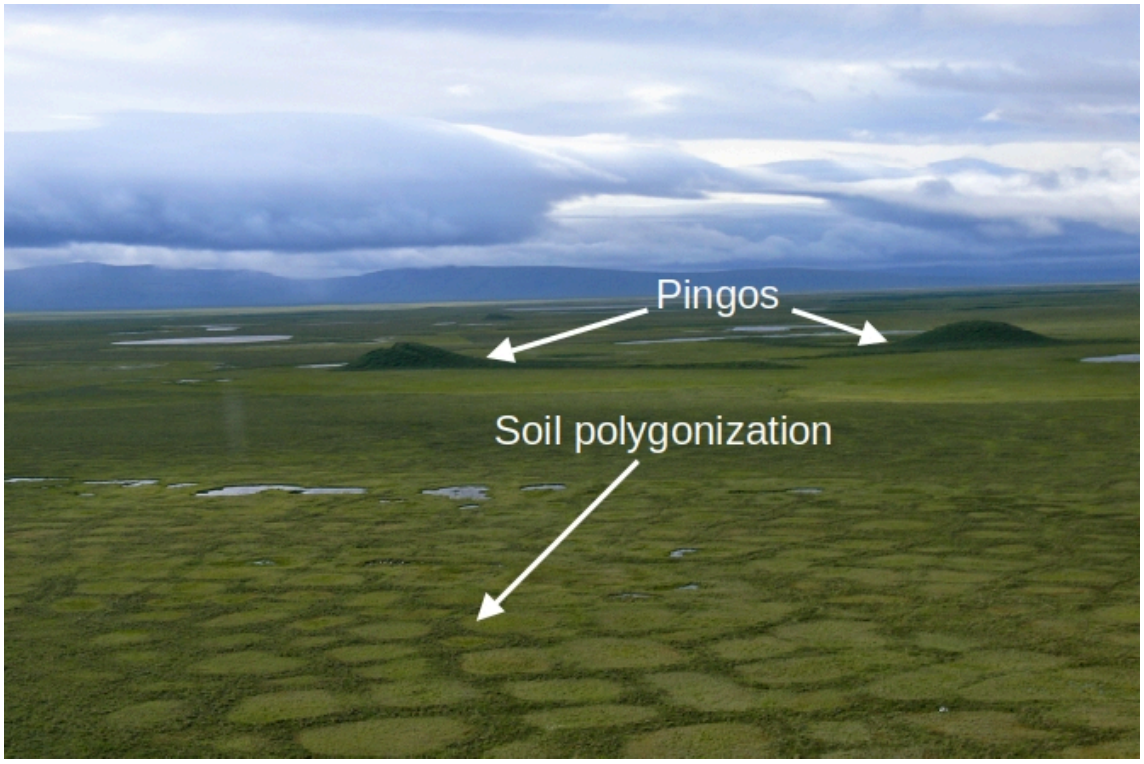

Figure 1.2.9 – Different cryoturbation structures occurring in permafrost-affected regions *CC-BY 2.0 Bering Land Bridge National Preserve*.

The formation of an ice-wedge may be simultaneous with the thawing of the active layer, which is referred to as syn-genetic. This is essentially the case where sedimentary material from upstream in the catchment is deposited simultaneously with the formation of ice polygons. On the other hand, ice-wedges may form after the permafrost has formed. This formation is therefore described as epi-genetic. Differential ice-wedge formation

occurs in particular when there is local warming of the permafrost (Liljedahl et al., 2016). Below the active layer, the lower layer represents the permanently frozen permafrost horizon. The permafrost layer in the strict sense has the lower and upper limits of the 0 °C isotherm. By definition, permafrost in the strict sense is considered impermeable (Woo, 2012). The permafrost layer in the strict sense stops when the permafrost temperature reaches the 0 °C isotherm again due to the Earth's geothermal gradient. The progressive formation of a polygonal soil causes the appearance of permeable vertical fractures that facilitate the infiltration of water into the soil. These vertical exchanges can have a significant impact on the hydrological balance of a catchment area. Another cryoturbation phenomenon is the formation of thermokarstic lakes, detailed in the following section.

1.2.4.2 *Thermokarstification*

Thermokarstification is a geomorphological phenomenon associated with thawing permafrost and soil subsidence. The term "karst" draws an analogy with the erosive processes that take place in carbonate geological formations. The difference in a cold environment lies in the nature of the processes involved in the erosion of the substrate. In the case of karstification in a carbonate domain, erosion is mainly achieved by the dissolution of carbonates or chlorides by meteoric water, resulting in vertical water exchange within a limestone formation. In the case of thermokarst, erosion is represented by the melting of the interstitial ice contained in the cryogenic soil horizon, leading to the gradual degradation of the permafrost. Thermokarstification essentially takes the form of a landscape covered with circular to ovoid lakes of small area (rarely more than few km^2) and shallow depth (around one meter). The formation of a thermokarst lake is illustrated in Fig. 1.2.10.

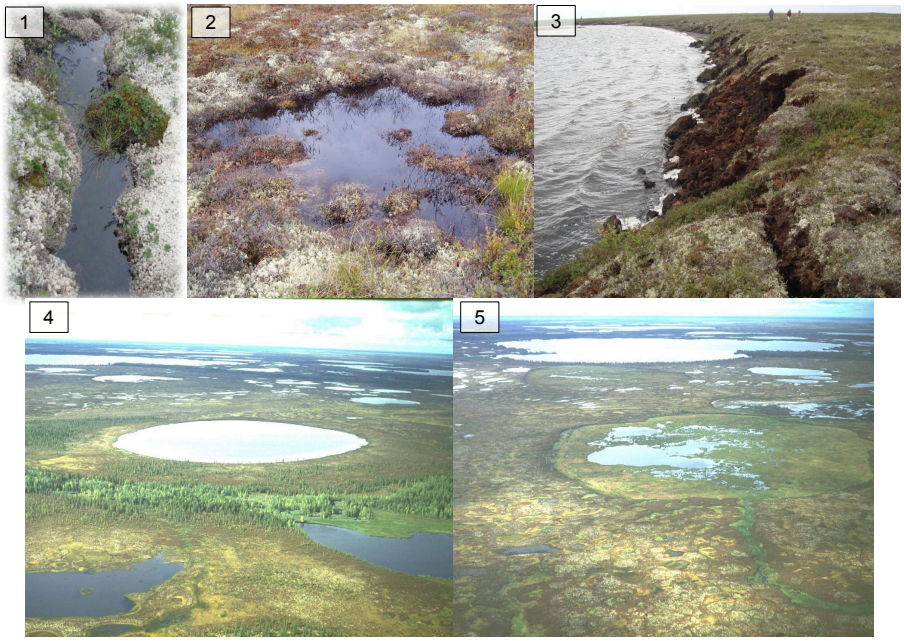

Figure 1.2.10 – Thermokarstic lake evolution in a typical Western Siberian Lowland watershed (Khanymey, Western Siberia, adapted from Pokrovsky et al., 2014).
1. Surface cracking of the cryptogamic cover and stagnation of residual water from winter snowmelt;
2. Submersion of mound *Sphagnum* and death of submerged lichens;
3. Acceleration of coastal erosion and gradual enlargement of the lake. Dissolution of the organic acids contained in the peat's porous constituent media;
4. Stabilization of the lake, named thermokarst lake at this stage;
5. Drainage of the lake into the hydrological network. Closing of the lake by bryophytes (*Khasyrei* in Russian).

The initiator of the formation of a thermokarst lake is a crack in the soil structure, particularly when a polygonal soil structure is formed. A depression then forms at the boundary of several ice wedges. The deepening of the depression, combined with the presence of an impermeable cryogenic horizon at depth, favors the accumulation of water in the depression. This submerges and kills the vegetation. The cessation of plant activity due to submergence in turn destabilizes the soil structure, accelerating the erosion of the banks of the thermokarst lake. When thaw water starts to accumulate in a depression, the thermokarst lake is formed. A thermokarst can also disappear and dry up as the lake bank erodes. Two lakes may merge, or the lake may drain into the river system. After drainage, the surface released by the thermokarst is recolonized by bryophytes.
The liquid water thus present at the surface causes a thermal disturbance, promoting the exchange of latent heat between the surface liquid water and the permafrost. The water content of the thermokarst lake is a direct result of aerobic degradation at the surface and anaerobic degradation at depth of the organic matter stored in the thawed cryogenic horizons (Pokrovsky et al., 2014). Dissolved organic matter content is studied in several

studies, especially in the Western Siberian Lowlands (Payandi-Rolland, L. Shirokova, Tesfa, et al., 2020) and in the Canadian Arctic (Olefeldt and Roulet, 2014). As a result of bacterial degradation, thermokarst lakes can be considered as emitters of greenhouse gases, mainly in the form of carbon dioxide and methane. The accumulation of organic matter is also the source of heavy element accumulation (mercury, lead, cadmium) due to bioaccumulation during the life cycle of living beings on one hand and low water flow in the arctic wetlands on the other hand. (Gordon et al., 2016).

1.3 CHALLENGES OF COLD ENVIRONMENTS UNDER CLIMATE CHANGE INDUCED PERMAFROST THAW

1.3.1 *Climatic model projections at a century time-scale*

The awareness of the fragility of arctic ecosystems dates from the 1980's when the first regular series of satellite images of the arctic ice pack became publicly available. During this same period, the development of remote sensing and remote monitoring techniques fostered the study of arctic environments. The first satellite images showed a significant reduction of the ice pack surface throughout the years (about -4.7% of the ice pack surface each summer since 1979, Yadav et al., 2020). The vulnerabilities of such ecosystems is pointed out in two early studies of the potential impacts of climate change in arctic regions (Manabe and Stouffer, 1980; Schlesinger and Mitchell, 1987). This vulnerability is due to the annual net radiative imbalance in arctic environments. This imbalance is caused by the significant seasonality of solar load in arctic regions, meaning that the ecosystems rely on latent heat flux exchanges occurring mainly through evapotranspiration (Hinzman and Kane, 1992).

The large amount of carbon stored in permafrost soils, particularly in peat bogs, is also one of the scientific questions to be asked about the impact of climate change on the polar regions. The amount of carbon stored as organic matter in cryosoils is estimated to be about $1.7 \cdot 10^{18}$ g. (Tarnocai et al., 2009). The organic matter can be considered stabilized in cryosoils if the increase of the active layer thickness is limited and if the mean annual temperature remains below 0 °C.

Successive IPCC reports show the significant impact of global climate change on arctic ecosystems. In particular, the special report on the arctic regions attached to the Fifth Assessment Report (Meredith et al., 2019) show significant upward trends in precipitation and temperature anomalies at the scale of the polar regions. Recent observations of mean temperature trends in arctic permafrost show an increase in mean annual temperature of $+0.4(\pm 0.25)\ ^{\circ}C.yr^{-1}$ for areas with continuous permafrost and $+0.1(\pm 0.1)\ ^{\circ}C.yr^{-1}$ for areas with discontinuous permafrost (Biskaborn et al., 2019). The observed trend in temperature increase is visible in Fig. 1.3.1.

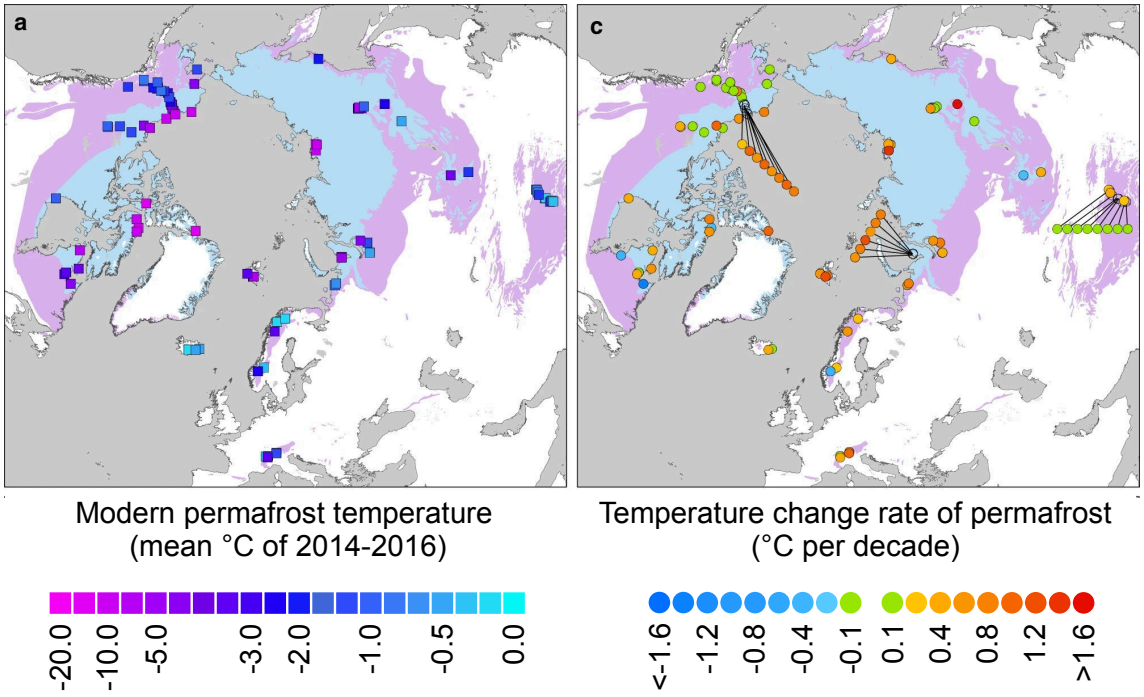

Figure 1.3.1 – Evolution of permafrost temperature and change rate for the arctic permafrost. The square plots represent the average modern temperature for years 2014 to 2016). The dots represent the temperature change rate for each location (from Biskaborn et al., 2019).

This temperature increase is higher than anywhere else on Earth for the time scale considered (from 2008 to 2016). This climatic phenomenon is known as *arctic amplification* (Davy, Chen, et al., 2018; Xie et al., 2023). If the observations made in the special report are combined with the result of the sixth climate model intercomparison session (CMIP6) and based on the most pessimistic greenhouse gas emission scenario (SSP8.5), the temperature anomaly is between +6 °C and +10 °C in the arctic regions by 2100. Precipitation anomalies range from +10 to +40%, with good reliability. A map of worldwide predicted temperature anomaly and for predicted precipitation anomaly for year 2100 are respectively shown in Fig. 1.3.2 and in Fig. 1.3.3.

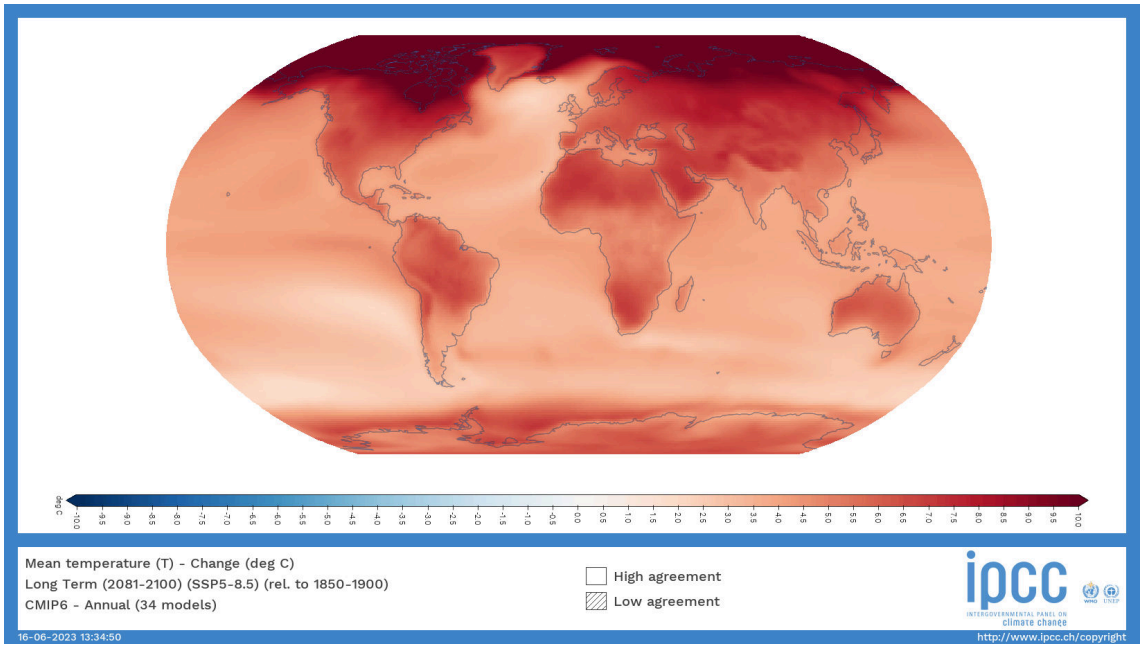

Figure 1.3.2 – Mean temperature anomaly (in °C) for year 2100 according to the SSP5-8.5 scenario for the CMIP6 climatic model intercomparison.

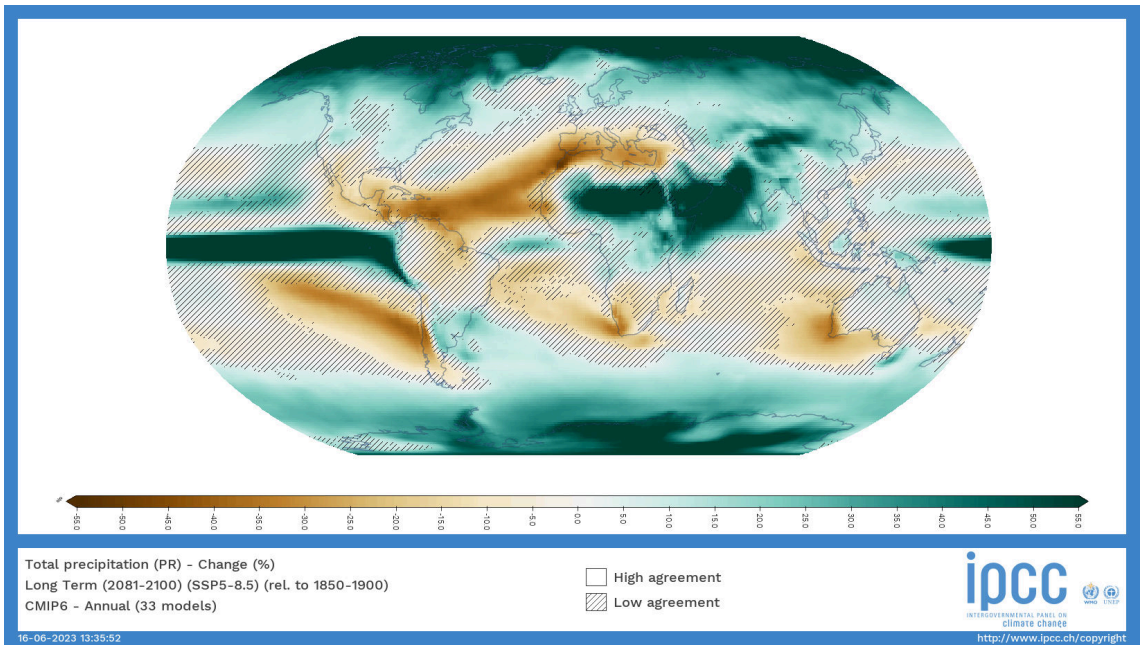

Figure 1.3.3 – Mean precipitation anomaly (in % of actual precipitation amount) for year 2100 according to the SSP5-8.5 scenario for the CMIP6 climatic model intercomparison.

From Fig. 1.3.2 and Fig. 1.3.3, it is possible to see that arctic regions are prone to shown positive temperature anomalies (from +5 °C to +10 °C) by 2100 and positive precipitations (from +5% to +55% of actual precipitation amount). In other words, the arctic climate is predicted to get warmer and rainier. The intensity of the arctic amplification is one of

the main unknowns in modeling of the climate for the coming century. The role and the recurrence of the arctic amplification in climate disruption have been and still are in the climate debate (Serreze and Francis, 2006; Davy and Griewank, 2023). This complexity comes from the climatic feedbacks of thawing permafrost that where identified by Walvoord and Kurylyk (2016) and shown in Fig. 1.3.4.

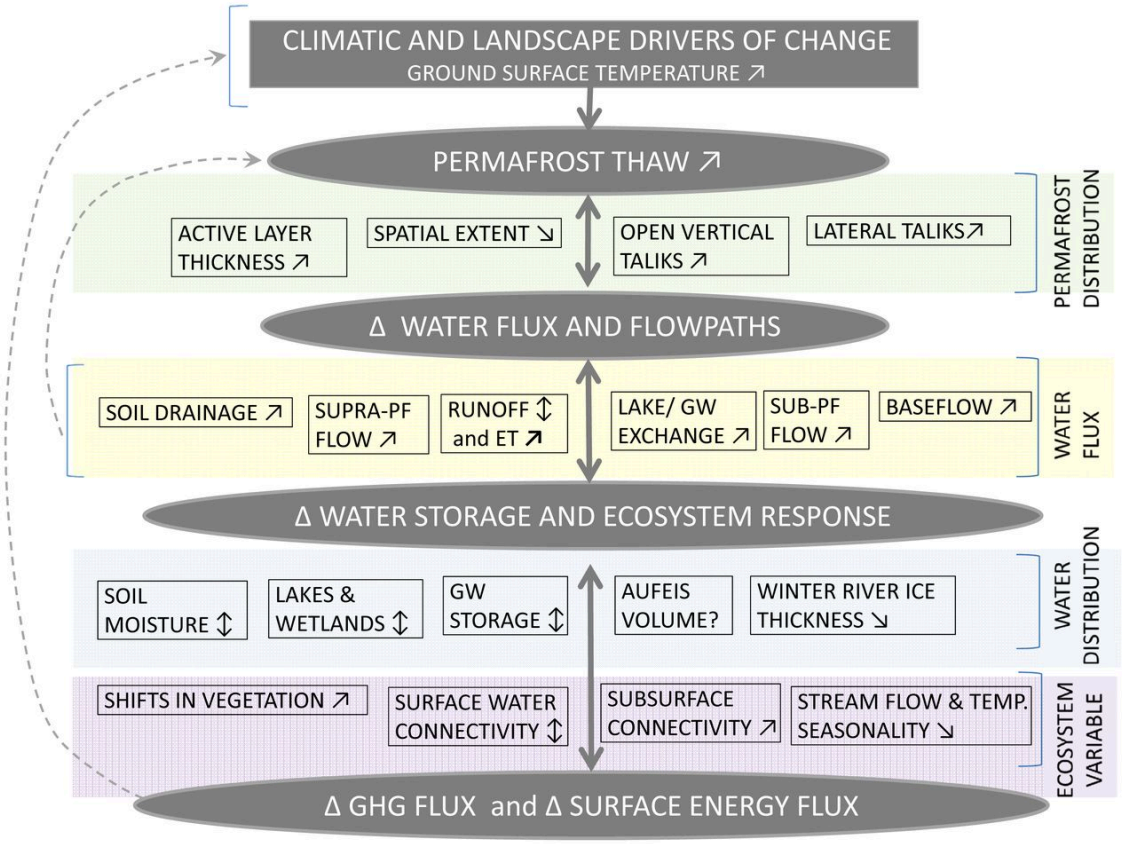

Figure 1.3.4 – Identified permafrost retroactions on different Earth System components (adapted from Walvoord and Kurylyk, 2016).

Indeed, Walvoord and Kurylyk (2016) shows that arctic permafrost is at the heart of numerous climate feedback loops that can significantly increase the effects of climate change on a regional to global scale. Firstly, increases in mean annual permafrost temperatures cause increases in active layer thickness and decreases in the lateral extent of permafrost. Indeed, regions where permafrost is continuous will be fragmented as a result of rising mean temperatures. It should be noted that the creation of such discontinuities causes the formation of taliks, enabling vertical exchanges within the permafrost. These retroactions cause in return various effects on hydrology and ecology and also in mass and energy at regional scale. Each consequence is presented in detail in section 1.3.2 for hydroecological threats, in section 1.3.3 for civil engineering challenges and in section 1.3.4 for direct anthropic issues.

1.3.2 *Hydroecological impacts due to permafrost thawing*

The stability of arctic ecosystems is threatened by permafrost degradation in several ways. From a hydro-ecological perspective, the risks posed by permafrost thawing, which in turn lead to feedback loops on global climate dynamics, are assessed in this section.

1.3.2.1 *Runoff and nutrient export*

Rivers are the main vector for the export of nutrients to the oceans for most chemical element cycles (carbon, nitrogen, phosphorus, Triska and Higler, 2009). As shown in section 1.3.1, predictive climate models for the year 2100 indicate a positive temperature anomaly and excess precipitation at the scale of arctic catchments. Thawing permafrost could also contribute in a greater amount of available mobile liquid water to the water balance of the catchments. Currently, increased precipitation is observed in several studies of arctic catchment hydrology (Pavelsky and Smith, 2006; Rawlins et al., 2009), and some increase in snowmelt runoff has been assessed in arctic catchments (as it can be seen in Stuefer et al. (2017) in Fig. 1.3.5). Greenhouse gas emissions from thawing permafrost are expected to be exacerbated by the increase in thawing permafrost, causing in addition significant soil subsidence (Park, Fedorov, Konstantinov, et al., 2021). However, the link between increased flow in major arctic rivers and permafrost thaw cannot be established as a general rule (Ye et al., 2004).
Thawing permafrost destabilizes soil structure, particularly in arctic peatlands, which consist of labile organic matter (Z. Zhang et al., 2023). In addition to the mechanical erosion of the soil described in section 1.3.3.2, the organic matter thus degraded by microbial activity is then washed away by precipitation.

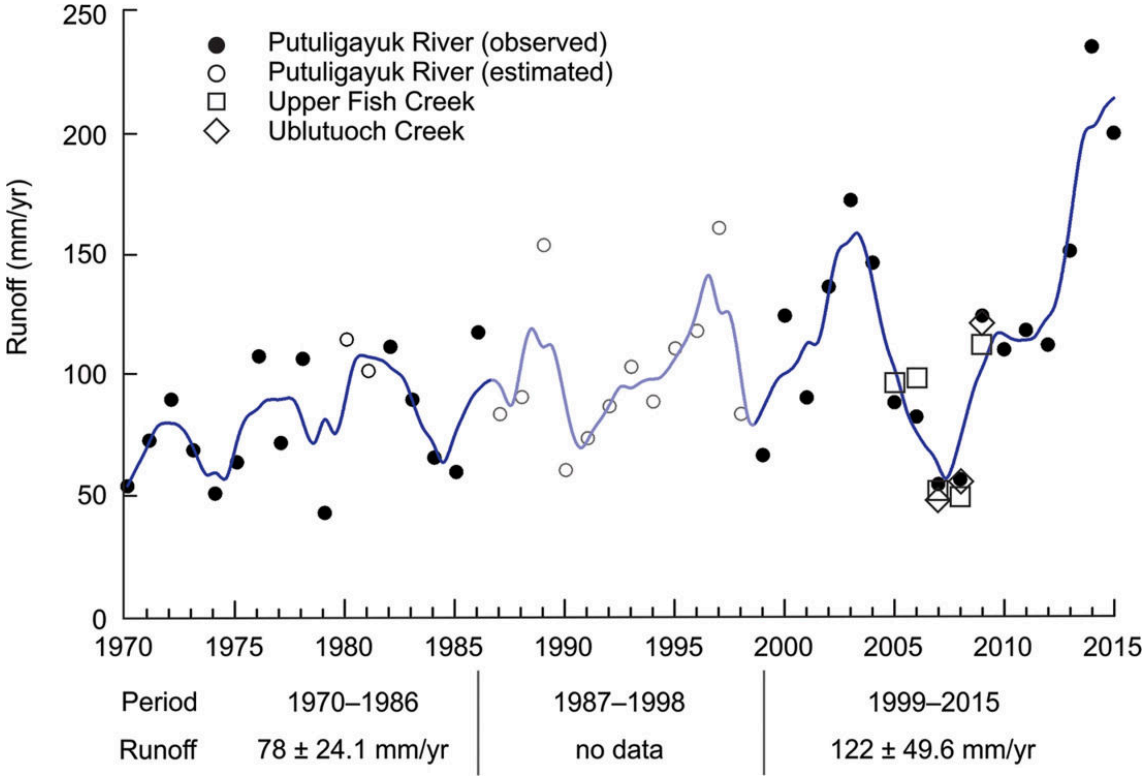

Figure 1.3.5 – Increased variability in the Putuligayuk River (North Alaska, USA) annual runoff with time. Mean annual runoff and standard deviation for two periods are summarized at the bottom of the figure. Fitted line shows locally weighted smoothing (LOESS) trend. The shorter runoff record from the Upper Fish and Ublutuoch Creeks overlays the Putuligayuk River record from 2005 to 2009 (from Stuefer et al., 2017).

1.3.2.2 *Ecosystem shift*

The increase in mean annual temperatures for all subarctic and arctic ecosystems may cause a northward migration of the taiga-tundra boundary, in addition to the thawing of permafrost and the degradation of organic matter. This ecosystem transition may lead to the disappearance of arctic ecoregions and a vegetation shift from tundra to taiga (Limpens et al., 2021). This ecosystem transition is initially taking place by the appearance of bushes and dwarf trees (in particular the dwarf birch, *Betulana nana*) in low tundra environments. The persistence of shrubs and bushes facilitates the growth of larger bushes (Frost and Epstein, 2014) and the germination of seeds from larger trees (Hobbie and Chapin, 1998). This reduces the carbon storage capacity of arctic peatlands [1], tipping the balance towards greenhouse gas emissions.

The extension of shrub cover and forest areas on land previously occupied by permafrost is quantified in Frost and Epstein (2014). An excerpt of these results are visible in Fig. 1.3.6.

1 The carbon storage capacity of tundra environments is about 100 $kgC.m^{-2}$ and about 40 $kgC.m^{-2}$ for taiga forests (Tifafi et al., 2018).

Of 11 study sites in northern Siberia, the vast majority saw an increase in shrub cover between 1960 and 2000. The same trend can also be observed for larch cover.

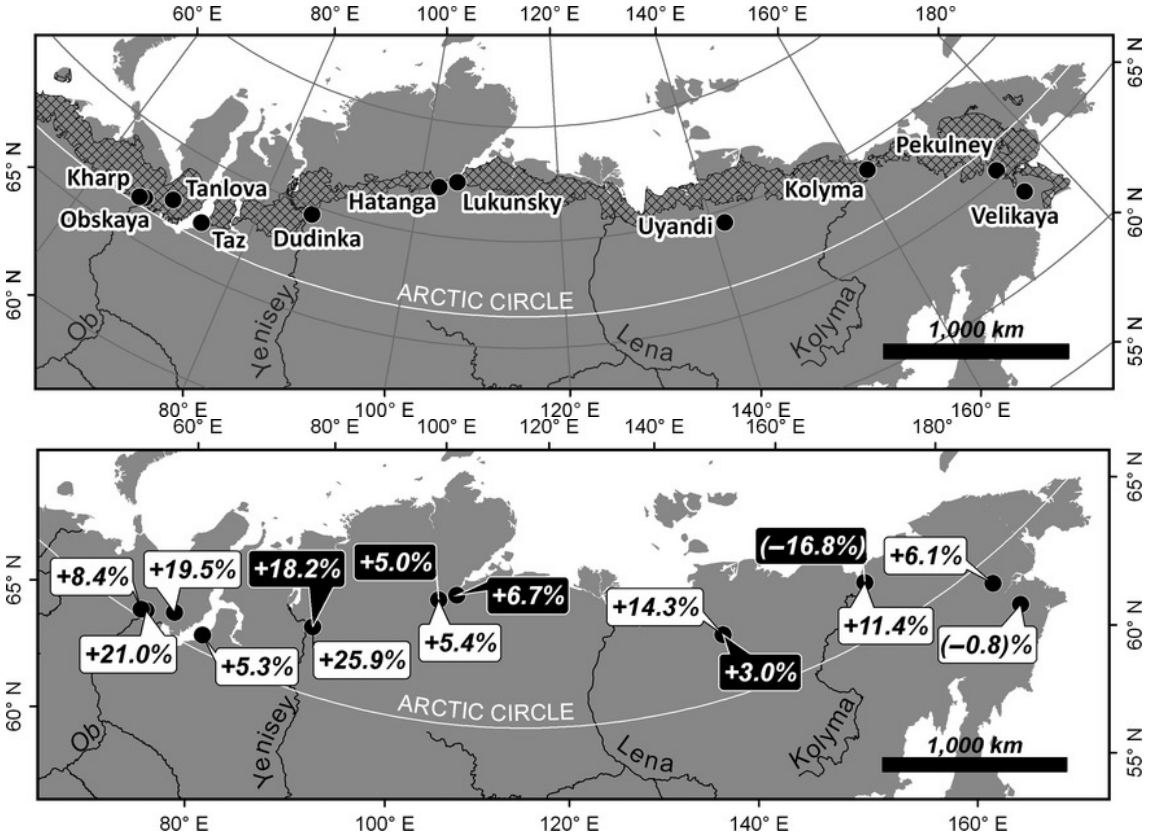

Figure 1.3.6 – Net changes in tall shrubs cover (white boxes) and larsh cover (black boxes) on 11 tundra study sites in Northern Siberia (Frost and Epstein, 2014).

1.3.2.3 *Wildfire and methane bubbles*

The IPCC report highlights the increased likelihood of forest fires in subarctic and arctic regions (Meredith et al., 2019). The occurrence of high-intensity wildfires can trigger a number of feedback loops. First, the burning of peat in the Arctic and trees in the subarctic generates large amounts of greenhouse gases. Such sudden release of greenhouse gases creates a suitable environment for the multiplication of thunderstorms, which in turn increase the risk of fire outbreaks. Carbon-rich ash deposition in turn leads to a reduction in albedo, increasing ground temperature and the risk of fire (Kharuk et al., 2023). Other triggers of wildfire increase include the change in dominant wind directions (Schaepman-Strub and Kim, 2022) and the atmospheric pressure cyclic anomalies (Arctic Oscillation, Kim et al., 2020). The increase in forest fires can already be seen in satellite data collected since the 1990s. Indeed, a steady increase in the spatial extent and intensity of forest fires has been observed, as presented in an article published online by Copernicus Climate Service (Copernicus, 2021), where Fig. 1.3.7 illustrates the soil moisture anomaly for summer 2021.

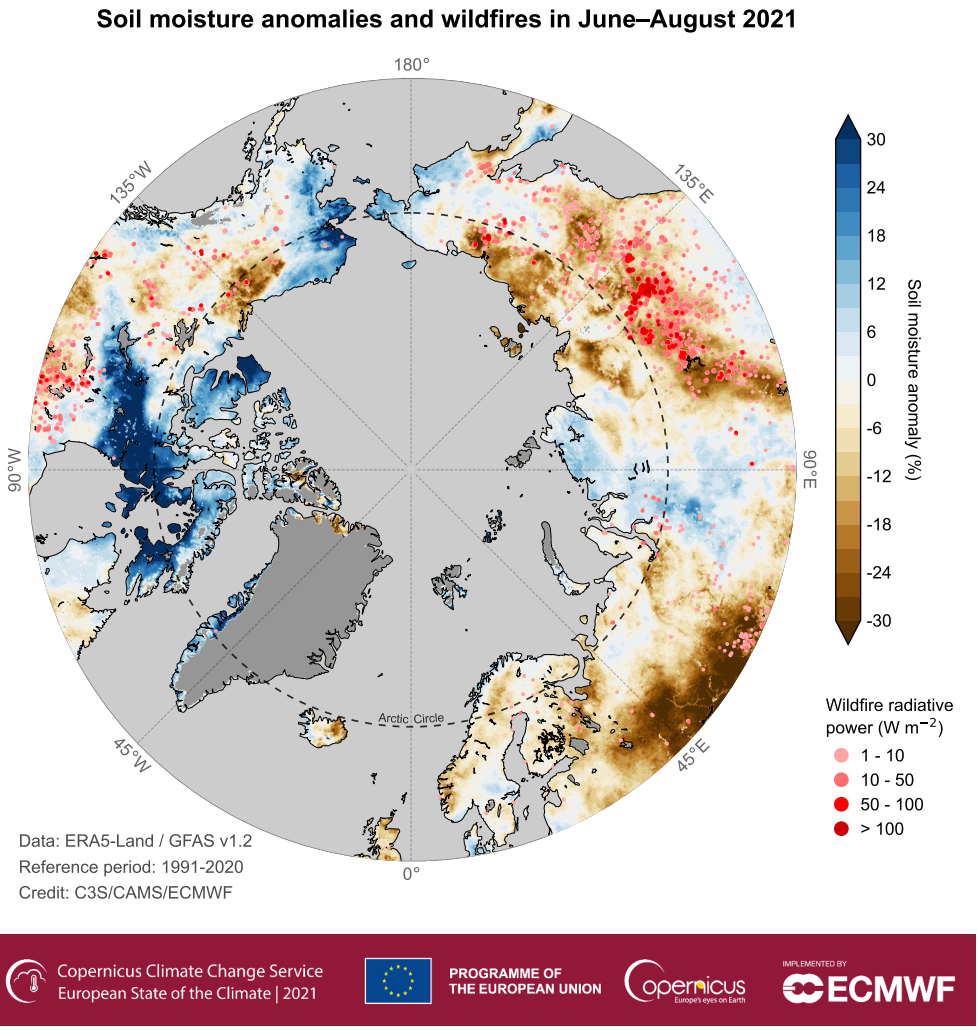

Figure 1.3.7 – Map showing soil moisture anomalies and locations[3] of wildfires in June–July–August 2021. The Arctic Circle is indicated with a dashed line. The red shaded dots represent the total wildfire radiative power (a measure of wildfire intensity). The anomalies are calculated as a percentage of the average for the 1991–2020 reference period. Data sources: ERA5-Land soil moisture and CAMS GFAS v1.2 wildfire data. Credit: C3S/CAMS/ECMWF. © Copernicus https://climate.copernicus.eu/esotc/2021/arctic-wildfires

The difficulty of controlling and extinguishing wildfires in the Arctic, partly because they are so widespread, is a major problem. The rapid spread of the fire and the lack of natural barriers (rivers) or man-made barriers (roads or railways) make the fire impossible to limit its progress. Another reason why arctic forest fires are rarely extinguished by humans is the lack of effective fire-fighting equipment for such a large area. However, human activities remain the main cause of the fires. The presence of high concentrations of methane in unsaturated soil horizons can also contribute to the spread of fire. Methane pockets in soil horizons can also lead to dormant fires lasting from several weeks to

several years. As these relic fires are not visible at the surface, they are difficult to quantify and predict (Kuklina et al., 2022).

1.3.3 *Geomechanical threats*

1.3.3.1 *Infrastructure stability*

Major infrastructures (gas and oil pipelines, roads, railways, airports) are present in the Arctic despite the generally low population density (Dmitry A Streletskiy, Suter, et al., 2019). Indeed, most of the major Arctic agglomerations derive their profits from mining (Tromsø in Norway and Kiruna in Sweden) or producing gas and oil (Norilsk in Russia). Because of its harsh climate, Arctic roads are often too few and far between. Maintaining these communication routes is also costly for the political structures involved, in North America as well as in Europe and Eurasia (Hjort, Karjalainen, et al., 2018; Hjort, D. Streletskiy, et al., 2022).
Cryogenic horizons, which are mechanically stable and inherently impermeable, are often sought for infrastructure foundations in arctic environments. It is common practice in arctic civil engineering to use systems to maintain subzero ground temperatures around infrastructure to avoid the thermal bridges that cause the permafrost to heat up. One example is the use of heat pipes on the Trans-Alaska Oil Pipeline (Fig. 1.3.8a).
As the thickness of the active layer increases and permafrost disappears, the stability of buildings and infrastructure becomes a major concern (Shiklomanov, Dmitry A. Streletskiy, et al., 2017). Examples of infrastructure damage caused by thawing permafrost are shown in Fig. 1.3.8b.

(a) **(b)**

Figure 1.3.8 – Different forms of infrastructure damage (a): Caloducts on the trans-Alaska pipeline CC-BY-SA 4.0 Enrico Blasutto, (b): Building collapse due to thawing permafrost in Alaska *CC-BY-SA 4.0 Fbaudoux.ir*.

The major cities of the Siberian Arctic, Murmansk (305,000 inhabitants) and Norilsk (176,000 inhabitants), are directly concerned by this issue, aggravated by the risk of technical accidents owing to the presence of environmentally hazardous facilities (Shiklomanov and Laruelle, 2017).

1.3.3.2 *Permafrost erosion*

Thawing permafrost causes the soil to become mechanically unstable and ductile. This instability can lead to gravitational collapses, which can be dangerous for human infrastructures at catchment scale. In certain circumstances, the presence of liquid water in contact with nanosized particles may cause a liquefaction phenomenon known as fluidization. If a flow of water is possible, a crater can then form similarly to the thermokarst dynamics described above. One of the most spatially extensive examples is the Batagaika 'crater' or mega-slump in Eastern Siberia (Turetsky et al., 2019), shown in Fig. 1.3.9. The spatial extent of the crater is directly dependent on the local climate, which allows the permafrost to melt. Permafrost erosion is also visible in the coastal regions of the Arctic, for example on Herschel Island (Alaska, Cunliffe et al., 2019).

(a) **(b)**

Figure 1.3.9 – (a) Permafrost thaw slump in Batagaika crater (Sakha Republic, Russia, adapted from Turetsky et al., 2019) ((b) Permafrost erosion front on Herschel Island (Yukon, Canada).

Coastal erosion is set to increase in intensity if combined with the sea level rise and the watershed runoff increase from continental areas.

1.3.4 *Risk for public health*

Global warming of average annual temperatures in arctic permafrost peatlands threatens the stability of the organic matter contained in these regions. The thawing of organic matter can cause a number of risks. At present, the best assessed risks are the hydro-ecological risks (presented in section 1.3.2) and the geotechnical risks (presented in section 1.3.3). However, other risks must be taken into account in the assessment of the

consequences of permafrost thaw, particularly at the level of human society due to the amount of carbon stored in these frozen soils.
Paleontological discoveries of Pleistocene or early Holocene animal or anthropological remains are common (Maschenko et al., 2021). The advanced preservation of animal organic matter, similar to a domestic freezer, is made possible by the stability of permafrost temperatures below the melting point of water. These discoveries have allowed an in-depth study of the Pleistocene fauna of Eurasia and, thanks to the optimal preservation of cellular DNA, have provided valuable information on the palaeoclimatic evolution of these regions. As the permafrost warms and thaws, the thermal stability of organic matter is broken and the bacterial fauna trapped in the permafrost is activated. In addition to the loss of important palaeontological information, melting permafrost raises questions about the preservation and reactivation of pathogens trapped in organic matter at the time of sedimentation. This issue is well known in epidemiology, particularly following the anthrax epidemic observed in reindeer herding populations in July-August 2016 (Liskova et al., 2021). Epidemiological modeling tends to show that an anthrax epidemic with human-to-human transmission is possible on a local scale, especially due to permafrost degradation (Hueffer et al., 2020; Revich et al., 2022).
The problem of reactivation of pathogenic organisms can also be observed for viral strains trapped in organic matter. The viability of preserved viral material has been demonstrated in several studies (Alempic et al., 2023; Wu, Trubl, et al., 2022; Wu, Bottos, et al., 2022). Epidemiological studies suggest that the risk of the emergence of new zoonoses pathogenic to humans is not negligible. This is particularly the case for coronaviruses and influenza viruses (Hofmeister et al., 2021). These health and economic risks directly affect arctic indigenous populations in Siberia, Canada and Alaska.

1.4 MAKING THE LINK BETWEEN PERMAFROST AND ATMOSPHERE DYNAMICS: THE LOW VEGETATION COVER

The complexity of the critical zone at the interface between atmospheric and geological processes has been addressed in this chapter through a number of different prospects. The effects of global climate change indicate a more rapid increase in temperature and precipitation anomalies, faster than in the rest of the world. Arctic low vegetation cover represents the biological interface between the atmosphere and the geosphere. That means that all the processes taking place respectively in the geosphere (permafrost thaw, soil erosion) and in the atmosphere (climate change) will have consequences and feedbacks on the low vegetation cover. This link between processes in the soil horizons and atmospheric processes is crucial for improving the quality of centennial climate predictions. The vegetation cover at the interface between these two major systems poses major challenges in terms of characterization and modeling.
The diversity of organisms present on the surface of the active layer poses specific modeling problems on both spatial and temporal scales. Indeed, permafrost-driven

processes can have different time scales than the growth of *Sphagnum*. Local heterogeneity in the soil cover can also have significant impact in the local hydrology balance which have to be taken into account. Moreover, some clues about the insulating role of the low vegetation cover can be given through temperature measurements in the field (section 1.4.1) and from some land surface models taking into account the role of the bryophyte and lichen cover (section 1.4.2).

1.4.1 *Field observations*

A measurement campaign between 2003 and 2005 on the experimental watershed of Kulingdakan (Eastern Siberia) was set up to collect long-term daily data for different moss cover, litter and soil depth. This data is partially reproduced in Fig. 1.4.1.

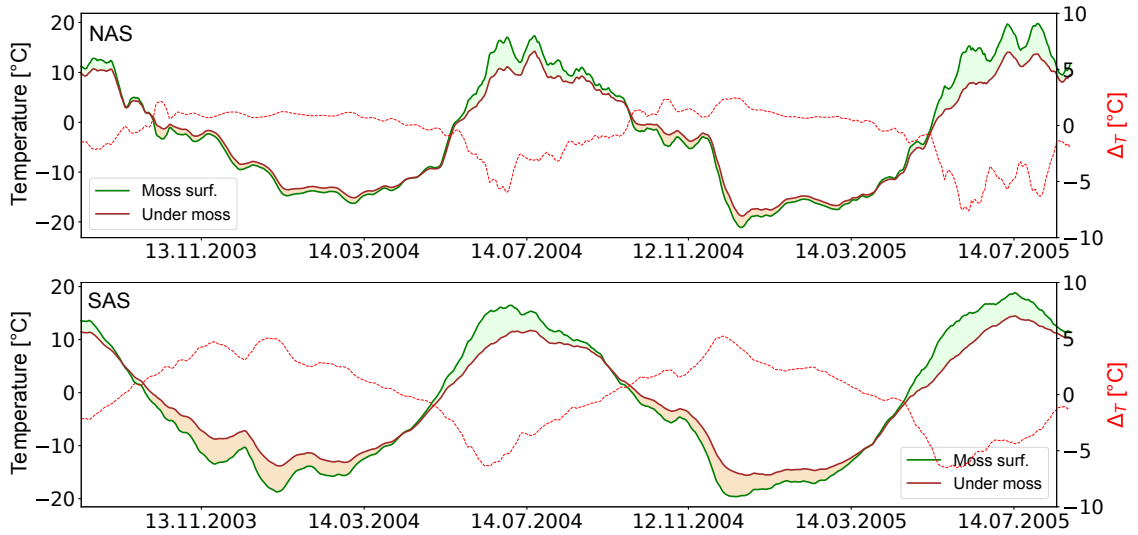

Figure 1.4.1 – Temperature evolution bryophyte surface temperature (Moss temp.) and sub-vegetation cover temperature (Under moss) at Kulingdakan watershed (Eastern Siberia). NAS stands for *North Aspected Slope*, SAS for *South Aspected Slope*. *Data courtesy of Anatoly Prokushkin*.

This data shows the temperature of moss surface temperature and litter temperature on a daily basis. One can see that during summers, the temperature of the moss cover is higher than the temperature of the litter, whereas it is the contrary for winter. During intermediate seasons (in spring and autumn), the temperature of the litter and the moss cover are the same. This temperature difference during the winter months on one hand, and summer months on the other hand can be explained by a capacity of this low vegetation layer to insulate the soil from solar radiative load in summer and from extreme cold below in winter with the help of the snow cover. This thermal insulation capacities are also shown in the results on some land surface models discussed below.

1.4.2 *Existing models*

Since the 1990s, various Earth System Models (ESM) have emerged in order to predict future impacts of climate change in a worldwide climate change scenario, and notably the CMIP (*Coupled Model Intercomparison Project*) model intercomparison series (Taylor et al., 2012; Eyring et al., 2016). For most of the models, the goal is to quantify the evolution in surface temperature, precipitation, and greenhouse gas fluxes. In this section, we will focus on one Earth System Model based on a grid description of the properties: JSBACH. Some early results found for the impact of the low vegetation cover will also be discussed in this section. Then, a brief presentation of the *permaFoam* solver, a open-source solver developed for the open-source computational fluid dynamics toolbox *OpenFOAM* for quantifying heat and mass transfers in a non-saturated porous medium with freeze/thaw is discussed. Finally, a summary of the work steps needed for the implementation of an effective boundary condition representing the arctic low vegetation cover (which constitute the main goal of this thesis) is presented.

1.4.2.1 *JSBACH model*

The land surface model JSBACH (for *Jena Schema for Biosphere-Atmosphere Coupling in Hamburg*) is a numerical model developed by the *Max Planck Institute für Meteorologie* at the University of Hamburg (Germany) since the early 2000's. The main aim of the JSBACH model is to create a predictive numerical model valid for several time and space scales of the condition at the lower boundary of the atmosphere. JSBACH is in fact a module of the ICON (Jungclaus et al., 2022) multi-element modeling package. The JSBACH model adopts a land surface representation in the form of a heterogeneity classification grid based on the land cover. The use of this model aims to provide the ICON supramodel with a quantification of heat and water transfers between the geosphere and the atmosphere, and to solve the energy balance equation at the interface. At present, development of the land surface model has resulted in JSBACH version 3. One can consult Reick et al. (2021) and Brovkin et al. (2009) for a broader description of the JSBACH model.
Some sensibility studies about the impact of low vegetation cover on global land surface model have been conducted using JSBACH model (Porada et al., 2016). The study aimed at considering a low vegetation cover between a seasonal snowpack and a soil on an arctic environment representative grid located in northern Alaska. This study showed a cooling effect induced by bryophytes and lichen to an average of 2.7 K (from 0 to 5.7 K). The parametric study on the thermal conductivity of bryophytes and lichen (available in Fig. 1.4.2).

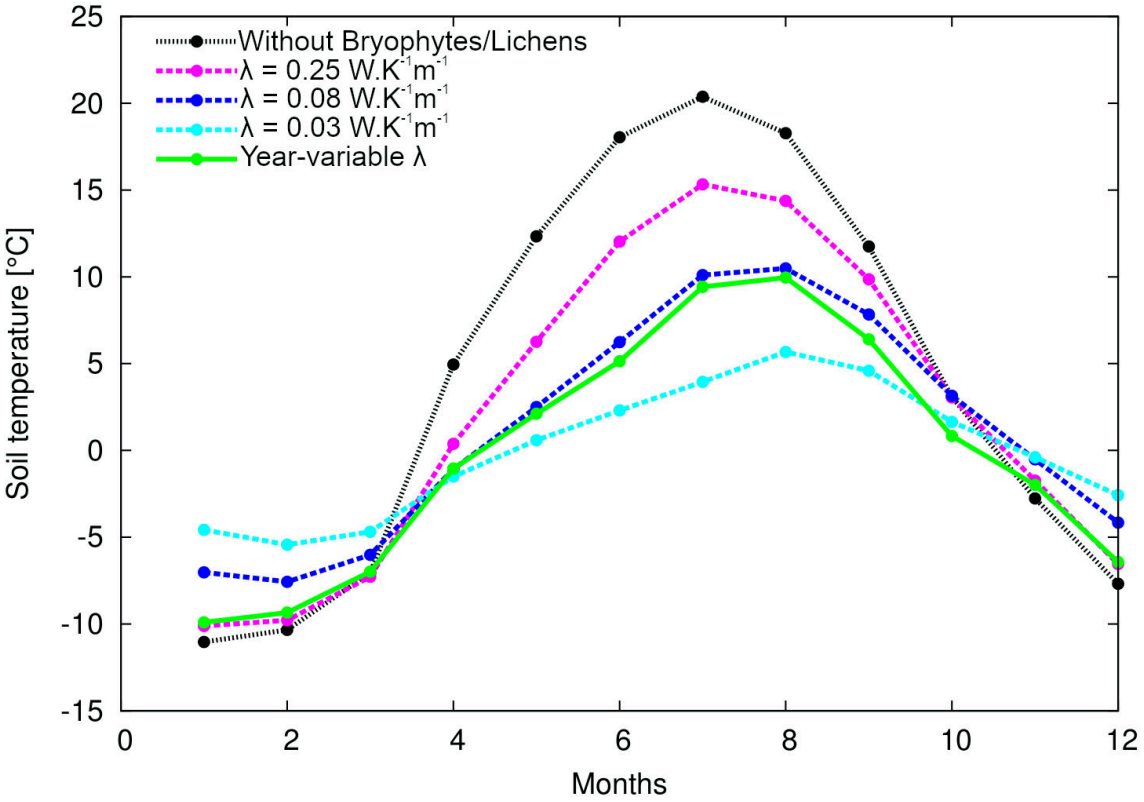

Figure 1.4.2 – Temperature of the uppermost soil layer of a model grid in JSBACH. The curves represents the temperature evolution throughout a year with a variable thermal conductivity λ in W.m^{-2} (modified, adapted from Porada et al., 2016).

The sensibility analysis conducted by the authors shows that applying different values for thermal conductivity of the bryophyte and lichen cover makes the thermal evolution significantly variable at a year scale. In a sense, adding a bryophytic/lichen cover between a snow cover and the soil layers flatten the temperature curve, causing the soil layer underlain by permafrost to be insulated from heat exchanges. On the contrary, the absence of a low vegetation cover makes the soil (and therefore permafrost) vulnerable to significant temperature variations.
The impact of the quantification of thermo-hydraulic properties of this low vegetation cover is crucial for an accurate modeling of heat and water fluxes in arctic domains, which means that quantifying transfer properties in various temperature and water saturation conditions is compulsory to refine the predictions on climate change impacts.

1.4.2.2 *PermaFoam*

Continental model have the advantage of being computationally lightweight and allow relatively accurate assessments of temperature changes worldwide taking into account a low vegetation layer in it. However, such models cannot precisely describe the physical phenomena occurring at a lower scale (freeze-thaw cycle, latent heat exchange). Such properties require the use of a mechanistic model in order to be considered a more de-

tailed physical description of the energy and mass fluxes in arctic regions. The *permaFoam* model (Orgogozo, Xavier, et al., 2023; Orgogozo, Prokushkin, et al., 2019) is a solver implemented in the open-source computational fluid mechanics toolbox *OpenFOAM* (Weller et al. (1998), `www.openfoam.org`, `www.openfoam.com`). This solver aims at computing energy and mass fluxes through a variably water-saturated porous medium. The solver is based on the resolution of a modified Richard equation (Richards, 1931) with a latent heat exchange coefficient incorporated in the solver. The first implementation of the Richards equation was made by Orgogozo, Renon, et al. (2014). This paper showed that a hysteresis between freezing and thawing of a uni-dimensional watershed, thus requiring the addition of a latent heat exchange coefficient in the solver. In the current version of permaFoam, four physical phases are considered:

- a solid matrix (soil, litter, or *Sphagnum* moss);
- liquid water;
- ice;
- air;

The model is based also on three assumptions for the computation of heat and water fluxes throughout a watershed:

- There are no density-driven flows and no advective heat transport (no convection),
- The solid phase in non-deformable,
- The melting temperature of ice is constant.

The *permaFoam* solver makes two computational steps. First, water and ice balance are computed using the modified Richards equation. When convergence is reached, the porous medium heat transfer equation is solved. The equations for both computation phase are presented in detail in Orgogozo, Prokushkin, et al. (2019) and in Orgogozo (2022). A summary of the inputs and outputs of the *permaFoam* solver are discussed in Fig. 1.4.3.

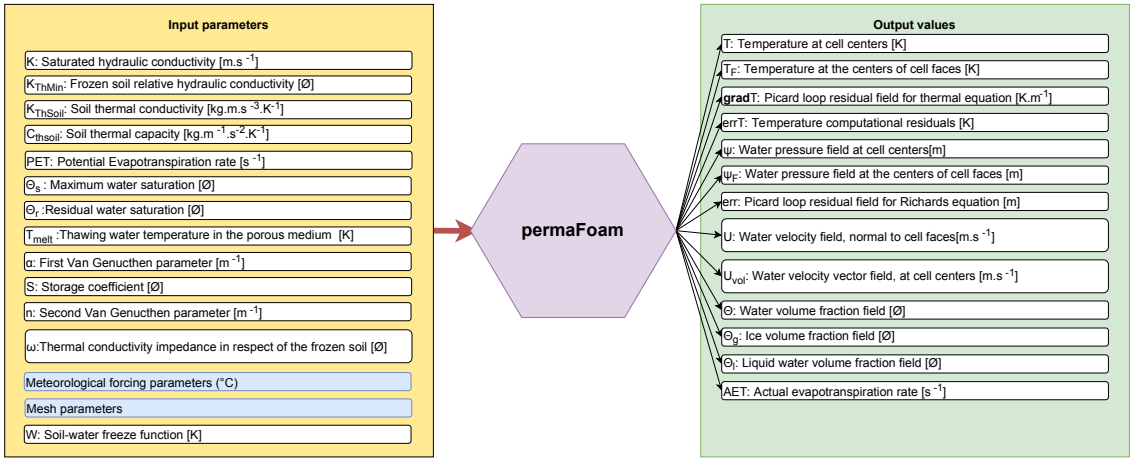

Figure 1.4.3 – Input and Output data in the *permaFoam* solver.

1.4.2.3 *Objectives of this thesis*

As part of this PhD project, we wanted to approach the problem of the arctic vegetation cover through its assimilation to a porous medium. Therefore, the following chapter aims to define the nature of a porous medium and the main techniques for characterizing the transfer of a porous medium. This characterization will be presented both experimentally and numerically. The choice to study the arctic vegetation cover by assimilating it to a porous medium is intended to avoid the spatio-temporal variability traditionally encountered in field studies. Indeed, each study site is peculiar to a given microclimate state and ecosystem, therefore obtained field results from a site cannot represent another site. In this thesis, statistical representativeness is no longer ensured by the multiplication of measurement replicates and samples in the field, but by the statistical establishment of a representative elementary volume (presented in detail in section 2.2.1.2). This approach restricts the study to the transfer properties of a given material of the vegetation cover. In addition to reproducibility, which is only limited by the available computational resources, digital characterization makes it possible to isolate physical properties from their interdependencies in the natural environment.

2

ARCTIC VEGETATION AS A POROUS MEDIUM

2.1 WHY CONSIDER THE ARCTIC VEGETATION COVER AS A POROUS MEDIUM?

A porous medium is by nature a composite medium, *i.e.* it contains at least two different phases, and at least one of which is solid. The other phases may be solids or other fluids, miscible or non-miscible. The fluid fraction in question forms a network of galleries around the solid matrix, which may be interconnected (open pore) or isolated (closed pore). The first basic property of a porous medium is its porosity, which is the ratio between the pore's (void's) volume on the total volume. Porous media are present in many domains in science and everyday life (sponges, heat exchangers, sand, clay among other materials). A representation of a ideal porous medium is shown in Fig. 2.1.1.

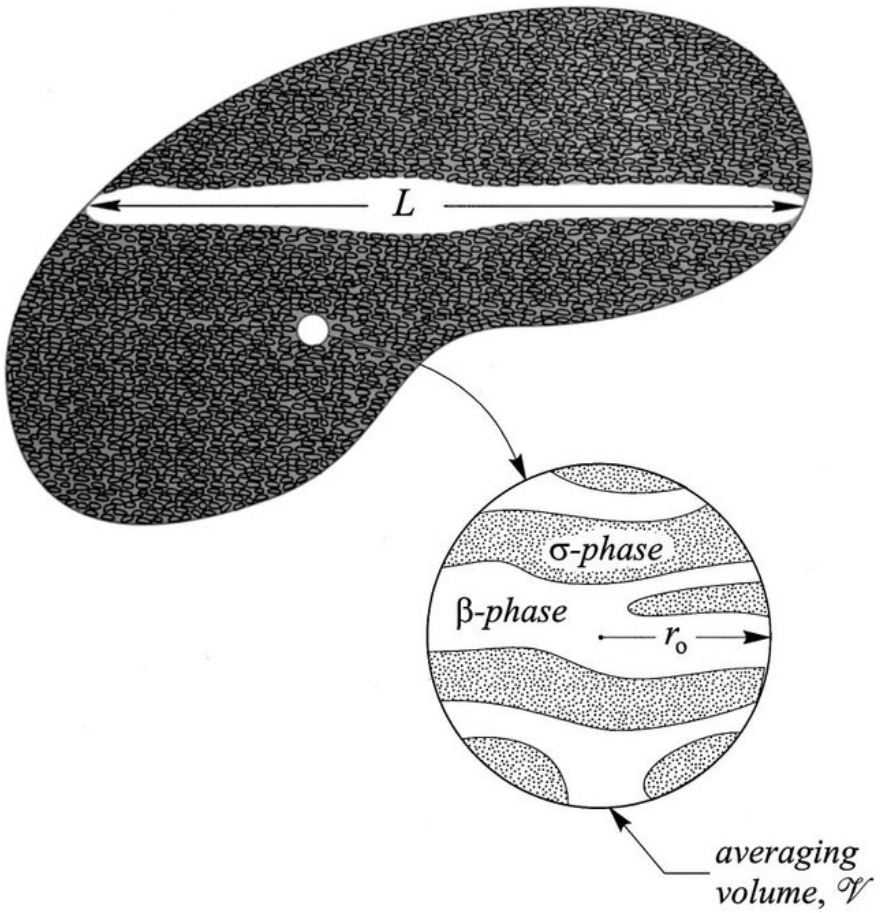

Figure 2.1.1 – Diagram of an ideal two-phase porous medium. β represents a fluid phase. Ω represents the solid structure of the porous medium. r_o is the characteristic size of pores. V is the volume used for homogenization (adapted from Quintard, 2015).

One of the main characteristics of porous media is their multi-scale nature. Indeed, several levels of porosity can be observed for the same type of sample. For example, in the case of sandstone, we might first consider inter-grain porosity. If we observe a sandstone not on the scale of a single sample (a few centimeters), but on the scale of a geological formation (a few tens to hundreds of meters), the porosity may cover different vacuolar spaces, from the size of the sandstone's original sand to the size of faults running through the formation. In addition to porosity, porous media can be characterized in terms of the total surface area of the solid matrix, known as the specific surface area. This specific surface area increases when the diameter of the solid grains becomes smaller. Thus, the tortuosity is often bigger in this case.

Some materials are naturally perceived and understood as porous medium (sediments, sponges) because these materials are made of a unique piece of structure with voids inside it. However, such description can also be formulated for an association of individual elements. This is the case for glass beads or sand grains that are understood as porous medium. However, vegetation is rarely considered as a porous medium other than for the surface processes. It is nonetheless possible to consider a complex patchwork of entangled

fiber of vegetation (for example, *Sphagnum* strains or lichen) as a porous medium. This hypothesis will be investigated in order to study arctic low vegetation cover as a porous medium.

2.2 POROUS MEDIA SCIENCES: A BRIEF INTRODUCTION

2.2.1 *Porous medium morphology*

2.2.1.1 *Definitions and general concepts*

In order to characterize porous media in a general definition, we will describe three characteristic scales generally considered in the study of a porous medium.
The first scale corresponds to the "microscale" of the porous medium, at which the morphology of each phase is described in detail, *i.e.* with the geometry of each pore. It is named the pore-scale. It is the scale at which classical continuum mechanistic processes can be described in detail (Navier-Stokes equations, adsorption-diffusion at the fluid-solid interface, etc.). It is also the scale at which the greatest heterogeneity of physical properties occurs.
The intermediate scale comprises a sufficiently large set of pores and solid matrix to be statistically representative of the microheterogeneities present at the microscopic scale. At this scale, the porous medium is described as a continuous medium with volume fractions of the different phases at every point. We will refer to this mesoscopic scale as the Darcy scale with reference to the formulation of the Darcy equation presented in section 2.3.1. Finally, the mesoscopic scale is usually assumed to be the scale of the representative elementary volume (described in section 2.2.1.2).
The upper scale, the macroscopic scale, comprises a large number of mesoscopic volumes to form a pseudo-continuous or "effective" medium. It is essential that the characteristic lengths of the different scales represented are separated by several orders of magnitude for a simple porous media description. The transformation of microscopic equations into macroscopic equations, for instance from pore-scale to Darcy scale, can be achieved through the use of analytical treatments (including volume averaging and upscaling) or through the simulation of transfers at the microscopic scale (direct numerical simulations).
For the purposes of this work, the microscopic scale is described as the scale characteristic of the sprigs of Bryophytes and lichens (around a millimeter). The mesoscopic scale or Darcy scale can be considered as the characteristic scale of a moss or lichen patch (hundreds of sprigs or around ten centimeters) and the macroscopic scale as the whole plant cover of the catchment.

2.2.1.2 *Representative Elementary Volume*

One of the key issues in porous media is the existence of a locally-repeatable structure (a pattern) that is representative of the entire porous medium. The mathematical conceptualization of such volume was provided by Hill (1963). This concept, known as the Representative Elementary Volume (REV), corresponds to the smallest volume over which it is possible to define a property as a continuous function of space. In the following explanation, we will consider the general evolution of a intensive φ_β property value. This property can be described as a function of a test volume as shown in Fig. 2.2.1.

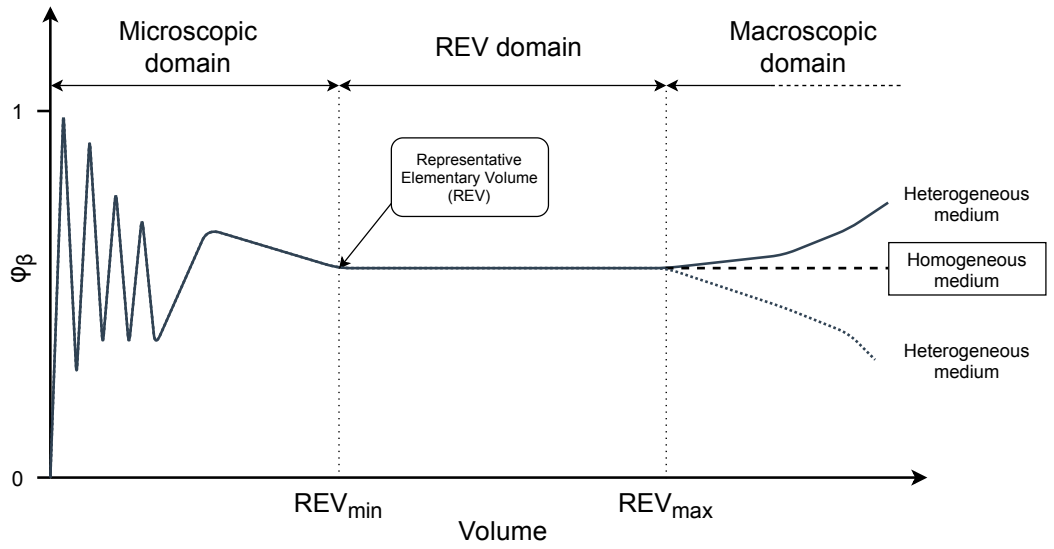

Figure 2.2.1 – Evolution of a given property φ_β depending of a the averaging testing volume V (adapted from Brown and Hsieh, 2000).

There are three main ranges visible in Fig. 2.2.1. The first range includes the lowest averaging volume values. The φ_β property values fluctuate abruptly and erratically. These fluctuations represent the heterogeneity observed at the microscopic scale. As the averaging volume increases, the fluctuations in the φ_β property value tend to decrease in amplitude and frequency. When the fluctuation becomes small enough, the minimum size of the representative elementary volume is reached (REV_{min}). As the size of the averaging volume increases, longer wavelength fluctuations may occur. The maximum size of the REV is reached when the amplitude of these fluctuations becomes large enough to break statistical representativeness. In most cases, therefore, there is a range of validity for the REV. By convention, and in order to simplify the underlying mathematical problems, the optimum size of the REV is considered to be the minimum size of the averaging volume that satisfies the chosen level of maximum fluctuation.

The principle of quantifying the size of a representative elementary volume is based on

the averaging over this volume for a statistically significant number of locations within the porous medium. We then obtain an average value with a fluctuation term, which must be compared with the chosen criterion of maximum fluctuation. There are several requirements for defining this volume. The porous medium studied must respect the separation of scale rule, *i.e.* the microscopic scale and the scale of the continuous medium must be distinct so that the characteristic length of the pore-scale is clearly smaller than the characteristic length of the Darcy scale. Otherwise, heterogeneity on one scale would interfere with the quantification of a REV on the other scale. Besides, the size of a REV is specific to a given physical property. Porosity is the most simple physical property for quantifying a REV. Porosity depends solely on the morphology of the porous medium under study.

2.2.1.3 *Porous media homogenization and upscaling*

Transfer equations in porous media are governed by the problems of flow in a matrix with complex interfaces. The more there are numerous fluid phases involved, the more complex are these equations due to interfacial phenomena. These equations can be solved using Direct Numerical Simulations (DNS). Solving these pore-scale equations by simulation can be a very time consuming and resource intensive process due to the structural complexity of a porous medium. The applications' scale is often not numerically solvable due to the number of meshes required to model such a domain. The solution of an upscaling problem is two-folds. The first step is to use a mesoscopic scale (or Darcy scale) model to resolve the effective properties on such domain and then find a representative elementary volume by successive simulations on different test volumes, as can be done for porosity. Then, the property representative of the macroscopic scale (or effective property) can be used in an effective (or continuous) numerical model at upper scale when the test volume statistically converges to a low standard deviation (typically 1% to 5%, depending on the physical property under study).
Several upscaling methods are available (volume averaging, homogenization theories, stochastic theories). In this work, we follow the framework of the volume averaging which involves a change of scale. The volume averaging method is described in detail in the monograph by Whitaker (1999) and in Quintard and Whitaker (1994). A practical example of volume averaging can be found in the study of heat transfer in a granular medium by Davarzani (2010).

2.2.1.4 *Pore Network Modeling*

The complexity of transfer phenomena in porous media has led to the desire for a simplified modeling of the pore network. The concept of a network of interconnected pores is described first by Fatt (1956), who demonstrated the possibility to represent a porous network using interconnected tubes and spheres on the scale of a sandstone sample. This method was initially developed for petroleum engineering to facilitate

reservoir rock properties computation. Since then, the use of pore networks has been generalized and applied to various types of porous media. In particular, the use of pore networks as a method for quantifying multiphase transfers has proved advantageous over the use of conventional analytical methods (volume averaging, upscaling) because it requires less computational resources while keeping reasonably good agreement in results obtained with other methods. There are numerous works in the literature on the study of morphological (Khan et al., 2020; Dong and Blunt, 2009), hydraulic (Agaesse et al., 2016) and thermal (Le et al., 2016; Thai et al., 2018) properties of geological porous media.

The constant improvement in the numerical resolution of porous media imaging techniques (particularly X-ray microtomography) is a key factor in the development of new techniques for studying porous media. The precision of these imaging techniques allows comparisons to be made between digital treatment of porous morphology and use of a pore network. The structural simplification achieved by generating pore-network models results in significant time savings, particularly for large size and complex porous media. Algorithmic processing of the image is required to generate a pore network from structural images of the porous medium. Several algorithms for numerical processing of pore networks exist in the literature, such as the *Maximal Ball* (Silin and Patzek, 2006) or the SNOW (*Sub-Network of the Oversegmented Watershed*, developed by J. T. Gostick, 2017) algorithm. The SNOW algorithm was chosen for the study of hydraulic properties. It has the advantage of being easily adaptable to algorithmic routines specific to the processing of images derived from X-ray microtomography. An example of pore-network model generation from a microtomography image is shown in Fig. 2.2.2.

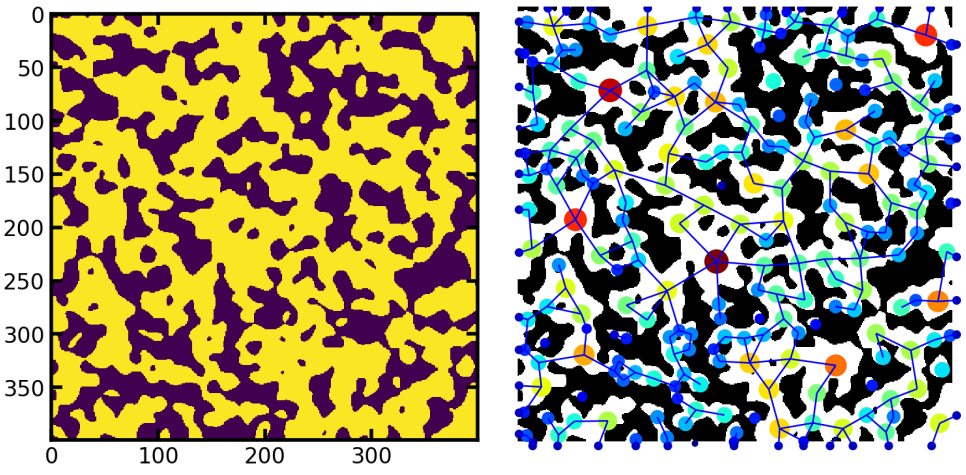

(a) Raw image. **(b)** Pore Network.

Figure 2.2.2 – Pore Network Model extraction using the SNOW algorithm on 2D image (a) Raw image with a fluid phase colored in yellow and a solid phase colored in purple (b) Pore Network generated from the model., (adapted from PoreSpy tutorial).

2.3 TRANSFERS IN POROUS MEDIA

2.3.1 *Water transfers*

The fundamental law governing water flow in porous media dates from the original work of Darcy (1856) for the water supply of the city of Dijon in France. The Darcy's law can be written as, if A is a section (in m^2) of the considered soil (*i.e.* a given porous medium) and h_1 and h_2 are two piezometric water levels (in meters):

$$Q = K_w A \cdot \Delta H \tag{2.1}$$

with Q the water flow (in $m^3.s^{-1}$), K_w the hydraulic conductivity (in $m.s^{-1}$) and ΔH the hater head or "metric pressure" (in $m.m^{-1}$). In essence, Eq. 2.1 is a macroscopic equation for a single-phase flow through a porous medium. Bear (1972) and later Whitaker (1999) demonstrated that resolving Navier-Stokes equations for an incompressible single-phase flow at the Representative Elementary Volume scale (REV) of porous medium by volume averaging leads to the definition of a tensorial Darcy equation. Some analytical tools will be presented hereafter to give the reader more information about this volume averaging application. At pore-scale, one can define a standard set of boundary and initial conditions for the resolution of the Navier-Stokes equations as:

$$\begin{cases} \rho\left(\frac{\partial v_f}{\partial t} + v_f \cdot \nabla v_f\right) = -\nabla p_f + \rho_f g + \mu \nabla^2 v_f & in\ V_f \\ \nabla \cdot v_f = 0 & in\ V_f \\ v_f = 0 & over\ A_{sf}\ (BC1) \\ v_f = G(r,t) & over\ A_{fe}\ (BC2) \\ v_f = H(r) & in\ V_f\ (IC) \end{cases} \tag{2.2}$$

with V_f being the volume of fluid in the averaging volume V so that $V = V_s + V_f$. In this problem, we will consider a porous medium Reynolds number Re_p defined as in Blunt (2017) upon the mean diameter of the pores noted d_f and kinematic viscosity of the given fluid, noted ν_f:

$$Re_p = \frac{v_f d_f}{\nu_f} \tag{2.3}$$

In the case where $Re_P << Re_{critical}$, the flow can be considered laminar so that turbulence factor can be neglected. Eqs. 2.2 can be simplified to a Stokes system which becomes at steady-state:

$$\begin{cases} -\nabla p_f + \rho_f g + \mu \nabla^2 v_f = 0 & in\ V_f \\ \nabla \cdot v_f = 0 & in\ V_f \\ v_f = 0 & over\ A_{sf}\ (BC1) \\ v_f = G(r,t) & over\ A_{fe}\ (BC2) \\ v_f = H(r) & in\ V_f\ (IC) \end{cases} \tag{2.4}$$

We will now define the averaged variable $\langle p \rangle$ and $\langle v_f \rangle$ to set the averaged Darcy equation, respectively as, if $d << r_0$ and $r_0^2 << L_\varepsilon L_p$ (separation of scales):

$$\langle p \rangle^f = \frac{1}{V_f} \int_{V_f} p dV \tag{2.5}$$

and,

$$\langle v_f \rangle = \frac{1}{V} \int_{V_f} v_f dV = \varepsilon \langle v_f \rangle^f \tag{2.6}$$

Applying volume averaging to the system shown in Eqs. 2.4, becomes the macroscopic Darcy equation as:

$$\begin{cases} \langle v_f \rangle = -\frac{\mathbf{K}}{\mu} \cdot \left(\nabla \langle p \rangle^f - \rho_f \mathbf{g} \right) & in\ V \\ \nabla \cdot \langle v_f \rangle = 0 & in\ V \\ \langle v_f \rangle = G(r,t) & over\ A_e\ (BC) \end{cases} \tag{2.7}$$

$\boldsymbol{K}$ represents the intrinsic permeability tensor, which is a structure-dependent physical property. Finally, the macroscopic Darcy equation can be written in a form combining the two first equations of the system 2.7 as:

$$\nabla \cdot \left(\frac{\mathbf{K}}{\mu} \cdot \nabla \langle p \rangle^f \right) = \nabla \cdot \left(\frac{\mathbf{K}}{\mu} \cdot \rho_f \mathbf{g} \right) \qquad in\ V \tag{2.8}$$

While Darcy's law is applicable for fully-saturated water flows, it cannot describe accurately flows in unsaturated porous medium. Therefore, such saturation-dependent flow can be described by the Richards equations (Richards, 1931). Richards equation is based on the Darcy-Buckingham law as:

$$\vec{q} = -\mathbf{K}(\theta) \left(\nabla h + \nabla z \right) \tag{2.9}$$

where $\vec{q}$ is the flow, $\mathbf{K}$ is the unsaturated hydraulic conductivity tensor, θ is the volumetric water saturation, ∇h is the pressure head and ∇z is the geodetic head gradient. In the case of an incompressible porous medium at constant density, mass balance can be written as:

$$\frac{\partial \theta}{\partial t} + \nabla \cdot \vec{q} + S = 0 \tag{2.10}$$

with S a sink term, for example root uptake. Combining Eq. 2.9 and Eq. 2.10 gives the mixed-form Richards equations:

$$\frac{\partial \theta}{\partial t} = \nabla \cdot \left(\mathbf{K}(\theta) \left(\frac{\partial h}{\partial z} + 1 \right) \right) - S \tag{2.11}$$

with t the time (in s), z the absolute elevation (in m), K the hydraulic conductivity (in $m.s^{-1}$), θ the water saturation, q being the flux (in $kg.s^{-1}$) and h the capillary induced water head (in m).

In the case of low vegetation cover hydraulic properties study, we will only consider a saturated porous medium, therefore the case of a non-saturated porous medium using the Richards equation will not be discussed in this thesis.

2.3.2 *Thermal transfers*

Thermal properties consists of interdependent variables that are mainly relying on the studied matter's molecular structure. Thus, adversely to hydraulic properties for which the properties are mainly structure-dependent, a careful experimental assessment is required before any numerical volume averaging. This chapter consists of two main parts. The first part is focused on the experimental assessment of thermal properties through various experimental setups using standardized protocols and more prospective methods. The latter part deals with numerical parameter fitting of the studied porous media. As an introductory reminder, every physical material thermal properties can be described upon three main variables:

- Thermal conductivity λ (measured in $W.m^{-1}.K^{-1}$) corresponds to the ability of a given material to allow heat to pass through. Thermal conductivity is purely depending of the structure at molecular scale of the studied material. This property is therefore complicated to study only numerically and experimental assessments are compulsory;
- Heat capacity (measured in $J.K^{-1}$) is the required energy amount to raise by one kelvin the temperature of a given material. In this work, the heat capacity will be quantified either related to mass (specific heat capacity C_p in $J.kg^{-1}.K^{-1}$) or to the volume (volumetric heat capacity C_w in $J.m^{-3}.K^{-1}$);

- Thermal diffusivity α or κ (measured in $m^{-2}.s^{-1}$) is a diffusion coefficient defined as in Eq. 2.12.

$$\alpha = \frac{\lambda}{C_w} = \frac{\lambda}{\rho C_p} \tag{2.12}$$

2.3.2.1 *Heat transfer mechanisms*

Heat is energy that is transferred between two thermodynamic systems and does not necessarily involve matter displacement. There are three main heat transfer mechanisms that are occurring:

- *Heat conduction*: Heat is transferred from atom to atom in a diffusive way. Conductive transfer only implies the intermolecular atomic agitation in the process of energy transfer. This energy transfer mechanism is the main energy transfer phenomenon taking place inside solids.
- *Heat convection*: Energy is both transferred through an advective phenomenon (*i.e.* implying a transport medium, generally a fluid such as air or water) and a conductive heat transfer. Thus, the occurrence and the intensity of this buoyancy-driven phenomenon is depending of the fluid's density, thermal expansion coefficient and volumetric mass in the case of thermally induced convection phenomenon.
- *Heat radiation*: In the latter case, energy is transferred from a thermodynamic system to another via electromagnetic radiation, and more especially under the form of infrared radiation (typically between 700 nm and 1 mm wavelengths). These radiations can be absorbed, transmitted or reflected depending of the radiative properties of the considered material. Hence, infrared emissivity and reflectivity are key variables in radiative thermal transfers.

In such natural systems that are under study in this thesis, it can be considered in a general vision that all the three mechanisms mentioned above are actually occurring. Conductive heat transfer phenomenon in the arctic vegetation cover is extensively studied in the framework of the thesis, through experiments (section 6.2) and through numerical modeling (section 6.3). Some clues about convective and radiative phenomena will be given in the last part of this thesis (part iv).

2.3.2.2 *General overview of heat transfer equation*

In a first approximation, we will consider that there is only conduction occurring in a porous medium. Conductive heat transfer is presented hereafter upon to the demonstrations made by Giovannini and Bédat (2012). For an isotropic homogeneous medium and at stationary state, Fourier's law (Fourier, 1822) gives the heat flux density φ linking thermal conductivity λ and the thermal gradient ∇T as described in Eq. 2.13.

$$\varphi = -\lambda \nabla T \tag{2.13}$$

This energy-balance equation will lead the experimental thermal conductivity quantification given in section 6.2. However, the complexity of the biological structure and the properties' difference between phases makes studying transient heat transfer richer in terms of information (Kaviany, 1995). In the following demonstration, we will consider the internal heat energy named hereafter Q. Hence, the time derivative of Q is proportional to the temperature derivative multiplied by the volumetric heat capacity ρCp as follows in Eq. 2.14.

$$\frac{\partial Q}{\partial t} = \rho C_p \frac{\partial T}{\partial t} \tag{2.14}$$

The heat accumulation at a point x representing the distance from the heat input is given by the heat flow derivative at that given point, according to the laws of energy conservation. In this case, there are neither sink nor source term. This relation is presented in Eq. 2.15.

$$\frac{\partial Q}{\partial t} = \frac{\partial \varphi}{\partial x} + \frac{\partial \varphi}{\partial y} + \frac{\partial \varphi}{\partial z} \tag{2.15}$$

Assuming that there is only conduction, it is then possible to write the one-dimensional conductive heat transfer equation as an equality to account for the influence of both thermal conductivity λ and volumetric heat capacity ρCp as described in Eq. 2.16:

$$\rho C_p \frac{\partial T}{\partial t} - \nabla \cdot (\lambda \nabla T) = 0 \tag{2.16}$$

From the heat equation given in Eq. 2.16, various analytical methods for solving this problem are available (*e. g.* separation of variables, Laplacian transform, Duhamel's theorem...). In the following work, the heat transfer equation will be solved using a finite-volume approach using the open-source computational fluid dynamics toolbox (*OpenFOAM*).

2.3.2.3 *Thermal conductivity in porous media*

In contrast to a homogeneous medium, the thermal conductivity of a porous medium takes into account the respective thermal conductivities of the constituent phases of the porous medium. Thermal conductivity is therefore considered to be an effective property, written λ^*. We can then write the effective heat diffusion equation in a homogeneous porous medium as:

$$\vec{\varphi^*} = -\mathbf{\Lambda}^* \cdot \nabla T \tag{2.17}$$

The effective thermal conductivity $\mathbf{\Lambda}^*$ is defined as a tensor, since the matrix of the porous medium is taken into account hence the possible anisotropy. The values of $\mathbf{\Lambda}^*$ are comprised between the values of the thermal conductivity of the liquid phase and the solid phase, λ_S and λ_F respectively, and also by the spatial structure of the porous medium. The value of the effective property tensor $\mathbf{\Lambda}^*$ may be obtained by a process of volume averaging of pore-scale transfer equation (Kaviany, 1995). One starts describing heat transfer by conduction at the pore-scale in a homogeneous porous medium. The associated equation system can be written as follows:

$$\begin{cases} \left(\rho C_p\right)_s \frac{\partial T_S}{\partial t} = \nabla \cdot \left(\lambda_s \nabla T_s\right) & in\ V_s \\ \left(\rho C_p\right)_f \frac{\partial T_f}{\partial t} = \nabla \cdot \left(\lambda_f \nabla T_f\right) & in\ V_f \\ T_s = T_f & on\ A_{sf} \\ \lambda_f \nabla T_f \cdot \vec{n}_{sf} = \lambda_s \nabla T_s \cdot \vec{n}_{sf} & on\ A_{sf} \end{cases} \tag{2.18}$$

It is possible to define two macro-scale temperatures $\langle T_s \rangle$ and $\langle T_f \rangle$ which corresponds to the volumetric mean of the temperature for both fluid and solid phase, written for the solid phase:

$$\begin{aligned} \langle T_s \rangle &= (1-\epsilon) \langle T_s \rangle^s \\ \langle T_s \rangle^s &= \frac{1}{V_s} \int_{V_s} T_s dV \end{aligned} \tag{2.19}$$

and for the fluid phase:

$$\begin{aligned} \langle T_f \rangle &= \epsilon \langle T_f \rangle^f \\ \langle T_f \rangle^f &= \frac{1}{V_f} \int_{V_f} T_f dV \end{aligned} \tag{2.20}$$

Volume averaging on the solid phases leads to:

$$(1-\epsilon)\left(\rho C_p\right)_s \frac{\partial \langle T_s \rangle^s}{\partial t} = \nabla \cdot \left[(1-\epsilon)\lambda_s \nabla \langle T_s \rangle^s + \frac{\lambda_s}{V} \int_{A_{sf}} \vec{n}_{sf} \left(T_s - \langle T_s \rangle^s\right) dA\right] + \frac{1}{V} \int_{A_{sf}} \vec{n}_{sf} \cdot \lambda_s \nabla T_s dA \tag{2.21}$$

and for the fluid phase:

$$\epsilon \left(\rho C_p\right)_f \frac{\partial \langle T_f \rangle^f}{\partial t} = \nabla \cdot \left[\epsilon \lambda_f \nabla \langle T_f \rangle^f + \frac{\lambda_f}{V} \int_{A_{fs}} \vec{n}_{fs} \left(T_f - \langle T_f \rangle^f\right) dA\right] + \frac{1}{V} \int_{A_{fs}} \vec{n}_{fs} \cdot \lambda_f \nabla T_f dA \tag{2.22}$$

If the characteristic length of the porous medium L and the characteristic length of the microscopic pore structure satisfy $\left(\frac{d}{L}\right)^2 << 1$, then a local thermal equilibrium can be considered true, which leads to:

$$\langle T_f \rangle^f = \langle T_s \rangle^s = T \tag{2.23}$$

It is possible to combine Eqs. 2.21, 2.22 and 2.23 to form a one-equation model of heat transfer in a homogeneous porous medium shown as follows:

$$\left(\rho C_p\right)^* \frac{\partial T}{\partial t} = \nabla \cdot \left[\left[\epsilon \lambda_f + (1-\epsilon)\lambda_s\right] \nabla T + \frac{\lambda_f - \lambda_s}{V} \int_{A_{fs}} \vec{n}_{sf} \left(T_f - T\right) dA \right] \tag{2.24}$$

with the effective calorific capacity as:

$$\left(\rho C_p\right)^* = \epsilon \left(\rho C_p\right)_f + (1-\epsilon) \left(\rho C_p\right)_s \tag{2.25}$$

From Eq. 2.24, one can assume the following closure assumption:

$$T_f - T = \overrightarrow{b_f} \cdot \nabla T \tag{2.26}$$

where $\overrightarrow{b_f}$ is the closure vector only dependent of the porous medium's structure, $\lambda_s$and λ_f. Combining Eq. 2.26 with Eq. 2.24 leads to the definition of the macroscopic conductive heat transfer equation:

$$\left(\rho C_p\right)^* \frac{\partial T}{\partial t} = \nabla \cdot \left(\mathbf{\Lambda}^* \cdot \nabla T\right) \tag{2.27}$$

with $\boldsymbol{I}$ the unit tensor, the effective thermal conductivity tensor$\mathbf{\Lambda}^*$ can be written as:

$$\mathbf{\Lambda}^* = \left[\epsilon \lambda_f + (1-\epsilon)\lambda_s\right] \boldsymbol{I} + \frac{\lambda_f - \lambda_s}{V} \int_{A_{fs}} \vec{n}_{fs} \cdot \overrightarrow{b_f} dA \tag{2.28}$$

It is possible to note that the determination of the effective thermal conductivity requires a precise knowledge of both fluid and solid thermal conductivity, and of the pore-scale spatial structure of the porous medium. When such condition is satisfied and that the porous structure is well assessed, experimental or numerical models can be compared to analytic models for λ^*determination. A review of the main effective thermal conductivity model is shown in Mojtabi et al. (2019), which is recalled here in Table 2.3.1:

Model	Expression
Parallel	$\frac{\lambda^*}{\lambda_f} = \epsilon + (1-\epsilon)\,\frac{\lambda_s}{\lambda_f}$
Series	$\frac{\lambda^*}{\lambda_f} = \frac{\frac{\lambda_s}{\lambda_f}}{\epsilon\frac{\lambda_s}{\lambda_f}+1-\epsilon}$
Geometric avg.	$\frac{\lambda^*}{\lambda_f} = \left(\frac{\lambda_s}{\lambda_f}\right)^{1-\epsilon}$
Maxwell (lower)	$\frac{\lambda^*}{\lambda_f} = \frac{2\epsilon+(3-\epsilon)\frac{\lambda_s}{\lambda_f}}{3-\epsilon+\epsilon\frac{\lambda_s}{\lambda_f}}$
Maxwell (higher)	$\frac{\lambda^*}{\lambda_f} = \frac{2\left(\frac{\lambda_s}{\lambda_f}\right)^2+(1-\epsilon)+(1+2\epsilon)\frac{\lambda_s}{\lambda_f}}{(2+\epsilon)\frac{\lambda_s}{\lambda_f}+1-\epsilon}$
Batchelor & O'Brian	$\frac{\lambda^*}{\lambda_f} = 4\ln\frac{\lambda_s}{\lambda_f} - 11$
Hadley (averaged mean)	$f_0 = 0.8 + 0.1\epsilon;\ \alpha_0 = \alpha_0(\epsilon)$
	$\frac{\lambda^*}{\lambda_f} = (1-\alpha_0)\,\frac{f_0\epsilon+\frac{\lambda_s}{\lambda_f}(1-\epsilon f_0)}{1-\epsilon(1-f_0)+\frac{\lambda_s}{\lambda_f}\epsilon(1-f_0)}\alpha_0\frac{2\left(\frac{\lambda_s}{\lambda_f}\right)^2+(1-\epsilon)+(1+2\epsilon)\frac{\lambda_s}{\lambda_f}}{(2+\epsilon)\frac{\lambda_s}{\lambda_f}+1-\epsilon}$
	$\log\alpha_0 = -4.898\epsilon \quad \epsilon \in [0; 0.0827[$
	$\log\alpha_0 = -0.405 - 3.154(\epsilon - 0.0827) \quad \epsilon \in [0.0827; 0.298[$
	$\log\alpha_0 = -1.084 - 6.778(\epsilon - 0.298) \quad \epsilon \in [0,298; 0.580]$

Table 2.3.1 – Effective thermal conductivity models (Mojtabi et al., 2019) adapted from Kaviany (1995).

2.3.3 *Experimental measurements of basic porous medium properties*

The ubiquitous use of porous media in industry and geology has led to a long-standing interest in the quantitative study of porous media. This section aims presenting some experimental and field study techniques for thermal properties quantification. While the techniques are not used straightfully in the thesis project, their presentation is important for the later understanding for the numerical modeling presented in section 6.3. As a reminder, porosity is a ratio between the pores volume and the total volume, as shown in Eq. 2.29:

$$\varphi = \frac{V_{pores}}{V_{Total}} \tag{2.29}$$

From Eq. 2.29, it is possible to differentiate the volume of open porosity V_{open}, *i.e.* the porosity representative of pores communicating with the outside of the sample. These are the pores that are active in flow transfer phenomena. On the other hand, it is possible to define a closed porosity, V_{close}, which corresponds to the porosity isolated from the rest of the porous network. This porosity is not taken into account in the flow problems, but must be considered as a porosity in the case of heat transfer. Closed porosity is used to calculate the density of a sample and in conductive heat transfer processes. Eq. 2.29 can be written as follows:

$$\varphi = \frac{V_{open} + V_{close}}{V_{Total}} \tag{2.30}$$

Then, either open or closed porosity can be determined using porosimetry techniques as described in the following section.

2.3.3.1 *Porosimetry*

Porosimetry is an experimental technique for calculating the volume occupied by a fluid phase (often air) in a porous medium. The technique involves saturating the porous medium with a fluid (generally a non-wetting liquid such as mercury). The porosimeter measures the volume of connected and open pores (open porosity). Mercury porosimetry is a reliable technique widely used in industry. However, it assumes that the medium under study contains little closed porosity, inaccessible to the non-wetting fluid. A schematic of a standard mercury porosimeter is shown in Fig. 2.3.1.

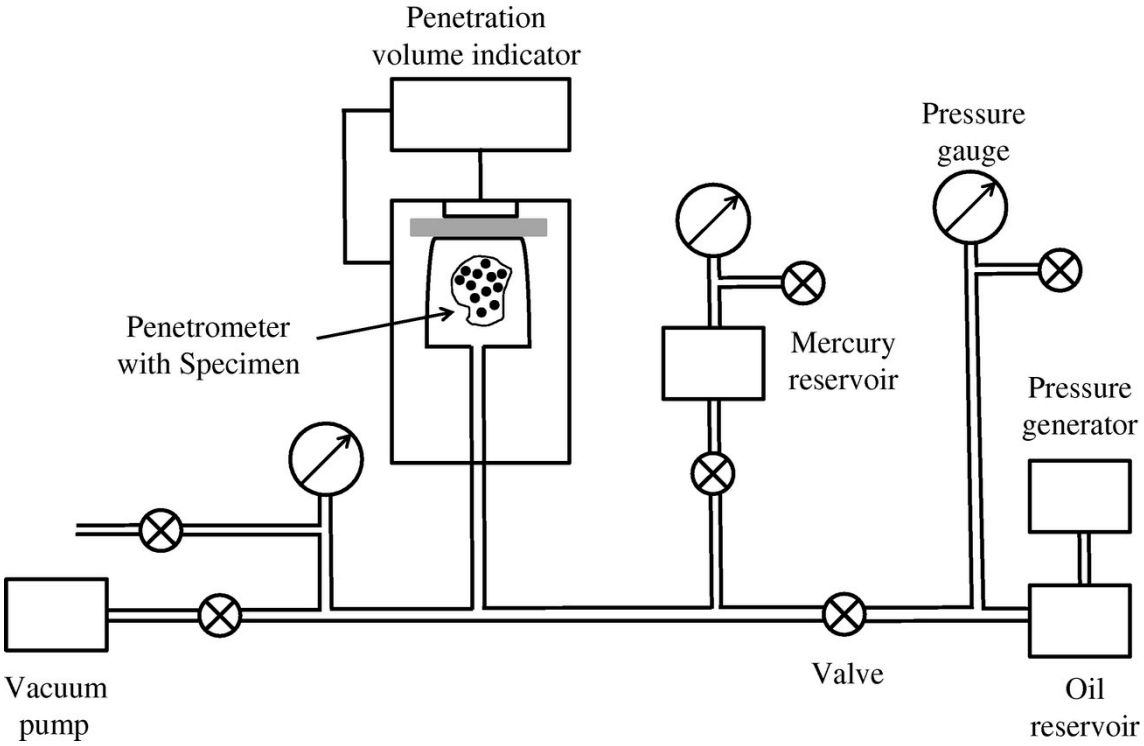

Figure 2.3.1 – Schematic representation of a standard mercury porosimeter (from Hong et al., 2018).

Such porosimetry is efficient for the assessment of the open and connected porosity. Indeed, the non-wetting nature of mercury enables it to fill the pores without any capillary film effect. One the main drawback of such experimental methods is such method is often destructive for the studied sample. Moreover, such technique is not suitable for some samples, for example living tissue samples. Therefore, other porosimetry techniques are required to avoid sample degradation and the assessment of enclosed porosity.

Some other technique for measuring overall porosity of porous media consists in estimating the volumetric mass and density of the sample using a pycnometer. Here, this works well for samples that are powders or solids. Working with deformable samples only allow one to estimate the sample's density without any information on the volume of enclosed pores.

2.3.3.2 *Permeametry*

In the same way than for porosimetry, permeametry allows the measurement of either intrinsic permeability or the water conductivity if the measurement device uses water as a fluid. The general concept of a permeameter is to maintain a hydrostatic pressure over a sample and to measure the volume of fluid that passed through for a given period of time, in the same way than the experiment of Darcy (Darcy, 1856). Thus, hydraulic conductivity represent an average speed of the fluid at hydrostatic conditions. The most common tool

for the measurement of hydraulic conductivity is the constant-head permeameter, shown in Fig. 2.3.2.

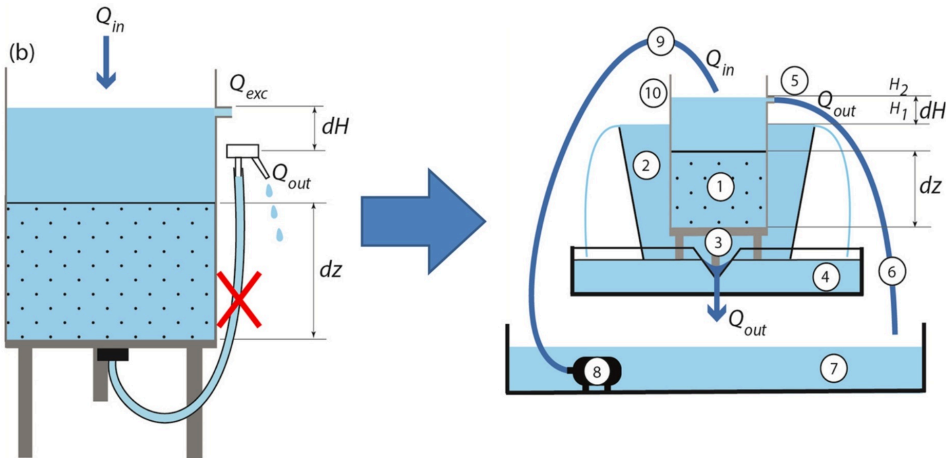

Figure 2.3.2 – Schematic representation of a standard constant-head permeameter apparatus (*left*) and a modified version of the apparatus for the measurement of high-permeability porous media (Nijp et al., 2017).

Some variations in the constant-head permeameter exists in the literature, depending on the considered problem. For example, Nijp et al. (2017) modified the standard constant-head permeameter to be used for high water conductivity samples, where a constant head of water is difficult to maintain due to the high hydraulic conductivity.

Hydraulic conductivity can also be measured in the field with an infiltrometer. Here, the infiltrated volume is quantified for a given time after the medium (often the soil) has been saturated with water. For constant-head in-field permeametry, one can also use double-ring infiltrometry which works in the same way.

Some results of hydraulic conductivity have been done during the field trip of sample collection, and especially for Siberian samples. Such results are presented in section 5.2.1.

2.3.3.3 *Infiltrometry*

Soil hydraulic conductivity can also be measured using an infiltrometer. The infiltrometer consists of a ring with a calibrated diameter (usually 30 cm) sunk into the surface of the ground. The ring is filled with water, and the variation in water height in the cylinder (i.e., water infiltration) is measured over time. Hydraulic conductivity can thus be calculated using Eq. 2.31, where Δh is the difference in water height between the start of measurement and the end of measurement, and ΔT is the measurement time:

$$K_{infiltro} = \frac{\Delta h}{\Delta T} \tag{2.31}$$

Figure 2.3.3 – Double-ring infiltrometer set-up (from Fatehnia, 2015).

The infiltrometer generally features an external guard ring (usually 60 cm in diameter), maintained at a constant water head in order to hydrically saturate the soil around the measurement surface, enabling here the characterization of vertical hydraulic conductivity. An example of a double-ring infiltrometer can be seen in Fig. 2.3.3:

The relative simplicity of the double-ring infiltrometer enables fast, reliable field measurements. This method is often used as a first measurement for pedological studies (Li et al., 2019; Shuster et al., 2021; Sidiras and Roth, 1987). On the other hand, it is not very reliable for measurements on highly permeable soils or soils initially saturated with water. Double-ring infiltrometry tests were carried out as part of the work on characterizing the hydraulic conductivity of arctic vegetation cover and presented in section 5.3.3.

2.4 OBJECTIVES OF THE VEGETATION COVER POROUS MEDIUM STUDY

Arctic vegetation includes a high diversity of bryophytes (including *Sphagnum* mosses) and lichens, both in tundra and boreal forest environments. The ecosystems in which these species are identified as being vulnerable to the effects of global climate change. The

latent heat exchanges in these environments cause a series of peculiar climatic retroactions known as the Arctic amplification. CMIP6 projections predict an increase in positive temperature anomalies and an excess of precipitation by the year 2100 (Intergovernmental Panel on Climate Change (IPCC), 2022). The future climate conditions described in these projections will induce the degradation of arctic permafrost (Biskaborn et al., 2019), whose cryohydrological and thermal dynamics are in close interactions with the entire energy cycle of arctic ecosystems (Loranty et al., 2018).

The literature review highlights the importance of the link between atmospheric and subsurface processes (Takata and Kimoto, 2000). The arctic vegetation cover thus represents the boundary layer at the interface between these two major reservoirs. Studying the transfer properties of the arctic vegetation cover is therefore an important part of the process of improving the accuracy of future climate models (Park, Launiainen, et al., 2018; Launiainen et al., 2015). In this thesis, we will focus on the quantification of the transfer properties of arctic moss and lichen based on the assumption that such vegetation cover is a porous medium. The aim of this thesis is therefore to study the physical properties of this vegetation cover by using techniques commonly used in the study of porous media.

Part II

SAMPLING AND DIGITALIZATION OF SUBARCTIC LOW VEGETATION STRATA

3

AREAS STUDIED IN THE FRAMEWORK OF THE THESIS

Since the beginning of the 20th century, many study sites and research stations in arctic and subarctic regions have been set up to gather meteorological data and later climatic and biochemical data. A large share of these research locations are regrouped in scientific networks such as the INTERACT network[1], standing for *International Network for Terrestrial Research and Monitoring in the Arctic*. This research network gathers 95 research stations across North America, Asia, and Europe. A map of the research stations' locations is available in Fig. 3.0.1. The HiPerBorea project in which this thesis is taking part of uses

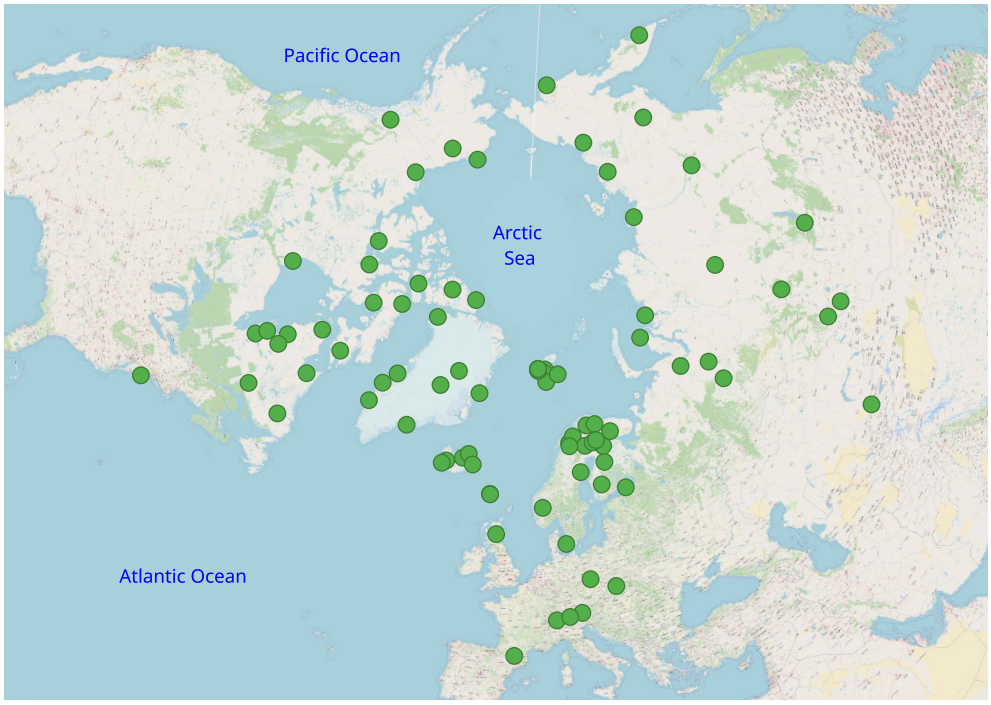

Figure 3.0.1 – Map of the research and scientific stations participating in the INTERACT program as of July 2023.

1 More information available on the INTERACT webpage (https://eu-interact.org/, last access July 31st, 2023).

data and samples that were collected in four of these INTERACT research stations: Abisko (Swedish Lapland), Khanymey (Western Siberian Lowlands), Kaibasovo (Central Siberia) and Kulingdakan (Eastern Siberia). A map showing the locations of these study sites is available in Fig. 3.0.2.

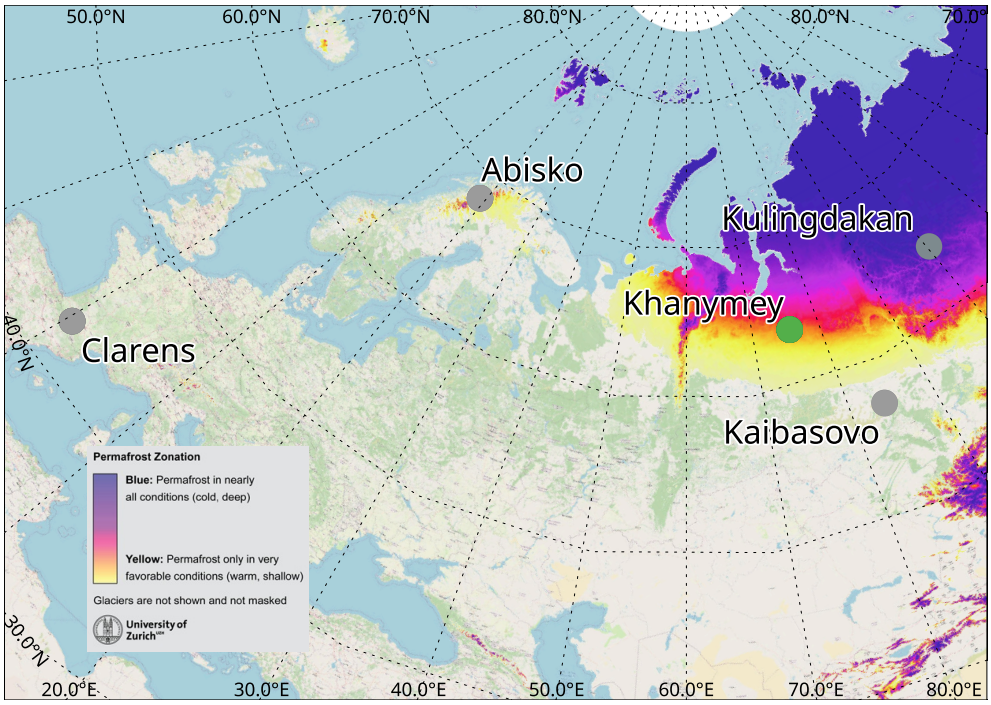

Figure 3.0.2 – Permafrost extension map and study site location placed over the map. The dots in green indicate the sites from which the sites are studied in depth in this thesis. The gray dots indicate the samples that were scanned at the IMFT during the thesis and used a comparison but their transfer properties are to be interpreted. Permafrost Zonation Map is adapted from Gruber (2012).

The study sites are plotted in the Whittaker diagram showing their respective bioregion in Fig. 3.0.3. The main study site for the work presented in this thesis is Khanymey. Most of the X-ray tomography analysis and transfer properties study (made in part iii) is done on the 12 samples collected at Khanymey research station. While to be interpreted, Abisko samples will give some information for the future works in the HiPerBorea project. Although not an arctic bog, an additional research site has been added to the research project of this thesis in Southwestern France (Clarens, Upper-Pyrénées) to provide this project with samples for comparative tests. The samples collected at both Abisko and Clarens are kept alive after their extraction and their growth has been monitored. Khanymey research station is presented in section 3.1 and Abisko research station is presented in section 3.2. One can find the description of Clarens site in section 3.3. Some climatological data will also be given, as well as some descriptions about the collected samples.

The timeframe of the thesis did not enable to make an in-depth study of the Kaibasovo and Kulingdakan samples, and thus their respective research sites are not covered in this thesis, although the collected samples have been scanned in December 2020.

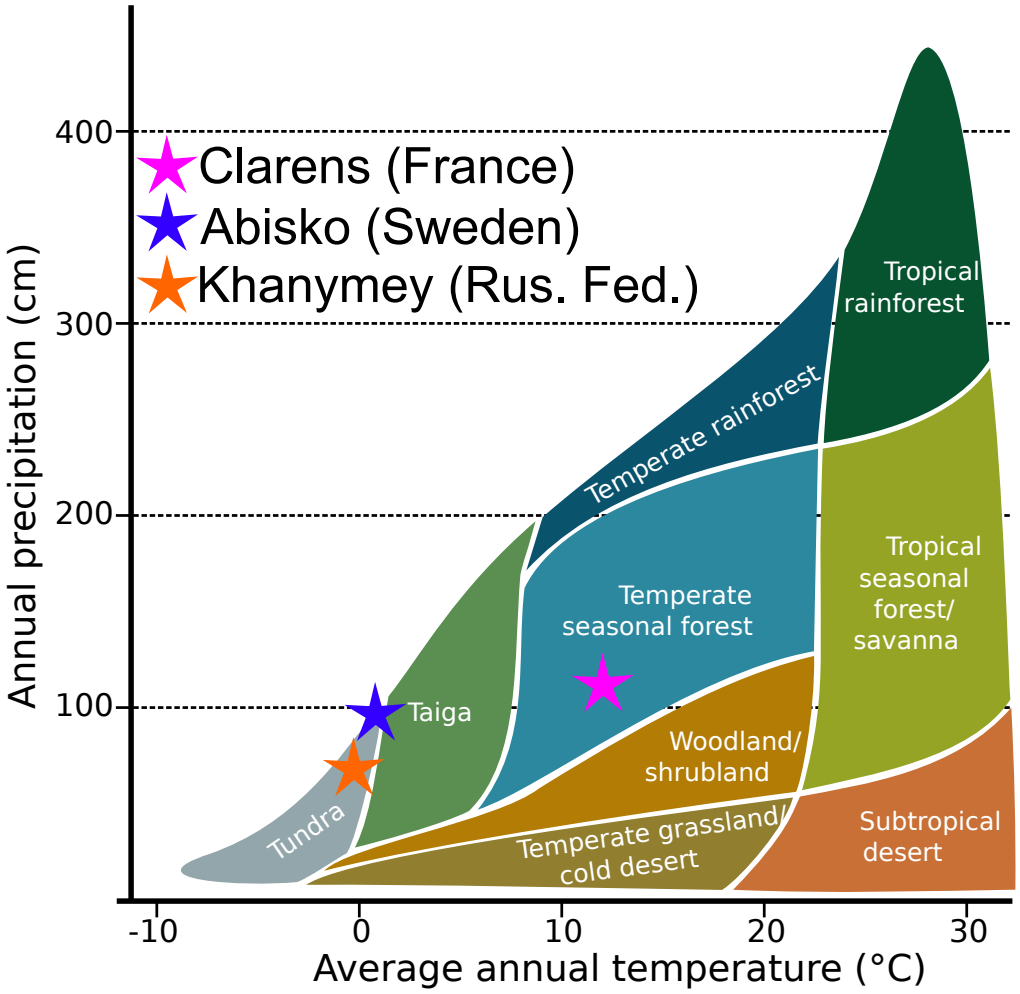

Figure 3.0.3 – Study sites replaced in the biome diagram of Whittaker (1975).

3.1 KHANYMEY (WESTERN SIBERIA)

The research station of Khanymey is located about 20 km north-east of the small town of Khanymey (3500 inhabitants) and 70 km north of Noyabrsk town (107 000 inhabitants). The research site itself is located at N63.72214722 ° E75.96330833 ° in the northern taiga ecoregion of the Western Siberian Lowlands. The permafrost coverage at Khanymey is discontinuous (Loiko et al., 2019). The permafrost layer is about one to three meters thick and is underlain by Pleistocene (-2.6 My – -11.6 ky BP) sandy formations (Klinova et al., 2012). The research station has been active since 2014 and is operated by Tomsk State University. The local climate at Khanymey research station is classified as subarctic (Dfc) according to the Köppen climate classification. From the 1991-2021 meteorological data

available from https://fr.climate-data.org/ (Fig. 3.1.1), the mean annual temperature (MAT) is about -3.85 °C. The mean annual precipitation (MAP) is about 637 mm. Using MAT and MAP values from the 1991-2021 meteorological data, one can see in Fig. 3.0.3 that the research station is situated at the edge of tundra and taiga ecoregions. Khanymey research station is located at the transition between taiga-coniferous forest and open mire.

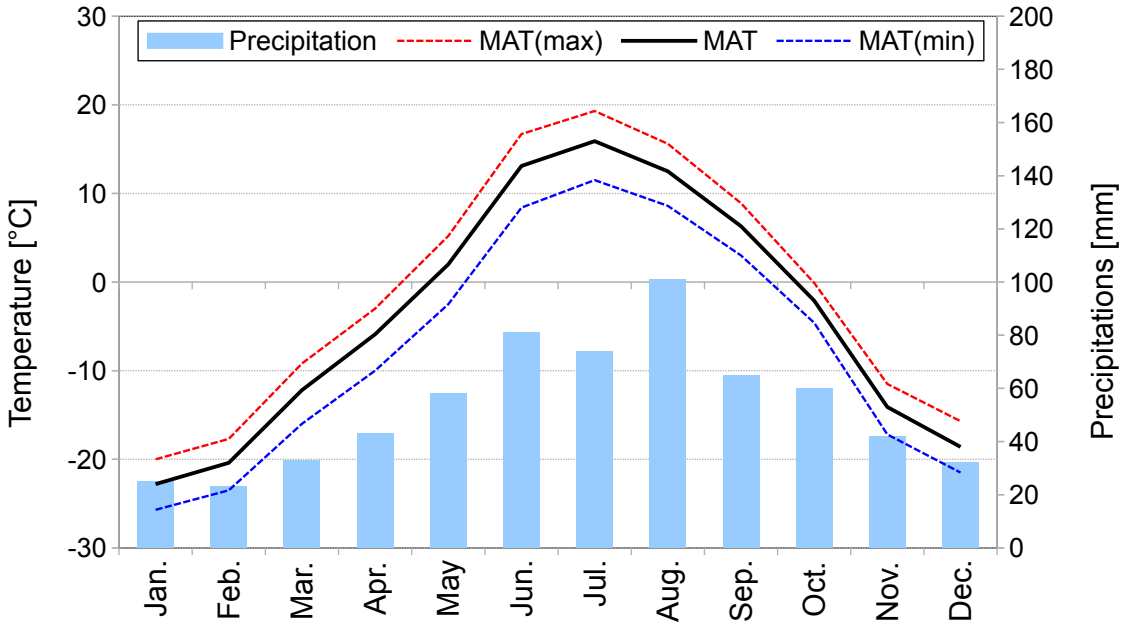

Figure 3.1.1 – Climatic data for Noyabrsk city (Russian Federation, about 70 km north of Khanymey) based on 1991-2021 meteorological records. MAT is the Mean Annual Temperature. *Climatic data distributed under CC-BY-NC 4.0 Creative Commons license by* https://fr.climate-data.org/.

Many studies have been performed since the setup of the research station, notably about the relations of thermokarst formations and functional ecology (Lim et al., 2017; L. S. Shirokova et al., 2013; Y. N. Morgalev et al., 2017; S. Y. Morgalev et al., 2023). One can consult also Raudina et al. (2018) for an exhaustive description of Khanymey research station. In this paper, the authors presented the low vegetation strata, permafrost type and depth. A general presentation of the local cryo-hydrological dynamics occurring on the site is also available in Fig. 3.1.2.

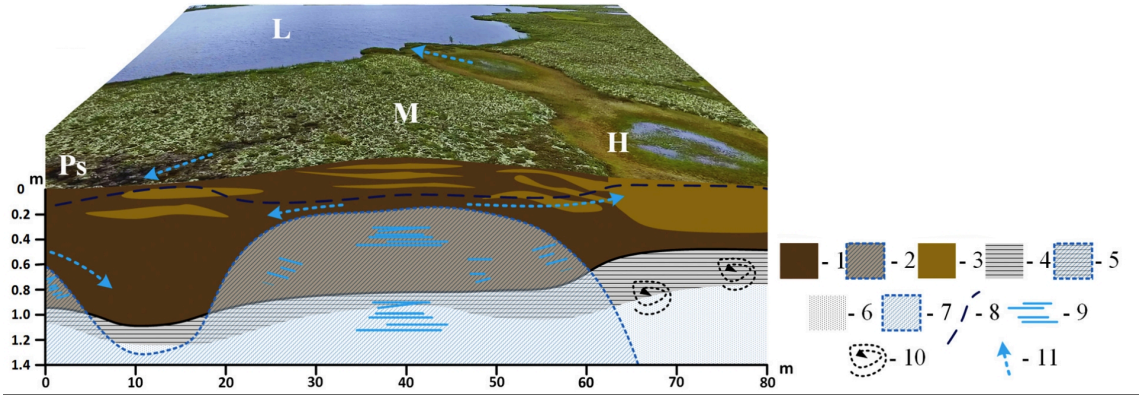

Figure 3.1.2 – General presentation of permafrost dynamics under Khanymey research station and slice cut through the soil horizons (after Raudina et al. (2018), modified).

1: *Moss-lichen-sedge peat of medium degree of decomposition (Hemic);*

2: *Permanently frozen peat;*

3: *Sphagnum peat of low degree of decomposition (Fibric);*

4: *Illuvial-humic (spodic) horizon;*

5: *Permanently frozen spodic horizon;*

6: *Sand deposits;*

7: *Frozen sand;*

8: *The level of supra-permafrost waters in August;*

9: *Ice wedges;*

10: *Cryoturbation features in soil;*

11: *Direction of flow.*

One can also refer to Payandi-Rolland, L. Shirokova, Tesfa, et al. (2020) and Payandi-Rolland, L. Shirokova, Nakhle, et al. (2020) for a complete description of the Khanymey site as well as L. Shirokova et al. (2021) for some biogeochemical data. Khanymey research station constitutes the main source of sample for the study of transfer properties of this thesis.

Khanymey research station faces strong thermokarstification, since permafrost is discontinuous and that some ice wedges can be found beneath the soil surface. A schematic soil profile representation and data about the nature of the soil horizons are available in Fig. 3.1.3.

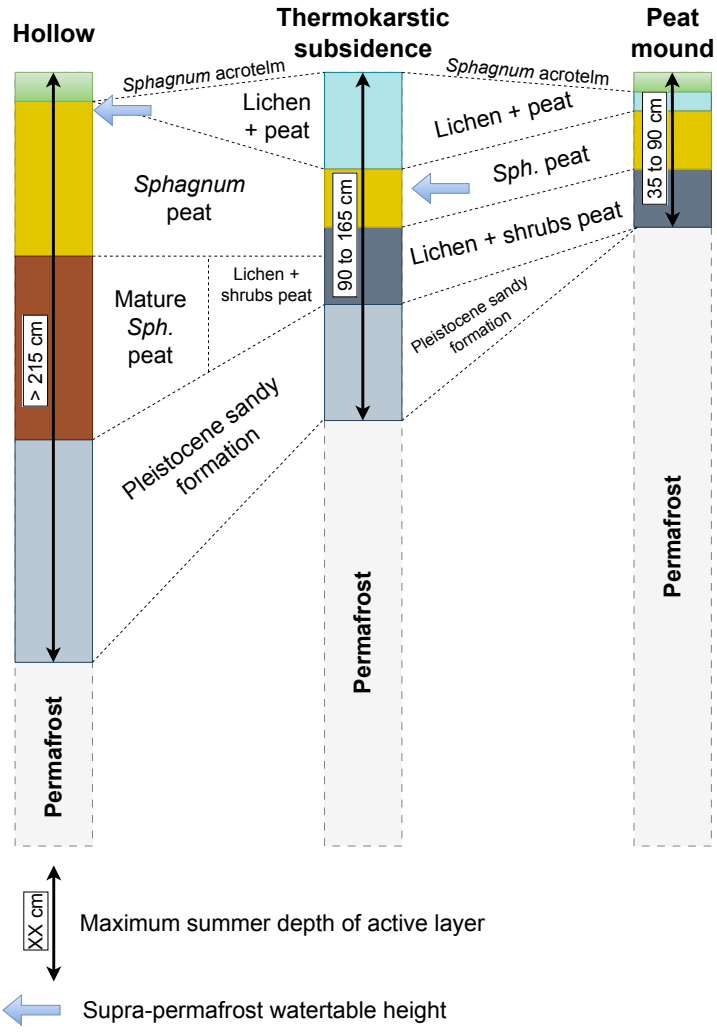

Figure 3.1.3 – Schematic representation of the soil profile at a moss mound (palsa) and moss depression at Khanymey research station.

The vegetation surface consists of a complex patchwork of lichen, moss and peat, which is the most common in Arctic regions as shown by Soudzilovskaia et al. (2013) and Volkova et al. (2018). One of the peculiarities of Khanymey is that the peatland is covered by a high number of thermokarstic lakes of various sizes, mostly round and about one meter deep. A more precise description of the thermokarstic lakes is given in Payandi-Rolland, L. Shirokova, Tesfa, et al. (2020) and in L. Shirokova et al. (2021).

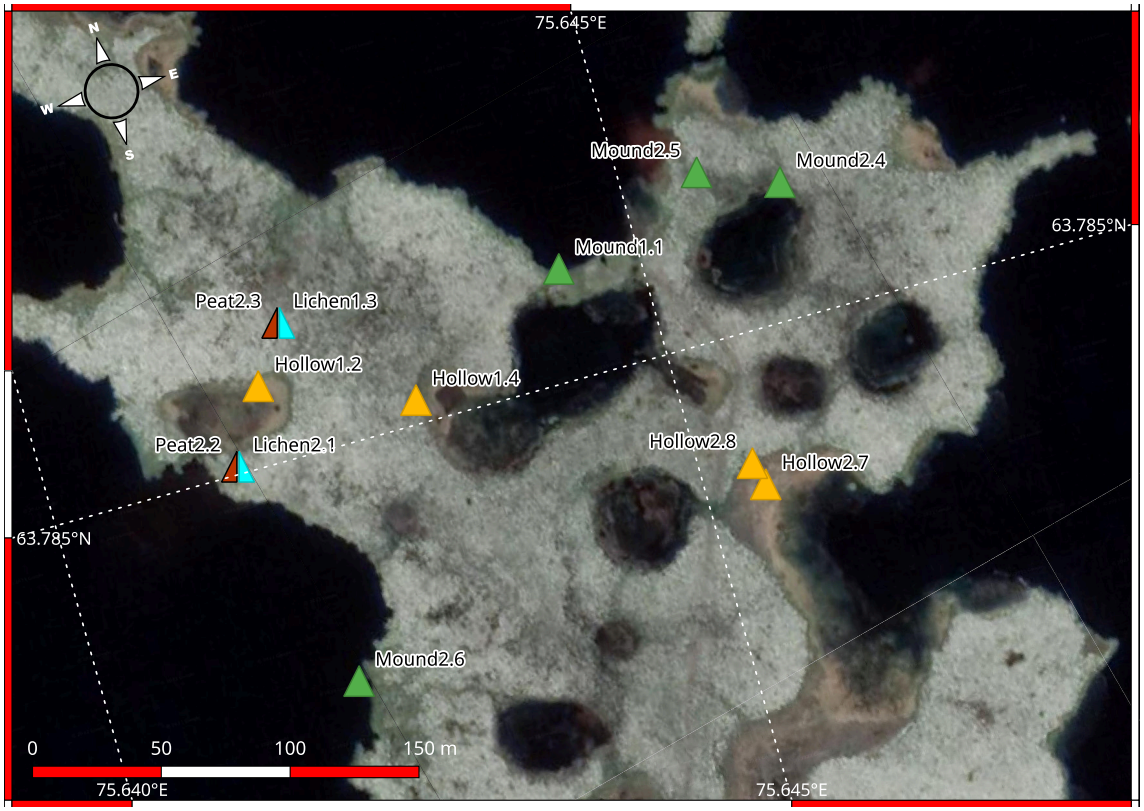

Figure 3.1.4 – Sample location on the Khanymey Research Station. Map scale: 1/1500. *Satellite image: ©Google Earth 2023 (all rights reserved).*

The sample collection from Khanymey consists of 12 samples collected in July 2018 by Laurent Orgogozo from *Géosciences Environnement Toulouse* laboratory assisted by Serguey Loiko and Georgiy Istigechev from Tomsk State University[2].

These 12 samples consists of eight *Sphagnum* samples, of which four *Sphagnum* were taken over peat mounds (palsas) and another four in thermokarstic subsidences. This sample collection also includes two lichen samples and two peat samples that were collected beneath the latter lichen samples. Some complementary information about sample characteristics are shown in Appendix 4.A. A map describing the location of the samples is available in Fig. 3.1.4. A general panorama of the sample location as well as the sample plots is shown in Fig. 3.1.5.

2 The sampling has been performed using an original sampling methodology developed by Stéphane Audry and Laurent Orgogozo aiming at minimizing the physiological disturbance of the samples. One can refer to section 4.1.1 for more details on the sampling methodology.

Figure 3.1.5 – (*left*) General panorama of Khanymey research station (*right*) Sample box placed on field ©*L. Orgogozo, 2018*.

Raudina et al. (2018) gives also a description of the vegetation species mostly occurring at Khanymey research station. The most common lichen species found at Khanymey research station is *Cladonia stellaris* and *Cladonia rangiferina*. This microtopography which consists in moss mounds and hollows, is due to a local persistence of permafrost forming peat mound and thereby a moss mound. On the other side, soil subsidence and permafrost degradation creates locally a depression that is filled with thaw water. On moss mounds, the predominant species are *Sphagnum angustifolium* and *Sphagnum lenense*. One can that see from the satellite image provided with Fig. 3.1.4 that in the case of Khanymey research station, a strong lichen cover is present over the surface. The landscape of Khanymey scientific station represents the typical terrain of the Western Siberian Lowlands. The study area features numerous thermokarstic lakes and a variety of soil profiles, combining Pleistocene sands and adjacent peat deposits.

3.2 ABISKO (SWEDISH LAPLAND)

Although not studied in this PhD thesis, sampling of the low vegetation strata of this environment has been done. The Abisko scientific research station is the next watershed to be simulated by HiPerBorea with the *permaFoam* numerical solver, with a first preliminary work already published (Auda et al., 2023). The collected samples will be used in the future for informing the permafrost simulations to come.

The Abisko research station is located in Swedish Lapland, at N68.355141°, E18.815286° on the southern shores of Lake Torneträsk. The Abisko village (around 650 year-round inhabitants) is located 200 km north of the Arctic Circle. The nearest city is about 100 km southeast, Kiruna (approximately 23 000 inhabitants). The station itself has been operated by the Swedish Polar Institute since 1913. It is the oldest European arctic research station still in operation to this date. Like the Khanymey research station

presented in the previous section, Abisko research station faces a subarctic climate (Dfc according to the Köppen classification). However, the Abisko research station is located in the Scandinavian Alps, with nearby summits up to 1900 m high. The mean annual temperature and the mean annual liquid precipitation for the 1913-2004 period are respectively 0.7 °C and 310 mm (Kohler et al., 2006). From the meteorological data available in Fig. 3.2.1 for the 1991-2021 period, the mean annual temperature is -1.66 °C and the mean average precipitation is 1012 mm[3]. The south shore of Lake Torneträsk is significantly drier than the surrounding areas due to a rain shadow effect of the Scandinavian Alps closing the lake on the northwest side of it, at the border with Norway. The research fields of this research station spans from ecology to meteorology and geomorphology. One can consult slightly dated nonetheless exhaustive description of the Abisko research station in Andersson et al. (1996). Some other studies around Abisko research station include a study of active layer thickness (Åkerman and Johansson, 2008), mercury export (Klaminder et al., 2008), and of methane fluxes' modeling (Petrescu et al., 2008), among other studies.

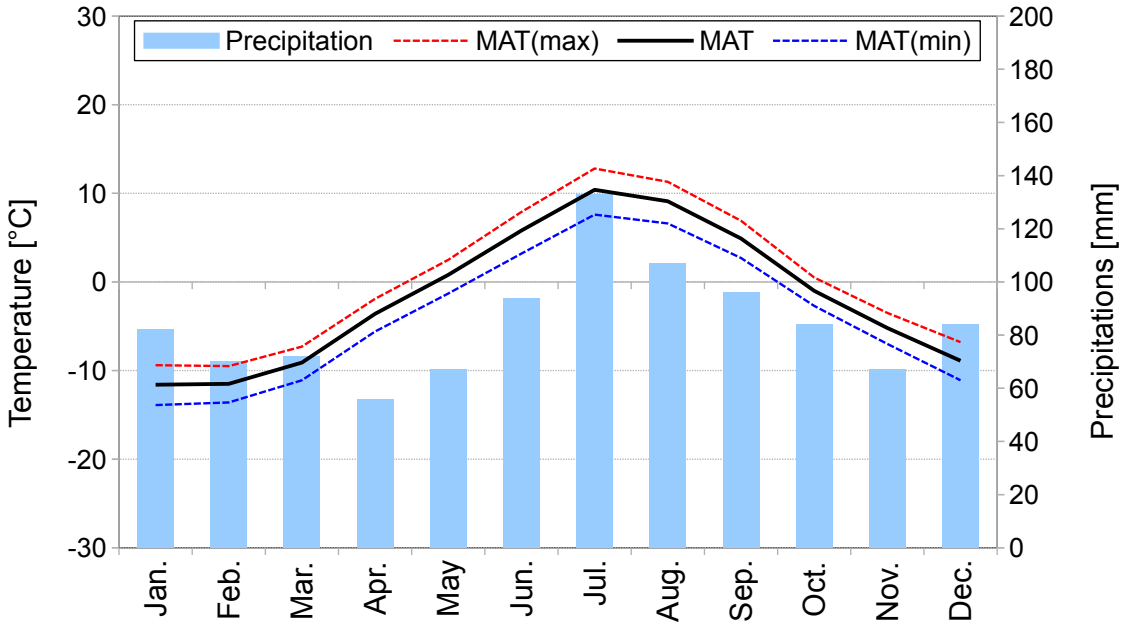

Figure 3.2.1 – Climatic data for Abisko (Sweden) based on 1991-2021 meteorological records. MAT is the Mean Annual Temperature. *Climatic data distributed under CC-BY-NC 4.0 Creative Commons license by* https://fr.climate-data.org/.

This station has been selected in the HiPerBorea project as a test site for the implementation of the numerical methods developed in the project. In July 2022, an expedition was organized to Stordalen and Miellajokka catchments to characterize the land surface of these catchments (Auda et al., 2023). A presentation of this both catchments is made

3 The difference of precipitation between the 1913-2004 data from Kohler et al. (2006) is due to the fact this value is taking only into account liquid precipitation (hence excluding snowfalls).

hereafter. This expedition gave also the opportunity to retrieve four living samples in real permafrost condition at the Stordalen mire. A presentation of the mire and the location of the samples is shown in subsection 3.2.2.

3.2.1 *Miellajokka catchment*

The Miellajokka catchment covers about 53.5 km² of land surface, the highest point is located above 1700 m Above Sea Level (ASL) and the lowest point is the reach of Lake Torneträsk at about 350 m ASL. The relative steep slopes of this catchment can be described into three main vegetation classes according to Lyon et al. (2018):

- birch forest (350-700 m ASL);
- meadow heath, dwarf birch and shrubs (700-1300 m ASL);
- and alpine tundra to bare rock soil cover above 1300 m ASL

A general map of Miellajokka catchment is given in Fig. 3.2.2.

(a) General overview.

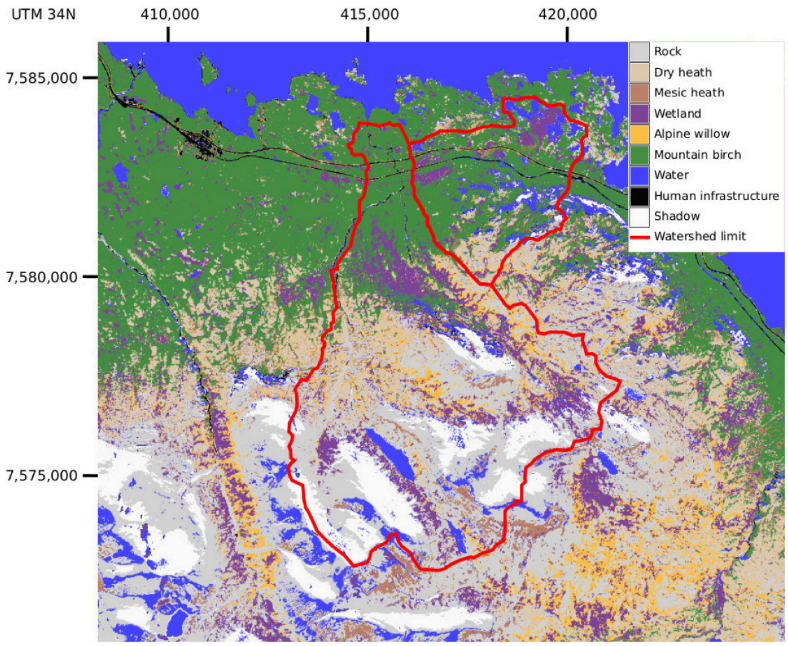

(b) Vegetation cover.

Figure 3.2.2 – (a) General overview of the location of the Miellajokka and Stordalen watersheds *Map from Lantmäteriet Fjällkartan* (b) Global vegetation map of the Stordalen catchment after Auda et al. (2023).

3.2.2 *Stordalen watershed and Stordalen mire*

The Stordalen catchment is located next to the Miellajokka catchment, sharing its eastern border. The Stordalen catchment follows similar hydrological trends than the Miellajokka catchment for its uppermost part. The lowlands of the Stordalen watershed is dominated by a mire of approximately 0.25 km^2. This mire is studied extensively in conjunction with the Abisko research station. The mire can be subdivided into three main categories depending on the local water input, according to Lupascu et al. (2012):

- Minerotrophic-sedge mire with the presence of *Eriophorum angustifolium* (common cottongrass) Honck., and big patches of *Sphagnum riparium* Angst., facing winter freezing and complete thawing during summer;
- Minerotrophic-*Sphagnum* mire, dominated by *Sphagnum spp.* and perennial freeze-thaw cyclic permafrost layer. The *Sphagnum* species present in the Stordalen mire are (by ordrer of presence): *Sphagnum balticum* (Russ.) C. Jens., *Sphagnum fuscum* Klinggr., *Sphagnum russowii* Warnst. and *Sphagnum lindbergii* Schimp. (Malmer et al., 2005);
- Ombrotrophic bog, dominated by *Rubus chamaemorus* (cloudberry) L., *Empetrum hermaphroditum* (black crowberry) Hagerup., and *Andromeda polifolia* (bog-rosemary) L.

Jackowicz-Korczyński et al. (2010) reported that the local mean annual temperature is lower of approximately 0.2 °C than the observed mean annual temperature at the Abisko research station. The authors give some clues about a local thermal inversion during summer due to the presence of Lake Torneträsk.
To complete the sample collection available for the thesis, four *Sphagnum* samples were collected at the Stordalen mire. A map of the Stordalen mire with the location of the four samples is available in Fig. 3.2.3.

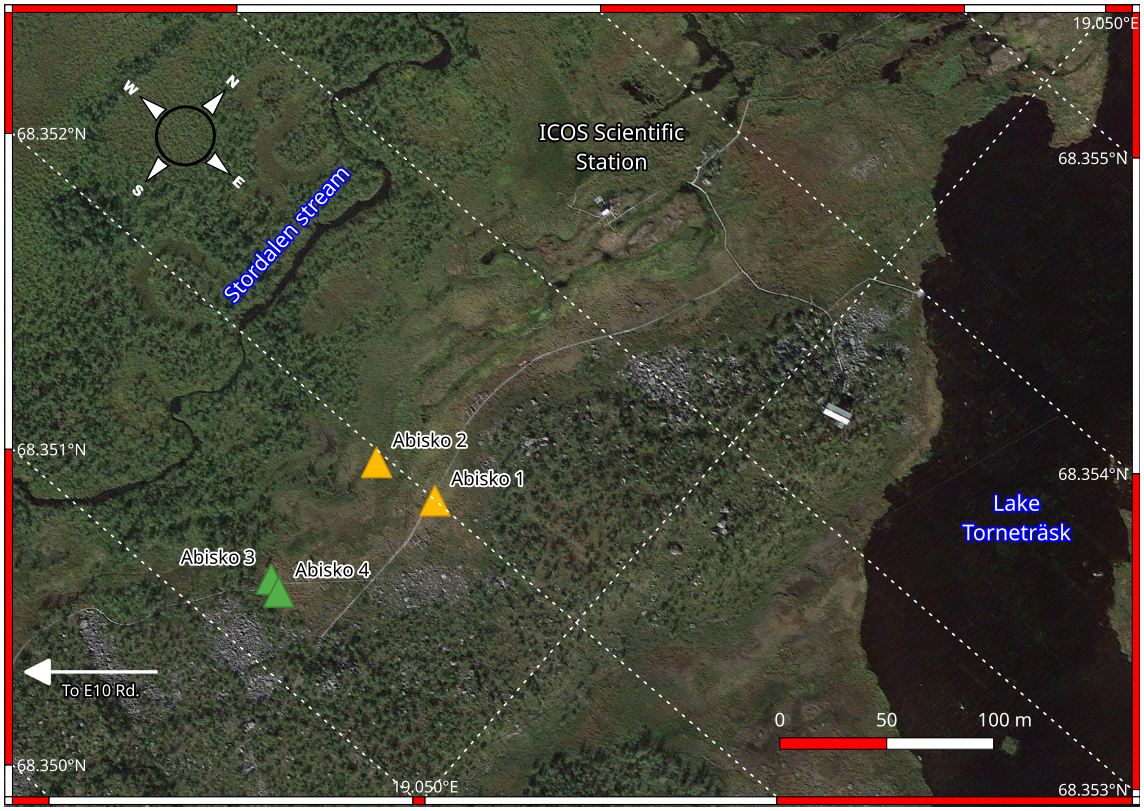

Figure 3.2.3 – Sample location at Stordalen mire, near the Abisko Research Station. Map scale: 1/1800. *Satellite image: ©Google Earth 2023 (all rights reserved).*

In this sample collection, two samples were collected in hollows in a saturated mire (samples Abisko1 and Abisko2) and the two others were collected on peat bogs where the water table was deeper. A picture of the four samples is available in Fig. 3.2.4.

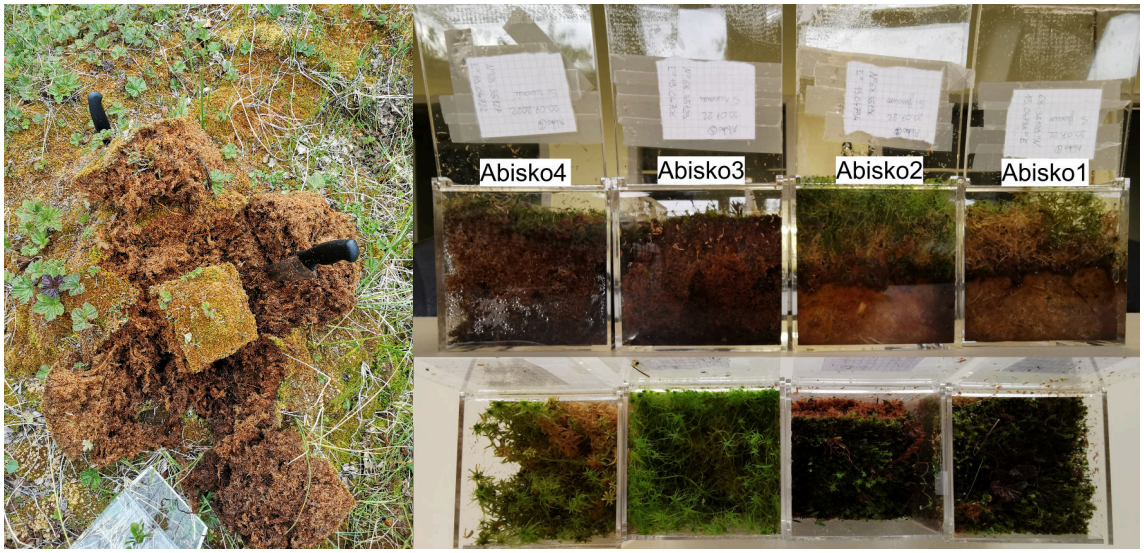

Figure 3.2.4 – Picture of the sampling of Abisko3 sample on field. Note the extraction of the side blocks to avoid perturbation to the main block.

3.3 CLARENS MIRE (PYRÉNÉES)

After the retreat of the glaciers covering the north Pyrenean valleys in late Pleistocene (11 600 years BP), some limited peatland mires formed due to the local microclimate and the hydrology of then ice-free small entrenched valleys. The Clarens mire is assumed to have its initial state at the end of the Pleistocene, making this site a case of post-permafrost retreat state for peatlands. The Clarens mire bog is located in the southwest of France, near the village of Clarens (495 inhabitants) and about 20 km north from the city of Lannemezan (5800 inhabitants). This study site is not part of the INTERACT network due to its meridional location. However, due to its proximity with Toulouse (about 130 km) and the protected status of the mire, the site was added to the site list for the study of this thesis.
From the meteorological data for the 1991-2021 period available in Fig. 3.3.1, the MAT is about 11.8 °C and the MAP is around 1132 mm. Indeed, Clarens mire cannot be considered as an arctic mire but as a temperate mire, although it is assumed that the local climate remains colder than the surroundings.

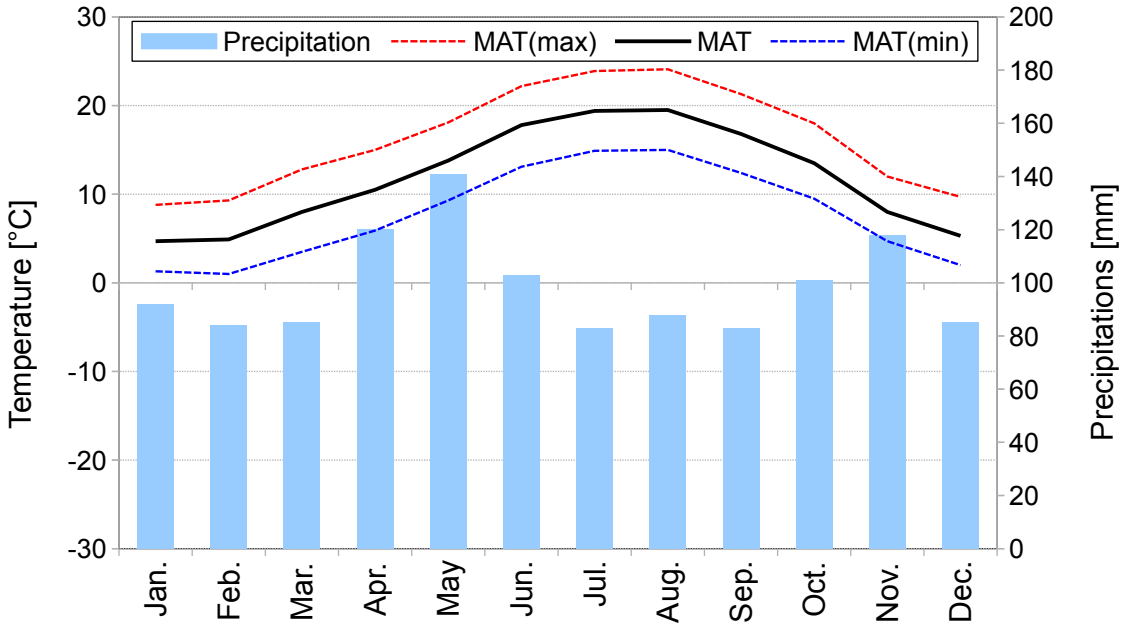

Figure 3.3.1 – Climatic data for Clarens (France) based on 1991-2021 meteorological records. MAT is the Mean Annual Temperature. *Climatic data distributed under CC-BY-NC 4.0 Creative Commons license by* https://fr.climate-data.org/.

The available literature on Clarens site is much scarcer than for Khanymey and Abisko research stations. To this date, only Corriol (2009) mentions the Clarens mire in their local mycological study. Some information about the mire is available in two Master's memoirs respectively Bousquet et al. (2016) and Durantez et al. (2014)[4] The mire has a

4 both Master's memoirs available on the mire park's website (last access August 8th 2023, reports in French)

total extension of 1.39 km² and is situated at about 420 m ASL. The mire can be divided into two sections:

- The north meadows consist of the northern part of the active Clarens mire. This area has an extension of about 0.83 km² representing approximately 60% of the total surface. In this area, various sedge plants can be found, such as *Molinia caerula* (purple moor-grass), *Carex punctata* (dotted sedge). One of the peculiarities of the northern part of the bog is that it faces closing phenomenon, meaning that the meadows are progressively replaced by trees and shrubs, causing the closing of the mire on the northern side.
- The south mire is the southern part of Clarens mire and is mainly constituted of a saturated mire of Bryopsidae (*Philonotis marchica*) and various *Sphagnum* species such as *Sphagnum russowii*, *Sphagnum fuscum* or *Sphagnum angustifolium*.

The Clarens mire is protected under the Natura 2000 biodiversity protection program. Therefore, sampling of *Sphagnum* mosses is restricted to scientific purposes. This accreditation was filled in February 2021 by the *Direction Départementale des Territoires de Hautes-Pyrénées* (DDT65, the French National administration responsible for Natura 2000 ecological zones' protection). Six living *Sphagnum* samples were collected at the Clarens mire during a field trip in March 2021. Four of the samples consists of *Sphagnum fuscum* (Schimp.) H.Klinggr and the other two samples consists of *Philonotis marchica* (Hedw.) Brid., 1827. A map presenting the locations of the sampling is shown in Fig. 3.3.2. A general overview of the collected samples is available in Fig. 3.3.3.

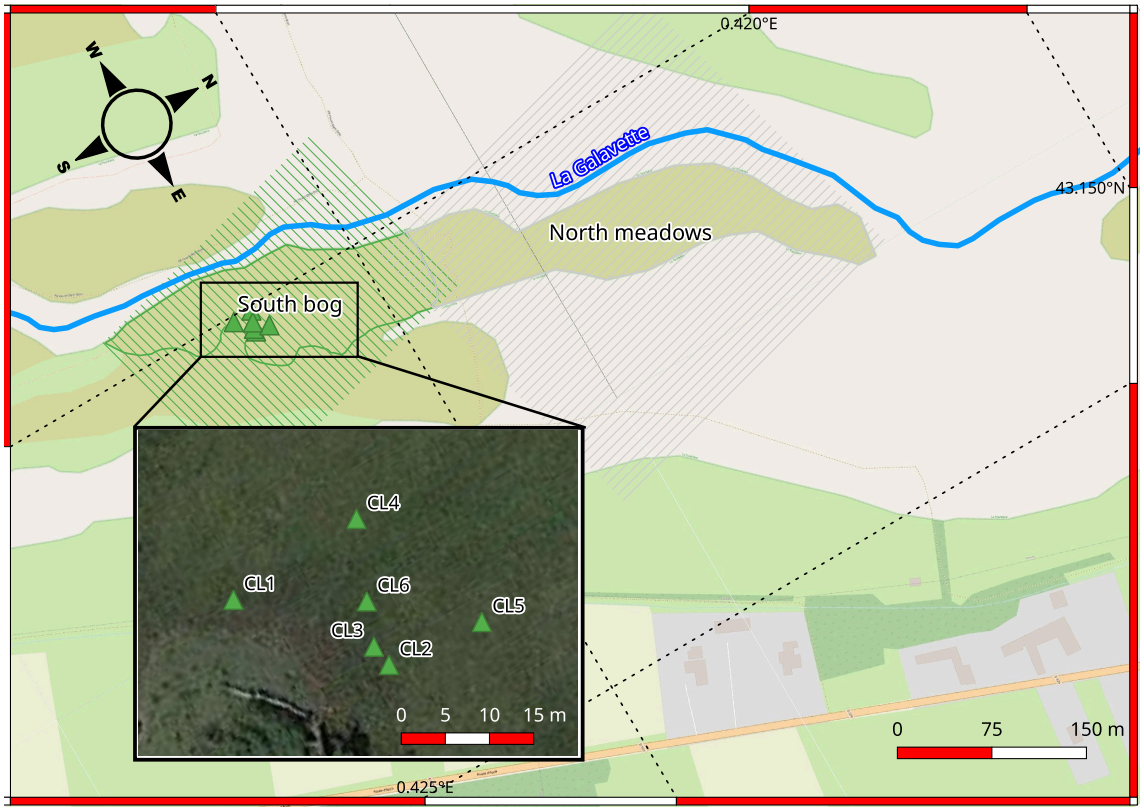

Figure 3.3.2 – Sample location on the Clarens Regional Park. General map scale: 1/3000. *Topographic map*: OpenStreetMaps Landscape, *Satellite image: ©Google Earth 2023 (all rights reserved)*.

3.4 CONCLUSION ON STUDY SITES

Three main study sites are investigated in this thesis: Khanymey (Western Siberia) where most of the study is conducted, Abisko (Swedish Lapland) and Clarens (Upper-Pyrénées). While the two first are attached to research stations where data is largely available in the literature, this is not the case for the latter study site. Khanymey and Abisko share both some permafrost characteristics (discontinuous permafrost for Khanymey and patchy permafrost for the Stordalen mire near Abisko). These study sites offer solid ground for arctic vegetation properties characterization and inter-comparison with other studies. The Clarens site, which was not initially in the HiPerBorea project, enabled the potential to provide this thesis with a significant quantity of test samples. The various methods presented in the following chapter are tested an validated using the samples collected at Clarens site.

It must be kept in mind, however, that the choice of study sites always limits the field of study of vegetation cover to specific samples. During the course of this thesis, the small number of samples collected was compensated by the use of a methodology specific

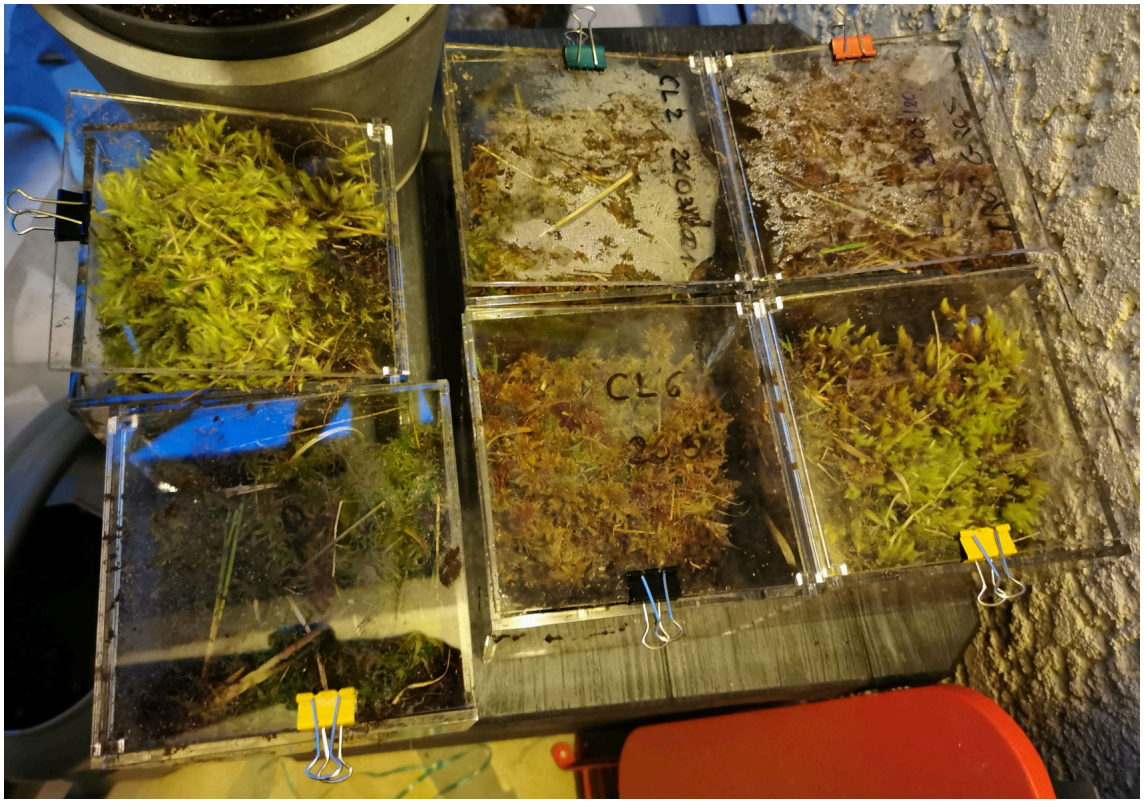

Figure 3.3.3 – Clarens samples pictures after their extraction on field.

to porous media. A discussion of the number of samples required and the validity of statistical studies considering arctic vegetation cover as a porous medium is presented in Chapter 5 of Part iii.

APPENDIX

3.A BOTANICAL OVERVIEW OF THE ENCOUNTERED SPECIES IN THE STUDY SITES

In this appendix, the reader can find a general presentation of the studied species in this thesis as well as a picture of the relative species. Many of the closeup pictures and microscopic slices of different *Sphagnum* species are from Mr. Hermann Schachner (alias *HermannSchachner*), available on the Wikimedia repository under CC0 license at the Wikimedia repository (in German).

3.A.1 *Bryophytes*

Bryophytes differentiate mainly upon the manner the fascicles are set on the main thallus and the aspect of the acrotelm (the growing topmost part of Bryophytes). For a general reference about the different acrotelm shapes, one can refer to the figure made by Heck et al. (2021) depicted in Fig. 3.A.1. One can also refer to Laine et al. (2018) for an exhaustive description of the different *Sphagnum* species.

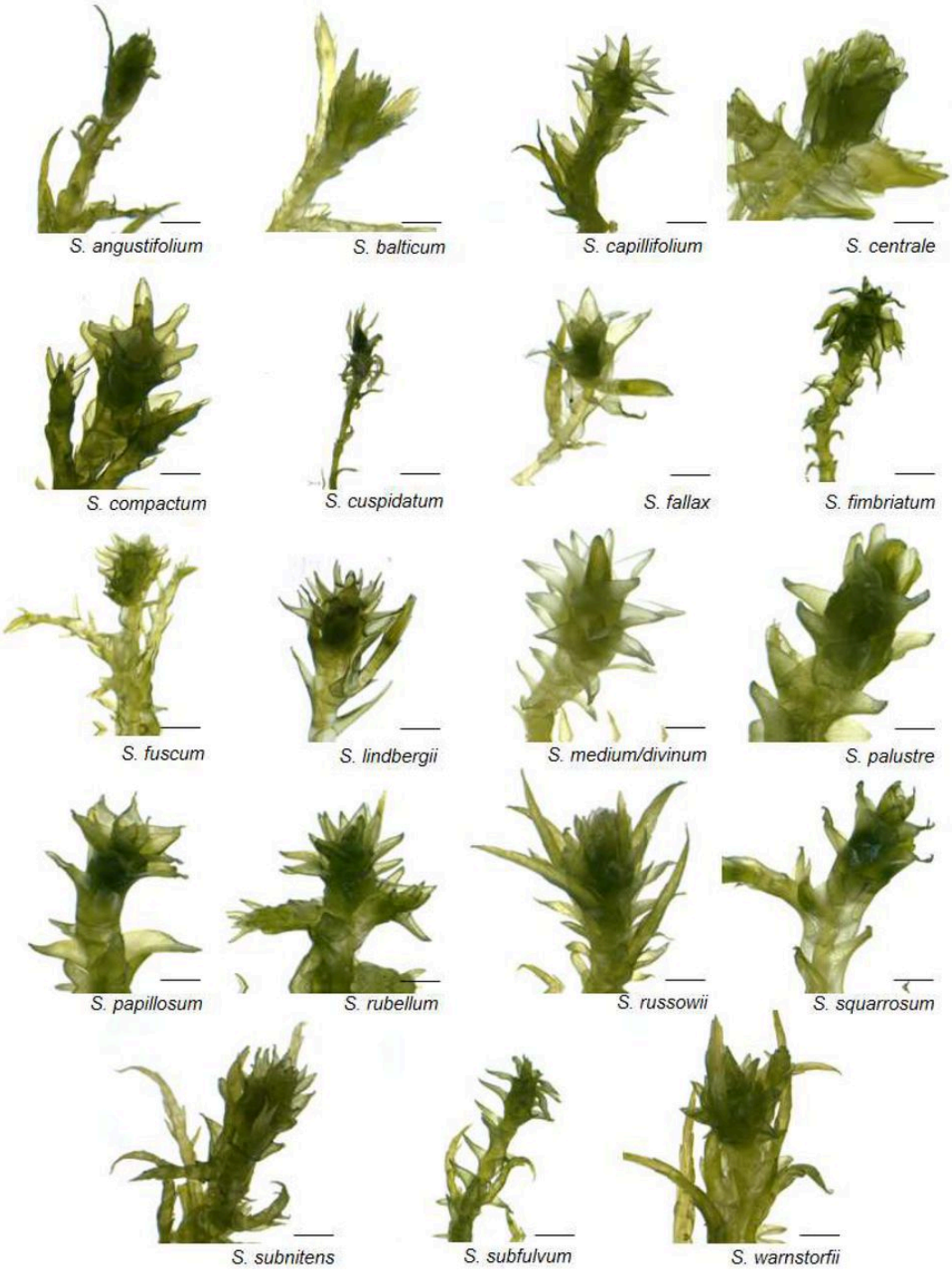

Figure 3.A.1 – Light microscopic images of characteristic gametophores of Sphagnum spp. after four weeks of axenic cultivation on solid *Sphagnum* medium. Scale bar = 1 mm (after Heck et al., 2021).

3.A.1.1 Sphagnum angustifolium *(C.E.O. Jensen ex Russow) C.E.O. Jensen*

(a) General closeup **(b)** Pseudo-leaf microscopic structure

Figure 3.A.2 – *Sphagnum angustifolium* (C.E.O. Jensen ex Russow) C.E.O. Jensen illustration pictures.

Latin name		*Sphagnum angustifolium* (C.E.O. Jensen ex Russow) C.E.O. Jensen
Common name	English	Fine bogmoss
	Français	Sphaigne à feuilles étroites
Phylogenetic classification	Kingdom	Plantae
	Division	Bryophyta
	Class	Sphagnopsida
	Subclass	Sphagnidae
	Order	Sphagnales
	Familly	Sphagnaceae
	Genus	*Sphagnum*
	Species	*S. angustifolium*
Description		Available on EFloras America
IUCN status		LC (Least Concern)
Occurrence (Worldwide)		Eurasia, North-America in peatlands
Occurrence on study sites	Abisko	Yes
	Clarens	No
	Khanymey	Yes

Table 3.A.1 – *Sphagnum angustifolium (C.E.O. Jensen ex Russow) C.E.O. Jensen* general data.

3.A.1.2 Sphagnum balticum *C.E.O. Jensen*

Figure 3.A.3 – *Sphagnum balticum* C.E.O. Jensen general closeup.

Latin name		*Sphagnum balticum* C.E.O. Jensen
Common name	English	Baltic bogmoss
	Français	Sphaigne de la Baltique
Phylogenetic classification	Kingdom	Plantae
	Division	Bryophyta
	Class	Sphagnopsida
	Subclass	Sphagnidae
	Order	Sphagnales
	Familly	Sphagnaceae
	Genus	*Sphagnum*
	Species	*S. balticum*
Description		Available on eFloras.org
IUCN status		LC (Least Concern)
Occurrence (Worldwide)		Eurasia, North-America in peatlands
Occurrence on study sites	Abisko	Yes
	Clarens	No
	Khanymey	Yes

Table 3.A.2 – *Sphagnum balticum* C.E.O. Jensen general data.

3.A.1.3 Sphagnum fuscum *(Schimp.) H.Klinggr.*

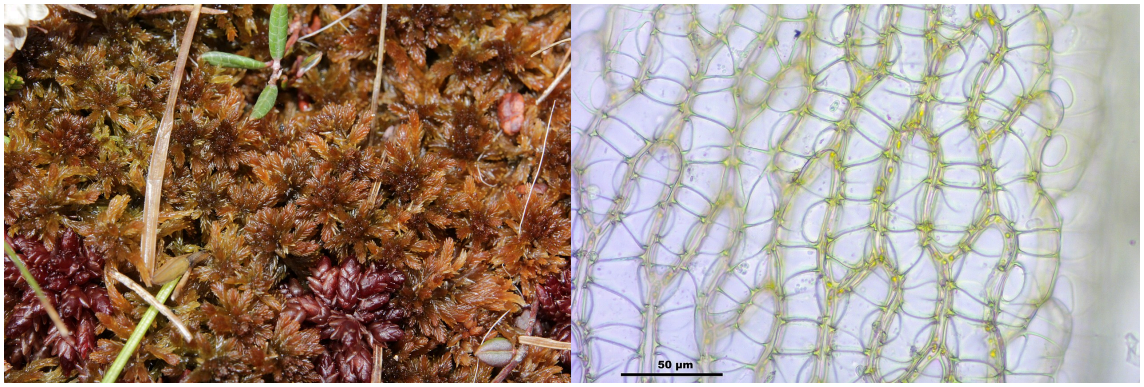

(a) General closeup **(b)** Pseudo-leaf microscopic structure

Figure 3.A.4 – *Sphagnum fuscum* (Schimp.) H.Klinggr. illustration pictures.

Latin name		*Sphagnum fuscum* (Schimp.) H.Klinggr.
Common name	English	Rusty bogmoss
	Français	Sphaigne brune
Phylogenetic classification	Kingdom	Plantae
	Division	Bryophyta
	Class	Sphagnopsida
	Subclass	Sphagnidae
	Order	Sphagnales
	Familly	Sphagnaceae
	Genus	*Sphagnum*
	Species	*S. fuscum*
Description		Available on eFloras.org.
IUCN status		Protected in some countries.
Occurrence (Worldwide)		Eurasia, North-America in peatlands
Occurrence on study sites	Abisko	Yes
	Clarens	Yes
	Khanymey	Yes

Table 3.A.3 – *Sphagnum fuscum* (Schimp.) H.Klinggr. general data.

3.A.1.4 Sphagnum lenense *H. Lindb. ex L.I. Savicz*

Figure 3.A.5 – *Sphagnum lenense* H. Lindb. ex L.I. Savicz general closeup ©Dale H. Vitt obtained from PhytoImages.siu.edu.

Latin name		*Sphagnum lenense* H. Lindb. ex L.I. Savicz
Common name	English	Lena river peat moss
	Français	Sphaigne de la Léna
Phylogenetic classification	Kingdom	Plantae
	Division	Bryophyta
	Class	Sphagnopsida
	Subclass	Sphagnidae
	Order	Sphagnales
	Familly	Sphagnaceae
	Genus	*Sphagnum*
	Species	*S. lenense*
Description		Available at eFloras.org.
IUCN status		Protected in some countries
Occurrence (Worldwide)		Eurasia, scarcely in North-America
Occurrence on study sites	Abisko	No
	Clarens	No
	Khanymey	Yes

Table 3.A.4 – *Sphagnum lenense* H. Lindb. ex L.I. Savicz general data.

3.A.1.5 Sphagnum lindbergii *Schimp.*

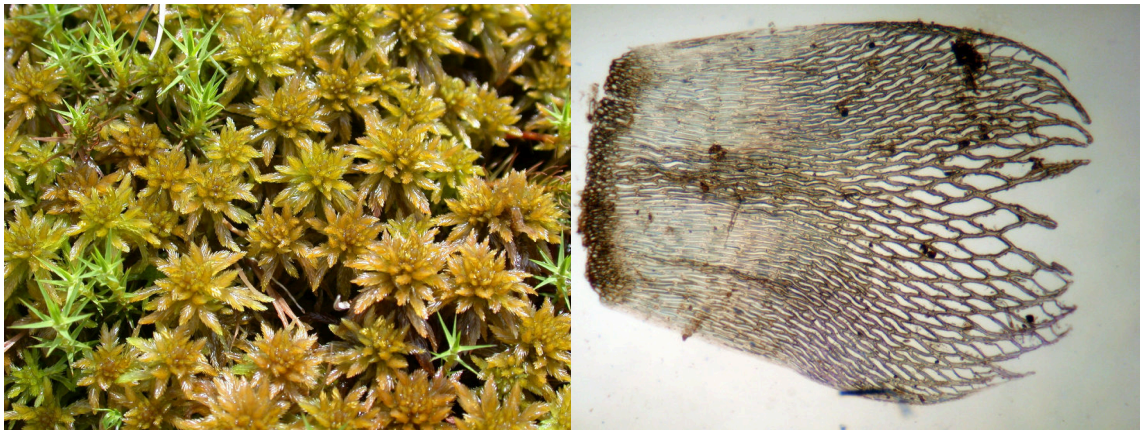

(a) General closeup © Gordon Rothero (British Bryological Society)

(b) Pseudo-leaf microscopic structure (CC-BY-NC Scot Loring, 2014)

Figure 3.A.6 – *Sphagnum lindbergii* Schimp. illustration pictures.

Latin name		*Sphagnum lindbergii* Schimp.
Common name	English	Lindberg's bogmoss
	Français	Sphaigne de Lindberg
Phylogenetic classification	Kingdom	Plantae
	Division	Bryophyta
	Class	Sphagnopsida
	Subclass	Sphagnidae
	Order	Sphagnales
	Familly	Sphagnaceae
	Genus	*Sphagnum*
	Species	*S. lindbergii*
Description		Available at eFloras.org.
IUCN status		NE (Non Evaluated)
Occurrence (Worldwide)		Eurasia, North-America in peatlands
Occurrence on study sites	Abisko	No
	Clarens	No
	Khanymey	Yes

Table 3.A.5 – *Sphagnum lindbergii* Schimp. general data.

3.A.1.6 Sphagnum majus *(Russow) C.E.O.Jensen*

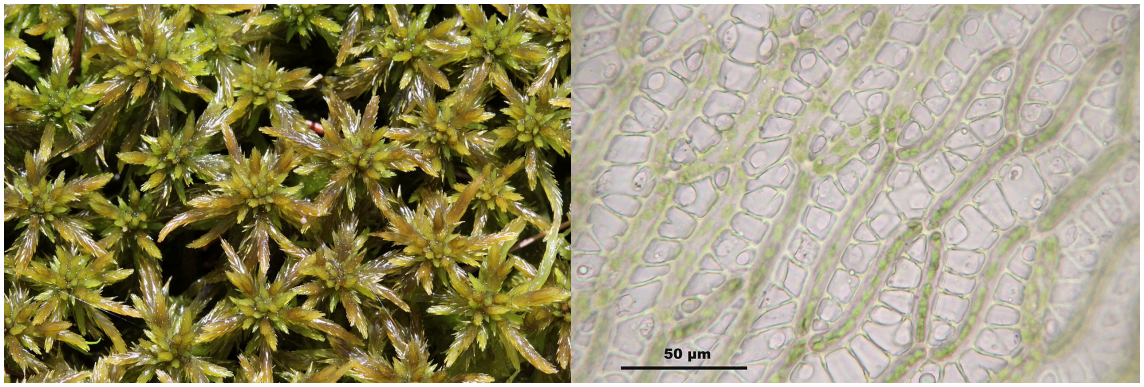

(a) General closeup **(b)** Pseudo-leaf microscopic structure

Figure 3.A.7 – *Sphagnum majus* (Russow) C.E.O. Jensen illustration pictures.

Latin name		*Sphagnum majus* (Russow) C.E.O. Jensen
Common name	English	Greater peat moss
	Français	Sphaigne majeure
Phylogenetic classification	Kingdom	Plantae
	Division	Bryophyta
	Class	Sphagnopsida
	Subclass	Sphagnidae
	Order	Sphagnales
	Familly	Sphagnaceae
	Genus	*Sphagnum*
	Species	*S. majus*
Description		Available at eFloras.org.
IUCN status		LC (Least Concern)
Occurrence (Worldwide)		Eurasia, North-America in peatlands
Occurrence on study sites	Abisko	Probable
	Clarens	No
	Khanymey	Yes

Table 3.A.6 – *Sphagnum majus* (Russow) C.E.O. Jensen general data.

3.A.1.7 Sphagnum riparium *Ångstr.*

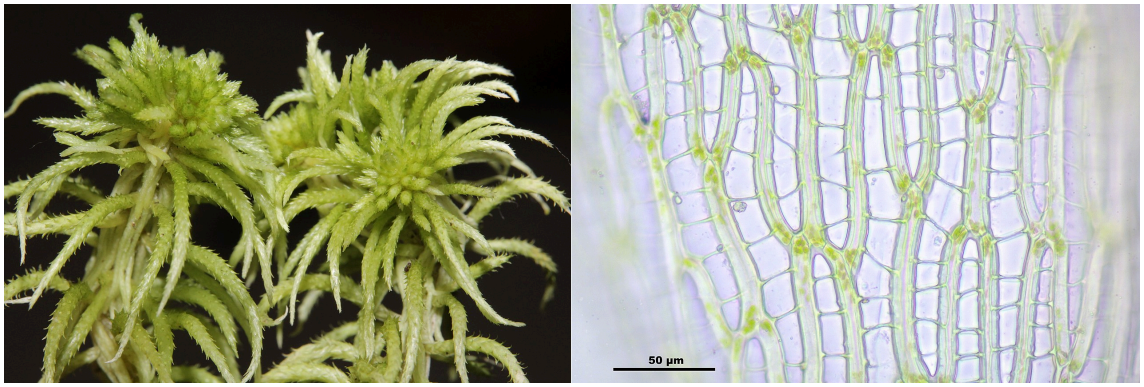

(a) General closeup © Gordon Rothero (British Bryological Society) **(b)** Pseudo-leaf microscopic structure (CC-BY-NC Scot Loring, 2014)

Figure 3.A.8 – *Sphagnum riparium* Ångstr. illustration pictures.

Latin name		*Sphagnum riparium* Ångstr.
Common name	English	Cleft bogmoss
	Français	Sphaigne des rivages
Phylogenetic classification	Kingdom	Plantae
	Division	Bryophyta
	Class	Sphagnopsida
	Subclass	Sphagnidae
	Order	Sphagnales
	Familly	Sphagnaceae
	Genus	*Sphagnum*
	Species	*S. riparium*
Description		Available at eFloras.org.
IUCN status		NE (Non Evaluated)
Occurrence (Worldwide)		Eurasia, North-America in peatlands
Occurrence on study sites	Abisko	Yes
	Clarens	No
	Khanymey	Probably

Table 3.A.7 – *Sphagnum riparium* Ångstr. general data.

3.A.1.8 Sphagnum russowii *Warstn.*

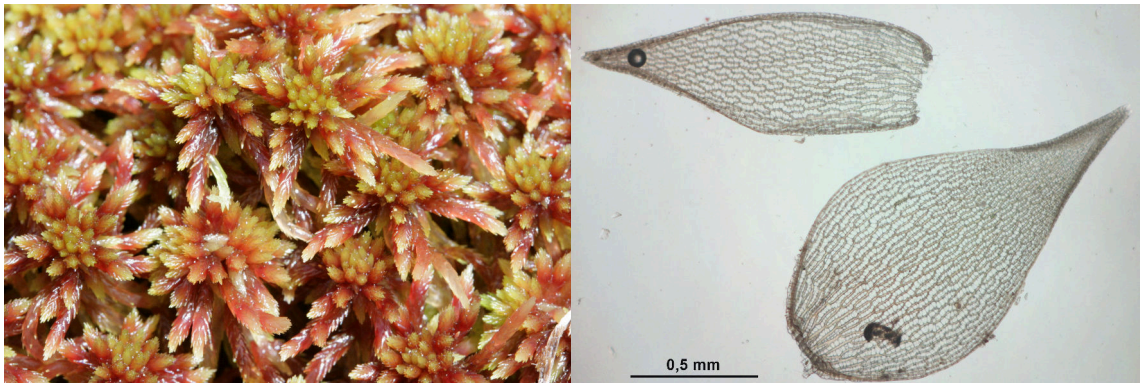

(a) General closeup **(b)** Pseudo-leaf microscopic structure

Figure 3.A.9 – *Sphagnum russowii* Warnst. illustration pictures.

Latin name		*Sphagnum russowii* Warnst.
Common name	English	Russow's bogmoss
	Français	Sphaigne de Russow
Phylogenetic classification	Kingdom	Plantae
	Division	Bryophyta
	Class	Sphagnopsida
	Subclass	Sphagnidae
	Order	Sphagnales
	Familly	Sphagnaceae
	Genus	*Sphagnum*
	Species	*S. russowii*
Description		Available at efloras.org.
IUCN status		LC (Least Concern)
Occurrence (Worldwide)		Eurasia, North-America in peatlands
Occurrence on study sites	Abisko	Yes
	Clarens	No
	Khanymey	Yes

Table 3.A.8 – *Sphagnum russowii* Warnst general data.

3.A.1.9 Philonotis marchica *Bridel.*

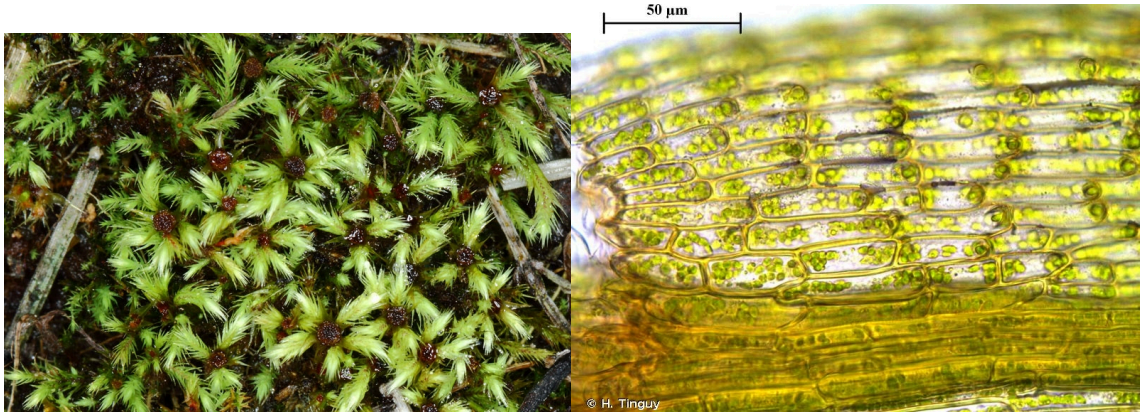

(a) General closeup © Jean Faubert (Société Québécoise de Bryologie)

(b) Pseudo-leaf microscopic structure (Creative Commons BY-NC-SA Hugues Tinguy)

Figure 3.A.10 – *Philonotis marchica* Bridel. illustration pictures.

Latin name		*Philonotis marchica* Bridel.
List	English	Bog apple moss
	Français	Petit philonotis
Phylogenetic classification	Kingdom	Plantae
	Division	Bryophyta
	Class	Bryophyta s.l.
	Subclass	Bryidae
	Order	Bartramiales
	Familly	Bartramiaceae
	Genus	*Philonotis*
	Species	*P. marchica*
Description		Available at eFloras.org.
IUCN status		EN (Endangered specie in France)
Occurrence (Worldwide)		Eurasia, North-America in peatlands
Occurrence on study sites	Abisko	No
	Clarens	Yes
	Khanymey	No

Table 3.A.9 – *Philonotis marchica* Bridel general data.

3.A.2 *Lichens*

3.A.2.1 Cladonia rangiferina *(L.) Weber ex F.H.Wigg.*

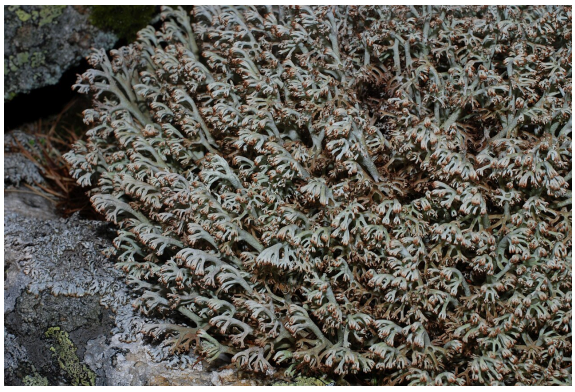

Figure 3.A.11 – *Cladonia rangiferina* (L.) Weber ex F.H.Wigg. *CC-BY-SA 3.0 Tigerente*.

Latin name		*Cladonia rangiferina* (L.) Weber ex F.H.Wigg.
List	English	Reindeer lichen
	Français	Cladonie des rennes
Phylogenetic classification	Kingdom	Fungi
	Division	Ascomycota
	Class	Lecanoromycetes
	Order	Lecanorales
	Familly	Cladoniaceae
	Genus	*Cladonia*
	Species	*C. rangiferina*
Description		Fruticose, mat-forming lichen in arctic regions
IUCN status		LC (Least Concern)
Occurrence (Worldwide)		Eurasia, North-America in tundra biomes
Occurrence on study sites	Abisko	Yes
	Clarens	No
	Khanymey	Yes

Table 3.A.10 – *Cladonia rangiferina* (L.) Weber ex F.H.Wigg. general data.

3.A.2.2 Cladonia stellaris *(Opiz) Pouzar & Vězda*

Figure 3.A.12 – *Cladonia stellaris* (Opiz) Pouzar & Vězda *CC-BY-SA 3.0 MPorciusCato*.

Latin name		*Cladonia stellaris* (Opiz) Pouzar & Vězda
List	English	Star-tipped cup lichen
	Français	Cladonie étoilé
Phylogenetic classification	Kingdom	Fungi
	Division	Ascomycota
	Class	Lecanoromycetes
	Order	Lecanorales
	Familly	Cladoniaceae
	Genus	*Cladonia*
	Species	*C. stellaris*
Description		Fruticose, mat-forming lichen in arctic regions
IUCN status		LC (Least Concern)
Occurrence (Worldwide)		Eurasia, North-America in arctic forests
Occurrence on study sites	Abisko	Yes
	Clarens	No
	Khanymey	Yes

Table 3.A.11 – *Cladonia stellaris* (Opiz) Pouzar & Vězda general data.

4

SAMPLING AND X-RAY DIGITALIZATION OF SUBARCTIC LOW VEGETATION STRATA

In order to study the arctic vegetation cover as a porous medium, some real samples of such layer are needed. Sampling arctic vegetation cover poses a number of technical and methodological challenges. In the case of this thesis, the distance separating the scanning and digital processing facilities is considerable and raises transport issues. Furthermore, we need a sample conditioning that allows the best long-term preservation as arctic plant cover represents a biological, soft, and deformable medium. The preservation of its structure must be achieved not only during transportation, but also during sampling and tomographical observation. Thus, preserving it in conditions as close as possible to those in which it was collected is essential to ensure the best possible representativeness for the study of subsequent physical properties.

This chapter will emphasize the sampling technique and the sample preparation protocol for sampling, X-ray tomography scanning and numerical processing. This digitalization work was first done for dried samples (section 4.2). The same protocol is after applied to multiphasic X-ray tomography with wet samples in liquid water condition (section 4.2.3) and in ice condition (section 4.2.4). In each section, a brief presentation of the X-ray scanning is done followed by the processing of the obtained tomographs. Some high-resolution scans are also presented. This chapter ends on a discussion about the representativeness of dried samples in comparison with living samples (section 4.3). One can get a general overview of the workflow in Fig. 4.0.1.

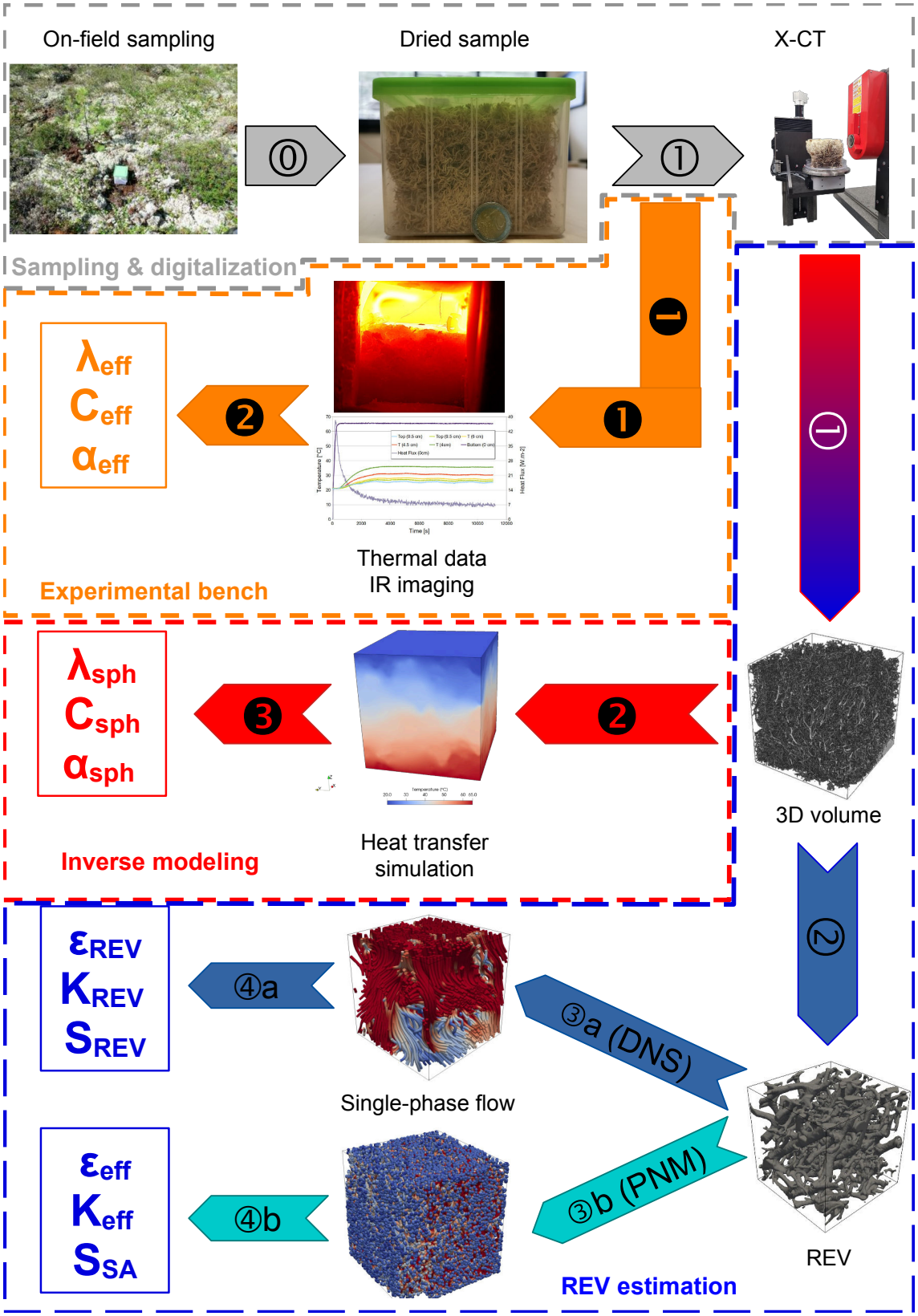

Figure 4.0.1 – General workflow from sampling to the use of reconstructed numerical model for transfer properties assessments.

These challenges and their technical answers developed for this thesis are presented for the sampling action in subsection 4.1.1, the CT scanning in subsection 4.2.2.1, and in subsection 4.2.2.2 for the preprocessing algorithms used to enhance the CT scan acquisitions before their use for properties assessments.

4.1 SAMPLING PROTOCOL

4.1.1 *Sample extraction from study site and drying*

Sampling of such biologically active layer and hence fragile interface needs to be conducted with great care. Some authors studying the arctic vegetation cover have addressed this question by sampling a so-called "monolith" of vegetation cover (O'Donnell et al., 2009). This "monolith" consists of a one meter by two meters peeling of the topmost layer of the arctic vegetation cover. Such method can be considered to be reproducible by itself due to the size of the sample, assuming that the "monolith's" center is undisturbed. As the sample is thus large and heavy, this method is suitable when sampling locations and laboratories are not so far from each other or that there is an easy transportation method. In the case of this study, one of the issue in sampling the vegetation cover was the balance between samples' size and number. Practical issues limits the number and size of the samples that can be transported on such long distances - more than 6000 km from Khanymey to Toulouse. The choice was set to have relatively small cubic samples (around 10 cm edge size) of various species with the least physical perturbation (*i.e.*, cracks, burns, dead tree leaves) over them. The samples are transported in plastic boxes of almost cubic shape, which are both rigid enough for ensuring protection of the sample during transportation and transparent to X-rays so that samples can stay in the box during tomography.
The size of each sampling cube has its importance in the representativeness of the samples in later chapters of this thesis (Chapter 5 of Part iii). A global cubic shape was adopted to ease the post-processing of the X-ray tomography reconstructions. The average size of a *Sphagnum* sprig is about one centimeter in diameter. Bearing in mind that this assembly is mostly contiguous, and that it constitutes an ordered tube assembly, it is possible to consider that a 10 cm square sample contains about a hundred individual strands.
The sampling must be conducted thoroughly to add the least porous structure perturbation possible. The field sampling is explained in detail in Fig. 4.1.1. An overview of the steps is shown in Fig. 4.1.2.

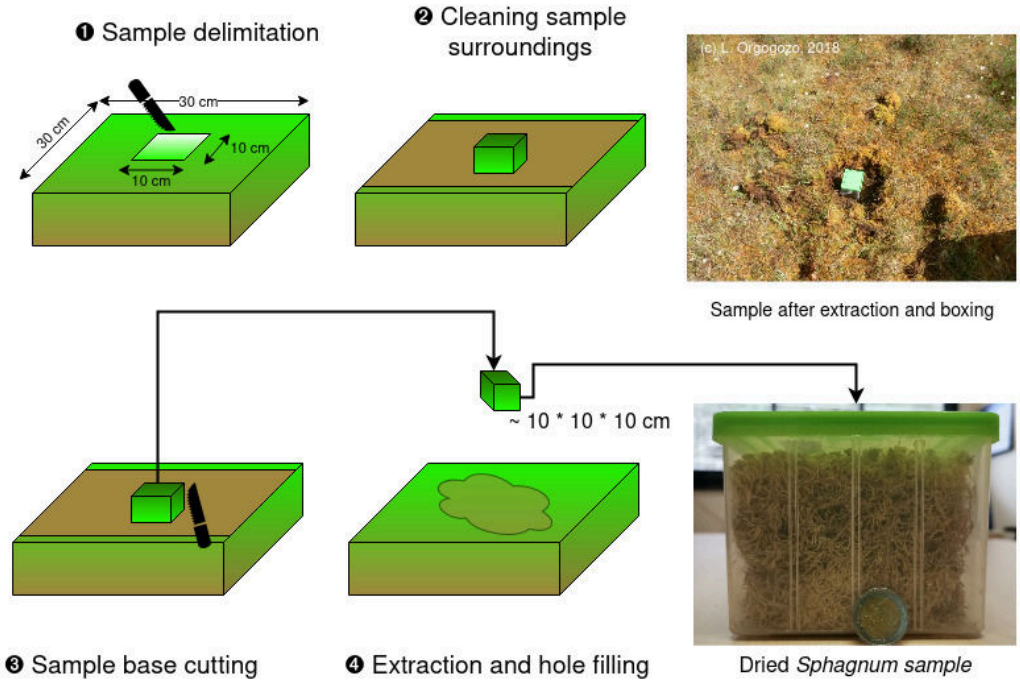

Figure 4.1.1 – Methodological overview of the in-field sampling protocol.

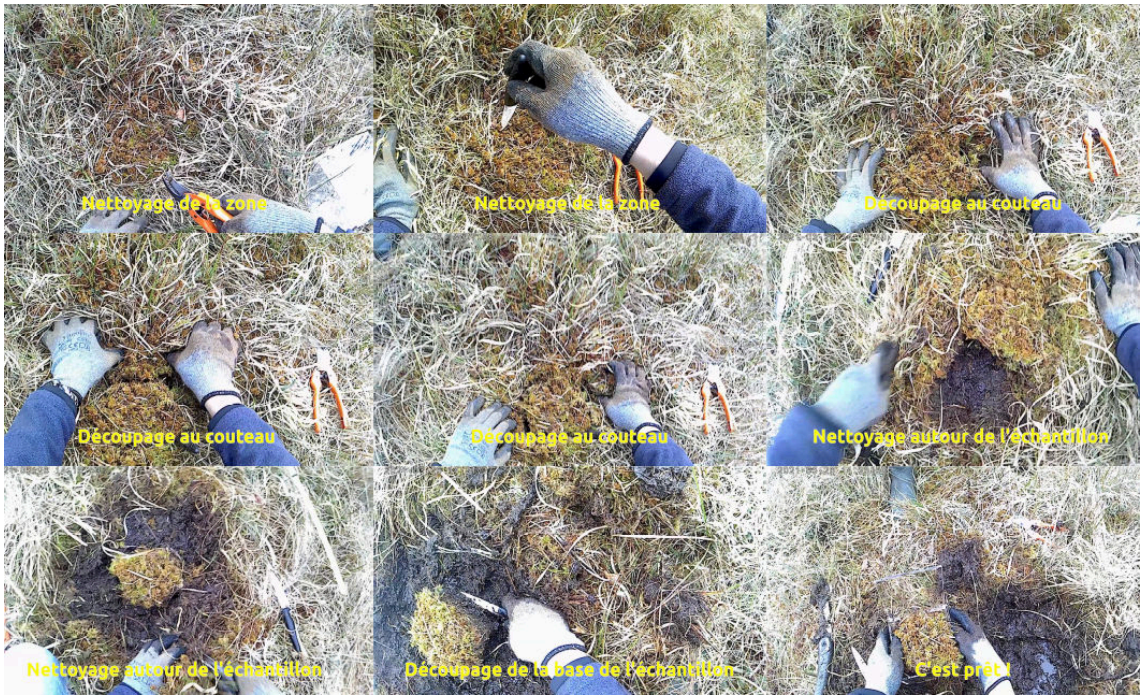

Figure 4.1.2 – Image sequence of the sampling at Clarens mire during the campaign. Translation of the the captions in French:
Nettoyage de la zone: Cleaning of the surrounding area;
Découpage au couteau: Cutting of the sample with a knife;
Nettoyage autour de l'échantillon: Cleaning of the sample's surroundings;
Découpage de la base de l'échantillon: Cutting of sample's base;
C'est prêt: It's ready.

After having selected the best location for the sample extraction (*i.e.*, having the least pre-sampling perturbation zone), the sampling protocol is described as such:

- One can start by making a 30 cm clearance zone around the desired 10 cm samples. The sample is uncoupled with the rest of the vegetation cover using a sharp knife and hand saw.
- The excess clearance zone material situated around the sample are removed by hand or using a small shovel. At this stage, the sample is only linked to the rest of the vegetation cover by its bottom side.
- When the sample's surroundings are clear and a depth of 10 cm from the sample's top is reached, one can cut the base of the sample with a sharp knife or a hand saw.
- The sample can be then put inside the transportation box, taking extra precautions during the introduction in the box (no pushing, no slamming). The transportation is done horizontally, ideally removing most of the free water before transportation to Toulouse.

For remote sampling campaigns (Khanymey and Abisko), the sample boxes are sealed using duct tape. After the samples reached their final destination, the boxes are again opened to ensure no mold growth occurs. Finally, after their arrival in Toulouse, some samples (Khanymey and two samples of the Clarens collection), the samples are put for 48 hours at 40 °C to dry out in an oven for long-term conservation of the samples. The effects of this drying process is discussed in section 4.3.

4.1.2 *Sample conservation and growth*

Whereas dried samples from Khanymey have to be kept them away from light and humidity, living samples from Clarens and Abisko require constant saturated humidity and diurnal lighting to survive. To do so, living samples are kept in transparent polymethyl methacrylate (Plexiglas®) boxes. The boxes have an inner size of 11.7 x 11.7 x 11.9 cm, and an inner volume of 1.628 L. During their growing phase, the boxes are kept on a north-faced windowsill from spring to autumn. In winter, the boxes are light up using a regular desktop lamp. The water level inside the boxes is kept constant from the original equilibrium after sampling. The boxes are filled with distilled water. For some samples (particularly those from which individual strands have been removed), accelerated regrowth is applied in the form of constant lighting of the plants. A small batch of *Sphagnum* sprigs has been put apart during the sampling process and kept apart in a small test tube for some growing experiments.

4.2 X-RAY TOMOGRAPHY OF THE SAMPLES

In the early stage of the thesis, dried samples are scanned only considering two phases: the vegetation structure (lichen, *Sphagnum*, or peat) and air contained in the porous structure. The method for CT scan acquisitions and image processing are respectively presented in subsection 4.2.2.1 and subsection 4.2.2.2. Some closeup scanning are also done as attempts to get a better perspective over the porous medium, available in subsection 4.2.2.3. For other sample plots such as Clarens and Abisko, some acquisitions with a partially saturated or fully-saturated porous media has been done, either with water (subsection 4.2.3) or with ice (subsection 4.2.4). The method for the digitalization remains the same than for the dry samples, thus the method is only presented in detail for dried samples.

4.2.1 *X-ray tomography principle and literature review*

After the accidental discovery of X-ray radiation by Wilhelm Röntgen in 1895, X-ray applications are omnipresent in many scientific domains. Notably, various medical applications (radiography, panoramic dental scan, cone beam scanners) have been developed since

the second half of the 20th century. All these medical equipment rely on the properties that shares X-ray radiation:

- X-ray radiation can penetrate the matter depending on its density (the more dense is the matter, more is the X-ray absorption);
- X-ray radiation allows characterizing different structures due to density differences (bones, soft tissues, blood vessels in the case of medical applications);
- X-ray radiation enables non-invasive observations of inner structure.

However, X-ray radiation is not harmless for plants or animals due to this matter-penetration and ionizing properties. This means that such radiation affects DNA and can cause hazard is one if unnecessary exposed to X-ray radiation therefore needing proper shielding for the user. If the device is isolated and the ionizing radiation is shielded, X-ray Computed Tomography (X-CT) is peculiarly interesting for other scientific fields apart from for medical applications, and especially for material sciences. CT scanner has its origin with the first scanner developed in the 1970s by Godfrey Hounsfield and Allan MacLeod Cormack. X-CT relies on a combination of a X-ray source (generally a cathodic tube) and a sensor. Both source and sensor can be installed in a rotating gantry (medical CT) or fixed source and sensor with a rotating platform (industrial CT).
In the field of Earth and environmental sciences, X-ray computed tomography has been largely used since its widespread applications in medical sciences (Cnudde and Boone, 2013). There are many examples of CT scanner use to describe porous space inside rocks (Dong and Blunt (2009), Kuva et al. (2018), Taud et al. (2005), Yun et al. (2013), and Noiriel and Soulaine (2021), among others). More precisely, CT scanner has also been used for peat properties characterization from field samples. One can refer to Fereidoun Rezanezhad et al. (2016) and Turberg et al. (2014) as introductory papers. Cnudde and Boone (2013) gives an exhaustive historical overview of CT scan developments for Earth sciences and the most notable discoveries that has been made using this technology. There are also some recent works published by Roustaei et al. (2022) that have shown the capacity of CT scanners to enable the quantification of the physical phases present in the porous structure of peat. However, there are no attempts of such work on *Sphagnum* samples known to this date. Therefore, the scanning of living *Sphagnum* samples will have the same technical base than the one used by Quinton, Elliot, et al. (2009) and Fereidoun Rezanezhad et al. (2016) on peat. The main difference is that the resolution of such scans will be coarsened from 45 µm.voxel^{-1} to 94 µm.voxel^{-1}[1] in order to have a numerical reconstruction of the complete sample.
In this thesis, the samples are scanned using an EasyTom™ XL150 (RX Solutions, Chavanod, France) industrial microtomography scanner installed at the Toulouse Fluid Mechanics Institute (IMFT). Fig. 4.2.1 gives an illustration of the industrial X-ray CT scanner principle as well as a general overview of the tomograph installed at the IMFT.

1 A *voxel* is an elementary volume of a 3D volume, equivalent of a *pixel* for a 2D image.

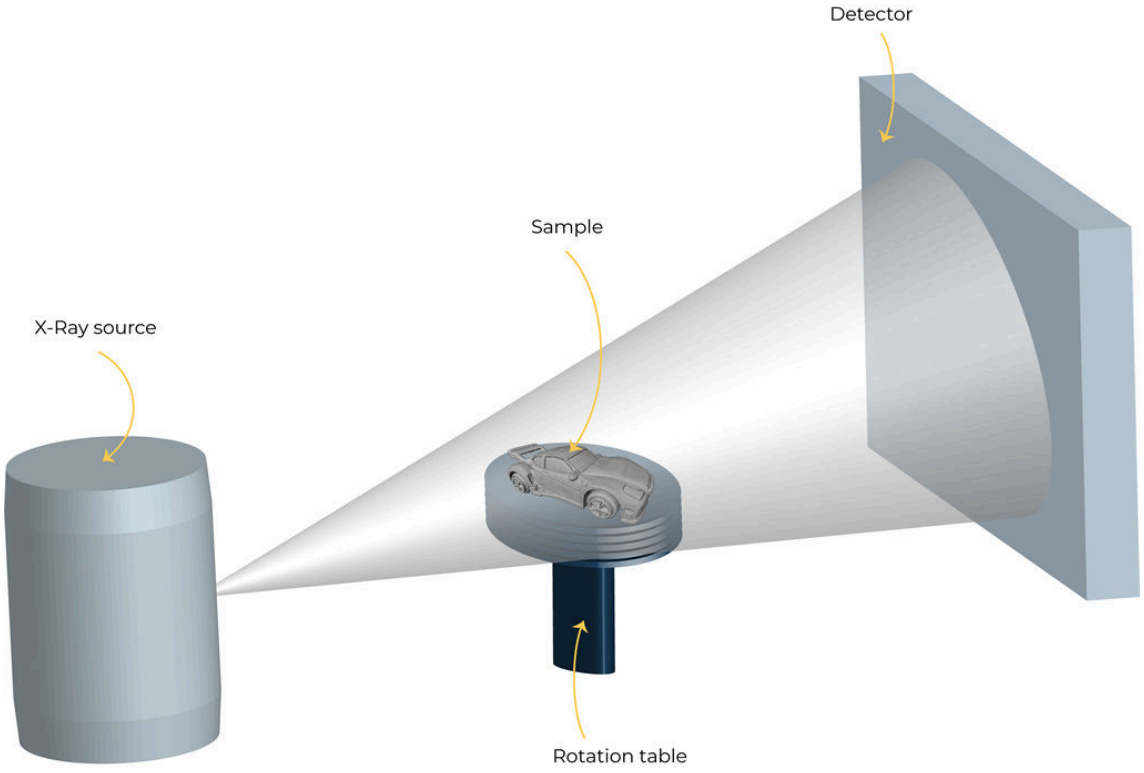

(a) X-ray tomography principle (image from the article *"How to use an industrial X-ray CT system"* by RX Solutions (*all rights reserved, available from this link*).

(b) Actual X-ray tomography device installed at the Toulouse Fluid Mechanics Institute.

Figure 4.2.1 – Industrial tomography principle and device installed at the Toulouse Fluid Mechanics Institute.

Scanning dried samples in a first place facilitates the tridimensional reconstruction of the sample as there are no other interfering phases in the porous medium. These first acquisitions are described in the next section.

4.2.2 *Monophase sample digitalization*

After having collected the samples in the field and put them in boxes, the samples are brought to the X-ray CT scanner installed at the Toulouse Fluid Mechanics Institute. Each sample collection scanning undergoes a series of steps. First, the sample must be scanned at the desired resolution. Then, numerical routines reconstruct the sample from the rotational acquisitions obtained for the given sample. Finally, some pre-processing is done after the scanning session to enhance the quality of the tomographic reconstruction.

4.2.2.1 *X-ray computerized scan*

The first sample lot is scanned in October 2018 by Laurent Orgogozo, Yohan Davit and Paul Duru approximately two months after the Khanymey sample collection campaign and their drying. The CT scanner's configuration allows stacking two or three samples on top of each other in order to save some acquisition time. The X-ray power source was set on average at 100 kV and 400 µA making a power of 25 W for the acquisition. Some precise data about the X-ray acquisitions are shown in Appendix 4.A to Appendix 4.C for each sample collection. A complete numerical reconstruction at a micrometer resolution requires to make about 1440 rotational shots with additional 6 reference images for samples of this size. A picture of Lichen2.1 sample from Khanymey sample collection set up on tomograph's rotating plate is shown in Fig. 4.2.2.

Figure 4.2.2 – Lichen2.1 sample from the Khanymey sample collection being set up for tomography on the CT scan of the Toulouse Institute of Fluid Mechanics. © Yohan Davit, 2018. The sample has been taken outside of its box, which has not been the case for the other acquisitions.

After the 1446 sequential rotational acquisitions are made, a computerized routine of the proprietary tomographic reconstruction tool *X-act*® is used in order to recreate a tridimensional volume of the sample. The reconstructed volume resolution for all the scanned samples are within the range of 17 to 94 µm.voxel^{-1}, with more details available in Appendix 4.A to Appendix 4.B for each sample collection.
At the end of the scanning process, one gets a set of rotational images of the sample (which are not directly usable in this case) and a tomographic reconstruction of the sample, with a stack of images representing each z-axis slice. Each digitized sample represents between 8 and 15 GB of uncompressed data. The pre-processing steps are designed to highlight the porous structure of the sample and reduce the volume of data to be processed.

4.2.2.2 *Image processing*

While scanning process gives an 16-bit image of the tomographic reconstruction of the studied sample, image processing can reveal features that can be hard to describe, while reducing the amount of data to be treated. In this section, a presentation of the image processing steps that were undertaken to get a workable volume of the sample are described. This process is mainly focused on the vegetation matter segmentation. For the segmentation of liquid water and ice, one can respectively consult section 4.2.3.2 and section 4.2.4.3.

After the samples have been scanned, whether in dry conditions, with liquid water (section 4.2.3), or with ice (section 4.2.4), one can obtain a series of evenly-spaced .tif image files. IMFT's X-ray tomograph generates tif files with a 16-bit numerical gray-value scale, meaning that each pixel on each slice has a value between 0 and 2^{16} thus making 65536 possible values. The lower values indicate least dense material (in this case air) and higher values denser material (vegetation tissues, water, ice, container...). As X-ray absorption significantly depends on the density of the studied material, the pixel's value will also be different in this case. One can then study the peaks in the image's histogram and find some peculiar feature peaks depending on the proportional number of considered objects. This process is called image segmentation and is common practice in the field of image processing. An illustrative example of such image processing method is shown in Fig. 4.2.3.

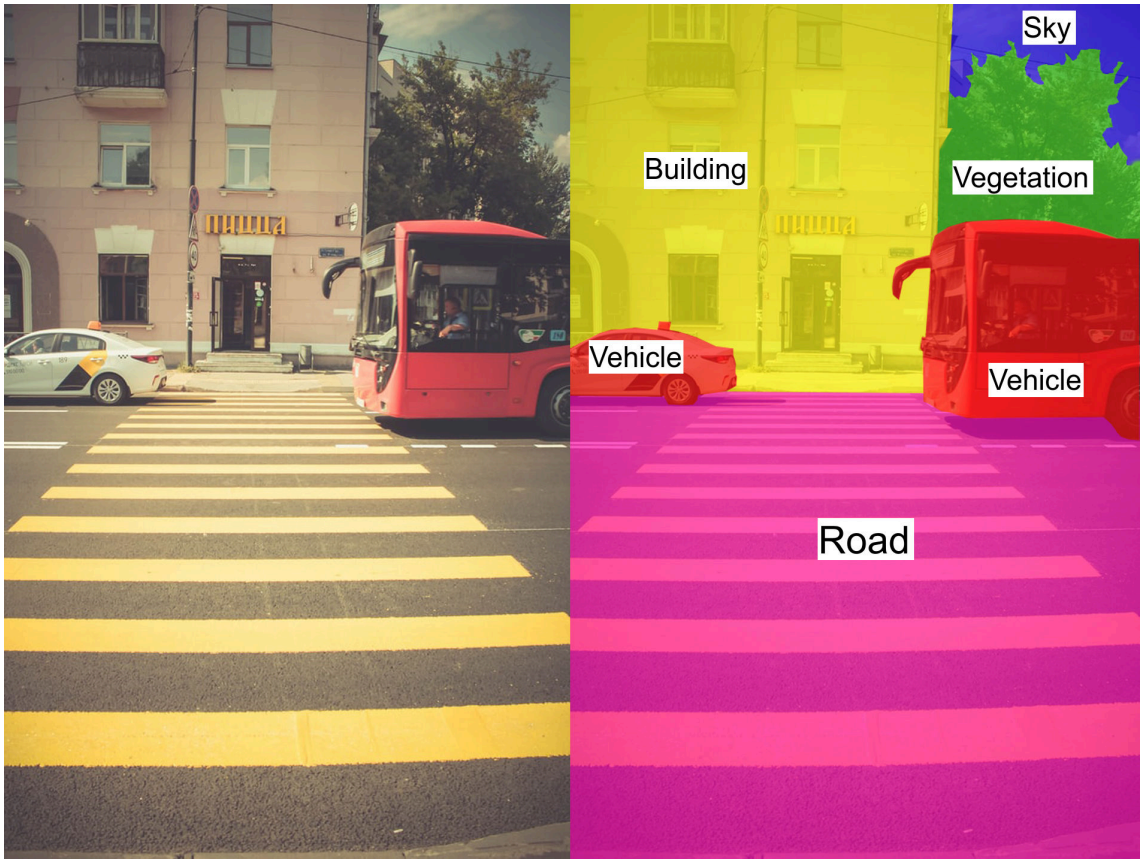

Figure 4.2.3 – Example of image segmentation and labeling on a picture. *CC BY-SA 4.0 B.Palac, modified*.

In the case of the vegetation cover, one issue is that the cellular structures are relatively thin if compared to other biological tissues (wood, leaves, organs). This means that the intensity of the signal is low, therefore it is sensitive to perturbation and beam hardening[2] (Brooks and Chiro, 1976). Beam hardening depends mostly on the used X-ray source and acquisition device, meaning that beam hardening artifacts are mostly removed by the acquisition device numerical routines during tomography.
After the reconstruction is computed and beam hardening artifacts are removed, one can proceed to prepare the data for further steps. First, after the tomographic reconstruction images are loaded in *ImageJ-Fiji* software (Schindelin et al., 2012), black and white balance is set to have the most contrasted image. Then, unnecessary elements such as fixations, covers, lids, and sampling boxes are removed from the tomographic image by a cropping process. Finally, the image stack is binarized to obtain an image mask of the solid phase (in white) and the void space (in black). An example of image processing treatment applied on a *Sphagnum* sample from the Clarens sample lot is shown in Fig. 4.2.4.

2 Beam hardening is an artifact occurring in CT scans due to polychromatic X-ray beams.

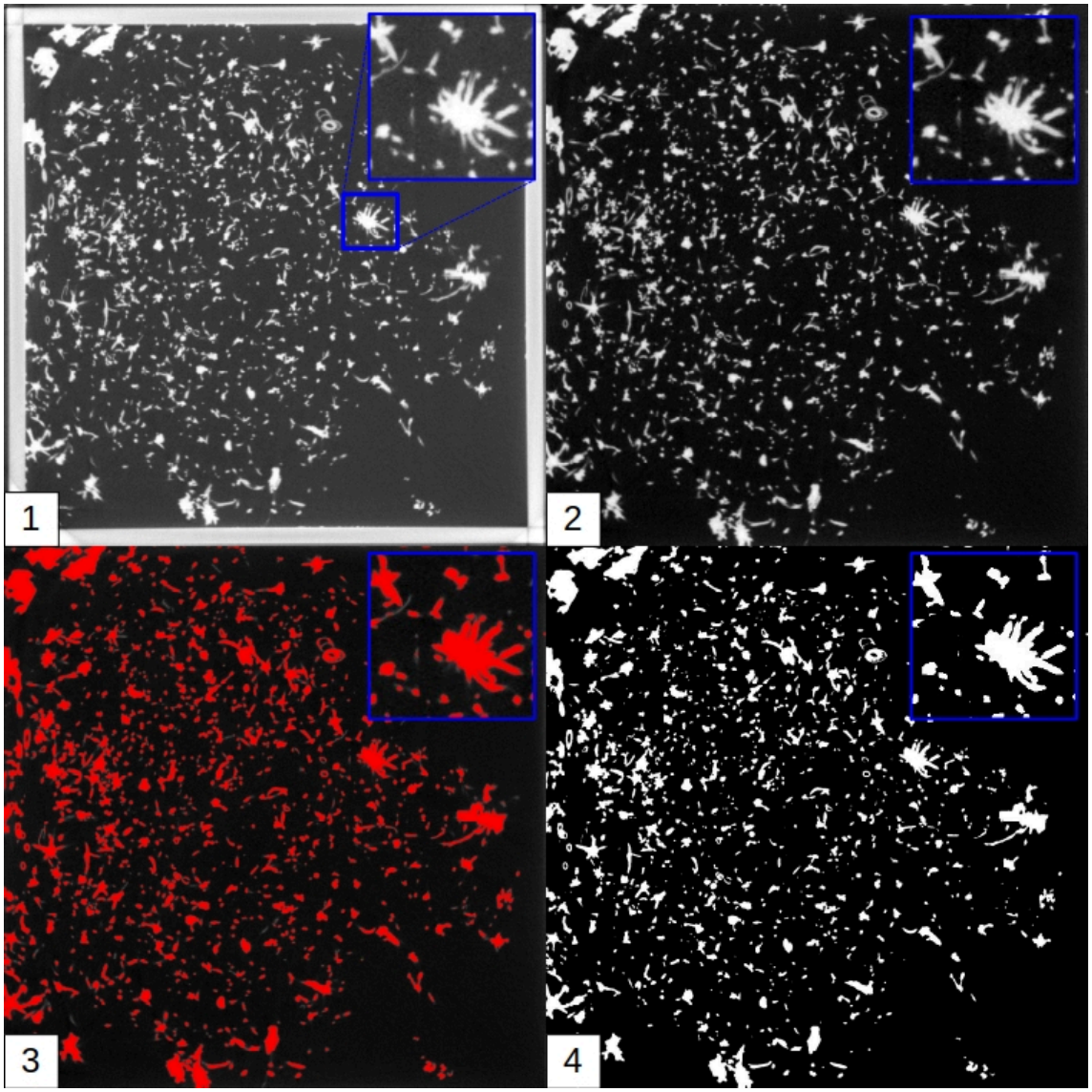

Figure 4.2.4 – Image processing workflow example applied on CL3 sample.
1: Raw tomographic reconstruction obtained after CT scan;
2: Cropping (removal of the sampling box) and white balance adjusting;
3: Ostu binarization (Otsu, 1979). The red contour represents the assigned data for the given threshold. The darker segments not included in the Otsu binarization corresponds to the reflection on the previous and next slice.

Image n°1 in Fig. 4.2.4 shows that the box is at least as X-ray absorbent than the vegetation. In image n°2, the container is cropped out of the field of view and the contrast is adjusted to enhance the black and white balance. Finally, in images n°3 and n°4, Otsu binarization (Otsu, 1979) is applied on the image which causes the segmentation of the image into two classes: air and void space. The final treated image stack can be considered as a matrix of 1 (white values representing vegetation matter) and 0 (black values representing void space).

In this case, the Otsu method for binarizing the image is well suited to segment the image because both phases are well separated in the voxel's intensity histogram, thus the intraclass variance is lower. However, the Otsu method does not suit well with multi-phase data where there can be more than two different elements described solely on their intensity. For such application, one can refer to the multi-phase Otsu binarization or *K-means* method.

4.2.2.3 *High-resolution CT-Scan*

The resolution of X-ray tomography can be increased by varying the imaging parameters. Increasing resolution enables a more precise description of porous structures, albeit the field of view reduction, hence limiting the studied volume. In this section, a high-resolution tomography test is shown and discussed. A similar demonstration is also given for a sample with water content (section 4.2.3.3).
High-resolution tomography requires greater attention to reduce vibrations in the experimental setup, as well as in the digital processing of the tomography. Indeed, the interaction of X-rays with materials of many different densities can cause diffraction and scattering phenomena, resulting in a "noisy" image. This issue is common in many CT scan applications and various mathematical filters have been developed for denoising CT scans. Al-Ameen et al. (2015) sums up some of the classical methods for denoising a CT scan that are currently used for medical applications where CT scan noise is very present due to patient's movement and the limited number of CT scan per patient without endangering their lives. One particular filtering method that is applied for the studied samples is the *Non Local Means* filtering (NLM). This filtering algorithm is first described by A. Buades et al. (2005) as a new method for denoising image, specifically devoted to filter low-dose CT scan tomographic acquisitions. In the review made by Zheng et al. (2013), *Non Local Means* filtering algorithms have been successfully used to filter CT scan data and has been used nearly as a routine filtering among other traditional filtering methods (Histogram equalization, Gamma-correction for the most used filters).
Image denoising is done after the common preprocessing routine shown in last subsection. Image denoising is applied using an *ImageJ* implementation of the *Non Local Means* filter available in the *BioMedGroup* repository proposed by Antoni Buades et al. (2011) and Darbon et al. (2008).

A high-resolution tomography of Mound2.6 sample treated with *Non Local Means* filter is available in Fig. 4.2.5. One can distinguish *Sphagnum* sprigs visible in white in the tomography.

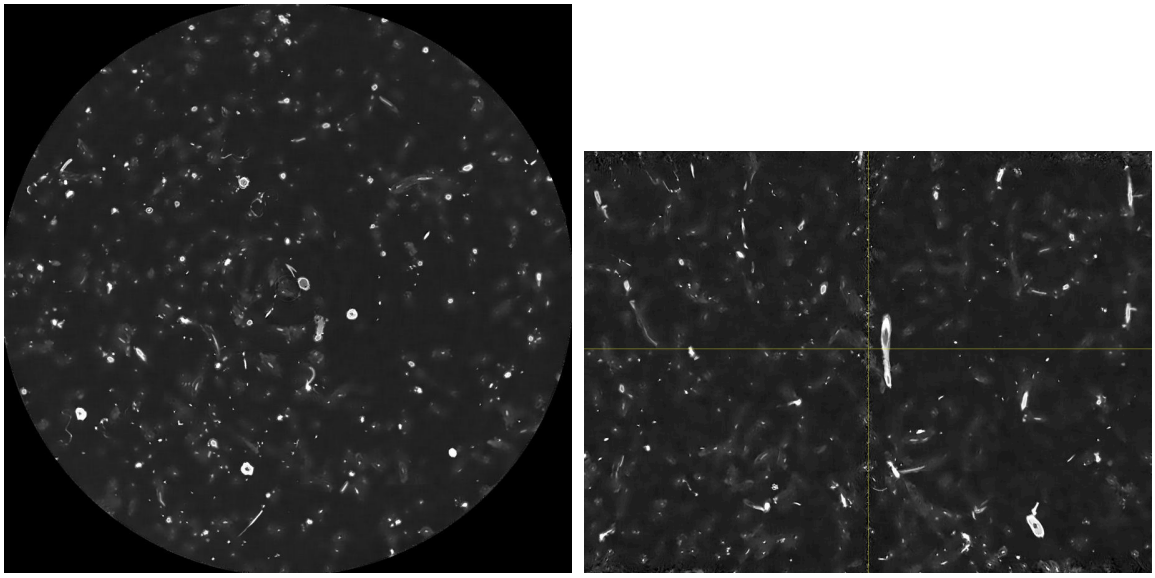

(a) Tomographic slice on *xy*-plane. **(b)** Tomographic slice on *xz*-plane.

Figure 4.2.5 – CT scan result of a high-resolution tomography of dried Mound2.6 sample from the Khanymey sample collection.

The process of tomography itself is fast, reproducible and non-invasive. Tomography can be considered as taking a 3D snapshot of the sample's structure. However, the ease of doing a tomography has to be put into perspective with the difficulty to compare two CT scans of a same sample. Indeed, the fragile nature of these samples makes the structure sensible to crushing and moving. This has to be taken into account and is discussed in later parts of this thesis (parts iii and iv). In the following section, an analogous work is done with samples that have either been kept alive from the sampling (Clarens and Abisko samples) or samples that have been re-hydrated with water after complete drying (samples Mound2.6 and Lichen1.3). Some tomographies for Khanymey, Abisko and Clarens are shown in the following section.

4.2.3 *Multiphase sample digitalization (liquid water)*

Water in its three physical states is present in arctic landscapes and particularly in peatlands. The samples that have been scanned and mainly used in this thesis are samples that were dried before scanning to reduce the number of phase to be assessed in the process and thus focusing on the porous structure itself. However, *Sphagnum* moss is widely present in highly saturated peatlands, meaning that water occupies the pore space, at least partially, if water saturation is not reached. One major issue is that water absorbs more X-ray than vegetal matter due to density differences. The absorption length of water is logarithmic from 100 eV to 100 keV with a step at 540 eV which is related to the X-ray absorption effect of oxygen. This phenomenon has a significant importance for X-ray tomography, as the X-ray beam will be heavily attenuated by water absorption. The same

effects are visible with ice, and discussed in section 4.2.4 although absorption wavelength is lesser than for water. This means that water films around *Sphagnum* branches can create an "absorption halo" around it, making the interpretation not straightforward.

Therefore, some CT scans are done with living samples, mainly on Abisko and Clarens samples. Some tomographic slices are shown in Fig. 4.3.1 for samples CL2 and CL4 of Clarens sample collection. Tomographic slices of Abisko samples are also available in Fig. 4.2.6 for which the watertable level is kept constant from the sampling campaign.

4.2.3.1 *X-ray computerized scan*

The same method of scanning is applied than for dried samples (section 4.2.2.1). The only difference is that the reference images for quality enhancement are deactivated. Indeed, such parameter creates fast rotational movements for the sample which disturbs the water distribution in the porous space, hence blurring the reconstruction. A CT scan result of living samples scanned under X-rays is available in Fig. 4.2.6a for Abisko2 sample and in Fig. 4.2.6b for Abisko4 sample.

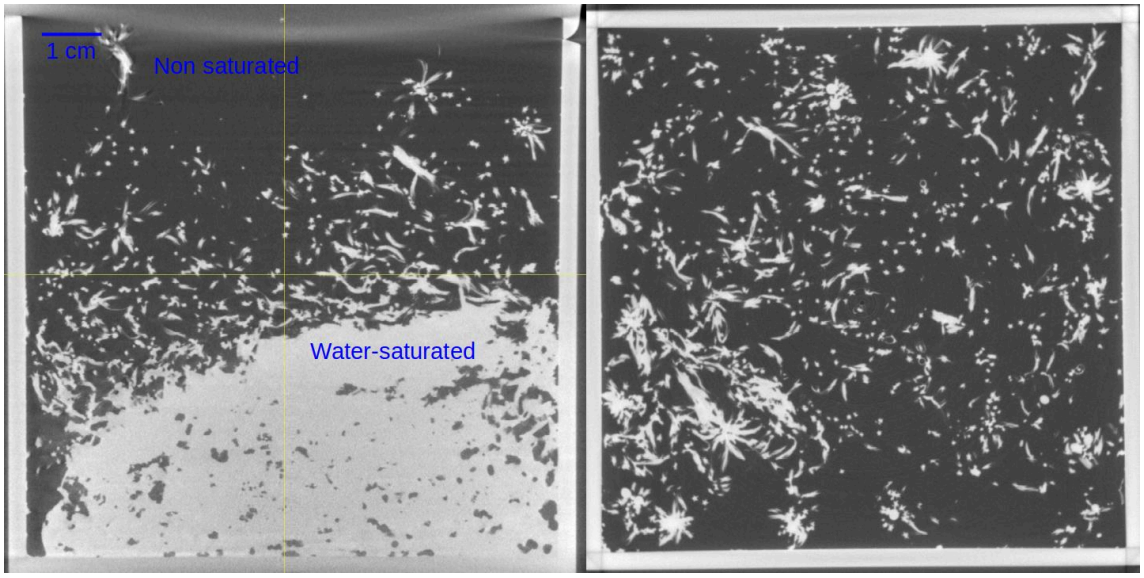

(a) (*left*) Abisko2 sample *z*-axis orthographic view and (*right*) tomographic slice.

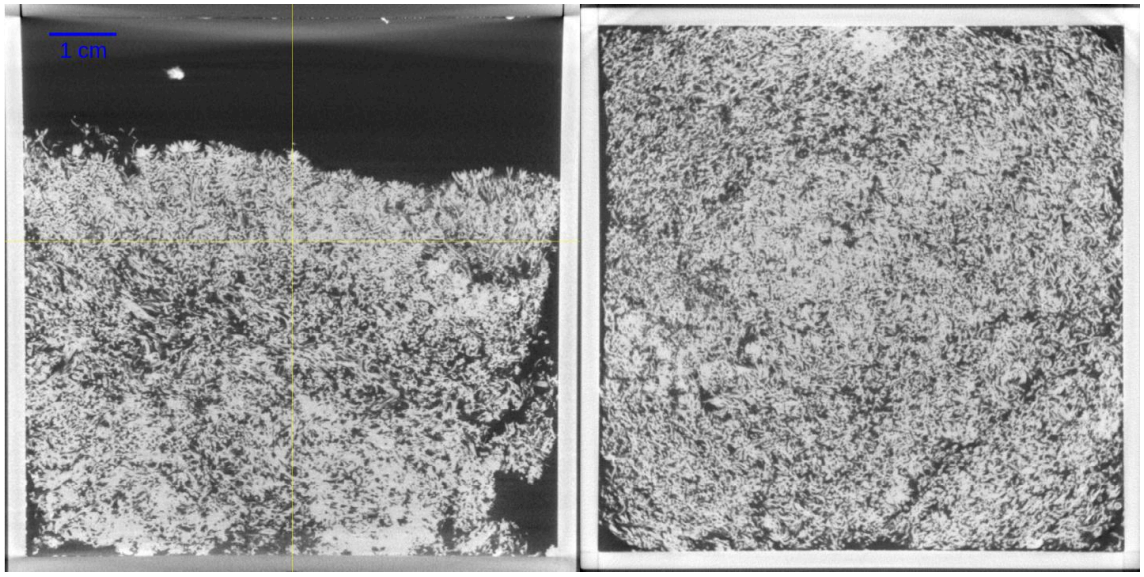

(b) (*left*) Abisko4 sample *z*-axis orthographic view and (*right*) tomographic slice.

Figure 4.2.6 – Tomographic reconstructions of Abisko2 and Abisko4 samples. The yellow lines indicate the position of the slices in the tomographic reconstruction.

In Fig. 4.2.6, Abisko2 sample is kept water-saturated at a constant level since its arrival in Toulouse whereas Abisko4 is kept unsaturated. A comparison of the two tomographic images shows that saturation of the Abisko2 sample is clearly visible thanks to the absorption front. The formation of water-unsaturated pores within the sample can also be noted in both Abisko2 and Abisko4 samples, characterizing a heterogeneous saturation front common in porous media. At this stage, however, it is not possible to differentiate the tomographic signature of pure water from that of hydrated *Sphagnum*. Then, a sample rehydration for one *Sphagnum* sample is done with a similar capillary water height than

for Abisko2 sample for some comparative tests with living samples. The resulting CT scans are shown in Fig. 4.2.7.

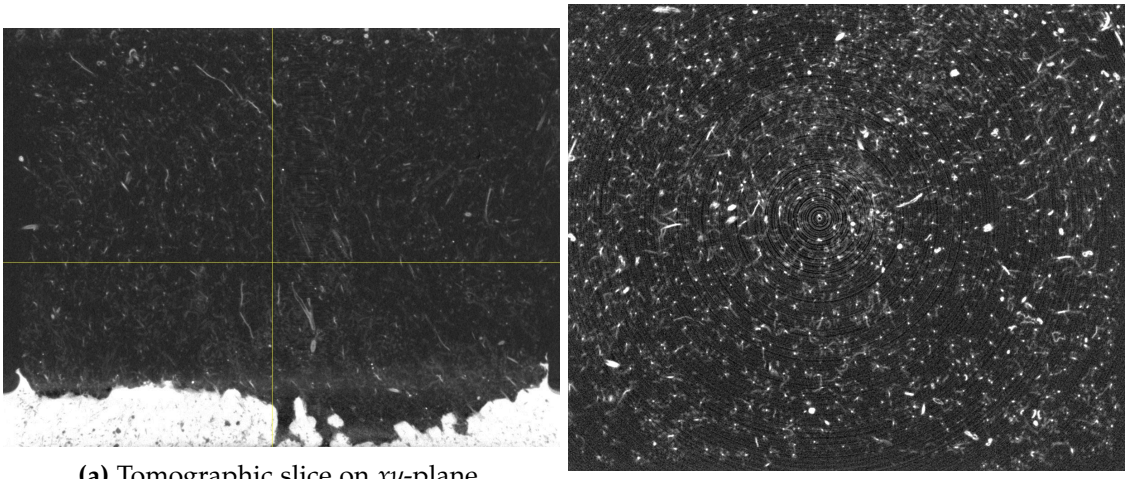

(a) Tomographic slice on *xy*-plane.

(b) Tomographic slice on *xz*-plane.

Figure 4.2.7 – CT scan result of a high-resolution tomography of hydrated Mound2.6.

From the images shown in Fig. 4.2.7, one can see that the tomographic signature of rehydrated *Sphagnum* is weaker than for living samples previously shown. This difference is due to the death status of the moss sample, so that the hyaline cells cannot be filled anymore due to a lack of biological activity. Thus, only other vegetation material present in the sample are rehydrated and strongly colored in white. The saturation water front is still visible however it is difficult to segment from the rest of the sample.

4.2.3.2 *Image processing*

The presence of an X-ray-absorbing phase (water) makes image processing more difficult. The problem lies in the fact that *Sphagnum* has a high water content, making their tomographic signature almost identical to that of water. Image subtraction analysis between a dry and a hydrated state provides no information, as the structure of the porous medium is deformed by water saturation. Nevertheless, it is possible to observe the height of the capillary front across the sample.

4.2.3.3 *High-resolution CT-scan*

After having done a general scan of three hydrated samples in the previous section, a high-resolution CT scan is done at a resolution of 17.19 µm.voxel^{-1} and shown in Fig. 4.2.8.

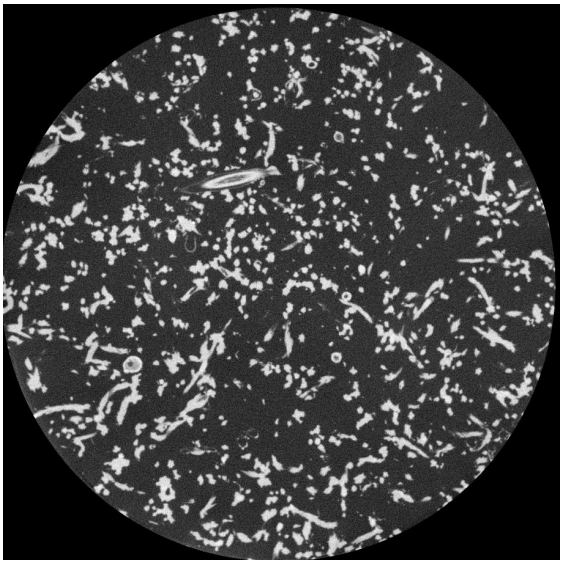

(a) Tomographic slice on *xz*-plane.

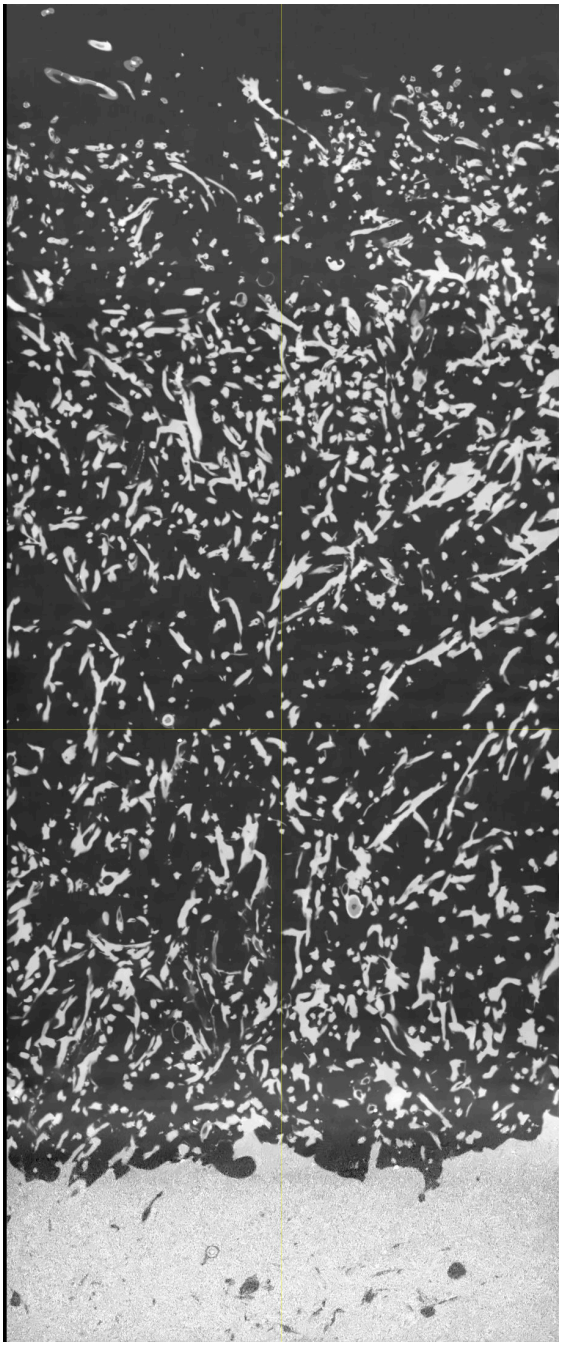

(b) Tomographic slice on *zy*-plane.

Figure 4.2.8 – CT scan result of a high-resolution tomography of hydrated Mound2.6 sample from the Khanymey sample collection.

One can note that increasing the resolution does not significantly enhance the structural information quality from the previous CT scans. However, the unsaturated air-filled pores are more visible in the lower part of the sample, where water is present. The increase in resolution does not give more information on the water film on the rehydrated moss samples but can thus bring more information about the air-pores formed in the saturation front of the porous media.

4.2.4 *Multiphase sample digitalization (ice)*

4.2.4.1 *Ice and water: can they be distinguished?*

Even though ice and water are made of the same atoms, their density difference makes them theoretically distinguishable from each other. To verify such assumption before scanning samples containing ice, a becher is filled with ice and water and the becher is scanned through X-ray tomography in the same conditions than the ones occurring for the samples. The result of the CT scan is shown in Fig. 4.2.9.

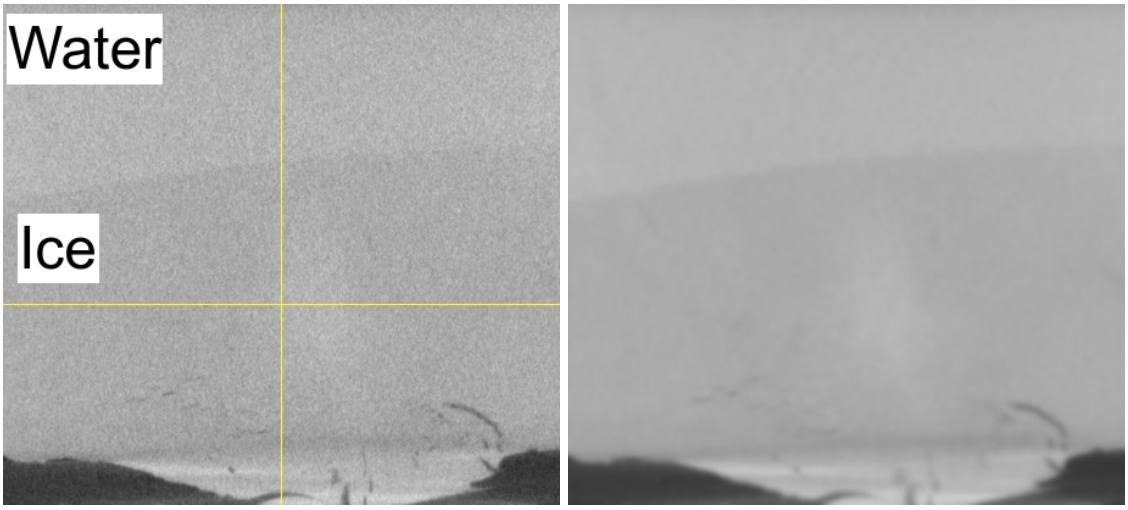

(a) Without processing. **(b)** With 3D gaussian blurring.

Figure 4.2.9 – Tomographic reconstruction of a becher filled with ice (bottom) and liquid water (top).

One can see from this scan that water and ice are distinguishable one from each other if the phases are well separated. It is possible to deduce that without any preprocessing, ice and water are distinguishable but not with enough confidence in the data, the standard deviation of both classes makes the value overlap each other. This overlapping can be reduced with a Gaussian blurring applied to the sample.

4.2.4.2 *X-ray computerized scan*

After having characterized water distribution in the pore space of the samples, some attempts to scan frozen samples is undertaken. To do so, one dried sample from Khanymey sample lot (Mound2.6), and one samples from Clarens sample lot are scanned first with their respective water content in them. The three samples are put at the same time in a regular freezer, in which they are kept during 24h to enable complete freezing of the interstitial water. The samples are then scanned again straight from the freezer. To reduce as maximum thawing effects on samples, each sample is scanned one-by-one, requiring

about 20 minutes per samples. Fig. 4.2.10 shows the evolution of the two studied samples with liquid water and then after freezing.

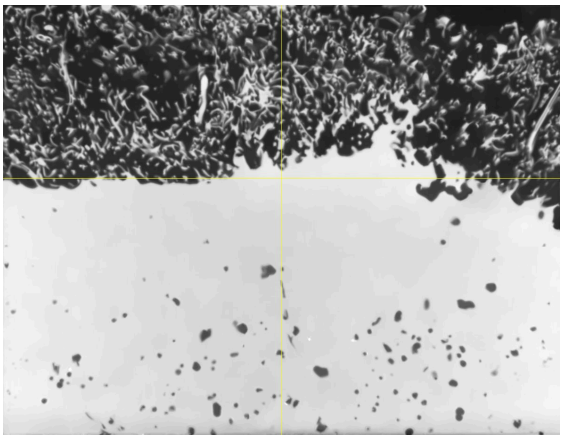

(a) Mound2.6 sample z-axis orthographic view.

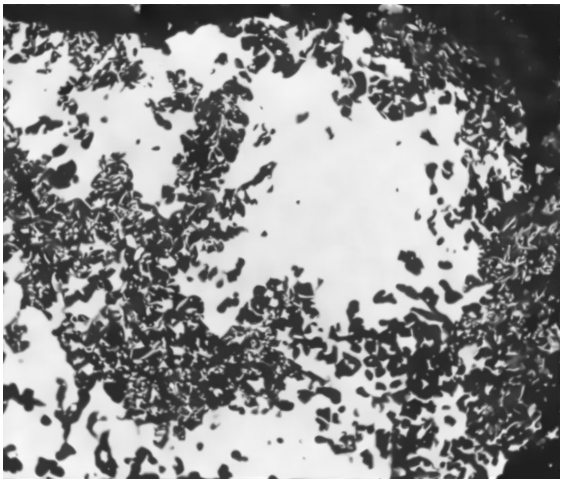

(b) Tomographic slice (xz plane).

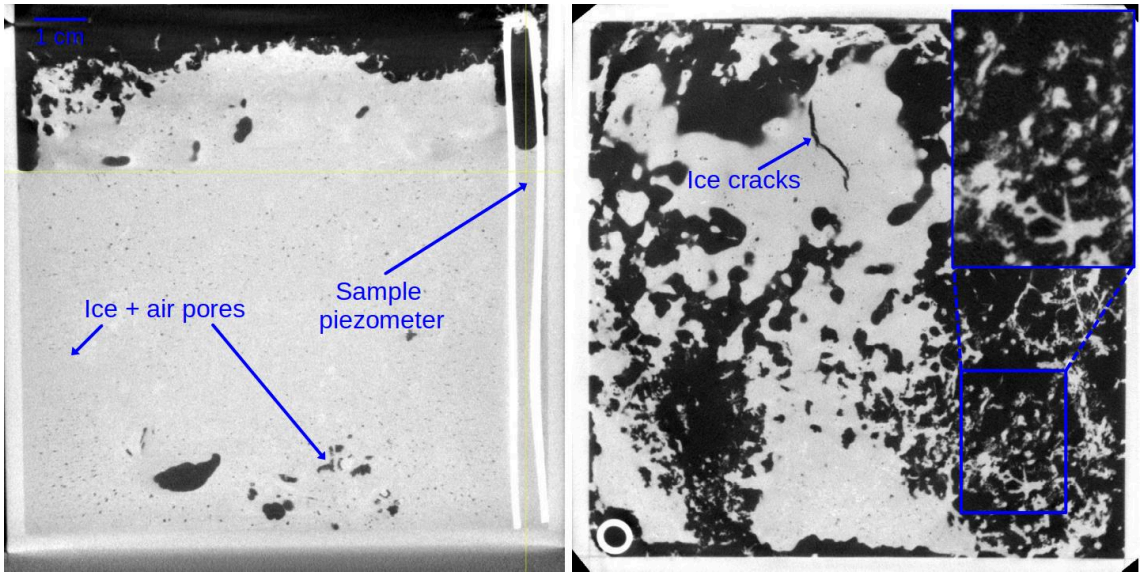

(c) Clarens2 sample z-axis orthographic view and tomographic slice (xz plane).

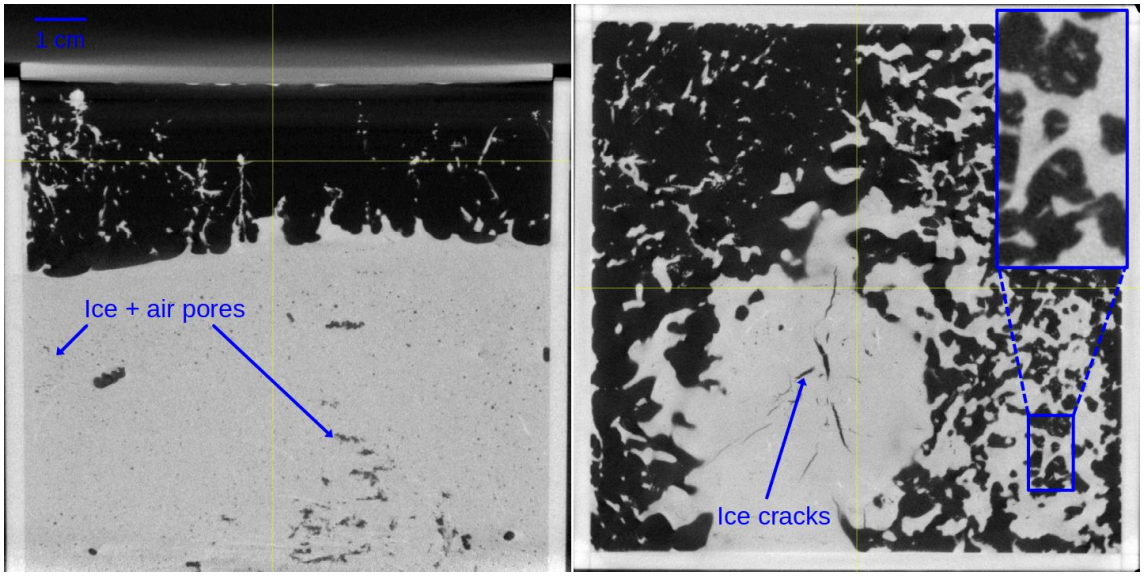

(d) Abisko2 sample z-axis orthographic view and tomographic slice (xz plane).

Figure 4.2.10 – Tomographic reconstructions of Mound2.6, Clarens2 and Abisko2 samples after their freezing. The yellow lines indicate the positions of the slices in the tomographic reconstruction.

Contrary to what has been shown in section 4.2.4, ice and water segmentation in real scanning conditions is not straightforward, especially in each of the tomography presented in Fig. 4.2.10. One can also see that ice generates a lot of artifact and numerical noise, which can be treated using denoising algorithms as shown in the following section.

4.2.4.3 *Image processing*

Image denoising of tomography is sometimes required to enhance the quality of a tomographic reconstruction. For this purpose, an example of image denoising using the *Non Local Means* filter used on a tomography of a sample containing ice is shown in Fig. 4.2.11.

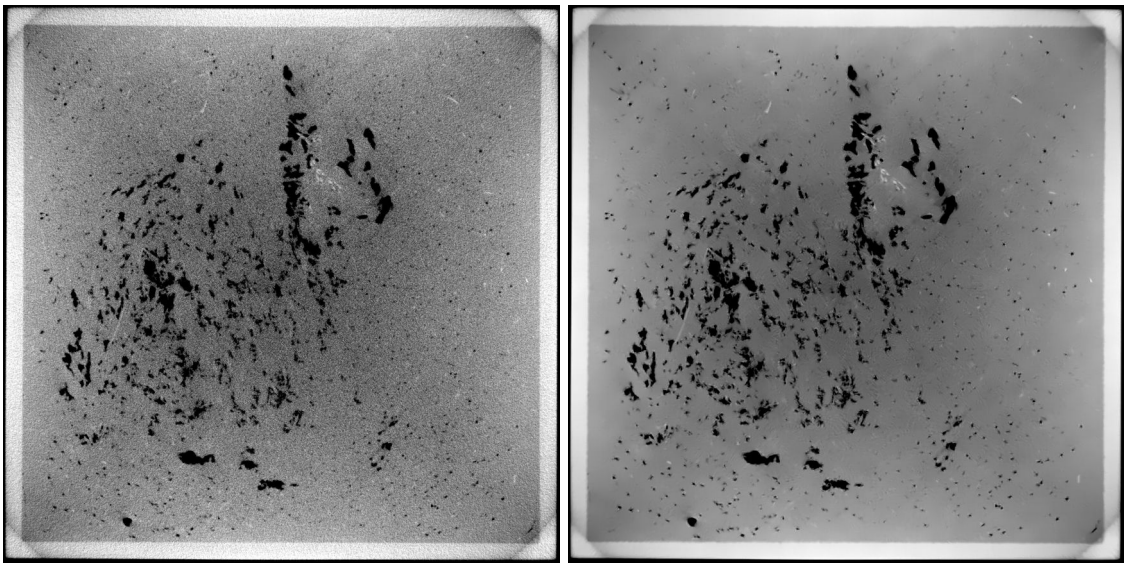

(a) Raw (unfiltered). **(b)** With *Non Local Means* filter.

Figure 4.2.11 – Comparison of the effect of Non-Local Means filter on a tomographic slice of Abisko2 sample with ice.

The filtering has a significant impact on the beam hardening effect, smoothing down the heterogeneities that are notably visible in ice. Nonetheless, there is a slight information loss for small and bright patches (called the "*gold nugget*" effect, Pitard, 1994). This information loss is not prejudicial for image processing since vegetation discrimination in ice remains difficult to this date.

4.2.4.4 *High-resolution CT-scan resolution*

In the case of the studied samples, high resolution CT-scans requires high X-ray energy input in order to get an output signal on the image. This means that the samples has to be set close to the X-ray source, therefore, the impact of x-ray absorption has been quantified. Indeed, tomograms taken in the presence of ice show images that are relatively noisy due to the relative attenuation of X-rays by water as shown by Näslund et al. (2005). Ge et al.

(2016) note in their study of the attenuation coefficient a value of 0.657 ± 0.023 cm^{-1} at 20 keV. According to the manufacturer's data, around 1% of the energy produced by the X-ray tube is emitted in the form of X-rays. Thus, according to the source consumption data, and assuming that each sample has a mass of one kg and that the acquisition time is 20 minutes, the sample absorbs 756.8 J of energy. This energy corresponds to a dose of 756.8 Gy. Knowing that the dose required to raise the temperature of one kg of pure water by 1 °C is 4.18 kGy, the hypothesis of water heating by X-rays is negligible in this case. An example of X-ray tomography reconstruction is available in Fig. 4.2.12.

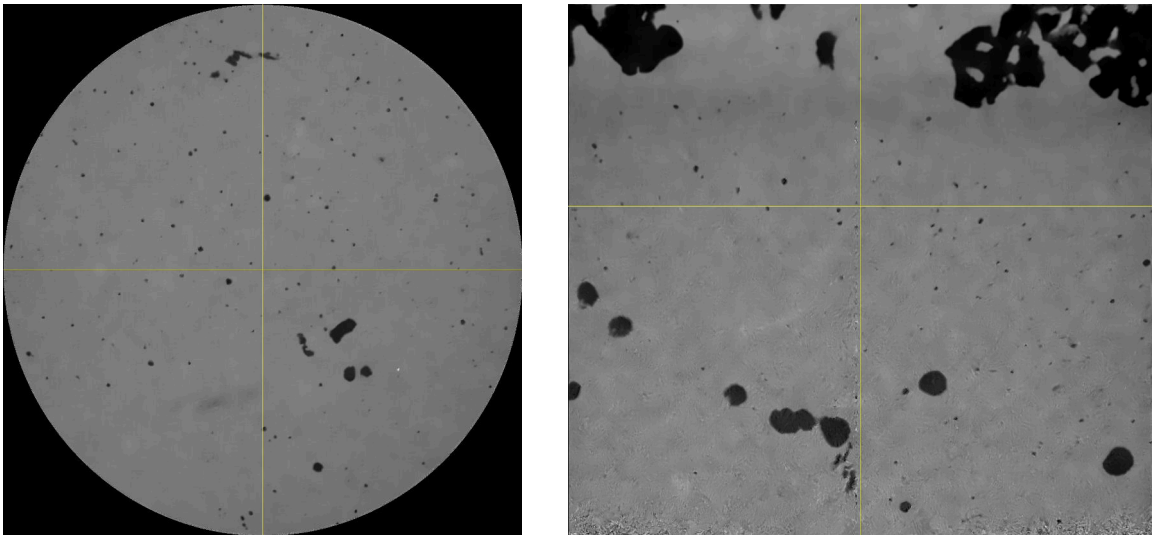

(a) Tomographic slice on *xz*-plane. **(b)** Tomographic slice on *xy*-plane.

Figure 4.2.12 – CT scan result of a high-resolution tomography of Mound2.6 sample with ice from the Khanymey sample collection.

After treatment, it is possible to see that only air-filled pores are visible in the tomograms of Fig. 4.2.12. The rest consists of *Sphagnum* sprigs and ice. Segmenting *Sphagnum* and ice is not straightforward in this case.

4.3 DRIED SAMPLES *VS.* LIVING SAMPLES: A METHODOLOGICAL DISCUSSION

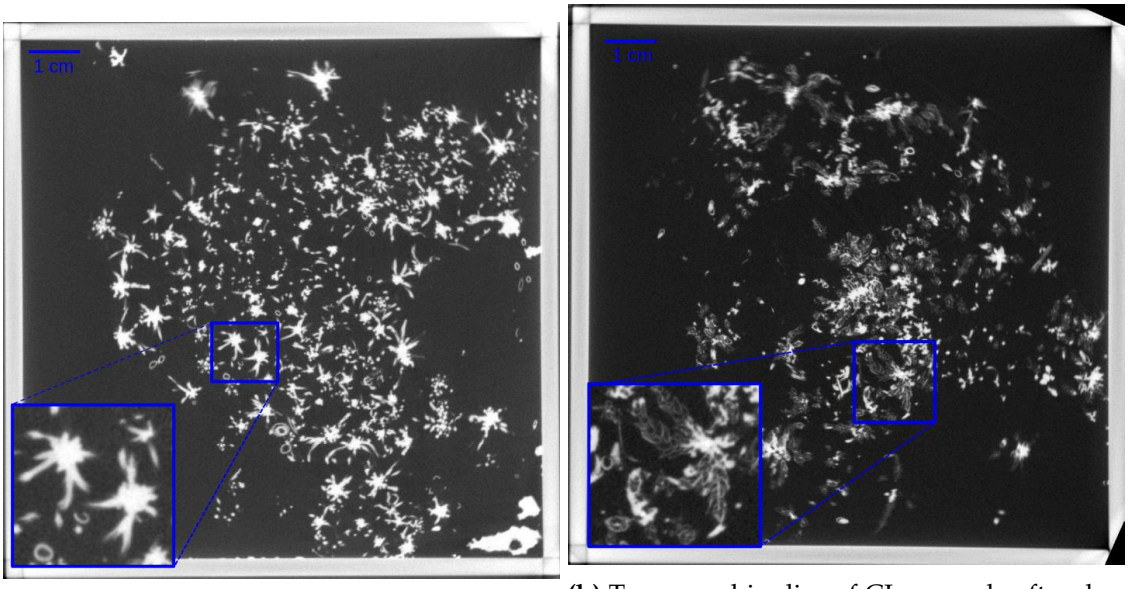

(a) Tomographic slice of CL2 sample before drying process. The white fibers represent *Sphagnum* elements filled with water.

(b) Tomographic slice of CL2 sample after drying process. Note the empty hyaline cell structure visible in the enclosement of this illustration.

Figure 4.3.1 – Tomographic reconstructions of CL2 and CL4 samples from Clarens sample collection.

Vegetation and more specifically arctic vegetation in wetlands has a high water content. This is true especially for *Sphagnum* samples. Dried samples can bring one question if compared to their living counterparts: is studying dried samples in laboratory conditions a reliable method for physical properties assessments? A study made by Kämäräinen et al. (2018) took two sample lots from a mire in Eastern Finland. They compared these two sample plots, with one being dried and one being kept moist. They showed that the hyaline cells of *Sphagnum fuscum* have been emptied of their water, however the physical structure of the branch stayed intact. Kämäräinen et al. (2018) showed that the cells became transparent and "papery" as Hayward and Clymo (1982) showed in this early work. These works give some clues on the fact that drying does not influence the porous structure of the sample. A similar test is conducted in this thesis to validate the observation of Kämäräinen et al. (2018) on the samples that were collected in Clarens. The experimental protocol consists of putting a strain of *Sphagnum* on a plate and let it dry on a plate. This experiment is shown in Fig. 4.3.2.

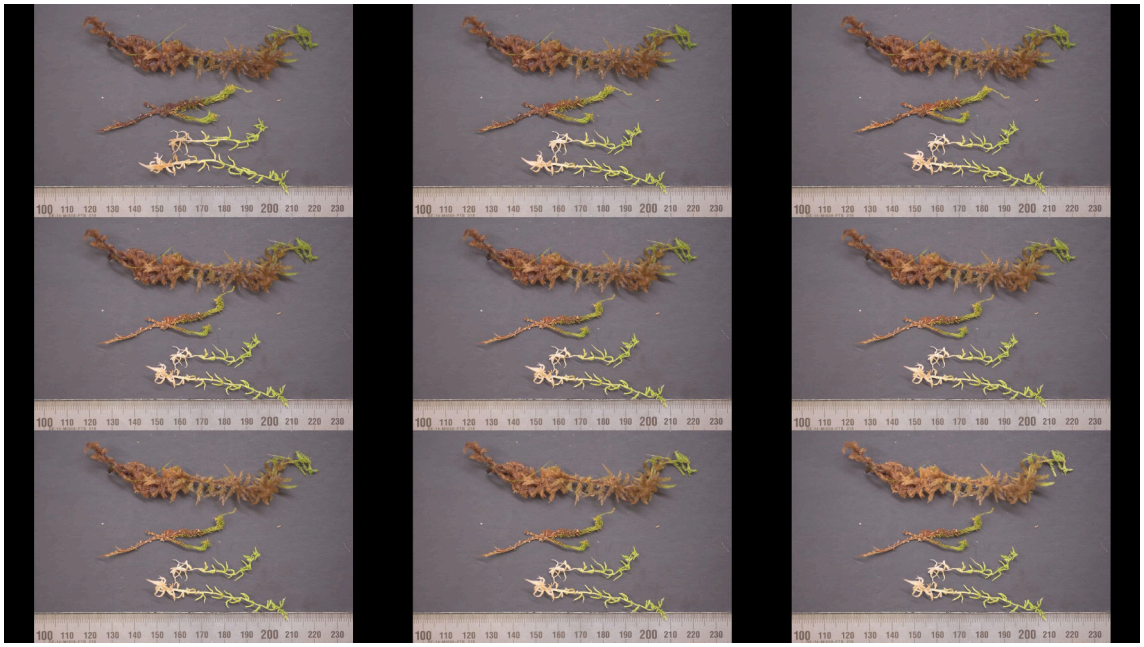

Figure 4.3.2 – Timelapse experiment of three *Sphagnum* sprigs and one *Philonotis* sprig let dry in ambient air during 18 h.

One can see that the *Sphagnum* strain is curving while drying, but the structure of the pseudo-leaves remains the same as when there were at a saturated state, at least in the pore-scale. If one compares the tomographic slices of Clarens samples when the samples are saturated and the dried sample seen under tomographic scanning it is possible to see the contours of surrounding hyaline cells' structures. In the slices showed in Fig. 4.3.1, the drying of the samples observed using tomographic reconstructions is marked by the emptying of the hyaline cells. At saturation, the hyaline cells are filled with water and appear white in the form of a single structure (acrotelms). On the other hand, during drying, the initial size of the acrotelm is retained, but absorption is significantly lower (darker color). Only the cell walls are thus highlighted by X-ray tomography.
This observation effectively demonstrates that keeping the *Sphagnum* samples alive or drying them has little effect on the porous macrostructure (the pore space formed by the entanglement of *Sphagnum* fibers). However, drying is not without consequences for the plant's metabolism, which enters a vegetative state. This effect needs to be taken into account when studying samples under real conditions, such as a summer drought.

4.4 CONCLUSION ON IMAGE PROCESSING TREATMENTS AND PERSPECTIVES IN FUTURE WORKS

After samples have been taken from various study sites, they are analyzed using an X-ray tomographic scanner. The scanning procedure provides a structural digital twin at a given time of a sample of Arctic vegetation cover. The digital nature of the tomography

results enables numerical estimation of effective properties, each calculation being able to be assimilated to the virtual equivalent of a sample taken in the field. Such estimation is repeatable and non-destructive as it is numerical.

While this method works optimally when the sample is dried, or when the sample is alive but unsaturated, some difficulties arise when the sample is water-saturated. The presence of ice, whose tomographic signatures are difficult to distinguish from the one of liquid water at first glance, also makes image segmentation complex. This obstacle to the optimal use of segmented images containing liquid water and ice could be overcome by using a chemical marker to modify the water signature on the tomogram, in the same way as a radiographic fluid used in the medical world (e. g.iodine contrast agent, Faggioni and Gabelloni, 2016). The use of high-resolution X-ray tomography provides this thesis with a detailed description of the constitutive porous structure of samples of arctic low vegetation cover. The obtained tomographic scans can be then used further to quantify transfer phenomena, and more specifically through measurements of hydraulic and thermal properties by numerical experiments. The simultaneous presence of water and ice in the porous medium makes it possible to interpret water saturation dynamics on a sample scale. However, the precise segmentation of *Sphagnum* strands in relation to liquid water and ice remains a complex operation. On one hand, the strong tomographic signature of liquid water and the high water content of *Sphagnum* complicate phase separation on the same image. On the other hand, the presence of ice modifies the very structure of the porous medium, making the comparison of an image without ice and with ice very difficult.

APPENDIX

4.A KHANYMEY SAMPLE AND TOMOGRAPHY DATA

Sample name	Sampling date	Species	γ	β	z_{sand}	z_{perm}	Observations
					cm	cm	
Hollow1.2	26.07.2018	*S.lindberghii*	-	+++	62	<180	Depression next to a unlinked lake, brown *Sph.* with grass, low density
Hollow1.4	26.07.2018	*S.lindberghii*	-	+++	74	<180	Brown Sph., in water connected to a lake
Hollow2.7	27.07.2018	*S.majus*	+++	?	73	?	Highy-saturated brown *Sph.*, connected to a lake. Sample is highly deformable.
Hollow2.8	27.07.2018	*S.majus*	+++	?	78	?	Highy-saturated brown *Sph.*, disconnected from a lake. Sample is highly deformable.
Lichen1.3	26.07.2018	*Cladonia sp.*	-	-	105	126	Mound between four lakes, peat underneath
Lichen2.1	27.07.2018	*Cladonia sp.*	-	-	?	40	Sampled over a ridge near a lake
Mound1.1	26.07.2018	*S.lenense*	-	-	<42	42	Mound between two small lakes, brown *Sph.* with peat and shrubs
Mound2.4	27.07.2018	*S.angustifolium*	-	-/+	<45	45	Mound *Sph.* next to a lake
Mound2.5	27.07.2018	*S.angustifolium*	?	?	50	50	Mound *Sph.* between two lakes. Thick *Sph.* layer with shrubs.
Mound2.6	27.07.2018	*S.angustifolium*					Green mound *Sph.* next to a lake (2.5m)
Peat2.2	27.07.2018	—	-	+	?	40	Sampled under Lichen2.1
Peat2.3	27.07.2018	—	-	+	105	126	Sampled under Lichen1.3

Table 4.A.1 – List of collected samples at Khanymey research station. γ indicates the qualitative water saturation state at sampling moment, β is the relative humidity of the samples at sampling moment.

Dataset name	Scanned sample	Date	r_{CT}	U_{CT}	I_{CT}	Observations
			µm.vx^{-1}	kV	µA	
sd1.2	Hollow1.2	03.10.2018	94.19	80	400	—
pileSTL	Hollow1.4	03.10.2018	94.19	90	120	Stack scanning Top
pileSLS	Hollow2.7	03.10.2018	94.19	100	327	Stack scanning Middle
pileSLS	Hollow2.8	03.10.2018	94.19	100	327	Stack scanning Bottom
pileSTL	Lichen1.3	03.10.2018	94.19	90	120	Stack scanning Bottom
Lichen2.1	Lichen2.1	03.10.2018	87.91	40	500	—
pileSTS	Mound1.1	03.10.2018	94.19	100	327	Stack scanning Middle
sb2.4	Mound2.4	03.10.2018	94.19	400	80	—
pileSLS	Mound2.5	03.10.2018	94.19	100	327	Stack scanning Top
pileSTS	Mound2.6	03.10.2018	94.19	100	327	Stack scanning Top
pileSTS	Peat2.2	03.10.2018	94.19	100	327	Stack scanning Bottom
pileSTL	Peat2.3	03.10.2018	94.19	90	120	Stack scanning Middle
sb2.6micro	Mound2.6	27.07.2022	17.19	108	237	Close scanning
sb2.6wet	Mound2.6	01.03.2023	94.17	146	430	Saturated with water
sb2.6ice	Mound2.6	28.04.2023	95.01	146	430	Frozen sample with same saturation level
sb2.6iceclose	Mound2.6	28.04.2023				Frozen sample with same saturation level - close caption

Table 4.A.2 – List of CT scans for taken for Khanymey sample collection. r_{CT} is the final volume resolution of the tomography [in µm.voxel^{-1}], $U_{CT}$is the voltage of the X-ray tube during scanning [in V], I_{CT} is the electrical intensity of the X-ray tube during scanning [in µA].

4.B ABISKO SAMPLE DATA

Sample name	Sampling date	Species	γ	β	Observations
Abisko01	20.07.2022	*S.balticum*	+++	+++	Sampled near the path. Very deep mire (>120 cm)
Abisko02	20.07.2022	*S.balticum*	+++	+++	Sampled near the path. Very deep mire (>80 cm)
Abisko03	20.07.2022	*S.russowii*	-	+	Sampled on a peat mound near dwarf birch trees.
Abisko04	20.07.2022	*S.russowii*	-	+	Sampled on a peat mound near dwarf birch trees.

Table 4.B.1 – List of collected samples at Clarens mire. γ indicates the qualitative water saturation state at sampling moment, β is the relative humidity of the samples at sampling moment.

Dataset name	Scanned sample	Date	r_{CT}	U_{CT}	I_{CT}	Observations
			µm.vx^{-1}	kV	µA	
Stack_Ab1_2	Abisko1	26.07.2022	94.16	123	239	Stack scanning Top
Stack_Ab1_2	Abisko2	26.07.2022	94.16	123	239	Stack scanning Bottom
Stack_Ab13_4	Abisko3	27.07.2022	94.16	123	239	Stack scanning Top
Stack_Ab13_4	Abisko4	27.07.2022	94.16	123	239	Stack scanning Bottom
Abisko2Ice	Abisko2	03.05.2023	94.72	146	432	Sample frozen

Table 4.B.2 – List of CT scans for taken for Clarens sample collection. $r_{CT}$is the final volume resolution of the tomography [in µm.voxel^{-1}], $U_{CT}$is the voltage of the X-ray tube during scanning [in V], I_{CT} is the electrical intensity of the X-ray tube during scanning [in µA].

4.C CLARENS SAMPLE DATA

Sample name	Sampling date	Species	γ	β	Observations
CL1	26.03.2021	*S.fuscum*	+	++	
CL2	26.03.2021	*S.majus*	-	+++	
CL3	26.03.2021	*P.marchica*	-	-	
CL4	26.03.2021	*S.angustifolium*	+	+	
CL5	26.03.2021	*P.marchica*	-	-	
CL6	26.03.2021	*S.fuscum*	+	+	

Table 4.C.1 – List of collected samples at Clarens mire. γ indicates the qualitative water saturation state at sampling moment, β is the relative humidity of the samples at sampling moment.

Dataset name	Scanned sample	Date	r_{CT}	U_{CT}	I_{CT}	Observations
			µm.vx^{-1}	**kV**	**µA**	
StackCLA	CL2	29.03.2021	93.75	90	357	Stack scanning Top
StackCLA	CL4	29.03.2021	93.75	90	357	Stack scanning Bottom
StackCLB	CL5	29.03.2021	93.76	90	357	Stack scanning Top
StackCLB	CL6	29.03.2021	93.76	90	357	Stack scanning Bottom
StackCLA_control	CL2	09.04.2021	91.91	90	357	Stack scanning Top
StackCLA_control	CL4	09.04.2021	91.91	90	357	Stack scanning Bottom
StackCLB_dried	CL5	09.04.2021	92.91	90	357	Stack scanning Top
StackCLB_dried	CL6	09.04.2021	92.91	90	357	Stack scanning Bottom
CL6_driedZoom	CL6	09.04.2021	19.53	89	333	Zoom tomography
CL2Ice	CL2	28.03.2023	94.72	146	430	Frozen sample

Table 4.C.2 – List of CT scans for taken for Clarens sample collection. $r_{CT}$is the final volume resolution of the tomography [in µm.voxel^{-1}], $U_{CT}$is the voltage of the X-ray tube during scanning [in V], I_{CT} is the electrical intensity of the X-ray tube during scanning [in µA].

Part III

ARCTIC LOW VEGETATION TRANSFER PROPERTIES

5

NUMERICAL ASSESSMENT OF MORPHOLOGICAL AND HYDRAULIC PROPERTIES OF MOSS, LICHEN AND PEAT FROM A PERMAFROST PEATLAND

This chapter deals with the study of the morphological and hydraulic morphological and hydraulic properties of *Sphagnum* mosses, lichens and peat collected in Western Siberia (Khanymey research station). The work presented here corresponds to the study published in January 2023 in the journal *Hydrology and Earth System Sciences* under the title *"Numerical assessment of morphological and hydraulic properties of moss, lichen, and peat from a permafrost peatland"*.

Due to its insulating and draining role, assessing ground vegetation cover properties is important for high-resolution hydrological modeling of permafrost regions. In this study, morphological and effective hydraulic properties of Western Siberian Lowland ground vegetation samples (lichens, *Sphagnum* mosses, peat) are numerically studied based on tomography scans. Porosity is estimated through a void voxels counting algorithm, showing the existence of representative elementary volumes (REVs) of porosity for most samples. Then, two methods are used to estimate hydraulic conductivity depending on the sample's homogeneity. For homogeneous samples, direct numerical simulations of a single-phase flow are performed, leading to a definition of hydraulic conductivity related to a REV, which is larger than those obtained for porosity. For heterogeneous samples, no adequate REV may be defined. To bypass this issue, a pore network representation is created from computerized scans. Morphological and hydraulic properties are then estimated through this simplified representation. Both methods converged on similar results for porosity. Some discrepancies are observed for a specific surface area. Hydraulic conductivity fluctuates by 2 orders of magnitude, depending on the method used.

Porosity values are in line with previous values found in the literature, showing that arctic cryptogamic cover can be considered an open and well-connected porous medium (over 99 % of overall porosity is open porosity). Meanwhile, digitally estimated hydraulic

conductivity is higher compared to previously obtained results based on field and laboratory experiments. However, the uncertainty is less than in experimental studies available in the literature. Therefore, biological and sampling artifacts are predominant over numerical biases. This could be related to compressibility effects occurring during field or laboratory measurements. These numerical methods lay a solid foundation for interpreting the homogeneity of any type of sample and processing some quantitative properties' assessment, either with image processing or with a pore network model. The main observed limitation is the input data quality (*e.g.*, the tomographic scans' resolution) and its pre-processing scheme. Thus, some supplementary studies are compulsory for assessing syn-sampling and syn-measurement perturbations in experimentally estimated, effective hydraulic properties of such a biological porous medium.

Hydrol. Earth Syst. Sci., 27, 431–451, 2023
https://doi.org/10.5194/hess-27-431-2023

Hydrology and Earth System Sciences
Open Access
EGU

Numerical assessment of morphological and hydraulic properties of moss, lichen and peat from a permafrost peatland

Simon Cazaurang[1], Manuel Marcoux[1], Oleg S. Pokrovsky[2,3], Sergey V. Loiko[3], Artem G. Lim[3], Stéphane Audry[2], Liudmila S. Shirokova[2,4], and Laurent Orgogozo[2]

[1]Toulouse Institute of Fluid Mechanics (IMFT), National Polytechnic Institute of Toulouse, Toulouse, 31400, France
[2]Geosciences Environnement Toulouse (GET) Laboratory, University Toulouse III – Paul Sabatier, Toulouse, 31400, France
[3]BIO-GEO-CLIM Laboratory, Tomsk State University, Tomsk, Russian Federation
[4]Laverov Federal Center for Integrated Arctic Research of the Ural Branch –
Russian Academy of Science, Russian Federation

Correspondence: Simon Cazaurang (simon.cazaurang@imft.fr)

5.1 INTRODUCTION

Covering a quarter of the Northern Hemisphere's land surface (*Circum-Arctic Map of Permafrost and Ground-Ice Conditions* 1997), permafrost soils are the most representative soil types in arctic and subarctic regions. Permafrost is a soil layer in which temperature remains below 0 °C for at least two consecutive years, thus holding ice in its porous structure. Frozen layers make permafrost hydrology peculiar, resulting in complex couplings between heat and water fluxes (Grenier et al., 2018; N. Tananaev et al., 2020).
Seasonal structural variations occur in permafrost soils, as surface thawing forms an "active layer". Most permafrost-related biogeochemical processes (especially organic matter degradation) take place in this layer. The active layer is at its maximum thickness in the early fall and is generally meters in scale (Clayton et al., 2021; Aalto et al., 2018; Guo and H. Wang, 2017). Active layer thickness is, nonetheless, spatially variable due to climatic conditions, land cover, and the micro- and macro-topography. The impact of hydrological

climate change is particularly drastic in permafrost-dominated environments because of deepening thaw fronts (Hinzman and Kane, 1992). Indeed, between 2008 and 2016, the average annual temperature of arctic permafrost soil increased by 0.4 (±0.25) °C (Biskaborn et al., 2019; Fox-Kemper et al., 2023). This causes positive feedback on average atmospheric temperatures (Meredith et al., 2019), reduces latent heat effects (Walvoord and Kurylyk, 2016) and increases water drainage in arctic watersheds (Liljedahl et al., 2016). Hence, quantifying heat and water transfer properties in permafrost-affected regions is compulsory.

Previous studies have addressed this quantification through field observations (Olefeldt and Roulet, 2014; Dmitry A Streletskiy, N. I. Tananaev, et al., 2015; Throckmorton et al., 2016; O'Connor et al., 2020) or field and laboratory experiments (Vedie et al., 2011; Roux et al., 2017; Wagner et al., 2018). Some recent studies have also dealt with this question using a modeling approach (Bense et al., 2012; Genxu et al., 2017; Burke et al., 2020; Du et al., 2020; Fabre et al., 2017).

Bryophytes (mosses) and lichens are widely present in tundra and taiga environments. The dominant ground cover consists of *Sphagnum* mosses and lichens in permafrost peatlands (Soudzilovskaia et al., 2013; Volkova et al., 2018). *Sphagnum* mosses are part of the *Bryophyta* plant division, which represents non-vascular plants (without xylem or phloem). *Sphagnum* colonies grow indeterminately from their apical structure, named the capitula. Their water content mainly relies on capillary forces maintained by each individual's density (Hayward and Clymo, 1982; Howie and Hebda, 2018). Lichens are not "vegetation" but consist of a symbiotic association between heterotrophic *Fungi* and autotrophic *Algae*. Both *Sphagnum* and lichens can be gathered into the *Cryptogamae* sub-kingdom. This cryptogamic layer has an important impact on permafrost dynamics because it influences heat and water exchanges between the soil and atmosphere (Soudzilovskaia et al., 2013; Launiainen et al., 2015; Porada et al., 2016; Park, Launiainen, et al., 2018; Loranty et al., 2018). Boreal vegetation is assumed to be a major nutrient and inorganic solute exchange medium at a watershed scale (L. Shirokova et al., 2021). Boreal vegetation is likely to accumulate in lowlands at a low degradation rate, resulting in the formation of *Sphagnum* peatlands, such as the Western Siberian Lowlands.

Ground vegetation transfer properties are key information for high-resolution hydrological modeling of permafrost-related catchments. Thus, reliable estimates of them are necessary for water flux studies for boreal soils and for climate change impact assessment of the hydrology of high-latitude continental surfaces. Therefore, some recent efforts have been put into emphasizing the role of the cryptogamic layer in Earth system models (Stepanenko et al., 2020; Shi et al., 2021). Devoted modeling tools have also been created to predict *Sphagnum* dynamics (the *Peatland Moss Simulator* by Gong et al., 2020). Furthermore, specific modeling work has been conducted on restored *Sphagnum* peatlands to link hydrological properties with dissolved organic carbon dynamics (Bernard-Jannin

et al., 2018) or soil moisture dynamics (Elliott and Jonathan Price, 2020). However, the mechanistic modeling of water and heat fluxes in ground vegetation layers remains difficult, as their porous-medium transfer properties are not straightforward to evaluate (Orgogozo, Prokushkin, et al., 2019).

Many studies are available for the decayed *Sphagnum* layer: peat. The hydrological and thermal properties of peat are well documented. Extensive reviews of the relation between hydrogeochemical processes in peatlands and peat's porous-medium structure were conducted by McCarter, F. Rezanezhad, et al. (2020). A study of peatland's hydraulic properties was initiated during the 1920s for peatland drainage (Malmström, 1925). Then, some introductory field experiments were conducted on Finnish peatlands (Virta, 1962; Heikurainen, 1963; Sarasto, 1963) as well as in the United States(Boelter, 1968) and Ireland (Galvin, 1976).
Only a few studies were conducted on the living part of this upper permafrost layer. Hence, quantitative assessments of some key hydrological properties of ground vegetation layers are needed, such as total, open and enclosed porosity, hydraulic conductivity and specific surface area. In terms of hydraulic properties, hydraulic conductivity has been assessed in the laboratory using constant or falling-head permeameters (Quinton, Gray, et al., 2000; J. S. Price, Whittington, et al., 2008; Hamamoto et al., 2016; Weber et al., 2017) or via field measurements (Päivänen, 1973; Crockett et al., 2016; this study). The results are presented in Table 5.2.1, with some peat results for comparison. Otherwise, arctic lichens have received little attention to date. To our knowledge, only one study has estimated lichens' hydraulic properties, considering unsaturated hydraulic conductivity without taking into account macropores (Voortman et al., 2014). However, the specific surface areas of some other lichen species are documented in the literature (Adamo et al., 2007). Some studies quantified arctic lichen properties in response to acid rain (Tarhanen et al., 1999) to clarify their interaction with the rhizosphere (Banfield et al., 1999) or in relation to their albedo properties (Bernier et al., 2011). Some trans-membrane transfer properties are also available in the literature (Potkay et al., 2020).

Thus, many field and experimental studies are available throughout the literature. However, field work and experimental studies are known to bring their own difficulties, due to the local conditions' variabilities, sampling biases, disturbances and measurement uncertainties. The aim of this study is to assess some of the transfer properties that are well documented with field and experimental studies with an innovative numerical scheme. Indeed, the use of numerical workflows enhances reproducibility and intercomparison capability between samples. Numerical workflows are often used when experimental studies are complicated to implement (reservoir engineering, aerodynamics, microfluidics).

In this work, such numerical workflow is intended to be used for evaluating the hydrological transfer properties of representative vegetation types of the Western Siberian Lowlands. To this end, natural samples collected from the Western Siberian Lowlands are digitally analyzed to characterize some morphological and hydraulic transfer properties. Thus, in contrast to previous works compiled in Table 5.2.1, this study aims to assess the hydraulic properties of lichens and *Sphagnum* mosses by numerical methods rather than experimental measurements. The arctic cryptogamic layer is assumed, hereafter, to represent a complex patchwork of biological porous media (J. S. Price, Whittington, et al., 2008; Voortman et al., 2014; Hamamoto et al., 2016).

To validate this hypothesis, a thorough analysis of sample homogeneity is carried out, based on porosity, as it is the main driver of flow dynamics in porous media (Koponen et al., 1997; Koponen et al., 1996). This enables the classification of samples according to their homogeneity. Indeed, for homogeneous samples, a smaller sample region can be considered an effective medium sharing the same properties as the whole sample. Multidimensional porosity description leads to a statistical study of the existence of a representative elementary volume (REV). Two standard porous-medium modeling methodologies are used throughout this study: direct numerical simulations on computed representative elementary volumes (DNS-REVs) and pore network modeling with a built-in solver (PNM). The impossibility of collecting a substantial number of samples is compensated for by a statistical quantification of a REV for each sample. This implies that the REV is smaller than the sample, and hence sampling size is chosen to match sizes that were used in the previous literature, such as (Weber et al., 2017).

Symbol	Description	Unit
	Greek letters	
ρ_{dry}	Dried bulk sample density	$kg.m^{-3}$
ρ_w	Water density	$kg.m^{-3}$
ϵ_{total}	Sample digital overall porosity	%
ϵ_{open}	Sample digital open porosity	%
μ_w	Dynamic viscosity of water	$Pa.s^{-1}$
σ	Generic symbol for ratios	–
σ_{S-T}	Ratio between sphere number and throat number (pore network)	–
	Roman letters	
d_{Sph}	Spherical pore density (pore network)	m^{-3}
d_{Thr}	Throat density (pore network)	m^{-3}
g	Gravitational acceleration	$m.s^{-2}$
i_{voxel}	Voxel intensity	–
k	Intrinsic permeability	m^2
K_W	Hydraulic conductivity	m^{-3}
L_i	Sample length along axis i	m
L_ϵ^{REV}	Representative elementary volume of porosity length	mm
L_K^{REV}	Representative elementary volume of hydraulic conductivity length	mm
N_b	Number of voxels of intensity $N = b$	–
p_{open}	Ratio between ϵ_{open} and ϵ_{total}	–
P	Pressure (water head)	Pa
Re	Reynolds number	–
S_{outlet}	Overall surface of the outlet (including void and solid phases)	m^2
$S_{SA(M)}$	Mass-specific surface area	$m^2.g^{-1}$
$S_{SA(V)}$	Volumetric-specific surface area	$m^2.m^{-3}$
V_v	Volume of an array v	m^3
v_i	Incompressible flow speed along direction i	$m.s^{-1}$
u_i	Darcy flow along axis i	$m^3.s^{-1}$

Table 5.1.1 – Notation glossary.

5.2 MATERIALS AND METHODS

5.2.1 *Sample collection and digital reconstruction*

Sample	Method	$K_W(m.s^{-1})$	Reference
Lichen	IM	$1.8 \times 10^{-9} - 3.7 \times 10^{-9}$	Voortman et al. (2014)
Peat	CHP	$1.8 \times 10^{-9} - 3.7 \times 10^{-9}$	Hamamoto et al. (2016)
Peat	CHP	$4.6 \times 10^{-6} - 4.2 \times 10^{-4}$	Quinton, Gray, et al. (2000)
Sphagnum	CHP	$3 \times 10^{-5} - 1.3 \times 10^{-3}$	Golubev, McCarter, et al. (2021)
Sphagnum	Modified CHP	$2.4 \times 10^{-4} - 1.8 \times 10^{-3}$	J. S. Price, Whittington, et al. (2008)
Sphagnum	FHP	$1.2 \times 10^{-4} - 1.2 \times 10^{-3}$	Weber et al. (2017)
Peat	FP	$1.7 \times 10^{-6} - 3.3 \times 10^{-5}$	Päivänen (1973)
Sphagnum	FP	$5.6 \times 10^{-5} - 1.7 \times 10^{-4}$	Crockett et al. (2016)
Sphagnum	NM	$2.9 \times 10^{-5} - 3.2 \times 10^{-3}$	McCarter and J. Price (2014)
Sphagnum	FP	$6 \times 10^{-5} - 2 \times 10^{-4}$	This study

Table 5.2.1 – Synthesis of saturated hydraulic conductivity ($m.s^{-1}$) of peat and *Sphagnum* found in the literature. *This study*'s values refer to field experiments conducted during sample collection (CHP: constant head permeameter; FHP: falling head permeameter; FP: field percolation; IM: inverse modeling; NM: numerical model, Hydrus-1D; see McCarter and J. Price, 2014).

Samples were collected at Khanymey Research Station (N63°43'19,73" E75°57'47,91") in Western Siberia (Autonomous District of Yamal-Nenets, Russian Federation) in July 2018. The mean annual temperature is −5.6 °C, and average precipitation is 540 mm (Payandi-Rolland, L. Shirokova, Tesfa, et al., 2020; Raudina et al., 2018). Eight moss samples (*Sphagnum sp.*) were collected, either on moss mounds or in thermokarstic hollows. Additionally, two lichen samples (*Cladonia sp.*, named Lichen1.3 and Lichen2.1) and two peat samples (named Peat2.2 and Peat2.3) were collected. Of the eight *Sphagnum* samples, three are *S. angustifolium* (C.E.O. Jensen ex Russow, named Mound2.4, Mound2.5 and Mound2.6), two are *S. lindbergii* Schimp (named Hollow1.2 and Hollow1.4) and two are *S. majus* (Russow) (C.E.O. Jensen, named Hollow2.7 and Hollow2.8). The last moss sample is *S. lenense* H. Lindb. ex L.I. Savicz (named Mound1.1).

Sampling is thoroughly conducted to minimize structural perturbations. In order to achieve this, each sample's surroundings are cleared with special care prior to extraction. Then, the sample is extracted using a ceramic knife directly at the right dimensions to fit in a high-density polyethylene box, where it remains from the moment of sampling and drying to the tomographic examination. Additionally, four in-situ hydraulic conductivity

measurements are performed on various *Sphagnum* plots, using a double-ring infiltrometer (Table 5.2.1). An overview of the sample collection method is shown in Fig. 5.2.1 as well as 3D tomographical visualizations of each sample type.

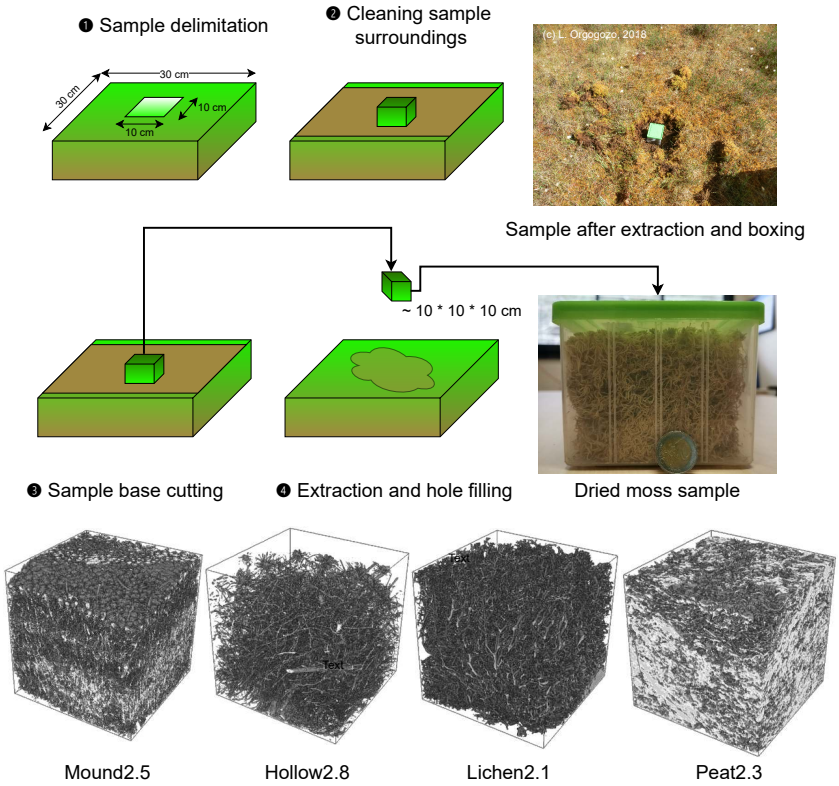

Figure 5.2.1 – Sampling collection method overview.

5.2.2 *Drying impact assessment of sample representativity*

The sampling locations and processing facilities were far away from each other. To ensure structural preservation, special care is taken throughout the sampling, transportation and scanning operations. The samples are oven-dried for 48 h at 40 °C, at atmospheric pressure, to halt biological degradation. As expected, *Sphagnum* mosses began to whiten and become papery, as described by Hayward and Clymo (1982). The samples are scanned at the Toulouse Institute of Fluid Mechanics under dry conditions, two months after their primary extraction at Khanymey Research Station and drying.

To ensure the dry samples' representativity, we used an analogous drying experimental protocol to the one carried out by Kämäräinen et al. (2018). This experiment is conducted on similar *Sphagnum* species (*S. fuscum* (Schimp.) H.Klinggr., *S. majus* (Russow) C.E.O. Jensen) and sampled according to the same method at Clarens mire (south-western France, N43° 08′41.3″, E0°25′12.9″) in March 2021, notwithstanding that *Sphagnum* acrotelm (growing section of a *Sphagnum* individual) is much thinner than Siberian

samples. Four samples are collected, two being dried at 40 °C for 48 h and the other two being left untouched, as control samples. Each of the four samples is scanned 2 d after their extraction and then again 14 d after extraction. Additionally, one *Sphagnum majus* individual is extracted and left to dry under ambient conditions.

A comparative study between each of the two sample lots and the lone individual show that drying does not affect structural preservation. Our validation experiment converges with the results found by Kämäräinen et al. (2018). This also confirms hyaline cells' structural durability: the early work of Puustjärvi (1977) showed that hyaline cells were well preserved during biological decay. Drying impacts aside, *Sphagnum's* continuous growth on non-dried control samples seems the most impactful structural factor, as each individual was striving to adapt itself to the sampling box hydric conditions. Fast drying before tomographic examination can be a reasonable solution for preserving the morphological structure, in conjunction with careful on-site sampling.

5.2.3 *Morphological analysis: total porosity (ϵ_{total}), open porosity (ϵ_{open}), specific surface area (S_{SA}) and pore size distribution.*

Global porosity (ϵ_{total}) is calculated for each sample using built-in ImageJ-Fiji tools and macro-scripting. Porosity is considered to be a ratio between the number of voxels representing the void phase i voxel (void phase's internal volume, including closed porosity) over the total number of voxels representing a sample N_{total} (void and matrix volume). This relation is shown in Eq. 5.1:

$$\epsilon_{total} = \frac{V_{i=0}}{V_{total}} \times 100 = \frac{\iiint_0^{N_i=0} i_{voxel}(x,y,z)\,dx\,dy\,dz}{\iiint_0^{N_{total}} i_{voxel}(x,y,z)\,dx\,dy\,dz} \times 100 = \frac{\sum_0^{N_i=0} i_{voxel}}{\sum_0^{N_{total}} i_{voxel}} \times 100 \quad (5.1)$$

Porosity is computed on bidimensional horizontal slices along the z axis to evaluate porosity variations along the samples. Image stacks are then reconstructed along the x and y axes to create two other image stacks. Finally, porosity is computed along the x, y and z axes using a voxel-counting algorithm shown in section 5.3.1.
The samples could then be classified into three types according to the porosity profile along the vertical axis (Table 5.2.2 and Fig. 5.A.2 of 5.A). As porosity appears to be almost constant over the x and y axes, sample classification is solely based on vertical porosity *z:*

- Type I: constant high porosity along the z axis, excluding border effects;
- Type II: low basal porosity, linearly increasing to the top of the sample;
- Type III: no specific trend observed in vertical porosity.

For each sample nature as well as each classified type, a dedicated color palette is chosen and kept consistent throughout the study for the sake of clarity. Open and connected porosities (ϵ_{open}) are retrieved using dedicated shape analysis and labeling tools provided in the IPSDK™ image-processing toolkit (a Reactiv'IP product used in Goubet et al., 2021). This enables a precise segmentation to associate each connected void space into a unique identifier. Here, since the samples have more void than matter, this first label is assumed to be connected void space, which plays a major role in the flow and transfers (porosity), the latter being a closed or non-communicating element. From the raw dataset, voxel intensity is integrated to get the first label's voxel sum divided by the overall voxel number, as shown in Eq. 5.2:

$$p_{open} = \frac{\epsilon_{open}}{\epsilon_{total}} = \frac{\sum_0^{N_i \in label0} i_{voxel}}{\sum_0^{N_{total}} i_{voxel}} \times \epsilon_{total}^{-1} \tag{5.2}$$

The specific surface area is deduced using the same shape analysis and labeling tools included in IPSDK™. Integrating the surface between both phases (void and solid) yields the total surface S. Thus, volumetric-specific surface area S_{SA} is obtained by dividing this surface by the sample's bounding box volume, expressed in $m^2.m^{-3}$, as shown in Eq. 5.3:

$$S_{SA_V} = \frac{S_{solid}}{V_{BBox}} = \frac{\int\int_0^{N-1} S\left((i,j)(i+1,j+1)\right) di\, dj}{L_x L_y L_z} \tag{5.3}$$

Specific surface area is conventionally expressed in relation to density ($m^2.g^{-1}$). For this purpose, each dried sample mass is obtained using an analytical balance and the sample's dry bulk density ρ_{dry}. Then, volumetric-specific surface values are converted into a mass-related specific surface by dividing volumetric-specific surface area by dry density, as shown in Eq. 5.4:

$$S_{SA_M} = \frac{S_{SA_v}}{\rho_{dry}} \tag{5.4}$$

Pore size distribution is calculated using ImageJ-Fiji's implemented image segmentation tools on the binarized image stacks. In each stack's image, a Euclidean distance transformation of the matrix phase from the void phase is first applied. Then, for each isolated void patch, the Feret diameter is computed.

5.2.4 *Darcy-scale morphological and hydrological property definition: REV*

In this study, the collected samples are assumed to form a complex fibrous porous medium. Resolving mechanistic equations in such large domains is not straightforward due to the extensive computational resources required. Conversely, resolving such equations on an arbitrary cropped sample would not aid the hydraulic property assessment. To make the link between microscale and macroscale phenomena, a reproducible pattern

is required to avoid microscale heterogeneities and lack of information due to a diminutive sample size. To do this, finding a representative region that validates scale separation assumptions with both microscale and macroscale heterogeneities is compulsory, thus defining the volumetric average of a microscale property that is continuous and informative at a macroscale. One of the first volume averaging methods consists of finding a statistical REV for the given studied property.
Indeed, REV is a theoretical concept clarifying the definition of the macroscopic scale (Darcy scale) and the microscopic scale (pore scale) and characterizing a given porous medium. This REV can be assumed to be a specific sample volume in which transfer-governing equations (single-phase flow, for example) may be defined along with the associated effective properties. A proper mathematical definition of a REV is given in Bachmat and Bear (1987), Quintard and Whitaker (1989) and Whitaker (1999) along with a thorough definition of volume-averaging methods. A generic profile for a given property ϕ_β is shown in Fig. 5.2.2.

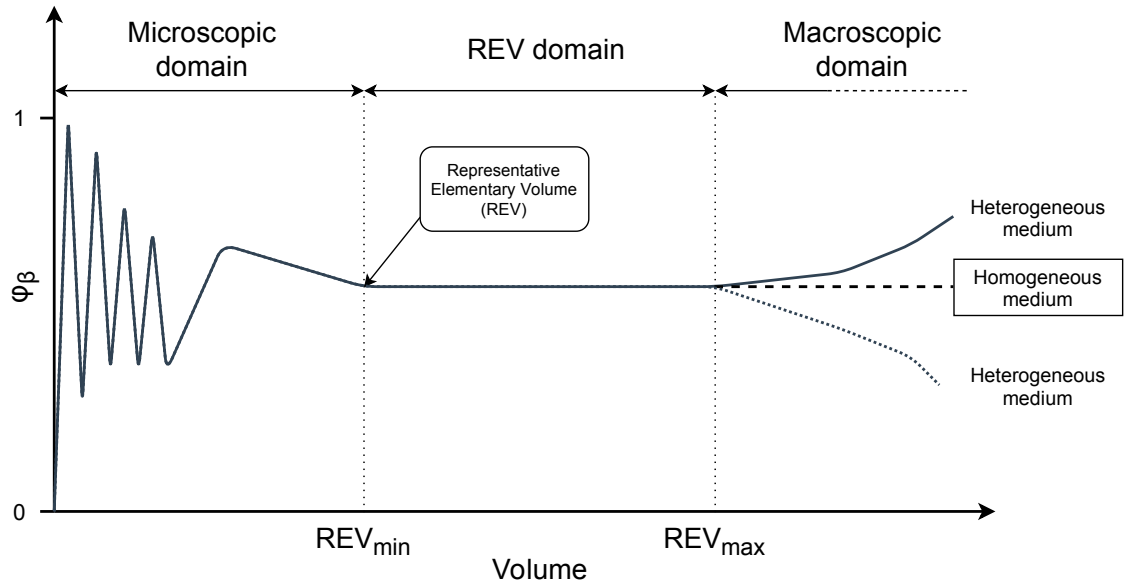

Figure 5.2.2 – Schematic representation of fluctuations of a generic property ϕ_β in conjunction with volume (adapted following Brown and Hsieh, 2000).

The fluctuation profile shows three main domains. Here, the REV is defined as the smallest volume for which statistical fluctuations of a given property in a given space are sufficiently low to consider its average value an effective property. Finding the representative elementary volumes of some key properties (*e.g.*, porosity and intrinsic permeability) is a routine workflow in porous-medium sciences. It is often used for fractured oil reservoirs (Durlofsky, 1991) or artificially packed glass bead media (Leroy et al., 2008). A REV is, by definition, large when compared to characteristic lengths of heterogeneities at a microscopic scale but small when compared to characteristic lengths of heterogeneities at the macroscopic scale. Thus, the properties computed for a REV of a

porous medium may be defined and computed as continuous functions of space and even constant, in the case of a homogeneous porous medium, as defined by Bear (1972). In general, REVs are described on the basis of morphological characteristics such as porosity, although a distinct REV can be found for any given porous-medium property. Porosity and hydraulic-conductivity-related REVs are characterized throughout this study, leading to two different sizes, one for each property.

5.2.4.1 *Porosity: binarization and voxel counting*

From previously binarized image stacks, a statistical REV analysis is conducted using dedicated high-performance image processing Python libraries (IPSDK™), encapsulated in a specifically designed batch process for which the flowchart is shown in Fig. 5.2.3.

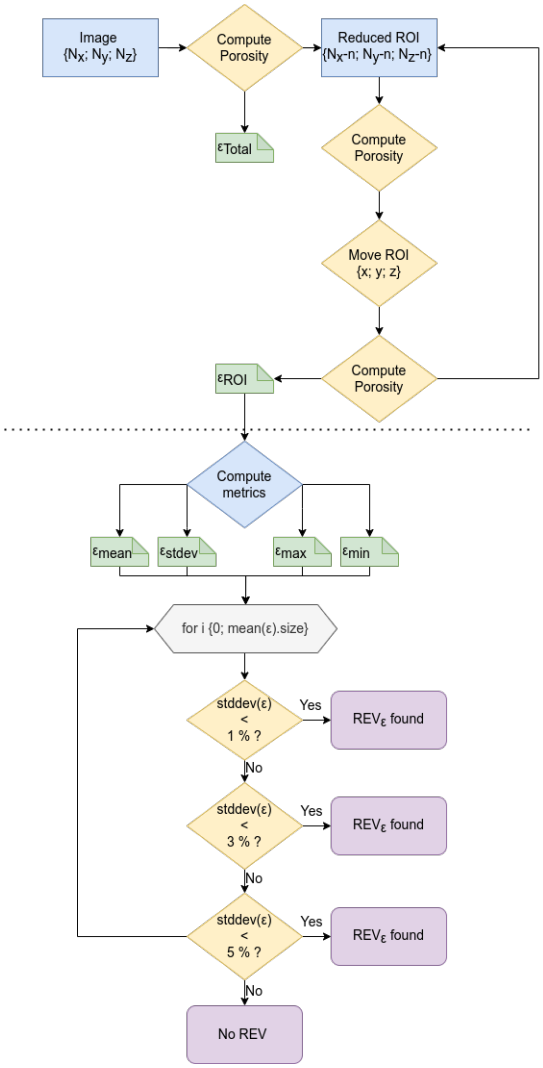

Figure 5.2.3 – Flowchart of the representative elementary volume of porosity (REV_ϵ) from a binarized image. For each sample, three thresholds are tested (5%,3% and 1% and standard deviation variation).

First, porosity (Eq. 5.1) is computed for a given sub-sampling volume within the whole sample. Then, the subsampling volume location is incrementally reduced and moved in every spatial direction. For each sub-volume, intermediate porosities are computed. The average and standard deviations are stored for each chosen sub-sampling volume. Then, an algorithmic routine is used to find the maximal size that satisfies a given threshold (1%, 3% or 5% of porosity fluctuation). These thresholds define the statistical representativeness of these REVs. Thus, a REV satisfying a 1% threshold can be assumed to be a high-grade REV, whereas the 5% threshold corresponds to lower-grade REVs. For 10 of the 12 studied samples, a REV of porosity is found. The two remaining samples, Hollow1.2 and Peat2.2, do not exhibit a REV for the chosen thresholds. A collection of tridimensional reconstructions of the samples as well as some examples of REVs for each sample are shown in Fig. 5.A.1 of Appendix 5.A. The graphical plots for each studied sample are available in Appendix Fig. 5.A.3 of Appendix 5.A. The black dot represents the smallest reached representative elementary volume for each sample.

5.2.4.2 *Hydraulic conductivity: direct numerical simulation*

Hydraulic conductivity is estimated through single-phase flow computations performed by solving a Navier–Stokes equation in the pore space of the considered sample. The concept is to carry out the numerical simulation of fluid flow, reproducing the conditions occurring in a constant-head (CHP) permeameter. Then, a sample's hydraulic conductivity is computed from the obtained velocity field. A virtual CHP is created by imposing a constant pressure on two opposite faces to one direction (inlet and outlet). Water-tight wall boundary conditions are applied to other faces, as shown in a conceptual representation of the initial and boundary conditions available in Fig. 5.A.2 of Appendix 5.A.

Due to computation time limitations, the biggest studied sub-volume with this approach corresponds to a quarter of the total sample. In section 5.2.4, we stated that the REVs of effective physical properties were valid for that particular physical property. Thus, a hydraulic conductivity REV is required to statistically assess hydraulic conductivity. For that purpose, instead of counting voxel value algorithms (as made for porosity), retrieving a representative elementary volume for hydraulic conductivity requires extensive fluid mechanics simulations. Here, a laminar single-phase flow induced by a pressure gradient is computed for each sub-sample, being consistent with the idea of reducing and moving a defined sub-volume inside the overall sample. From open-porosity data in Table 5.2.2, we can show that most porosity is connected to each one. This leads to the assumption that considering all pores can be considered effective in permeability-driven phenomena. As these simulations are resource-costly, Type-I samples (constant porosity) are selected as they are sufficiently homogeneous for the establishment of REVs. Other types are treated by another method presented in section 5.2.4.3. The implemented method relies

on Mohammadmoradi and Kantzas (2016) in conjunction with automatic mesh manipulation tools (*trimesh* Python library, Dawson-Haggerty et al., 2019). For each Type-I sample, single-phase flow simulation through a fraction of the solid volume (representing a sample) is conducted. The *simpleFoam* algorithm is used to solve a velocity field from an initial pressure gradient. The *simpleFoam* solver is an enhanced version of the original *SIMPLE* algorithm (*Semi-Implicit Method for Pressure-Linked Equations* – Patankar, 1980) nested in the open-source Computational Fluid Dynamics toolkit *OpenFOAM* (Weller et al., 1998, https://openfoam.org/, last access: 17 January 2023; https://www.openfoam.com/, last access: 17 January 2023).

For each sample, four potential REV sizes are computed (23.5, 15.7, 11.8 and 9.4 mm), consisting of 8, 27, 64 and 125 simulations on the x, y and z axes, respectively, representing 672 simulations per sample. These sizes are chosen from the beginning to limit computation times, as using the same scanning method than what was developed for porosity is computationally prohibitive. This is run on the tier-2 supercomputer Olympe (CALMIP computational mesocenter, Toulouse, France). These calculations are run simultaneously, each occupying one node (36 physical cores), representing 10 500 h CPU (about 12 d of physical time) per sample. For each simulation, the velocity field u_i is integrated with the overall outlet surface S_{outlet} (including the surface occupied by the solid matrix) to get an averaged outlet flux value v_i, according to Eq. 5.5:

$$v_i = \frac{1}{S_{outlet}} \int_0^S u_i dS \tag{5.5}$$

A careful convergence study is also conducted so that numerical errors, associated with discretization resolutions and iterative procedures for the approximated inversions of the linear systems involved, are low enough to be neglected in the analysis of the results. Inlet pressures are chosen to avoid turbulent flows (Re<<1). The computed Darcy velocity v_i could then be injected into a regular Darcy law, as shown in Eq. 5.6, where k_{ii} is a tensorial component of intrinsic permeability (m²) and μ_w is the dynamic viscosity:

$$k_{ii} = v_i \frac{\mu_w}{\nabla P} \; with \; \nabla P = \frac{P_{inlet} - P_{outlet}}{L_i} \tag{5.6}$$

To avoid artifacts related to the physics of a specific fluid, the *simpleFoam* solver uses kinematic pressure (expressed in $m^2.s^{-2}$) and kinematic viscosity ν ($m^2.s^{-1}$) to solve Navier–Stokes equations. These equations are based on intrinsic permeability k expressed in m². However, in the field of hydrology the hydraulic conductivity ($m.s^{-1}$), abbreviated to K_w, is generally used. One can relate hydraulic conductivity K_w to intrinsic permeability k by using Eq. 5.7 described by Claisse (2016).

$$k = \frac{K_w \mu_w}{\rho_w g} \tag{5.7}$$

In continental surface hydrology, liquid water's physical property variations (*e.g.*, volumetric mass ρ_w and dynamic viscosity μ_w) are generally neglected. Thus, intrinsic permeability values obtained from the numerical computations were converted using water's thermodynamic properties at 293.15 K and 1.013 kPa (Chemical Rubber Company and Lide, 2004), considering the following conversion equation (Eq. 5.8):

$$k = 1.0217 \times 10^{-7} K_w \tag{5.8}$$

This method is suitable for samples meeting porosity homogeneity requirements, classified into Type-I samples. However, another method is needed to compensate for Type-II and Type-III sample heterogeneity, as using direct numerical simulations on a complete usable volume is prohibitive in terms of computational resources. The results obtained for hydraulic conductivity REV computations are available in Appendix section 5.A.5. A double-ring infiltrometry test was also conducted during the sampling campaign. For the sake of comparison, hydraulic conductivity values obtained using this method are also shown in Table 5.2.1.

Sample	$\epsilon_{total}(\%)$	$p_{open}(\%)$	**Class**	$\epsilon_X Class(\%)$	$\epsilon_Y Class(\%)$	$\epsilon_Z Class(\%)$
Lichen1.3	83.5	0.9999				
Lichen2.1	88.2	0.9999				
Mound2.6	93.3	0.9999	I	90.6±0.7	90.6±0.6	90.0±4.4
Hollow2.7	96.5	0.9999				
Hollow2.8	94.3	0.9999				
Hollow1.2	74.4	0.9984				
Hollow1.4	53.1	0.9980	II	57.4±1.2	57.5±3.7	56.7±11.8
Peat2.2	49.8	0.9931				
Peat2.3	55.0	0.9938				
Mound1.1	39.1	0.9917				
Mound2.4	57.7	0.9900	III	56.7±1.3	56.5±0.8	56.2±3.2
Mound2.5	72.9	0.9998				

Table 5.2.2 – Computed global porosity (ϵ_{total}), ratio of open porosity (p_{open}), classification (I, II, II) and average planar porosity (%) for each sample obtained using a voxel-counting algorithm.

5.2.4.3 *No REV for hydraulic conductivity: use of PNM*

For the samples that do not exhibit a REV for hydraulic conductivity (Type-II and Type-III samples), the hydraulic conductivity is then studied using a pore network model, generated from the binarized image stacks. Pore network models are based on the structural simplification of a complex pore structure (rocks or reactive porous industrial media, for example) into a two-state model: spheres and throats. This method often uses various image processing and segmentation tools to generate a network of spheres and linking throats, based on an initial tridimensional volume. Introduced by Fatt (1956), pore network modeling was first studied in conjunction with predefined network properties. Then, pore network generation was adapted to model some porous media, scanned with X-ray tomography using image-processing algorithms as accurately as possible (Dong and Blunt, 2009). Various algorithms are used to create the internal pore network structure, such as the *maximal ball* algorithm (Silin and Patzek, 2006). More recently, other algorithms based on the morphological properties of the studied porous media have emerged, such as the *Sub-Network of the Oversegmented Watershed* (SNOW) algorithm (J. T. Gostick, 2017). This alternative algorithm is considered to be computationally efficient, allowing a porous medium to be accurately modeled by numerical imagery (Khan et al., 2020). The SNOW algorithm showed a good fit with the standard *maximal ball* algorithm. Generating a pore network and simulating a flow in it is often cheaper, in terms of computational resources, when compared to direct numerical simulation. However, more complex transfer mechanisms, such as imbibition and drainage, are still in the study phase, and some extensive work on computational optimization has yet to be conducted, specifically on non-user-generated porous media (Maalal et al., 2021).

For each binarized Type-II and Type-III image stack, a direct pore network extraction is conducted using the SNOW algorithm implemented in the *OpenPNM* and *PoreSpy* open-source Python libraries (J. Gostick et al., 2019). Then, a synthetic porosity and a synthetic specific surface area may be computed for the obtained simplified representation of the pore space of the porous medium. Using the implemented Stokes equation solver, a diagonal permeability tensor is retrieved from the generated pore networks, applying the identical boundary conditions based on the method given by (Sadeghi and J. Gostick, 2020). Once again, intrinsic permeability tensors are converted into a hydraulic conductivity tensor using the relation in Eq. 5.8.

In Appendix 5.A.5, a comparative study is described based on Type-I samples between both developed workflows. Then, some clues are given as to whether DNS or PNM is suitable for a given sample.

5.3 RESULTS

5.3.1 *Morphological analysis*

The global-porosity and open-porosity proportion (p_{open}) for each sample is shown in Table 5.2.2, ranging from less than 40% (Mound1.1) to more than 95% (Hollow2.7). On average, lichens are the most porous of the collection, and peat is the least porous. Porosity values are in line with previously obtained data from the literature for the highest porous media of the collection (Yi et al., 2009). However, important variability can be observed for *Sphagnum* samples, gathering minimal and maximal porosity values. Mound mosses have an average porosity of 65.9 ± 22.3%, whereas the average hollow moss sample porosity is 79.6 ± 20.2%. Porosity profiles for each sample are presented in Fig. 5.3.1.

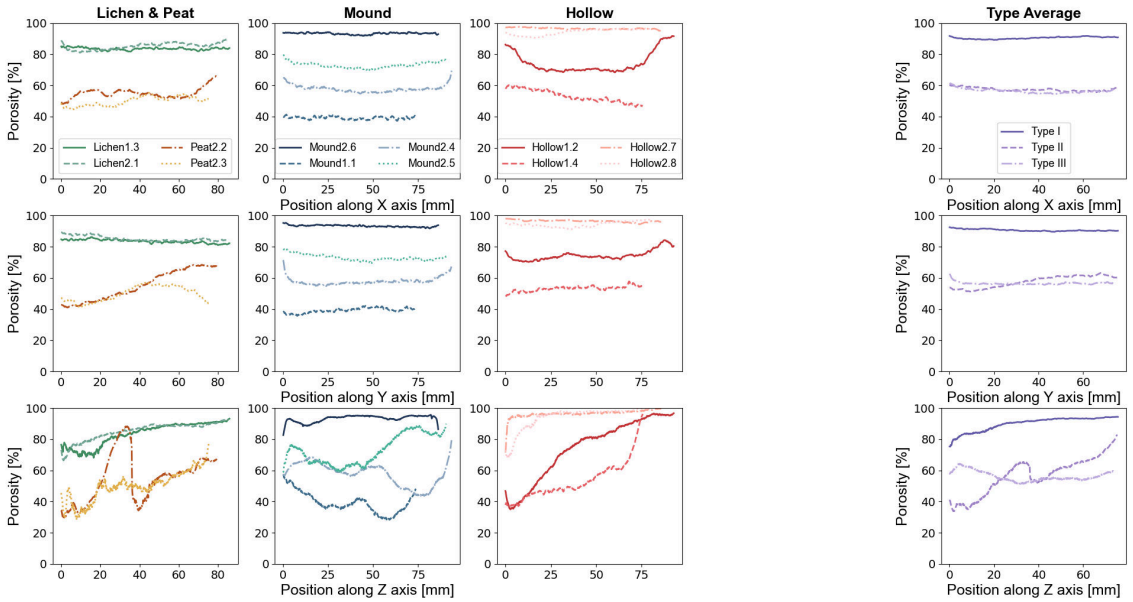

Figure 5.3.1 – Planar porosity plot along the x, y and z axes for moss, lichen and peat samples. An averaged value is computed for each sample type, each color nuance representing each type. *Type I: stable high-porosity profile samples, excluding border effects. Type II: low basal porosity, linearly increasing to the top of the sample. Type III: no specific trend observed in vertical porosity.*

No specific trend can be accessed from the x- and y-axis porosity profiles, and yet variations can be observed on the z axis. Again, three trends can be observed, clustering samples into three groups according to their respective porosity profile trends:

- Type I: stable high-porosity profile samples, excluding border effects (ϵ_{total} >80%): Mound2.6, Hollow2.7, Hollow2.8, Lichen2.1, Lichen1.3;
- Type II: medium to high porosity profile samples associated with a progressive increase from the bottom to the top: Hollow1.2, Hollow1.4, Peat2.2, Peat2.3;

- Type III: medium to low porosity associated with no specific trend porosity profiles: Mound1.1, Mound2.4, Mound2.5.

The Type-I class contains both lichen samples (Lichen2.1, Lichen1.3), whereas Type III only consists of mound *Sphagnum* (Mound1.1, Mound2.4, Mound2.5). The Type-II class contains half of the hollow *Sphagnum* samples as well as both peat samples (Peat2.2, Peat2.3).

Open and connected porosity (p_{open}, Table 5.2.2) represents nearly all the void space volume in each sample. Open porosity ratio values range from 0.99 to 0.9999. Thus, we can assume that, due to the fibrous nature of the studied material, enclosed porosity does not play a major role in the flow dynamics of the studied samples.

Pore size distribution (Fig. 5.3.2) is heterogeneous in each sample, and the sizes are concentrated between 0.01 and 1.00 mm of pore radii. The median pore size varies from 0.23 mm (for peat samples) up to 0.88 mm (for lichen samples).

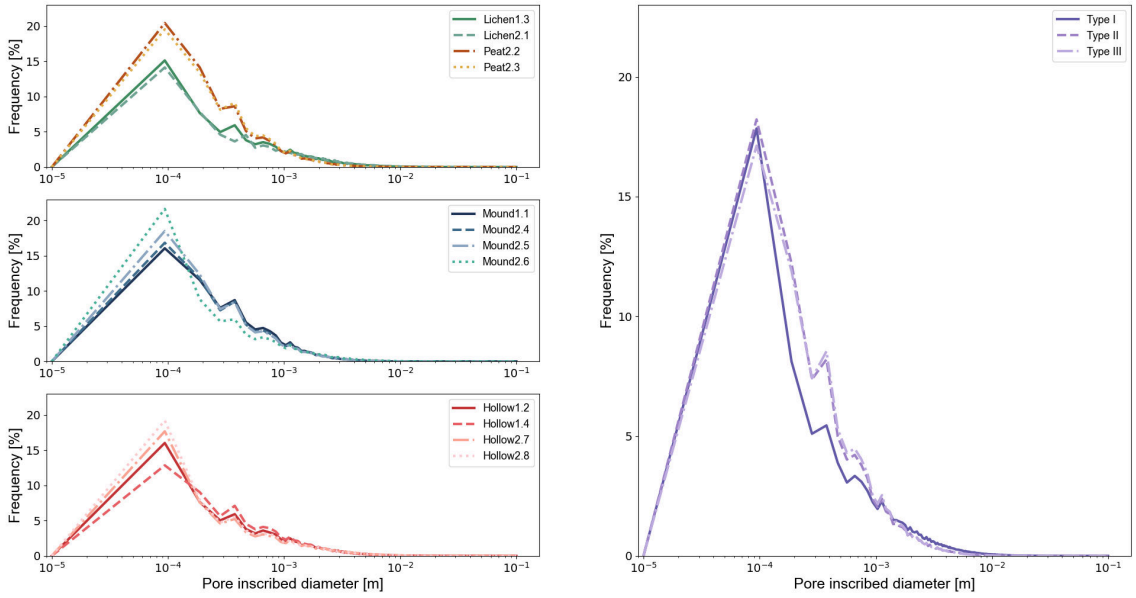

Figure 5.3.2 – Inscribed pore size distribution by classified type using particles' Feret diameter measurement. An averaged value is computed for each sample type, each color nuance representing each type.

Intermediate median pore size values can be found for mound *Sphagnum* samples at average values between 0.34 and 0.70 mm (for hollow *Sphagnum* samples). According to the previous classification, the median pore size for each sample type (I, II and III) is 0.66, 0.42 and 0.33 mm, respectively. While Type-II and Type-III curves differ in bidimensional porosity along z, they share similar global pore size distributions. Type-I samples are distinct from Type-II and Type-III curves. Specific surface area (S_{SA}) values for each sample are shown in Fig. 5.3.3.

Specific surface area values seem to be uneven between each sample type. For instance, low specific surface areas can be observed for some hollow *Sphagnum* samples (2.6×10^{-2}

and 2.9×10^{-2} $m^2.g^{-1}$ for Hollow2.7 and Hollow2.8, respectively). Higher specific area values can be found for one mound of *Sphagnum* (2.0×10^{-2} $m^2.g^{-1}$ for Mound2.4) and for one hollow *Sphagnum* sample ($1.7 \times 10^{-1} m^2.g^{-1}$for Hollow1.2).

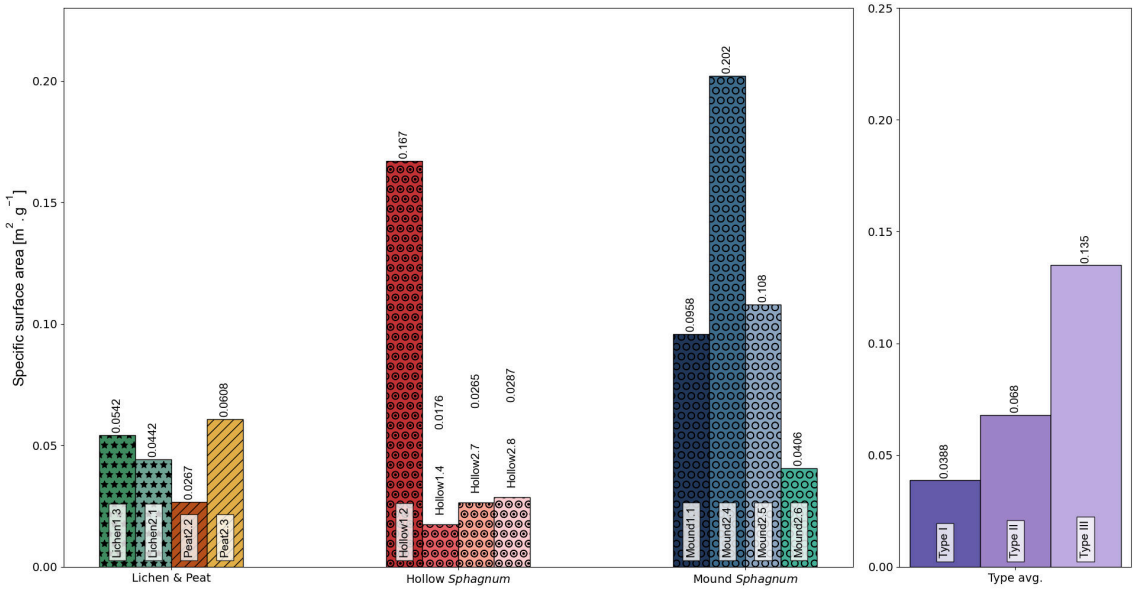

Figure 5.3.3 – Specific surface area ($m^2.g^{-1}$) plots for each sample. Colors refer to each sample type.

5.3.2 *Porosity*

Representative elementary volumes for porosity have been computed when possible. For samples exhibiting a REV, porosity has been computed using Eq. 5.1 applied to the REV. For samples admitting no REV, porosity has still been computed using Eq. 5.1 but applied to the whole usable volume of the sample. A REV retrieval algorithm was applied to all 12 studied samples, although 2 of them (Hollow1.2 and Peat2.2) did not admit a REV. Obtained REV sizes are shown in Table 5.3.1. Some examples of tridimensional visualizations of REVs of porosity are shown in Fig. 5.A.1of Appendix 5.A. Due to the numerous graphs obtained during REV computation, tridimensional porosity plots are available in Fig. 5.A.3 of Appendix 5.A.

Sample	$L_\epsilon^{REV}(mm)$	$\epsilon_{mean}^{REV}(\%)$	Ratio (%)
Hollow1.2	No REV	74.4	100
Hollow1.4	13.4	56.6 ($\pm$4.9)	17.4
Hollow2.7	2.82	96.1 ($\pm$0.3)	3.3
Hollow2.8	7.52	96.3 ($\pm$3.0)	9.4
Lichen1.3	1.88	83.4 ($\pm$3.9)	2.1
Lichen2.1	14.1	86.7 ($\pm$4.9)	16.5
Mound1.1	5.64	38.2 ($\pm$4.9)	7.7
Mound2.4	9.40	62.6 ($\pm$2.7)	10.0
Mound2.5	11.3	67.9 ($\pm$4.9)	12.4
Mound2.6	26.3	93.5 ($\pm$1.0)	30.5
Peat2.2	No REV	49.8	100
Peat2.3	3.76	50.3 ($\pm$3.0)	5.1

Table 5.3.1 – Obtained representative elementary volume based on porosity (REV_ϵ). L_{REV} is the side length of a cubic REV of porosity. ϵ_{mean}^{REV} is the average porosity of a given cubic REV. The ratio represents the volumetric percentage of the sample included in the REV.

REV_ϵ sizes vary from 2 mm to 2 cm, representing 8.0×10^{-3} to 2.19×10^{-6} voxels. Substantial morphological variations are visible, spanning from simple tubular structures (visible in the REV of Hollow2.7) to a complex and fibrous medium (for the Mound2.6 sample, Fig. 5.A.1 of Appendix 5.A). The average porosity obtained for these REVs (shown in Fig. 5.A.3 of Appendix 5.A) varies from 83.4% to 96.0%, which confirms the high porosity factor of these biological media. Computation times for porosity–REV retrieval range from 3 to 6h, using two Intel® Xeon® E5-2680 v2 (2.80 GHz) processors and 128 GB of RAM, using high-performance Python image-processing libraries (IPSDK™). Graphical synthesis of the digital porosity assessment is presented in Fig. 5.3.4.

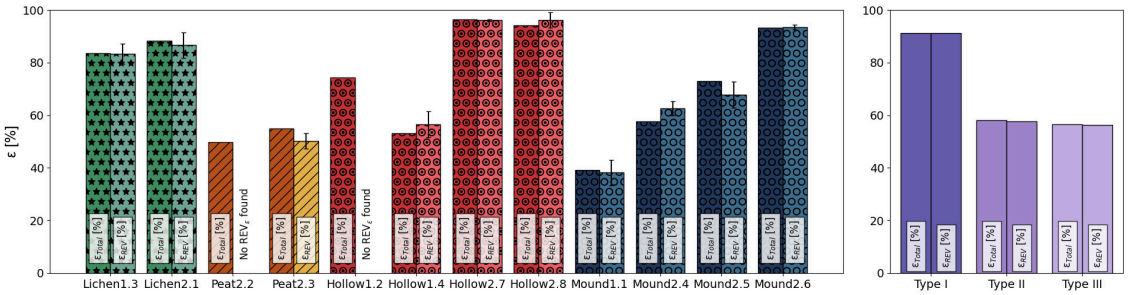

Figure 5.3.4 – Numerical porosity estimations (%) for each sample. An averaged value is computed for each identified sample type (I, II, III) with corresponding color nuances. Peat 2.2 and Hollow1.2 did not admit any REV.

5.3.3 *Hydraulic conductivity*

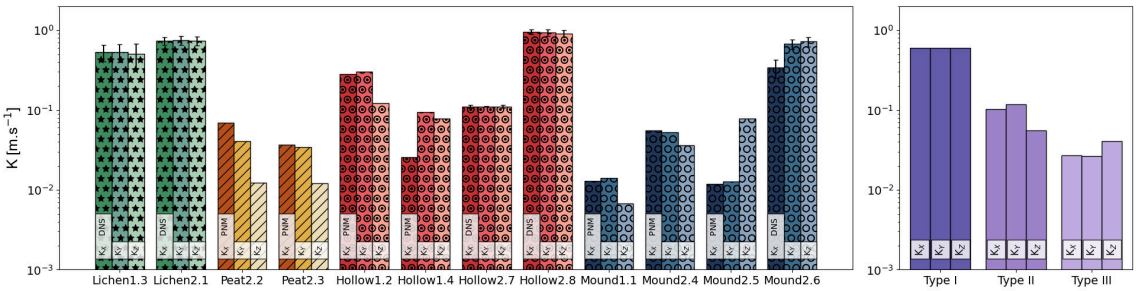

Figure 5.3.5 – Diagonal components of the hydraulic conductivity tensor ($m.s^{-1}$) on the x (K_{xx}), y (K_{yy}) and z axes (K_{zz}) based on DNS on a representative elementary volume of hydraulic conductivity (REV_K) for Type-I samples and with a PNM for Type-II and Type-III samples.

Due to the time and computational resources needed to achieve a careful study of a representative elementary volume of hydraulic conductivity, only Type-I samples were studied by DNS, as they represent the most homogeneous samples of the collection. Computed REVs of the hydraulic conductivity sizes are given in Table 5.3.2. Diagonal hydraulic conductivity tensor components are shown in Fig. 5.3.5, and box plots are available in Appendix section 5.A.5. Computations for the largest sub-sample size (on a 23.5 mm edge) showed higher component hydraulic conductivity values than for the three smaller sizes. This discrepancy can be related to an insufficient computation number for obtaining a good average value, hence the wider statistical spread around the mean value. Moreover, the higher values for the largest studied sizes can also be correlated with heterogeneous hydraulic conductivity behavior, as theoretically shown in Fig. 5.2.2, such as effects related to the existence of macropores. An example of a pressure field obtained on a sub-sample of Hollow2.8 through DNS is shown in Fig. 5.3.6-right.

Sample	$L_K^{REV}(mm)$	$L_{xx}^{REV}(m.s^{-1})$	$L_{yy}^{REV}(m.s^{-1})$	$L_{zz}^{REV}(m.s^{-1})$
Hollow2.7	15.7 (167 vx)	1.1×10^{-1} $\pm 5.0 \times 10^{-3}$	1.1×10^{-1} $\pm 6.07 \times 10^{-4}$	1.1×10^{-1} $\pm 5.1 \times 10^{-3}$
Hollow2.8	15.7 (167 vx)	9.5×10^{-1} $\pm 6.6 \times 10^{-2}$	9.3×10^{-1} $\pm 8.73 \times 10^{-2}$	9.1×10^{-1} $\pm 9.4 \times 10^{-2}$
Lichen1.3	9.4 (100 vx)	5.3×10^{-1} $\pm 1.3 \times 10^{-1}$	5.3×10^{-1} $\pm 1.31 \times 10^{-1}$	5.1×10^{-1} $\pm 1.7 \times 10^{-1}$
Lichen2.1	15.7 (167 vx)	7.4×10^{-1} $\pm 8.3 \times 10^{-2}$	7.5×10^{-1} $\pm 9.46 \times 10^{-3}$	7.4×10^{-1} $\pm 9.6 \times 10^{-2}$
Mound2.6	11.8 (125 vx)	6.8×10^{-1} $\pm 9.0 \times 10^{-2}$	6.7×10^{-1} $\pm 9.1 \times 10^{-2}$	7.2×10^{-1} $\pm 9.9 \times 10^{-2}$

Table 5.3.2 – Diagonal components of the hydraulic conductivity tensor ($m.s^{-1}$) for the studied REV_K for Type-I samples using direct numerical simulations.

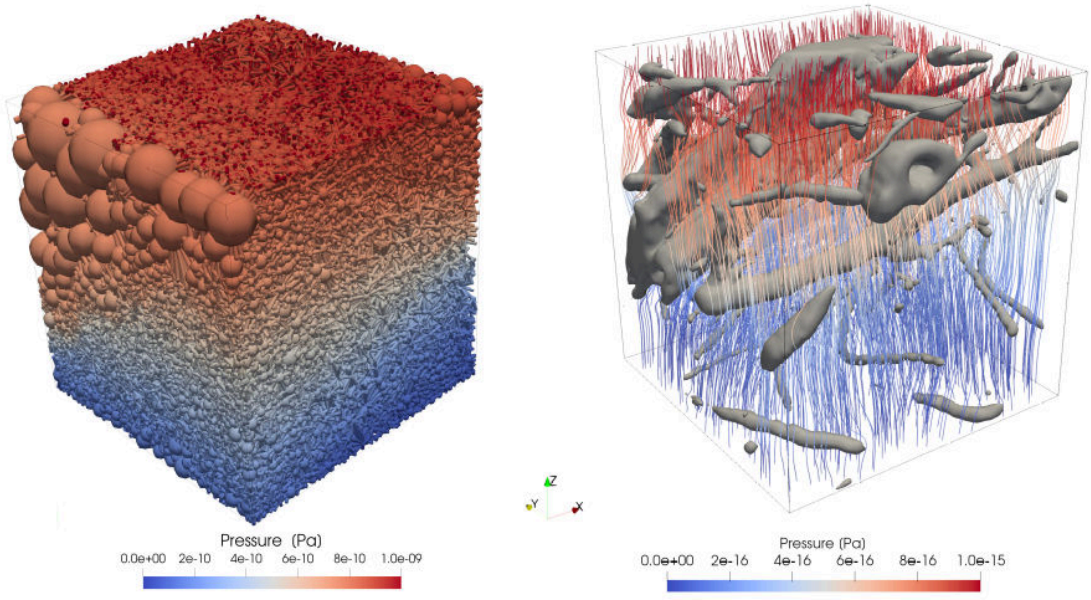

Figure 5.3.6 – *(left)* Pressure field (Pa) after a single-phase flow simulation thorough a pore network model based on a Mound2.5 sample. Spherical pore sizes are represented according to their respective size in the network. (*right*) Pressure field lines (Pa) after a single-phase flow simulation through a sub-sample of the Hollow2.8 sample. The gray mesh corresponds to the isolated biological phase.

For three of the Type-I samples, REV_K length is computed as 15.7 mm, which is the second-largest computed size. Variations in hydraulic conductivity, with respect to study volume reduction, are smaller than those found for porosity, although study points were scarcer in the case of hydraulic conductivity assessment. Lichen1.3 shows the smallest REV_K. It can be seen that the smallest $REV_\epsilon$was also described for Lichen1.3.

Size differences can be seen between REV_ϵ and REV_K, up to 5 times larger for Lichen1.3 and half the REV_ϵ for Mound2.6. This seems to show that the representative elementary volume found for porosity cannot accurately describe properties such as hydraulic conductivity. This is often the case, as porosity REV is smaller than the REVs defined for other properties (D. Zhang et al., 2000; Costanza-Robinson et al., 2011).
Numerical estimations of hydraulic conductivity are presented in Fig. 5.3.5. For each sample of Type I, the axial components of the hydraulic conductivity tensor are given, based on the representative elementary volume of hydraulic conductivity. For Type-II and Type-III samples, hydraulic conductivity estimates are given based on pore network modeling. An example of pressure field computation is shown on sample Mound2.5 in Fig. 5.3.6 on the left. Using a pore network allows the estimation of properties in a model based on the whole sample. The use of a pore network is an affordable alternative to direct numerical simulations at the cost of accuracy.
The values obtained vary from 1.1×10^{-1} to 9.5×10^{-1} $m.s^{-1}$ for Type-I samples and from $7.8 \times 10^{-3}$to 4.8×10^{-1} $m.s^{-1}$ for Type-II and Type-III samples. Type-I samples can be assumed to be highly water-conductive biological media. Mean hydraulic conductivity decreases when the computed region size becomes smaller, for each direction and each sample (Appendix section 5.A.5). *In-situ* measurements, conducted by infiltration (Table 5.2.1), give an average of 10^{-5} $m.s^{-1}$, which is on the same order of magnitude as previously published field measurements (Crockett et al., 2016) and computed values (McCarter and J. Price, 2014). Analogous values for vertical hydraulic conductivity have been found in the literature at $k_{zz} \approx 10^{-5}$ $m.s^{-1}$ (Päivänen, 1973; Crockett et al., 2016; Golubev, McCarter, et al., 2021). However, other studies showed results of a different order of magnitude for *Sphagnum* samples, with values under 10^{-4} $m.s^{-1}$ (Hamamoto et al., 2016). These differences could be explained by the experimental method used to retrieve hydraulic conductivity as well as *Sphagnum* bog oscillation occurring during sampling (mire breathing) (Strack et al., 2009; Golubev and Whittington, 2018; Howie and Hebda, 2018), which is going to be discussed in the next part.

5.4 DISCUSSION

Digital assessments of the morphological and hydraulic properties of *Sphagnum* and lichens of the Western Siberian Lowlands presented in this work suggest extremely porous, connected media with high specific surfaces and high hydraulic conductivities. These results are in line with the biogeochemical observations of L. Shirokova et al. (2021), demonstrating the overwhelming role of *Sphagnum* mosses in organic carbon, nutrient and inorganic solute fluxes in the Western Siberian Lowlands. Nonetheless, discrepancies between the numerical results presented in this work (Figs. 5.3.4 and 5.3.5) and previously published measurements of the hydraulic properties of *Sphagnum* are noteworthy (Table 5.2.1).
Weaker but still sizable differences can be seen between the results given by both of

the numerical methods used here for the estimation of hydraulic conductivity on the same sample, namely, DNS and PNM. This last methodological point is discussed in Appendix 5.A.5, where a comparative validation is performed between DNS and PNM on homogeneous samples (Type I).

5.4.1 *Numerical reconstruction after scanning*

Due to technical limitations, scanning devices have a minimal resolution that causes a loss of information, acting as a threshold. In this study, minimal resolution fluctuated between 88 and 94 µm.voxel^{-1}, meaning that two elements of this size could not be distinguished. In our study, technically unreachable porosity (porosity that is smaller than the minimal scanning resolution) is assumed to play a negligible role in transfers through a saturated medium, reacting as an enclosed porosity. Pre-processing algorithms (especially binarization) can cause information loss due to the arbitrary categorization of each voxel. This erroneous description can be seen for small elements (such as *Sphagnum* leaves) which shrink them. Mesh generation may also bring some additional "over-erosion" that helps flows inside a sample. These impacts could be studied by reducing scanning resolution, albeit not available at the time of the scans. However, hydraulic conductivity overestimation in DNS that could be related to these pre-processing effects is likely to be negligible. Indeed, the high porosities encountered and the preferential flow paths that occur in the largest pores (macropores) predominate over enclosed pore dynamics. This might not be the case for unsaturated hydraulic property assessments.

5.4.2 *Numerical results vs. field experiments: porosity and specific surface*

As described in previous sections of this study, the samples collected are considerably porous. Porosity values are in line with past results found in the literature (Yi et al., 2009; Kämäräinen et al., 2018), with porosities above 90% for some of the samples. Interestingly, a volumetric digital-specific surface can be well linked with the porosity of complete samples as well as the average porosities found for representative elementary volumes. A clustering can be seen for the three studied sample types (Figs. 5.4.1), although mathematical relations between specific surface and porosity are not well defined for such porous media. The specific surface values obtained are of the same magnitude as previous values obtained for other natural moss and lichen species using geometrical calculations ($1.4 \times 10^{-1} m^2.g^{-1}$for *Hypnum cupressiforme* (Hedw., 1801) moss and $2.4 \times 10^{-3} m^2.g^{-1}$ for *Pseudevernia furfuracea* ((L.) Zopf, 1903) lichen in Adamo et al. (2007). These values are still notably lower than the values obtained using the B.E.T. method of N_2 adsorption isotherms ($1.1 \times 10^{1} m^2.g^{-1}$ for artificially grown *Sphagnum denticulatum* (Brid., 1926) in Gonzalez et al., 2016). As discussed in section 5.4.1, a lack of micropores could explain

the observed discrepancies (1 to 2 orders of magnitude) between calculated geometry and B.E.T.

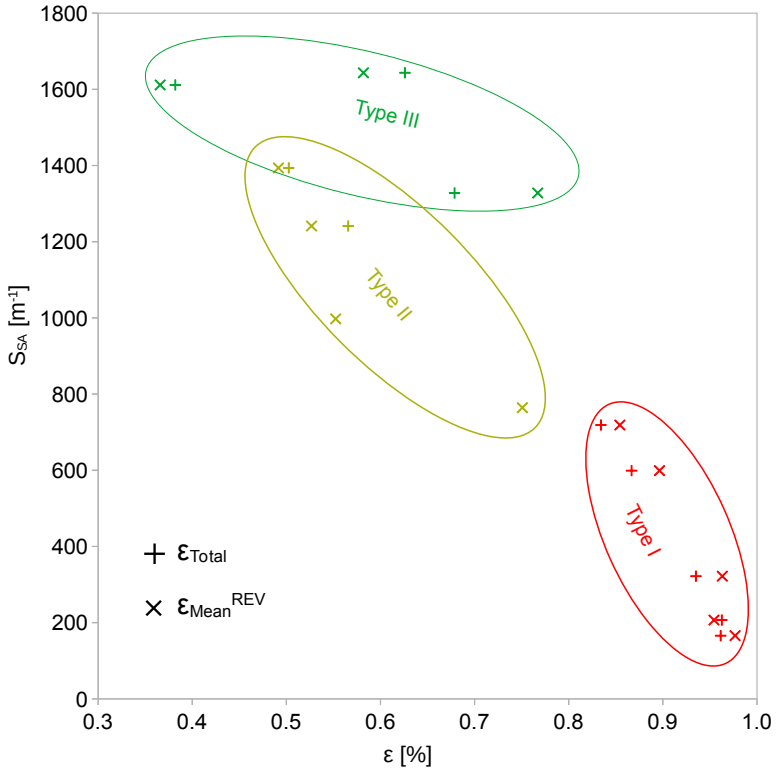

Figure 5.4.1 – Specific surface (m^{-1}) as a function of total porosity REV_{ϵ}^{Total}(%) and representative elementary averaged porosity ϵ_{mean} (%).

5.4.3 *Numerical results vs. field experiments: hydraulic conductivity*

In Appendix 5.A.5, a comparison between direct numerical simulations and pore network modeling is made showing that pore network modeling is suitable for bypassing the heterogeneity issues observed in our samples. Indeed, the obtained porosity values with PNM are in a 5% threshold compared to voxel-counting results (Eq. 5.1). The hydraulic conductivities computed by PNM and DNS are more contrasted, with 1 to 2 orders of magnitude of difference. One should bear in mind that the range of hydraulic conductivity of natural porous media is huge, with up to 15 orders of magnitude between coarse gravel (10^{-1} $m.s^{-1}$) and unweathered shale (10^{-15} $m.s^{-1}$). Besides this, it is logical that the simplifications involved in the PNM method result in information loss compared to the DNS method. On the other hand, computational time savings (by using the PNM method) are huge (counted in tens of days for DNS and hours for PNM). In some cases

(*e.g.*, samples of Types II and III), DNS is simply not possible with the current regional-scale supercomputing means.
The obtained numerical hydraulic conductivities tend to show high and relatively isotropic hydraulic conductivity tensor values. Hydraulic conductivities found using DNS are sizably higher than previous values found in the literature using field percolation (Table 5.2.1), often by up to 1 to 3 orders of magnitude. The hydraulic conductivities found using pore network modeling seem to be more in line with the values in Table 5.2.1 as well as the field experiment results shown in Table 5.4.1. Nevertheless, it should be kept in mind that the results obtained by this method are less structurally accurate that those obtained from DNS, since they rely on a simplified description of the pore structure. Some clues can be advanced to explain this discrepancy, the first being the impact of numerical reconstruction routines and mesh generation procedures (discussed in section 5.4.1), the latter being moss compression during field experiments.

Sample	Date	$K_{field}(m.s^{-1})$
Hollow1.2	26 July 2018	1.8×10^{-4}
Hollow2.7	27 July 2018	9.3×10^{-5}
Hollow2.8	27 July 2018	5.6×10^{-5}
Lichen2.1	27 July 2018	9.9×10^{-4}
Mound1.1	26 July 2018	1.8×10^{-4}
Mound2.4	27 July 2018	$> 10^{-4}$
Mound2.6	27 July 2018	$> 10^{-4}$

Table 5.4.1 – Hydraulic conductivity values ($m.s^{-1}$) obtained using a double-ring infiltrometer during the sampling campaign.

Our digital, constant-head permeameter experiments were conducted in a fully saturated medium. Technically unreachable porosity (porosity that is smaller than the minimal scanning resolution) is assumed to play a negligible role in transfers through a saturated medium, reacting as enclosed porosity. In the case of low-permeability porous media, such sub-resolution porosity may affect flow (Soulaine et al., 2016).
However, in the case of highly porous and connected media like mosses and lichens, the effects related to sub-resolution porosity are assumed to be low when compared to the effects of the large macropores, which has been shown by Baird (1997). It should also be noted that most of the porosity is opened and connected in our case.
However, moss and lichen samples are compressible Golubev and Whittington (2018), Howie and Hebda (2018), and J. S. Price, Whittington, et al. (2008). Field percolation experiments induce a sizeable and rapid mass imbalance on this bryophytic cover, compacting the pore space more than would occur under natural rainfall conditions.

This might notably affect flow patterns in macropores and explain the lower hydraulic conductivities found in field experiments. Indeed, some clues are given with the results of Weber et al. (2017) on hydraulic conductivity variations according to water saturation. Therefore, the numerical hydraulic conductivity assessments carried out in this study enable property quantification of the medium without perturbation, such as compression of the biological pore structure, which is not possible in field experiments.

5.5 CONCLUSIONS AND PERSPECTIVES

A numerical assessment of morphological and hydraulic properties was carried out on digital X-CT reconstructions of samples of *Sphagnum* moss, lichen and peat from the Western Siberian Lowlands' bryophytic cover. This porous-medium-centered approach confirmed the high porosities (from 70% to 95% for most samples) already found in previous studies involving experimental measurements. Hydraulic conductivity estimation was conducted using direct numerical simulations for Type-I samples and pore network modeling for Type-II and Type-III samples, both fluctuating around 10^{-1} $m.s^{-1}$. Indeed, both methods used in this study converge to classify macroscopic lichen, *Sphagnum* moss and peat as being considerably porous and pervious biological media. The hydraulic conductivity tensor shows isotropic horizontal components; however, some differences can be seen, particularly in the vertical component. Both methods reach higher values than seen before in the literature. This may have been caused by interfering phenomena, such as moss compressibility, occurring during field experiments.
The methods developed for this application show that a numerical work scheme based on image processing allows retrieval of the morphological properties of any variety of sample. Using such a method permits a nearly unlimited number of property assessments of the same sample, whereas an experimental work scheme requires many samples. Numerical methods enable a qualitative classification of the overall homogeneity of a sample, which is not easily doable using solely experimental methods. Image processing seems to be a satisfactory method, provided that the studied sample is sufficiently homogeneous for the studied property. For heterogeneous samples, image processing is not optimal. However, in the absence of another method, pore network modeling allows us to obtain some information on the studied property which is close to the one found for the homogeneous samples using image processing.

These results provide firm ground for quantitative hydrological modeling of the bryophytic cover in permafrost-dominated peatland catchments, which is crucially important for a better understanding of the global climate change impacts on arctic areas. Using numerical methods potentially enables the assessment of moss and lichen's structural hydraulic conductivity without disturbance by any biological or physical phenomena. Therefore, the porous-medium approaches developed throughout this study led to unprecedented

qualitative and quantitative descriptions of such peculiar, highly porous biological media.

These physical properties can then be used as input parameters to describe ground vegetation layers in high-resolution hydrological models of arctic hydrosystems and extensively refine simulations of this critical compartment of boreal continental surfaces. For example, they will be used in further modeling studies of permafrost under climate change at the Khanymey Research Station in the framework of the HiPerBorea project (hiperborea.omp.eu). Further studies are needed to assess variable water content consequences for peat and vegetation pore structure. Indeed, water content is one of the main drivers controlling effective transport properties, such as unsaturated flow, volume change and thermal conductivity.

APPENDIX

5.A APPENDICES OF CHAPTER 5.

5.A.1 *Global characteristics*

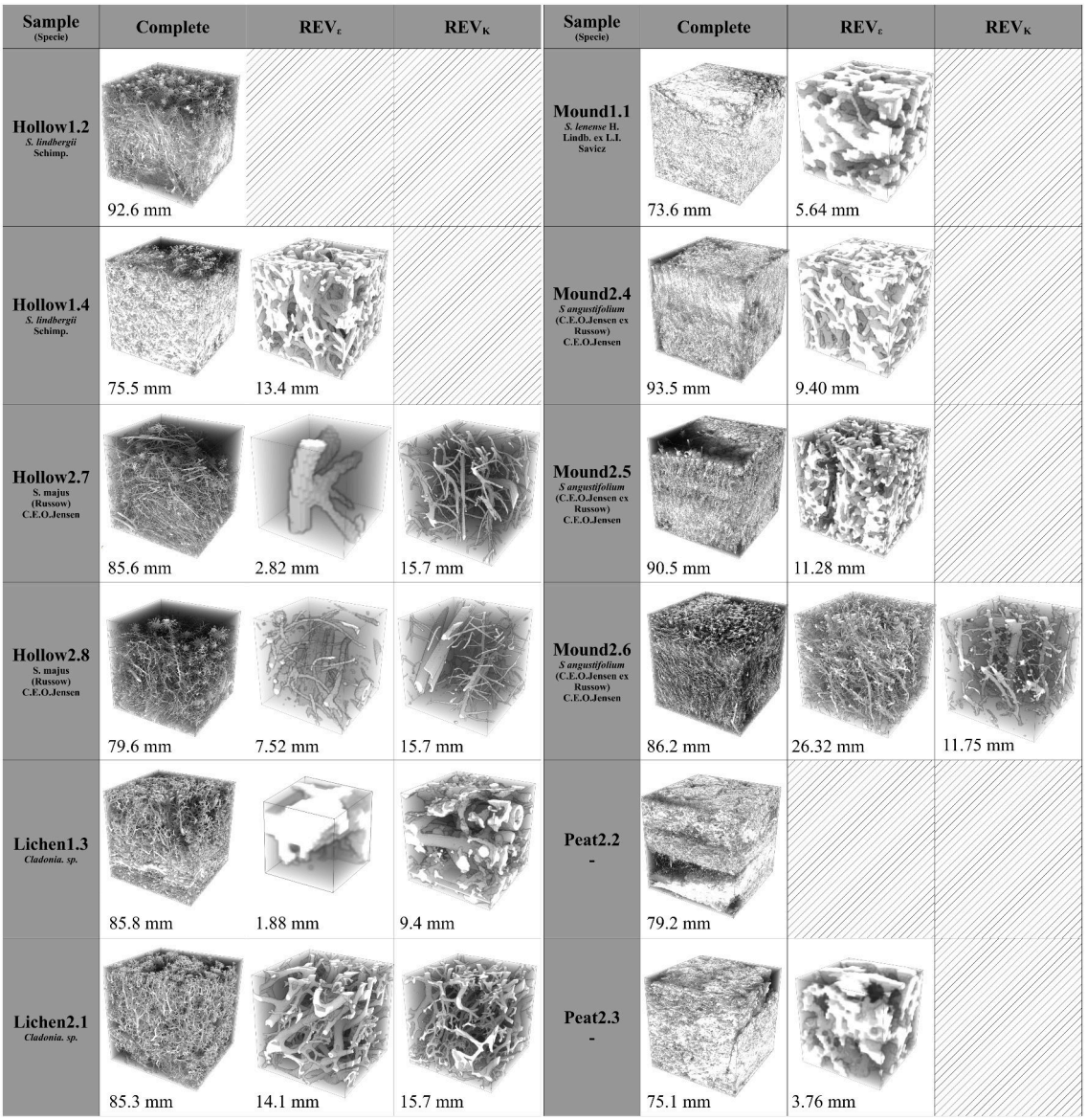

Figure 5.A.1 – Global characteristics of collected samples' Usable Volume, numerical reconstructions and examples of Representative Elementary Volumes of Porosity and Hydraulic conductivity. Species were identified according to the morphological descriptions given in Volkova et al. (2018).

5.A.2 *Initial and boundary conditions*

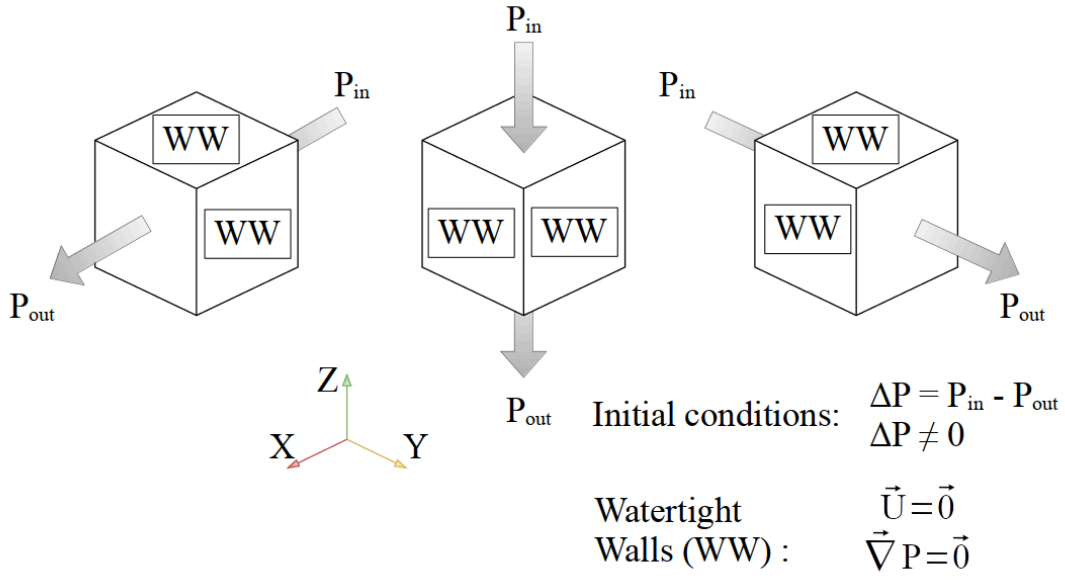

Figure 5.A.2 – Initial and boundary conditions used for the Direct Numerical Simulation on sub-volumes of samples and pore network models.

5.A.3 *Representative Elementary Volume of porosity results*

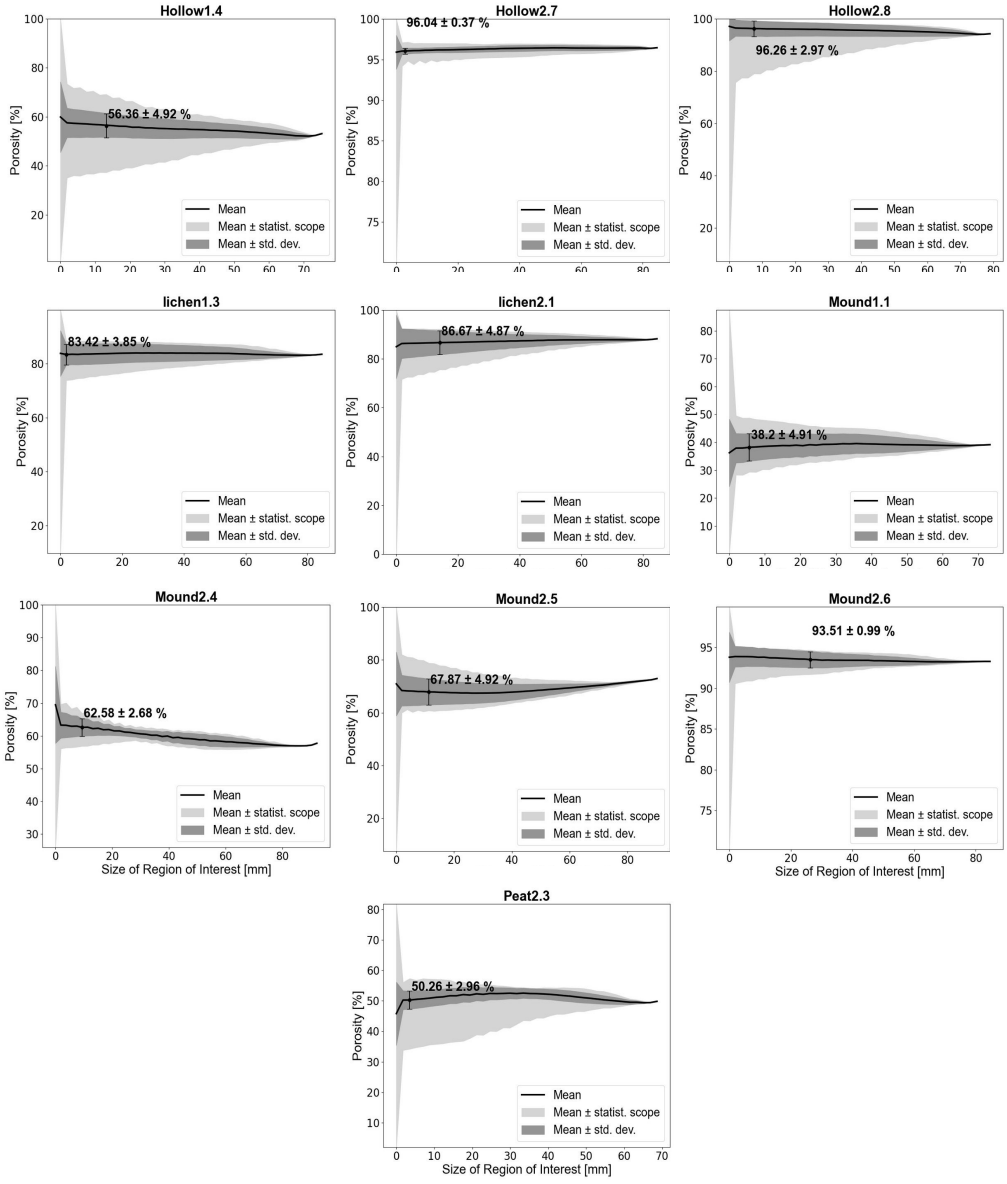

Figure 5.A.3 – Overview of results of Representative Elementary Volumes of porosity for 10 of 12 samples (2 of them did not converge to a solution). Convergence result for each sample is shown with a point and an error bar.

5.A.4 *Representative Elementary Volume of hydraulic conductivity results*

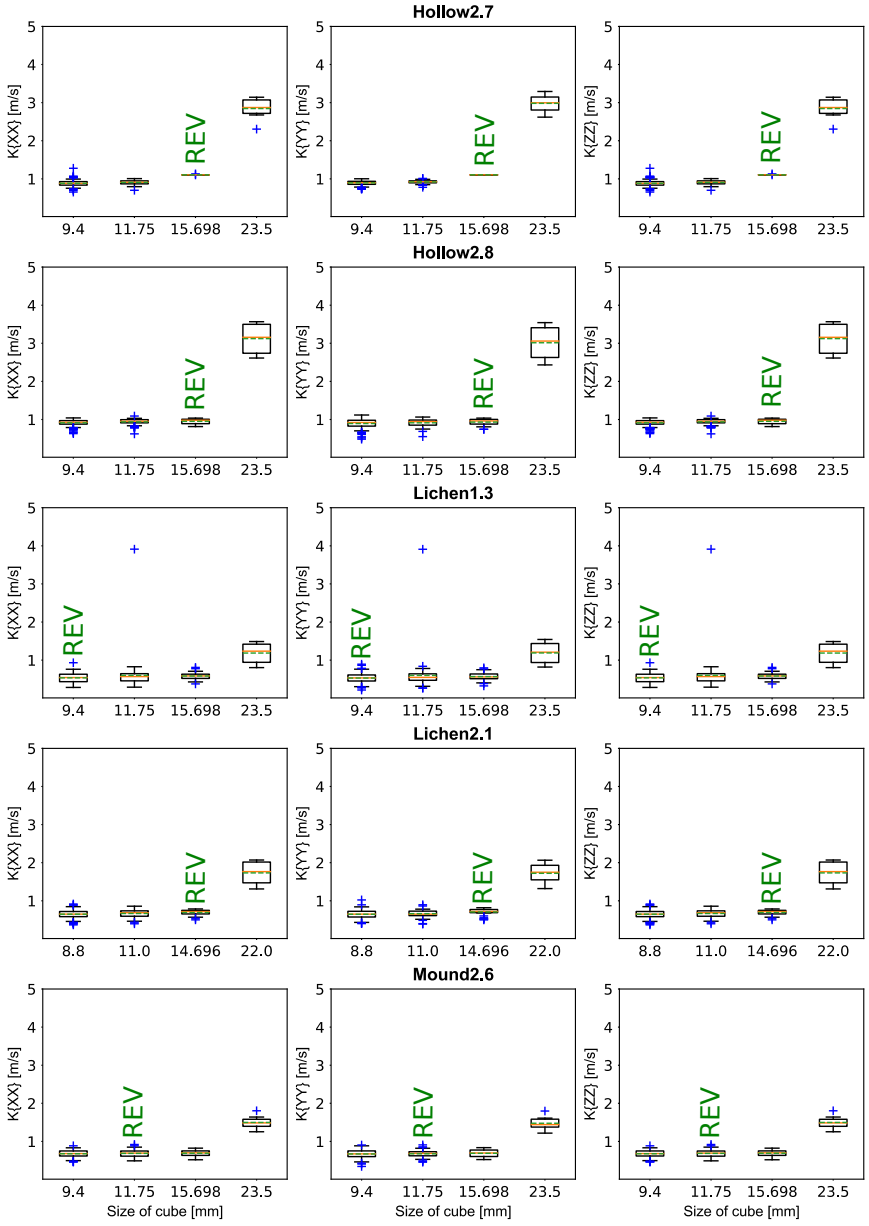

Figure 5.A.4 – Overview of results of Representative Elementary Volumes of hydraulic conductivity for Type I samples. Each size matching the minimal standard deviation of diagonal hydraulic conductivity tensor is marked with a "REV" sign.

5.A.5 *Comparison between Direct Numerical Simulations and Pore Network Modeling for homogeneous samples*

As a reminder, volume averaging technique requires a sufficient homogeneity on a given property to function properly. In our study, sample of the samples could not be considered as sufficiently homogeneous do to their peculiar structure. Instead, Pore Network Models (PNMs) are generated for these samples and properties are then assessed through this proxy. In this supporting information, a short validation of pore-network against Direct Numerical Simulation is done on homogeneous samples. Then, some details are given on heterogeneous samples' pore network models. This study concludes on clues for choosing either Direct Numerical Simulations or Pore Network Models as a significant and effective property assessment technique.

5.A.5.1 *Pore Network validation on morphologically-homogeneous samples*

In the main article, we showed that volume averaging methods such as finding a Representative Elementary Volume for each sample is possible if the latter is sufficiently homogeneous upon the given property. For heterogeneous samples, finding a REV does not match the required statistical strength to be considered as a continuum of both microscopic and macroscopic. To counterfeit the heterogeneities upon porosity for Type II and Type III samples, we decided to generate a pore network made of interconnected throats and spheres. Then, morphological properties could be then retrieved based on computations directly done on the whole pore network.
To validate this method, the same procedure used for Type II and Type III samples is retroactively applied on Type I samples. Table 5.A.1 shows results of a morphological analysis, overall pore network porosity and specific surface area. Then, a ratio is computed to compare respectively porosity and specific surface area obtained from image processing and from pore networks.

Sample	σ_{S-T} $(-)$	d_{Sph} (cm^{-3})	d_{Thr} (cm^{-3})	ϵ^{PNM} $(\%)$	S_{SA}^{PNM} $(m^2.m^{-3})$	$\sigma(\epsilon)$ $(-)$	$\sigma(S_{SA})$ $(-)$
Lichen 1.3 (I)	4.2	8.3×10^1	3.5×10^2	84.9	2.7×10^3	1.02	3.7
Lichen 2.1 (I)	4.4	7.4×10^1	3.3×10^2	89.7	2.7×10^3	1.04	4.5
Mound 2.6 (I)	5.4	1.2×10^1	5.9×10^2	94.5	3.5×10^3	1.01	10.9
Hollow 2.7 (I)	5.4	5.0×10^1	2.7×10^2	98.1	2.5×10^3	1.02	15
Hollow 2.8 (I)	5.2	5.4×10^1	2.8×10^2	96.0	2.6×10^3	0.998	13

Table 5.A.1 – Morphological properties of Type I based on a pore network model (σ_{S-T} : Ratio between spherical pores and throats; d_{Sph} : Spherical pore density; d_{Thr}: Throat pore density; σ_ϵ): Ratio between image processing-based porosity and pore network-based porosity; σ_{SSA}: Ratio between image processing-based specific surface area and pore network-based specific surface area).

Then, a single-phase flow simulation is made on the whole pore networks in the same way as for Type II and Type III samples. Results for diagonal components of the hydraulic conductivity tensor are available in Table 5.A.2.

Sample	$K_{xx}^{PNM}\,(m.s^{-1})$	$K_{yy}^{PNM}\,(m.s^{-1})$	$K_{zz}^{PNM}\,(m.s^{-1})$
Hollow2.7	4.7×10^{-1}	4.7×10^{-1}	3.0×10^{-1}
Hollow2.8	4.7×10^{-1}	4.6×10^{-1}	2.7×10^{-1}
Lichen1.3	7.7×10^{-3}	6.9×10^{-3}	2.7×10^{-3}
Lichen2.1	3.4×10^{-1}	3.4×10^{-1}	2.8×10^{-1}
Mound2.6	3.4×10^{-1}	3.4×10^{-1}	3.0×10^{-1}

Table 5.A.2 – Diagonal components of the hydraulic conductivity tensor (in $m.s^{-1}$) for the studied type I samples using Pore Network Modeling.

To compare hydraulic conductivity results obtained with both methods, a comparative ratio is computed according to the equation given in Eq. 5.9. Results of these computations are shown in Table 5.A.3.

$$\sigma(K_{ii}) = \frac{K_{ii}(PNM)}{K_{ii}(DNS_{REV})} \tag{5.9}$$

Sample	$\sigma(K_{xx})\,(-)$	$\sigma(K_{yy})\,(-)$	$\sigma(K_{zz})\,(-)$
Hollow2.7	10^{-2}	10^{-2}	10^{-2}
Hollow2.8	4.7×10^{-1}	4.6×10^{-1}	3.9×10^{-1}
Lichen1.3	4.9×10^{-1}	5.0×10^{-1}	4.2×10^{-1}
Lichen2.1	4.3	4.26	2.8
Mound2.6	5.0×10^{-1}	4.9×10^{-1}	2.9×10^{-1}

Table 5.A.3 – Comparison between diagonal components of the hydraulic conductivity tensor (in $m.s^{-1}$) for the studied type I samples using Direct Numerical Simulation and Pore Network Modeling.

A comparison of Pore Size Distribution of Type I samples between image processing and pore network is available in Fig. 5.A.5.

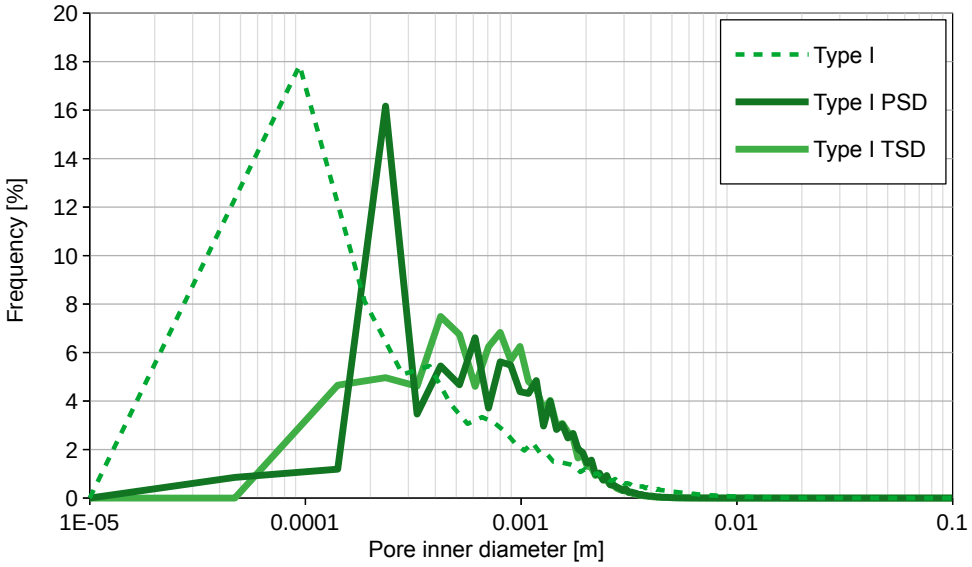

Figure 5.A.5 – Average Pore Size Distribution (PSD) and Throat Size Distribution (TSD) of Type I sample's pore networks. The pore size distribution obtained using image processing is shown as a comparison.

PSD and TSD are beginning from smaller sizes and seem more abrupt than pore size distribution obtained by traditional image processing, although median size value is relatively consistent between both methods (between 0.4 and 0.9 mm for the generated pore networks). Most differences appear to be more dependent of PSD and TSD statistical spreads than raw pore sizes. Indeed, pore size distribution computed for Direct Numerical Simulation seems homogeneous if compared to PSD and TSD. Nonetheless, specific surface is always higher using a pore network compared with traditional image processing methods, from one to 15 times higher. This difference could be explained by the fact that the Pore and Throat Size Distributions obtained using Pore Network Modeling have smaller pore diameters than for those obtained using image processing, thus multiplying specific surface.

In terms of morphological properties, comparing Direct Numerical Simulations (DNS) and Pore Network Modeling (PNM) shows that PNM results are in a 5% threshold with DNS results for porosity. However, this is not the case for specific surface area. In this case, PNM results have bigger specific surface areas, up to 15 times higher than results obtained with DNS for Hollow2.7. In terms of hydraulic conductivity, diagonal components are in a one order of magnitude range except for Hollow2.7 sample with PNM results 100 times lower than those found using DNS. This span is still smaller than the observed hydraulic conductivity spread in relation with water saturation Weber et al. (2017). It is then possible to conclude that Pore Network Modeling seems to be a valid methodology to bypass heterogeneity problems in porous media.

The case of Hollow2.7 has to be related to the fact this sample is the most porous of the studied sample ($\epsilon > 95\%$). During pore-network generation, image processing artifacts can be mistakenly interpreted causing the split of a throat into many other pores.

5.A.5.2 *Morphological description of heterogeneous samples-based pore networks*

Parallelly to image processing and Direct Numerical Simulations,Pore Network Models (PNMs) are generated from the binarized image stacks. PNMs of type II and III samples are described in detail because they will be used to compute single-phase flow to assess hydraulic conductivity for such heterogeneous samples. Using Direct Numerical Simulations on a complete sample is computationally inefficient and would not lead to sufficient significance. Some information about key morphological values for pore networks of Type II and Type III samples is available in Table 5.A.4.

Sample	$\sigma_{S-T}\,(-)$	$d_{Sph}\,(cm^{-3})$	$d_{Thr}\,(cm^{-3})$	$S_{SA}^{PNM}\,(m^2.m^{-3})$	$\sigma(S_{SA})\,(-)$
Hollow1.2 (II)	4.2	7.4×10^1	3.1×10^2	2.4×10^3	3.18
Hollow1.4 (II)	3.1	1.2×10^2	3.2×10^2	2.0×10^3	1.58
Peat2.2 (II)	3.6	7.4×10^1	2.6×10^2	2.5×10^3	2.46
Peat2.3 (II)	3.1	7.8×10^1	2.4×10^2	2.3×10^3	1.63
Mound1.1 (III)	2.9	7.1×10^1	2.0×10^2	1.9×10^3	1.20
Mound2.4 (III)	4.1	1.0×10^1	4.2×10^2	2.5×10^3	1.51
Mound2.5 (III)	4.8	8.6×10^1	4.1×10^2	3.0×10^3	2.28

Table 5.A.4 – Morphological information on Type II and III sample-based Pore Network Models (PNM). (σ_{S-T}: Ratio between spherical pores and throats; d_{Sph}: Spherical pore density; d_{Thr}: Throat pore density; σ_ϵ): Ratio between image processing-based porosity and pore network-based porosity; σ_{SSA}): Ratio between image processing-based specific surface area and pore network-based specific surface area).

Average Pore Size Distribution (PSD) and Throat Size Distribution (TSD) for Type II and Type III are shown in Fig. 5.A.6.

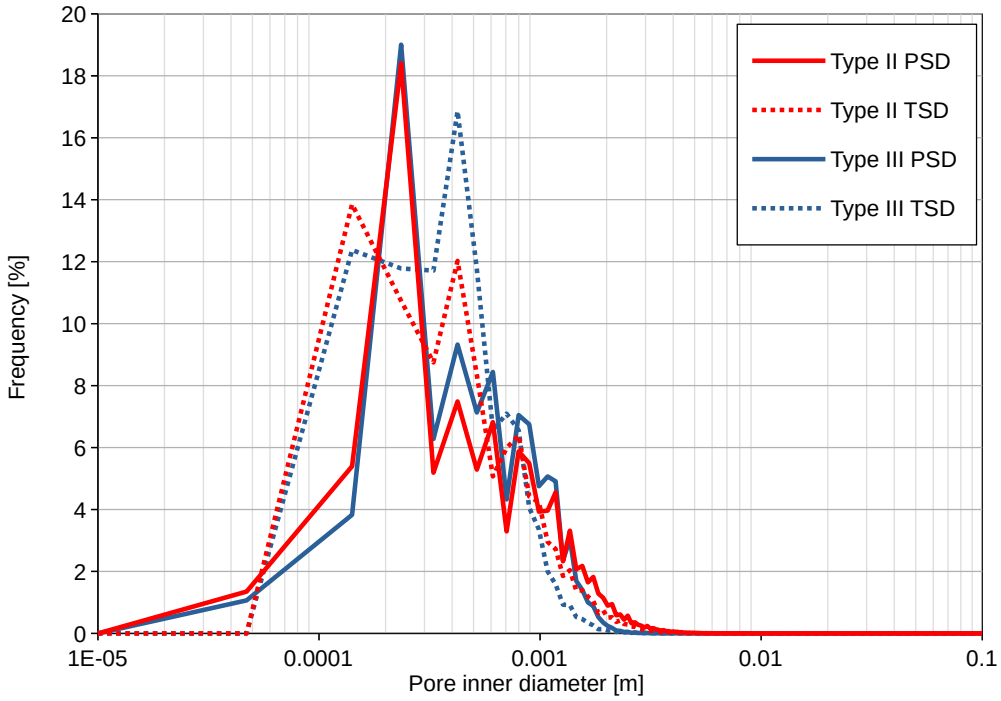

Figure 5.A.6 – Average Pore Size Distribution (PSD) and Throat Size Distribution (TSD) for Type II and Type III samples based on generated pore network model.

Below this size, Type II shows higher frequencies whereas bigger pores are more frequent for Type III. TSD is closer to a bimodal distribution with a first peak at 1.05×10^{-5} m and 1.3×10^{-5} m of pore radii. The first peak is predominant for Type III, the latter for Type II samples. PSD for both Type II and III are equivalent in terms of generic dynamic, with a frequency peak at 1.15×10^{-5} m of pore radii.

There are from 2.81 to 5.39 times more linking throats than spherical pores. Pore and throat densities fluctuate between 50.1 pores.cm^{-2} and 108.8 pores.cm^{-2} and between 201.0 throats.cm^{-2} and 587.6 throats.cm^{-2}. These values are independent of sample's nature or classified type, with an overall mean of 4.18 more throats than spherical pores. Therefore, we can assume that spherical pores have mainly four-neighbor connectivity in the generated models. Specific surface area obtained using PNM is always bigger than those obtained by image processing. Biggest deviations are shown by Hollow1.2 and Peat2.2 samples.

5.A.5.3 *Direct Numerical Simulations and Pore Network Modeling: which one to choose?*

One of the least corresponding sample is Hollow2.7, with specific surface area and hydraulic conductivity being respectively 15 times higher and 100 times lower. One explanation to this could be that high porosity ($\epsilon > 90\%$) is a caveat for pore network generation algorithm. Small artifacts in the base image stack such as isolated pixels could lead to an excessive segmentation of the pore space inducing a smaller pore

or throat than reality, thus increasing tortuosity. Some correlations between tortuosity and permeability (and extensively hydraulic conductivity) are assessed in the literature (Koponen et al., 1996). Increasing the tortuosity as well as the connectivity causes the decrease of permeability (and hydraulic conductivity). In the same way, supernumerary throats could also lead to a more fragmented flow path than what is observed in Direct Numerical Simulation.

When porosity is not extreme, PNM seems to enable the reach of effective morphological and hydraulic properties, confirming the possibility to use it on Type II and Type III samples. However, these sample lack of a comparison tool, making the results lower class than those found for Type I samples. Nonetheless, emphasis can be put on the fast processing abilities of PNM to give an efficient estimates of effective properties. Results are obtained in an hour time frame and even less with recent code parallelism upgrades made in *PoreSpy* and *OpenPNM*. In the other hand, DNS requires several days to complete a full hydraulic conductivity study.

Yet, image processing used in this study could lead to an excessive smoothing, eliminating under-resolution pores (not resolvable due to tomograph's own minimal resolution, here 94 μm) that play an important role in flow dynamics. It would be possible to assume in this case that Direct Numerical Simulation coupled with Representative Elementary Volumes could allow the assessment of phenomena occurring at higher pore sizes, the interplant void space (Baird, 1997). Alternatively, pore network models could be better descriptors for the middle pore size fractions, which corresponds to the space between each *Sphagnum* leaves (intraplant void space, as described by J. S. Price and Whittington (2010) and Weber et al. (2017)).

6

THERMAL PROPERTIES

6.1 LITERATURE REVIEW ON THERMAL PROPERTIES ASSESSMENTS

Contrary to hydraulic property assessment, the determination of thermal properties is difficult to conduct numerically if the properties of the studied material are not well known. Indeed, thermal properties are significantly dependent on the molecular structure of the material, which is not easy to model. Fundamentals of heat transfers in porous media are deeply studied in Bird et al. (2002) and in Kaviany (1995). A brief recall on the standard heat equation has been made in section 2.3.2.2. Then, a synthesis of the thermal properties measurements available in the literature will be shown.

6.1.1 *Thermal properties quantification techniques*

6.1.1.1 *Review of available techniques*

Various thermal properties measurements methodology have been developed using either a steady-state (*i.e.* the solution of the heat equation is solely dependent of a spatial vector space) or a transient approach (*i.e.* the solution of the heat equation is dependent both of a spatial vector space and of time). In this part, a succinct theoretical presentation of both approaches will be made. In every case, the common philosophy is a punctual and brutal thermal perturbation on a top face of the sample. The thermal perturbation can be incremental, periodic or even pulsative. A synthesis of the available methodologies is described in Table 6.1.1.

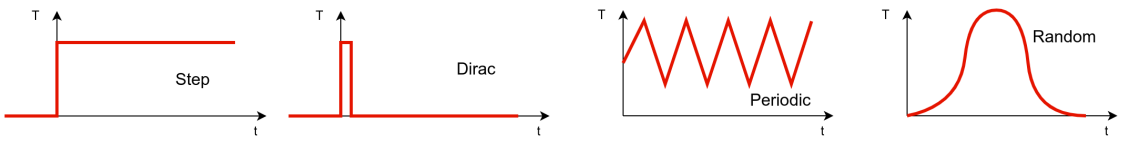

Figure 6.1.1 – Different heat pulse schemes presented in the method catalog from Degiovanni (1994).

Perturbation	Step			Dirac			Periodic			Random		
Geometry	**Wa**	**Cy**	**Sp**	**Wa**	**Cy**	**Sp**	**Wa**	**Cy**	**Sp**	**Wa**	**Cy**	**Sp**
$T_{perturbation}$				A			B					
$T_{out\ of\ perturbation}$		C		D	E, F		G					
T_{inlet} and T_{outlet}	H						I	J		K	L, M	
Φ_{outlet} and T_{inlet}	N	O	P	Q								

Table 6.1.1 – Transient regime thermal properties assessment techniques overview (translated and adapted from Degiovanni, 1994).

***Wa.**: Wall-shaped theoretical model*

***Cy.**: Cylinder shaped theoretical model*

***Sp.**: Spherical theoretical model*

Key names for each study technique. Measured thermal properties for each technique are shown between braces.

A: Front-faced Laser-Flash (α)

B: Front-faced sinusoidal regime (α)

C: Double-wired thermal sensor (α)

D: Standard Laser-Flash (α)

E: Cylindrical Laser-Flash (α)

F: Convergent wave thermal regime (α)

G: Back-faced sinusoidal regime (α)

H: Fluxmetric method (λ)

I: Back and front-faced sinusoidal regime (α)

J: Thin layer sinusoidal regime (α)

K: Fin method (α)

L: Triple-wired thermal sensor (α)

M: Radial thermal conduction fin method (α)

O: Hot-wire method (λ)

P: Spherical sensor method ($\frac{\lambda^3}{C_w}$)

Q: Front-faced Laser-Flash variation (λ^{-1})

In this study, we will consider a set of three techniques for measuring thermal properties. The first technique is a steady-state methodology based on heat flux measurements and two others are based on the interpretation of transient periodic heat transfer regime (Laser-Flash technique and pulsative heat source). Fluxmetric approach based on a steady-state heat transfer is described in the following section. Laser-Flash technique for thermal properties assessment is described in section 6.1.1.3 and pulsative radiative heat source is explained in section 7.1.1.

6.1.1.2 *Steady-state methodology: Fluxmetric method (EN 12667 standard)*

The fluxmetric methodology is a steady-state technique developed for highly insulative material. The workflow of this is described in the EN 12667 standard (AFNOR, 2001). This method uses the principles of the guarded hot-plate with the addition of a fluxmeter. The EN 12667 methodology has been specially developed to make thermal properties assessments of low-porosity samples such as mortar, brick or concrete. Here, as samples studied in the thesis can have a porosity of over 90%, the main identified drawback in the application of the standard for highly porous samples is that it could induce a non-negligible convective effect if the sample is heated from the bottom. The possibility of free convection cells initiation (Rayleigh-Bénard condition) is discussed in section 8.A. Some clue on the impacts of porosity and pore size on thermal exchange coefficients have been shown by L. Zhang et al. (2009). To avoid any convective cell formation, hot plate and cold plate are inverted from the original setup provided in the EN 12667 standard (hot on top, cold on bottom). This setup modification will cut convective cell formation, hence causing convective heat transfer to be negligible at this point. Moreover, the setup is modified to take into account the fragile nature of the collected samples. A comparison between the original setup and the setup used in the framework of the thesis is available in Fig. 6.1.2.

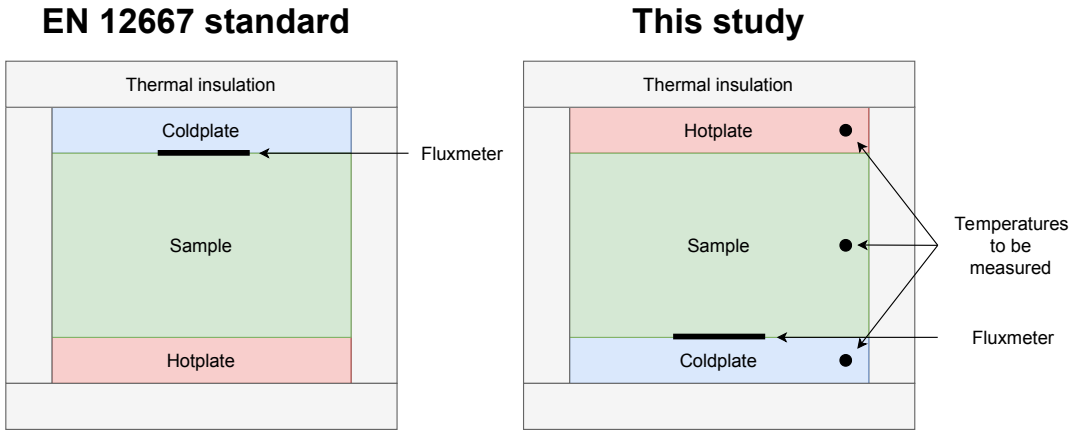

Figure 6.1.2 – Theoretical experimental layout and adapted experimental layout for this thesis.

Therefore, a measurement chamber in polystyrene is created to fit the samples. The remaining gaps between the samples and the box are filled with glass wool. This material will help avoiding lateral thermal exchanges thus keeping the heat flow (*i.e.* the thermal gradient) as much vertical as possible. A sudden yet constant heat input is created on the top of the sample and temperature rises at various locations is monitored. When steady-state is observed in the measurement chamber, thermal conductivity values can be then calculated using the equation given in Eq. 6.1.

$$\lambda_{eff} = \frac{f e_h d}{T_{hot} - T_{cold}} \tag{6.1}$$

with f being the conversion factor between voltage and effective heat flux, e_h the electric voltage measured with the fluxmeter, and d the diameter of the fluxmeter's surface.

6.1.1.3 *Laboratory assessment: Laser-Flash methodology*

The Laser-Flash technique for studying thermal properties was first theoretically described in Parker et al. (1961). The Laser-Flash method is extensively used for powder thermal properties quantification. This methodology allows describing thermal diffusivity, thermal conductivity and heat capacity. To perform a measurement, the studied sample is put in place in a compressible sample holder with graphite-covered plates on both top and on the bottom of the sample (Fig. 6.1.3).

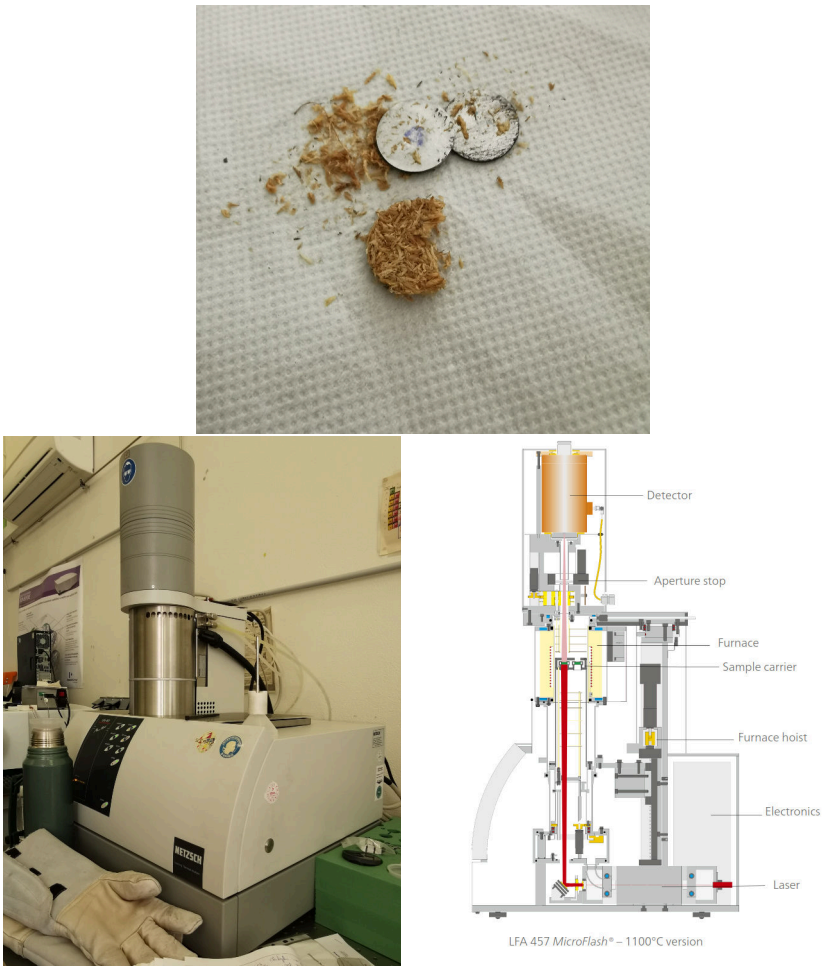

Figure 6.1.3 – *(top)* Sample holder with some *Sphagnum* taken outside (the sample broke after extraction). The aluminum disc has a diameter of 2.54 mm. *(bottom left)* Netzsch LFA 457 Micro-Flash™ device at PROMES laboratory *(right)* Internal schematic description (©Netzsch-Gerätebau GmbH).

Sample's thickness is carefully measured with a micrometer. Then, a monochromatic light source (laser beam) is shot on the bottom face of the sample and the consecutive thermal signature is acquired with an infrared sensor over sample's top face. One dried sample (Mound2.5) has been studied using a Netzsch LFA 457 Micro-Flash™ apparatus installed at *Procédés Matériaux et Énergie Solaire* (PROMES) laboratory (Odeillo, France) as well as two living samples. One of the main advantage is that it allows a fast measurement of the thermal properties. However, such quantification heavily relies on the volumetric mass of the studied sample, which is not straightforward to measure on such fragile porous media.

6.1.1.4 *Infrared thermography*

Infrared thermography is a contactless temperature measurement method based on the observation and acquisition of an image of infrared electromagnetic radiation in the near environment. Infrared thermography is a concept that originated from Sir William Herschel's theorization of infrared in 1800 (*i.e. lesser wavelength than red*) radiations. This discovery lead to the conceptualization of sensors that can receive thermal radiations and convert it to an electrical current. To a first approximation, thermography can be described as an analogy of photography in the infrared spectrum. Infrared wavelengths are subdivided into three main spectrum domains according to ISO 20473–2007:

- Near infrared (NIR) with wavelengths from 7.8×10^{-7} to 1.4×10^{-6} m;
- Mid infrared (MIR) with wavelengths from 1.4×10^{-6} to 1.5×10^{-5} m which can be subdivided into three sub-spectra:
  - Short wavelength infrared (SWIR) from 1.4×10^{-6} to 7.8×10^{-6} m;
  - Mid wavelength infrared (MWIR) from 3×10^{-6} to 8×10^{-6} m;
  - Long wavelength infrared (LWIR) from 8×10^{-6} to 1.5×10^{-5} m;
- Far infrared (FIR) with wavelengths from 1.5×10^{-5} to 5×10^{-3} m.

The subdivisions of each infrared domains are available in Fig. 6.1.4.

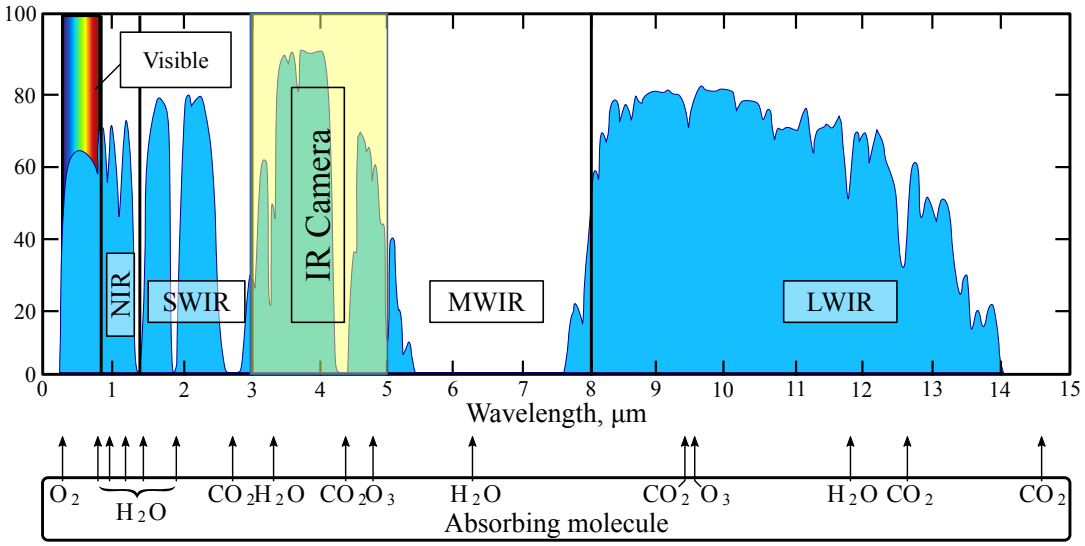

Figure 6.1.4 – Transmittance profiles for infrared radiations (*CCo D.Ilyin*).

According to Planck's law (Eq. 6.2), any body with a temperature greater than o K emits a maximum amount of radiation energy W at the maximum wavelength λ_{peak}:

$$L_\lambda = \frac{2hc^2}{\lambda_{peak}^5} \frac{1}{\exp\left(\frac{hc}{k\lambda_{peak}T}\right) - 1} \tag{6.2}$$

where h is Planck's constant, k is Boltzmann constant and c the speed of light. Wien's law is used to describe the spectral distribution of the energy emitted by radiation on the basis of Planck's law. Wien's law (Eq. 6.3) can therefore be written as:

$$\lambda_{max} = \frac{\sigma_w}{T} \tag{6.3}$$

where $\sigma_w = 2.897 \cdot 10^{-3}\ m \cdot K$ is the Wien's constant. As for all electromagnetic radiation, infrared radiation obeys Wien's law. However, only part of infrared radiation is experienced and felt by humans as "heat transfer". Indeed, near infrared and far infrared radiations are usually not considered as thermal infrared. Near infrared radiations are occurring for objects at high temperatures (*e.g.* stars, incandescent and halogen light bulbs) and are emitted at small amounts in natural systems at atmospheric temperatures. However, far infrared radiations are ubiquitous in the environment due to their maximal emission temperature at around 173 K. Most of infrared thermography applications are operating in mid infrared spectrum. More precisely in this study, we will consider the mid-wavelength infrared spectrum between 3×10^{-6} to 5×10^{-6} m. One of the advantage of using this infrared frame is that the atmosphere gaseous composition have a good transmissivity for the considered wavelength range thanks to a transmissivity window for the main atmospheric gases.

The observed temperature of an object will mainly depend on its emissivity. Thus, where a theoretical blackbody should emit infrared radiations as much as it absorbs it (thus having the same radiance), a greybody does not necessarily emit all the absorbed radiation, nor it does in the same wavelengths. In the same way, the reflected temperature or the temperature of the surrounding environment has to be taken into account. One can refer to the schematic presented in Fig. 6.1.5 showing the radiative equilibrium that has to be taken into account for infrared thermography.

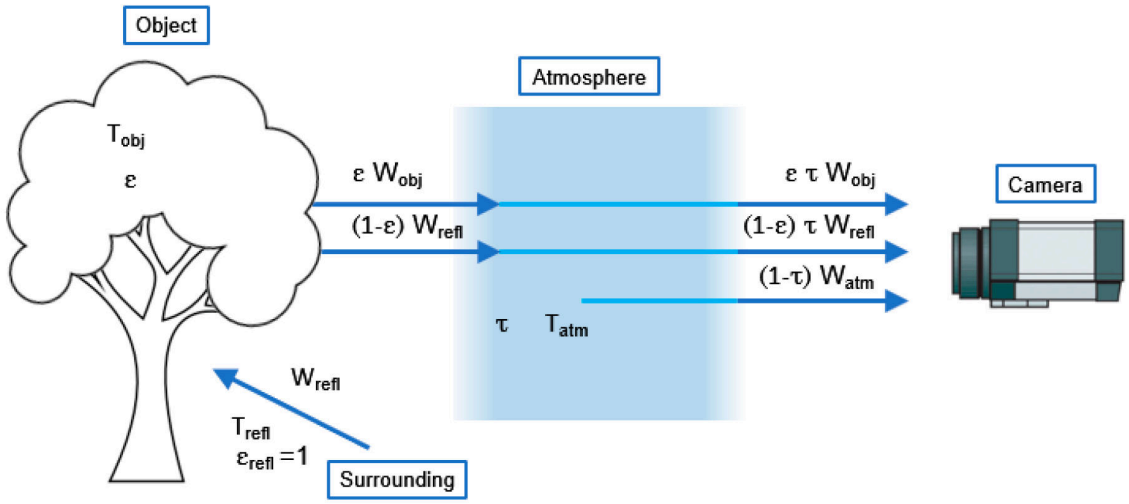

Figure 6.1.5 – General synthesis of an infrared thermography acquisition chain after Vidal and Pitarma (2019).
T_{obj}**:** True temperature of the object (*i.e.* the temperature that can be measured with a thermocouple);
T_{refl}**:** Reflected temperature (*i.e.* the background temperature);
ε*:* Emissivity of the object;
W_{obj}*:* Radiative energy emitted from the object;
W_{refl}*:* Radiative energy emitted from the background;
W_{atm}*:* Radiative energy emitted from the atmosphere.

6.1.2 *Available studies*

Whereas thermal properties are well studied for industrial porous media and more precisely insulating materials, the literature on arctic cryptogamic cover transfer properties is scarcer. There are less records of measurements attempts in the literature for thermal properties than for hydraulic properties of such low vegetation cover. Indeed, few of the studies are either field experiments or laboratory experiments. Early modeling work of thermal conductivity as a function of volumetric water content has been conducted by de Vries (1963). Some work done on general soil thermal properties demonstrates a global estimation of thermal properties taking into account the thermal conductivities of

air, water and organic matter (Farouki, 1981). The earliest work consists of a study from Canadian mires (Williams, 1968). Then, some extensive work has been conducted from the 1990's onwards. There are some notable studies on field measurements by Kettridge and Baird (2007). Most of the available literature is related to either building engineering (Bakatovich and Gaspar, 2019; De Guzman and Alfaro, 2018; Kain et al., 2021) or for climate impact models and thermal regime models (Baird, 1997; Dimitrov et al., 2010; Kellner, 2001; Laurén and Heiskanen, 1997; Soudzilovskaia et al., 2013; van der Molen and Wijmstra, T.A, 1994). A synthesis of the values found in the literature is available in Table 6.1.2.

6.2 EXPERIMENTAL THERMAL PROPERTIES' ASSESSMENT METHODOLOGY

6.2.1 *General overview*

In order to perform experimental thermal property quantification for the studied samples, a complimentary experimental methodology has been developed. This experimental bench is based on the fluxmetric thermal conductivity assessment protocol presented as a European standard NF EN12667, AFNOR (2001). This approach is also presented in Degiovanni (1994).

This experimental bench unfolds in two parts. One first part consists of a thermocouple and heat fluxmeter acquisition chain for respectively temperature and heat flux measurements. The second part is an infrared thermography camera connected to a storage computer. Both setups are used for describing the observed thermal regimes for each sample type.

6.2.2 *Fluxmeter and thermocouple method*

6.2.2.1 *Experimental design*

A sample is placed in a polystyrene box. The free space between the sample and the experimental chamber walls is filled with glass wool to prevent transverse heat transfers. 28 thermocouples and one heat flux sensor are connected to two Keithley® multiplexed data acquisition devices. 10 thermocouples connected on the first data logging device, recording data at a rate of one measurement every 8 seconds. The other 18 thermocouples and the heat flux sensor are connected to the other data logging device, storing the readings every 16 seconds. A picture of the complete setup with the location of the thermocouples is shown in Fig. 6.2.1.

Sample type	Methodology	λ [W.m^{-1}.K^{-1}]	α [m^2.s^{-1}]	Cw [J.m^{-3}.K^{-1}]	Reference
Mound *Sphagnum*	Simulation	4×10^{-2} 5×10^{-1}	–	–	Dimitrov et al. (2010)
Mound *Sphagnum*	Analytical	3×10^{-3} 5×10^{-1}	–	–	Kellner (2001)
Sphagnum	Field	4.4×10^{-2} 5.9×10^{-2}	1.3×10^{-8} 2.3×10^{-8}	2.7×10^{6} 3.4×10^{6}	van der Molen and Wijmstra, T.A (1994)
Mor layer†	Field	3×10^{-2} 2.4×10^{-1}	–	–	Laurén and Heiskanen (1997)
Peat	Experimental	5×10^{-2} 4.5×10^{-1}	–	–	van Wijk and de Vries (1963)
Peat	Experimental	6×10^{-2} 5×10^{-1}	–	–	de Vries (1963)
Peat	Experimental	4×10^{-2} 2.4×10^{-1}	–	–	Harlan and Nixon (1978)
Lichen & *Sphagnum*	Analytical	3.5×10^{-2} 5.0×10^{-1}	-	-	O'Donnell et al. (2009)
Organic matter	Experimental	2.5×10^{-1}	10^{-7}	2.5×10^{6}	Beringer et al. (2001)
Sphagnum	Field	6×10^{-2} 5×10^{-1}	1.2×10^{-7} 1.42×10^{-7}	5×10^{5} 3.5×10^{6}	Soudzilovskaia et al. (2013)

Table 6.1.2 – Thermal properties' values available in the literature. λ is the thermal conductivity in W.m^{-1}.K^{-1}, α is the thermal diffusivity in m^2.s^{-1} and C_w is the volumetric heat capacity in J.m^{-3}.K^{-1}.
†: The mor cover is a soil litter rich in humic acid frequently present under boreal coniferous forests.

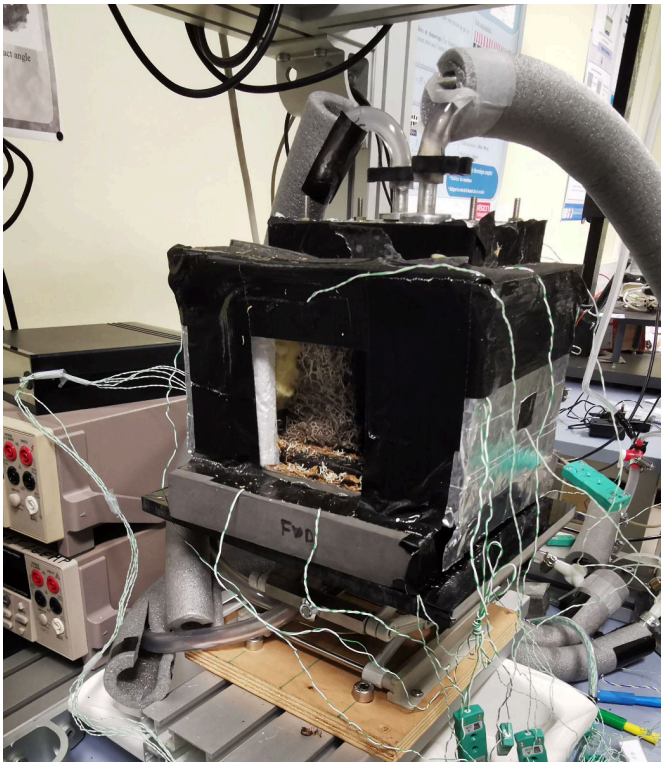

(a) Picture of the actual experimental setup.

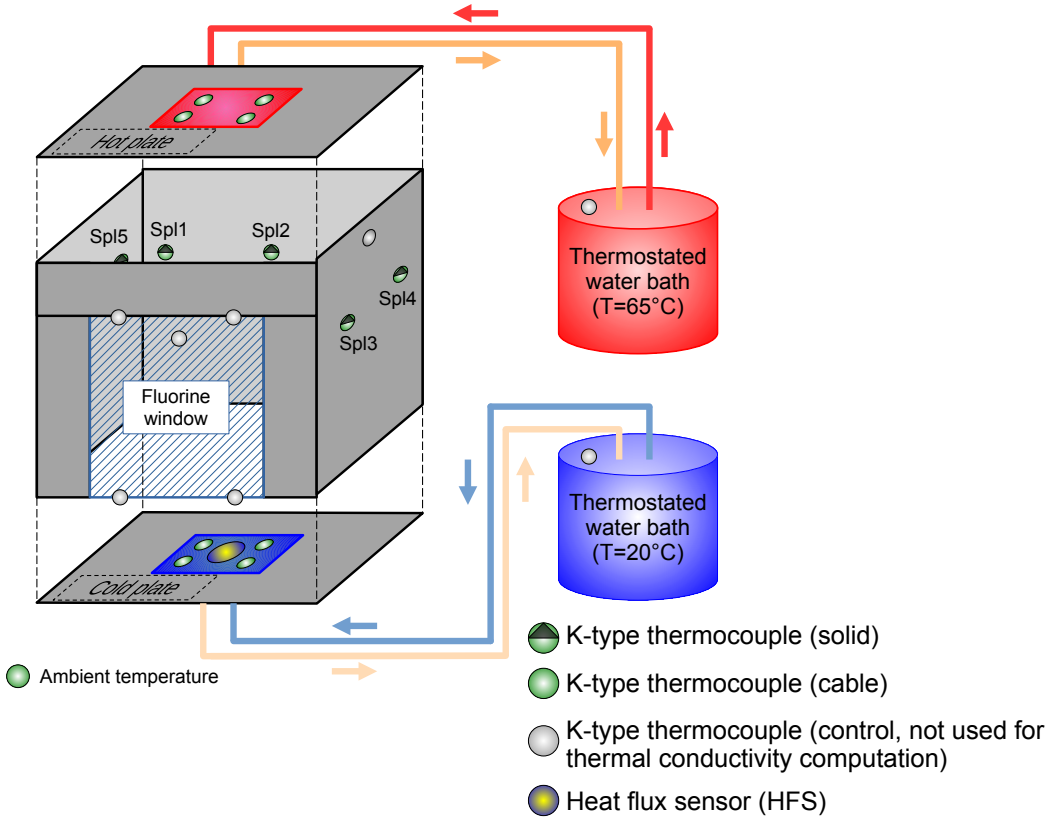

(b) Experimental setup scheme.

Figure 6.2.1 – Experimental setup with the thermocouples installed.

Two thermostated baths are connected to their respective heat exchangers. One bath will account for heating the measurement chamber from the top (the hot plate) and the other will maintain the lower surface to the room ambient temperature (the cold plate). On each plate, four control thermocouples at each corner are placed. The heat flux sensor is placed on the bottom plate with its temperature kept at room temperature. Sample's thickness is computed according to the tomographic scans for each sample. The experiment is started when a sudden rise in temperature is caused by the opening of a valve on the heating circuit. The valve is kept open throughout the experiment. The measuring chamber is then kept enclosed during at least four hours and up to nine hours, allowing the sample to heat during this time. The experiment is stopped when a thermal equilibrium is reached according to both thermocouple data and heat flux sensor data readings.

6.2.2.2 *Signal processing*

6.2.2.2.1 Temperature drift due to dielectric effects in thermocouples

Some signal processing routine are compulsory to take into account various dielectric effects that occurs on wired thermocouples. Cold junction temperature was measured with a dedicated electronic setup for the Keithley® 2700 and numerically simulated for Keithley® 2000. However, preliminary results showed that there is a temporal temperature drift for this apparatus. This temperature drift cause the lower the voltage of the connected thermocouples, and thus showing a lower temperature than reality. As both cold plate and hotplate measurements are made using Keithley® 2000, this drift can be neglected if one decides to work solely on the temperature difference ΔT. However, a correction function is required in order to be able to interpret individual measurements and compare them to the others.

A 12^{th} order polynomial regression function of the temporal drift is generated with a MatLab/Octave function, allowing to retrieve ΔT_{drift} as a function of time. The source code is available in Appendix 6.A.3. The comparison between the raw experimental data and the corrected data is available in Fig. 6.2.2.

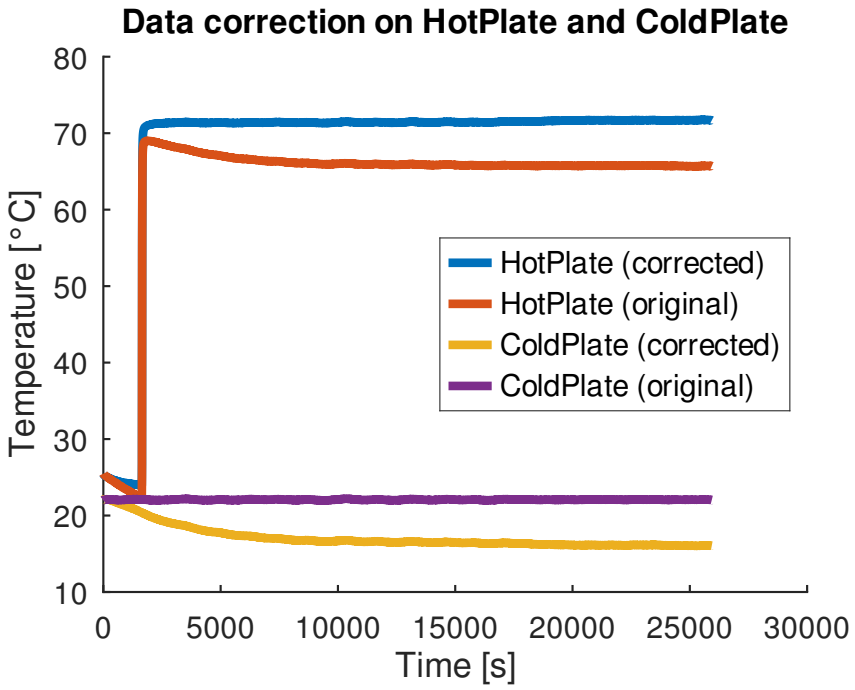

Figure 6.2.2 – Example of initial and processed signal for thermocouple results on sample Mound2.5. *HotPlate* stands for the averaged temperature of the thermocouples installed on the heating plate. *ColdPlate* stands for the averaged temperature of the thermocouples installed on the cooling plate.

6.2.2.2.2 Effective thermal conductivity computation

As shown in Eq. 6.1, the effective thermal conductivity according to the EN 12667 standard takes into account the thermal difference ΔT and the heat flux on the cold plate. Although the thermal gradient is well known due to the fact that both plates are thermostated, the heat flux sensor brings a lot of measurement noise. This discrepancy will be reduced by computing a temporal average effective thermal conductivity. The temperature difference between the heating plate (T_{hot}) and the cold plate (T_{cold}) is averaged over the associated thermocouples over 15 minutes time slots. The measured voltage by the fluxmeter is converted to a heat flux value and also averaged during 15-minutes time slots. After steady-state is identified with the end of the stabilization of both outlet flux and of the five inserted thermocouples, λ_{eff} is computed for each set of value for a given time. Then, λ_{eff} values are averaged over a 15-minutes period for the rest of the experiment to validate the steady-state.

6.2.2.3 *Results*

Results for each studied sample type are shown in Fig. 6.2.3.

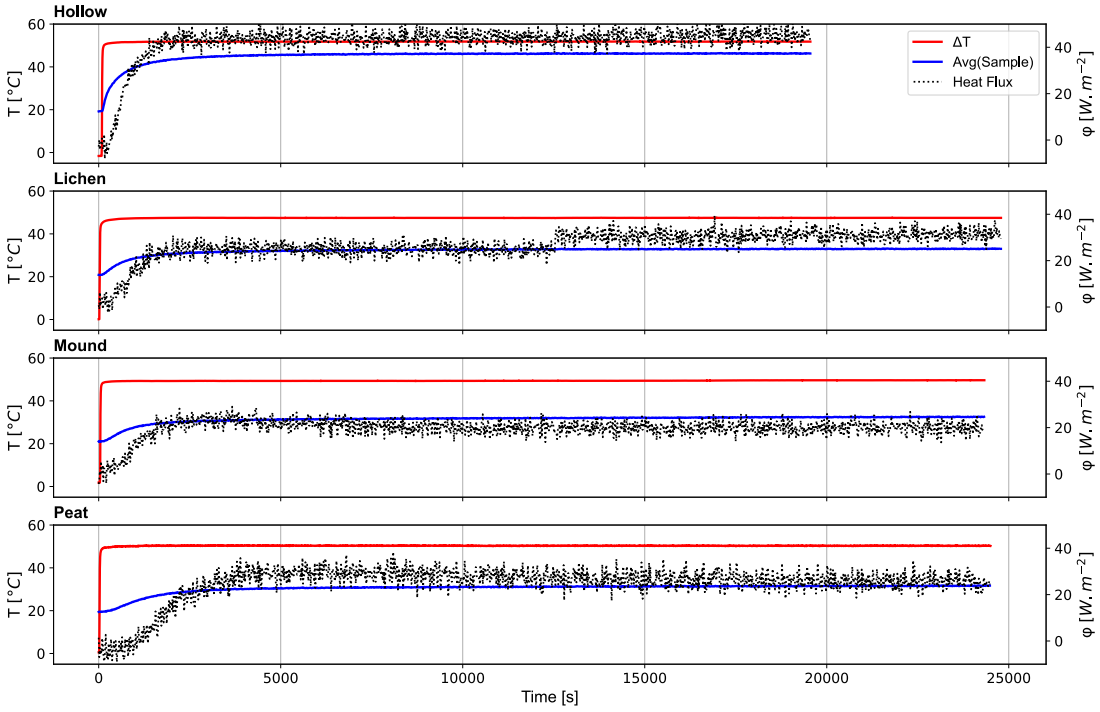

Figure 6.2.3 – Time evolution of the average temperature at the middle of the sample (*Avg(Sample)*), of the temperature difference between the hot plate and the cold plate (ΔT) and of measured heat flux at the fluxmeter located in at the interface of the bottom side of the sample and the cooling plate (ϕ).

On each plot, a representation of the heat flux ϕ at the outlet, the thermal difference ΔT as well as the averaged temperature for the five inserted thermocouples are plotted. For each sample type, one can note that the steady-state phase is set up from t+20 minutes for Hollow sample to t+60 minutes for Peat sample. One can note that there is a jump in the measured heat flux (ϕ) for the Lichen sample at about t+13000 seconds. A detailed plot of the average temperature for the five inserted thermocouples is shown in Fig. 6.2.4 with the thermal envelope (*i.e.* the minimum temperature and the maximum temperature measured by the five inserted thermocouples) for each type.

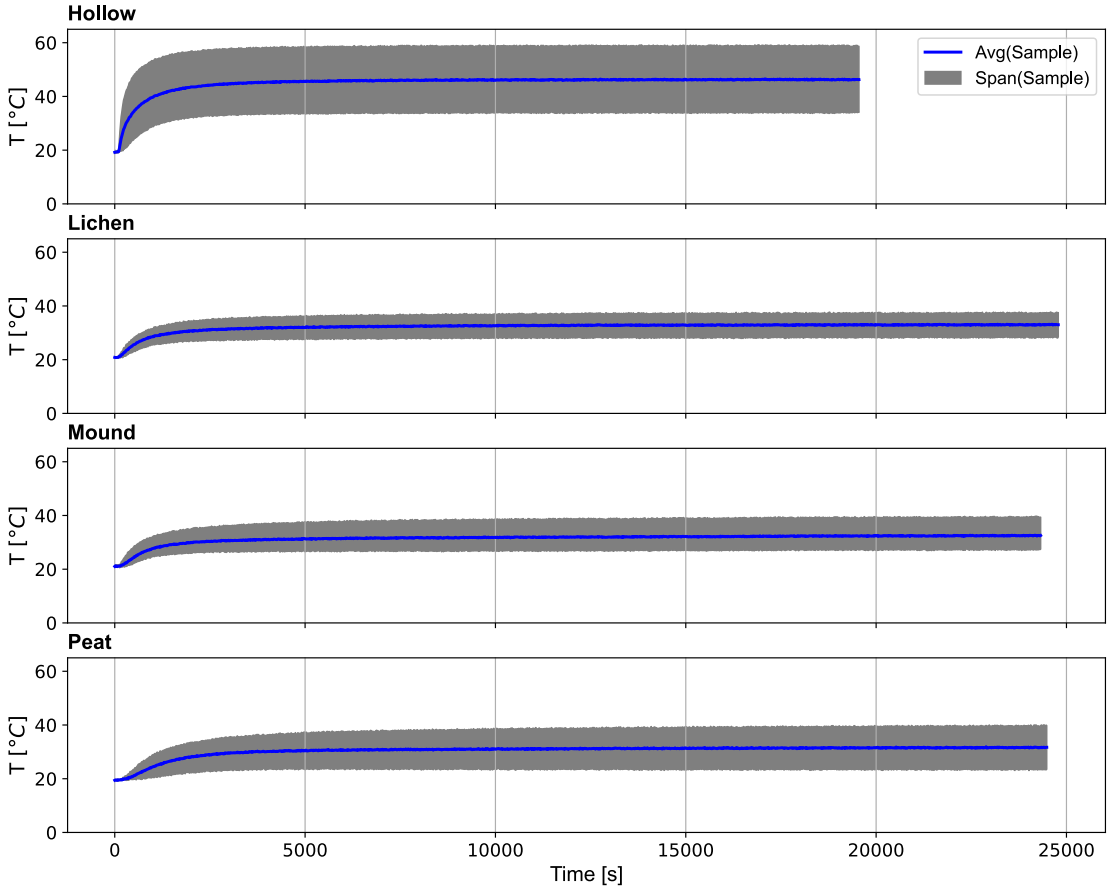

Figure 6.2.4 – Temperature average *Avg(Sample)* and temperature divergence between the five inserted thermocouples located in the middle part of the sample (thermocouples *Spl1* to*Spl5*, see Fig. 6.2.1).

From these graphs, one can note that the thermal amplitude is the biggest for the Hollow sample and the smallest for the Lichen sample. Mound and Peat samples have nearly the same thermal amplitude for the five inserted thermocouples. Effective thermal conductivity for each sample type is available in Fig. 6.2.5 on 15-minutes averaged evolution with time. A synthesis of the average values with their associated standard deviation is shown in Table 6.2.1.

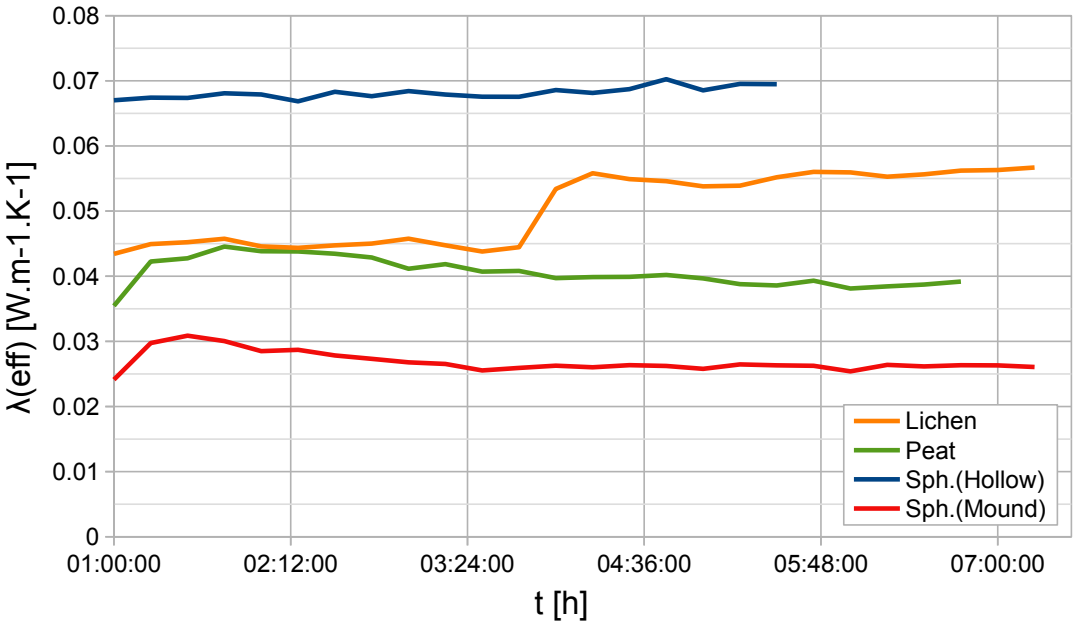

Figure 6.2.5 – Averaged thermal conductivity (in W.m^{-1}.K^{-1}) evolution with time. Effective thermal conductivity λ_{eff} (in W.m^{-1}.K^{-1}) is averaged every 15 minutes according to Eq. 6.1.

Sample	λ_{eff} (W.m^{-1}.K^{-1})
Hollow2.8	$6.817 \times 10^{-2} \pm 8.836 \times 10^{-3}$
Lichen2.1	$5.015 \times 10^{-2} \pm 5.423 \times 10^{-3}$
Mound2.5	$3.74 \times 10^{-2} \pm 2.152 \times 10^{-3}$
Peat2.3	$4.058 \times 10^{-2} \pm 2.224 \times 10^{-3}$

Table 6.2.1 – Effective thermal conductivity λ_{eff} (W.m^{-1}.K^{-1}) assessed using thermocouples.

λ_{eff} spans from 3.74×10^{-2} W.m^{-1}.K^{-1} for Hollow2.8 sample to 6.817×10^{-2} W.m^{-1}.K^{-1} for Mound2.5 sample. Standard deviations of λ_{eff} fluctuates around 10%, which is the amount of standard deviation obtained for the EN 12667 standard. One can see that the highest effective thermal conductivity value is obtained for hollow *Sphagnum* and the least for the mound *Sphagnum*. Peat and lichen effective thermal conductivities are very similar at the beginning of the experiment while the thermal conductivity jump for lichen makes the difference bigger. Standard deviations are sensibly consistent between each sample type.

6.2.2.3.1 Discussion and synthesis of thermocouple measurements

The effective thermal conductivity results are consistent between each sample type with a mean value of 5.8×10^{-2} W.m^{-1}.K^{-1}. These effective thermal conductivities fit well

in the values available in the literature presented in Table 6.1.2. The low uncertainty of the thermal conductivity can be explained by the fact that the 15-minutes averaged values have low fluctuations, confirming the establishment of a steady-state in the measurement chamber. However, the stationary heat transfer for lichen sample is not that clear. This brutal change is linked to a jump in the measured heat flux shown in Fig. 6.2.3. Adversely to peat and *Sphagnum* samples, lichen sample has thermally expanded during the heating of the sample. Some clues of the deformation of the porous medium due to this thermal expansion is shown in Appendix 6.A.1. This behavior could be explained by the fact that lichen samples are composite samples that are able to survive in extreme conditions. In this way, the expansion could be linked to an evapotranspiration and thus the formation of larger (*i.e.* more heat conductive) channels for thermal transfers.

One of the major drawback of using physical temperature sensing in a porous media (*i.e.* using thermocouples or other contact sensor) is the difficulty in defining the phase in which the thermocouple is located. For example, the thermocouple may be located in the fluid phase, in this case in a connected or closed pore, or touching the solid matrix (in this case the plant). The use of several thermocouples inserted in the porous medium provides a statistical estimate of the average temperature for a given depth. By studying the stationary state of thermal equilibrium within the sample, a local thermal equilibrium can be obtained. As a result, thermocouple assessment can be considered as a good methodology to retrieve some effective thermal properties on such porous medium. The method presented in the EN 12667 standard for thermal properties' characterization for construction materials appears to be suitable with the appropriate modifications to the heating zone. However, using thermocouples and heat flux have the drawback of being point measurements. This means that the measured values for a given position will mostly not be the same for another location at a given elevation. Moreover, inserting some thermocouples causes alterations of the porous structure of the samples. In a long term, this can threaten sample integrity for other experiments. Infrared thermography, has the advantage of keeping a good representativeness for later experiments thanks to its non-invasive factor. Therefore, an infrared thermal camera is coupled to the thermocouple experiment and will be discussed in the following section.

6.2.3 *Infrared image acquisitions*

Infrared thermography is a measurement technique allowing to get a temperature estimate of a given surface according to its infrared radiance. This technique is well known in medical applications such as body activity monitoring, high capacity body temperature quantification or cerebral cortex activity (Lahiri et al., 2012). Other main applications include industrial quality assessment.

According to the available literature, plants are most often recognized to absorb and re-emit the incident radiation, making them relatively good blackbodies. For instance,

Harrap and Rands (2021) estimated the infrared emissivity of some usual flowers. Their study lead to the conclusion that flowers have an emissivity above 0.95. The authors estimated infrared emissivity to be consistent for most of the plant species. Harrap, Hempel De Ibarra, et al. (2018) give an extensive overview of the methods and the results in infrared thermography for biology. This means that using thermal imaging as a tool for assessing thermal properties is possible in conjunction with other methods.

6.2.3.1 *Infrared thermography experimental layout*

To gather more information about the heat diffusion across the sample, an infrared thermography chain consisting of a FLIR X8501SC camera is installed next to the thermocouple experimental bench. An infrared transparent window made of fluorine (CaF_2) is put in place on one side of the box, allowing to control the sample's surface temperature remotely. This setup is used here for two main purposes, one being the calibration of the infrared camera raw values and the second the observation of thermal heat front propagation throughout the sample. The main advantage of infrared thermography is that it is a non-invasive technique avoiding structural modifications compared to thermocouple insertion. However, one of the main challenges encountered in infrared thermography is the accountancy of every infrared source in the near environment, including multiple reflections. A presentation of the experimental setup including the thermography acquisition chain is available in Fig. 6.2.6.

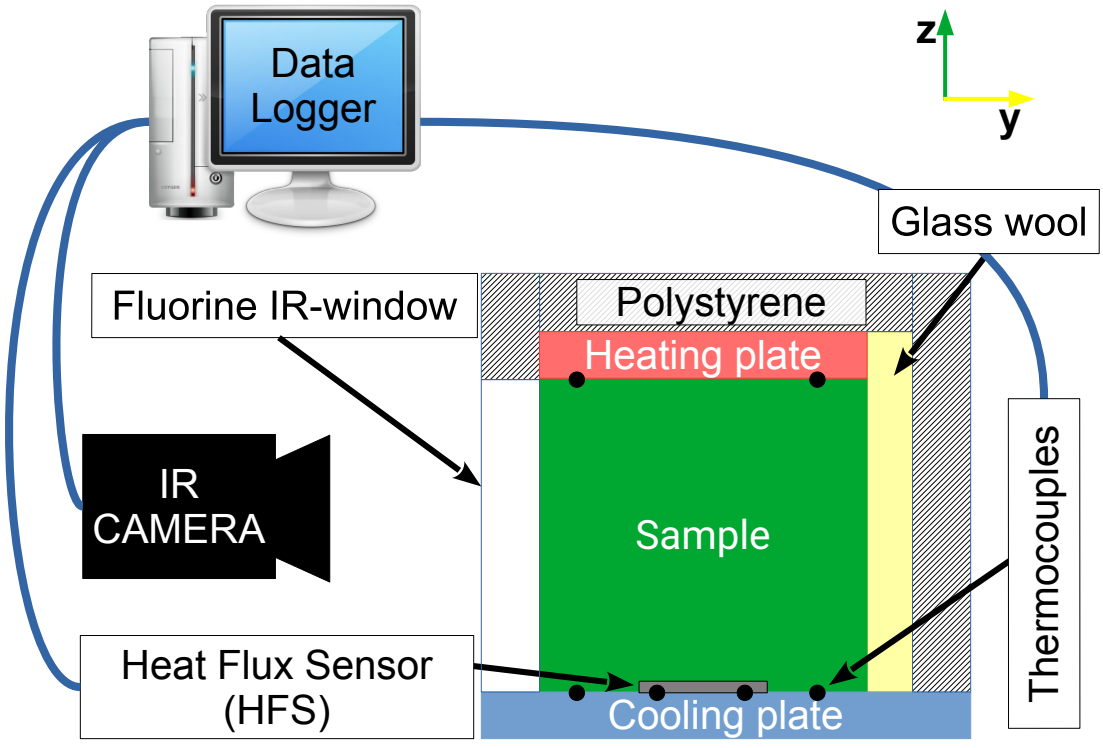

Figure 6.2.6 – Effective thermal conductivity assessment setup.

Fig. 6.2.7 shows the infrared camera installed for the setup with the measurement chamber in place.

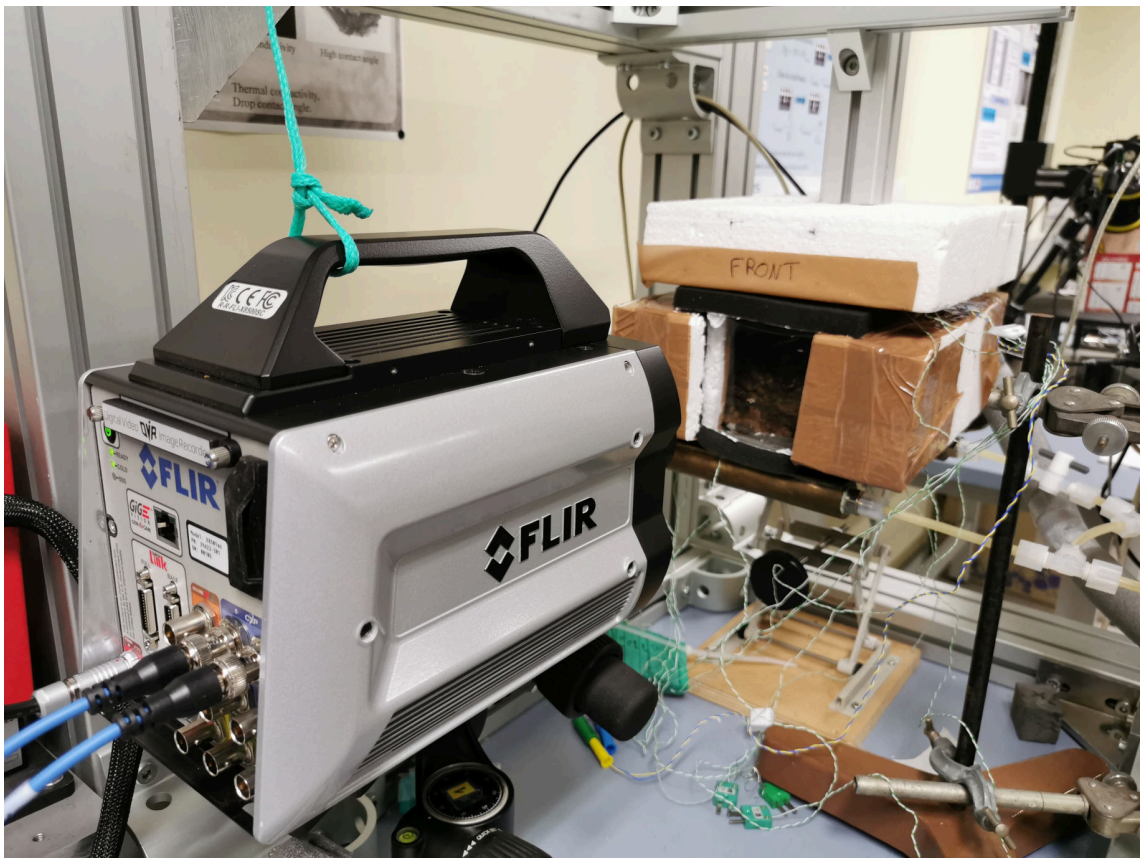

Figure 6.2.7 – FLIR™ x8501sc thermal camera used for the experiment.

The close distance between the measurement chamber and the infrared camera avoids the influence of background temperature as a refection on the infrared window.

6.2.3.2 *Transmissivity and background temperature correction*

An IR-transparent window made of fluorite (CaF_2) is put in place on one side of the measurement chamber to allow the observation of the heat propagation through the sample while keeping the chamber thermally insulated. However, as it can be seen in Fig. 6.2.8, the transmissivity of the window is not 100%, meaning that the consecutive absorption and reflection of infrared radiations must be taken into account.

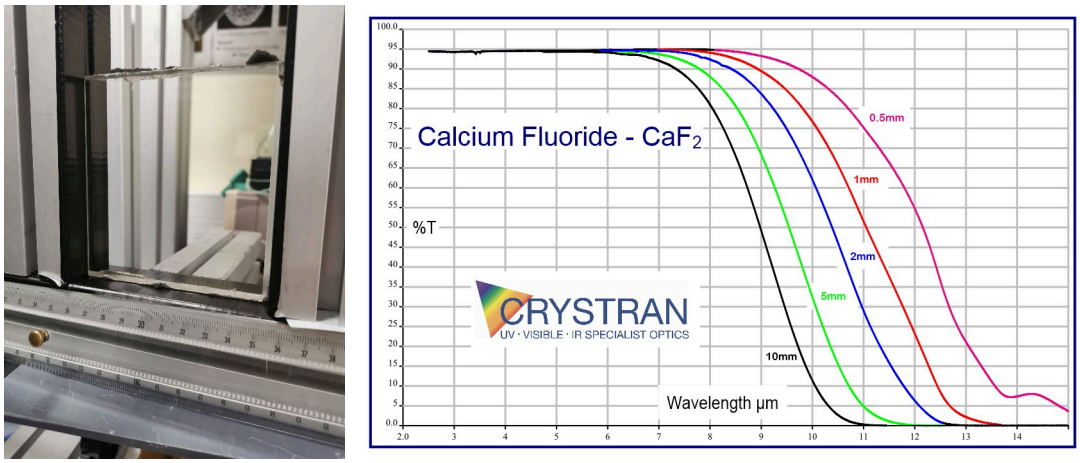

Figure 6.2.8 – Picture showing the fluorite (CaF_2) window and infrared spectrum for different CaF_2 plate sizes indicated with colored curves (spectrum available at https://www.crystran.co.uk/optical-materials/calcium-fluoride-caf2).

To do so, a calibration experiment is set up. A linear temperature increase from 14 °C to 78 °C is applied on a calibration blackbody. IR-camera raw values are then computed for each temperature steps twice (with the window in between and without it as a control experiment). The resulting setup is available in Fig.6.2.9.

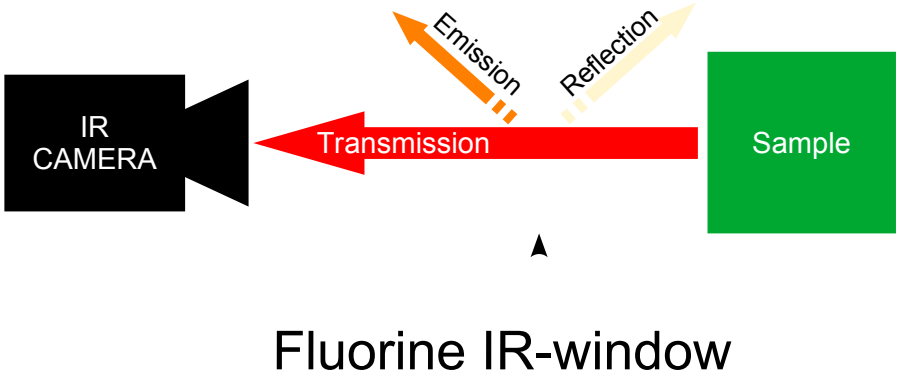

Figure 6.2.9 – Radiative balance between an infrared camera, an infrared-transparent window made of fluorine (CaF_2) and the sample to be measured.

The difference of sensor raw values are subtracted and a difference with and without the fluorine window is computed using a linear regression, with i the pixel's raw intensity shown in Eq. 6.4.

$$\Delta_{correction} = 5.96 \times 10^{-2} i - 1.612 \times 10^{2}, \qquad R^2 = 0.999 \tag{6.4}$$

and,

$$i_c = i + \Delta_{correction} \tag{6.5}$$

Then, a corrected dataset is created by adding the correction factor to the raw pixel value leading to Eq. 6.6 and Eq. 6.7:

$$T_{sensor} = -2.41 \times 10^{-14} i_c^4 + 6.77 \times 10^{-10} i_c^3 - 7.39 \times 10^{-6} i_c^2 + 4.3 \times 10^{-2} i_c - 48.12, R^2 = 0.999 \tag{6.6}$$

and, with $T_{background}$= 22 °C,

$$T_{true} = \sqrt{\frac{T_{sensor}^4 - (1-\epsilon) \cdot T_{background}^4}{\epsilon}} \tag{6.7}$$

The corrected pixel value can be implemented in the general equation for computing the sensor's temperature as a fourth-order polynomial regression, available in Fig. 6.2.10.

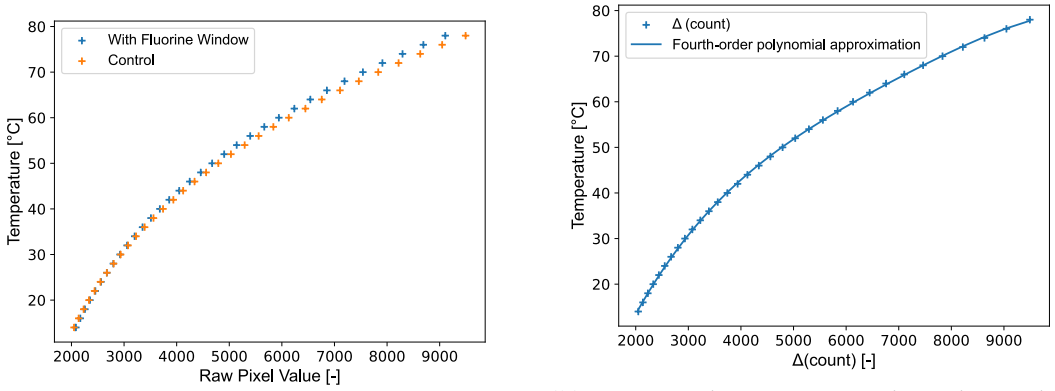

(a) Raw calibration values with the fluorine window installed and without it (Control).

(b) Deviation between raw values obtained with and without the window and associated polynomial regression.

Figure 6.2.10 – Regression plots for raw infrared acquisitions.

6.2.3.3 *Emissivity quantification*

One of the main challenge in infrared thermography is to account for the emissive property of any studied material, for which dedicated methods have to be implemented (Vellvehi et al., 2011). For instance, each material hit by an infrared beam will be affected by three phenomena:

- Reflection: The ability of a given material to redirect a ray normal to the incident ray;

- Emission: The ability of a given material to absorb the incident ray as energetic differential (in the case of a perfect black-body) and to emit it either in the same spectrum or in another way;
- Transmission: The ability of a given material to transmit a ray through it with a certain refraction angle depending of the density of the transmissive material.

These three phenomena have to be taken into account to compute a surface temperature that is representative of the real surface temperature, as it would be measured with a thermocouple. To avoid reflections, the fluorine window is slightly tilted to that the infrared reflection of the infrared camera is not visible in the field of view. Moreover, a *Non-Uniformity Correction* is performed to average the pixels' value so that outliers are removed from the raw interpreted thermography.

To assess the infrared emissivity spectrum of *Sphagnum*, some complementary measurements are done at CNRS-PROMES laboratory in Odeillo (France). Measurements are done with a SOC-100 HDR® reflectometer (Surface Optics Corporation™) coupled with a Nicolet™ 6700 Fourier Transform IR (FTIR) spectrophotometer which has a scanning range from 1.25 µm to 25 µm (Fig. 6.2.11). This device allows measuring hemispherical directional reflectance at different detection angles from 8° to 80°. The SOC-100® is equipped with 2π gold-coated imaging semi-ellipsoid to illuminate the sample from all directions using a 700 °C blackbody source. A movable mirror collects the reflected collimated light and directs it to the FTIR spectrometer to obtain the reflectance spectrum. A spot of 12 mm diameter is measured on samples that need to have a minimum of 25 mm side for squares or 25 mm diameter for discs. A gold-plated calibrated diffuse reflectance standard is used as reference during the measurements. The FTIR is fitted with a deuterium triglycine sulfate detector with a potassium-krypton beam splitter. Reflectivity is then measured once the temperature inside the chamber is stabilized. Emissivity can be computed using the relation $1 = \epsilon + r$, with r being the measured reflectivity.

In the peculiar case of the studied sample, the emissivity spectrum will only be computed for a 3 to 5 µm spectrum due to high inflammability of dry *Sphagnum* sample. The obtained spectra for two dry *Sphagnum* samples and one live sample are available in Fig. 6.2.12.

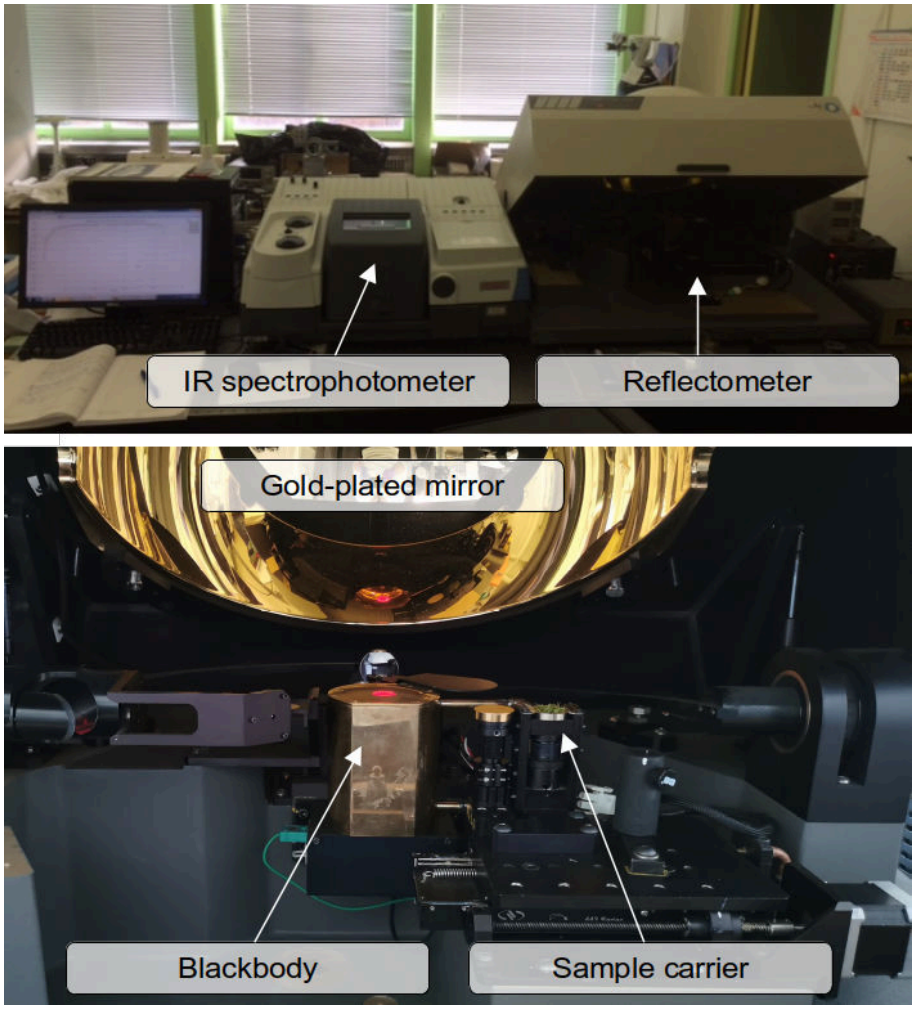

Figure 6.2.11 – *(Upper picture)* Nicolet® FTIR 6700 infrared spectrometer and Surface Optics Corporation® 100 HDR reflectometer installed at PROMES Laboratory (Odeillo, France,©Christophe Escape). *(Lower picture)*: Reflectometer closeup with living *Sphagnum* installed in the sample carrier.

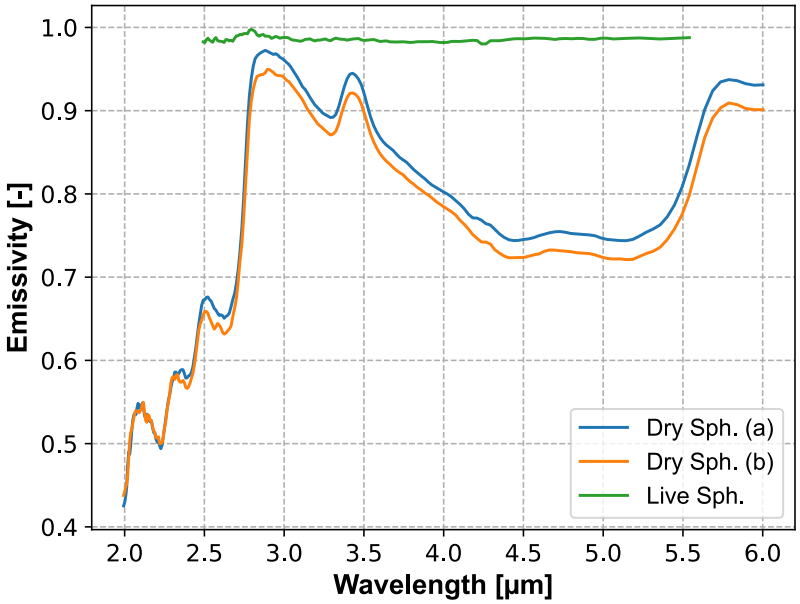

Figure 6.2.12 – Emissivity spectrum between 2 and 6 µm wavelengths for two dried *Sphagnum* samples (Dry Sph. (a) and Dry Sph. (b)) and a living *Sphagnum* sample (Live Sph.).

Dry *Sphagnum* emissivity is significantly non-linear and varies with wavelength. However, this is not the case for live *Sphagnum* sample for which emissivity is above 0.95 for the whole studied spectrum. Although the results for dry *Sphagnum* does not seem consistent with literature, the results for humid *Sphagnum* is of the order of magnitude of water emissivity on one hand (Robinson and Davies, 1972), and of plant emissivity on the other hand (Harrap, Hempel De Ibarra, et al., 2018). This lead to the conclusion that water saturation is the main driver of emissivity variation for the samples, and more extensively for field observations.

6.2.3.4 *Infrared thermography results*

The thermal temporal plots for three locations in the infrared thermographies are shown in Fig. 6.2.13.

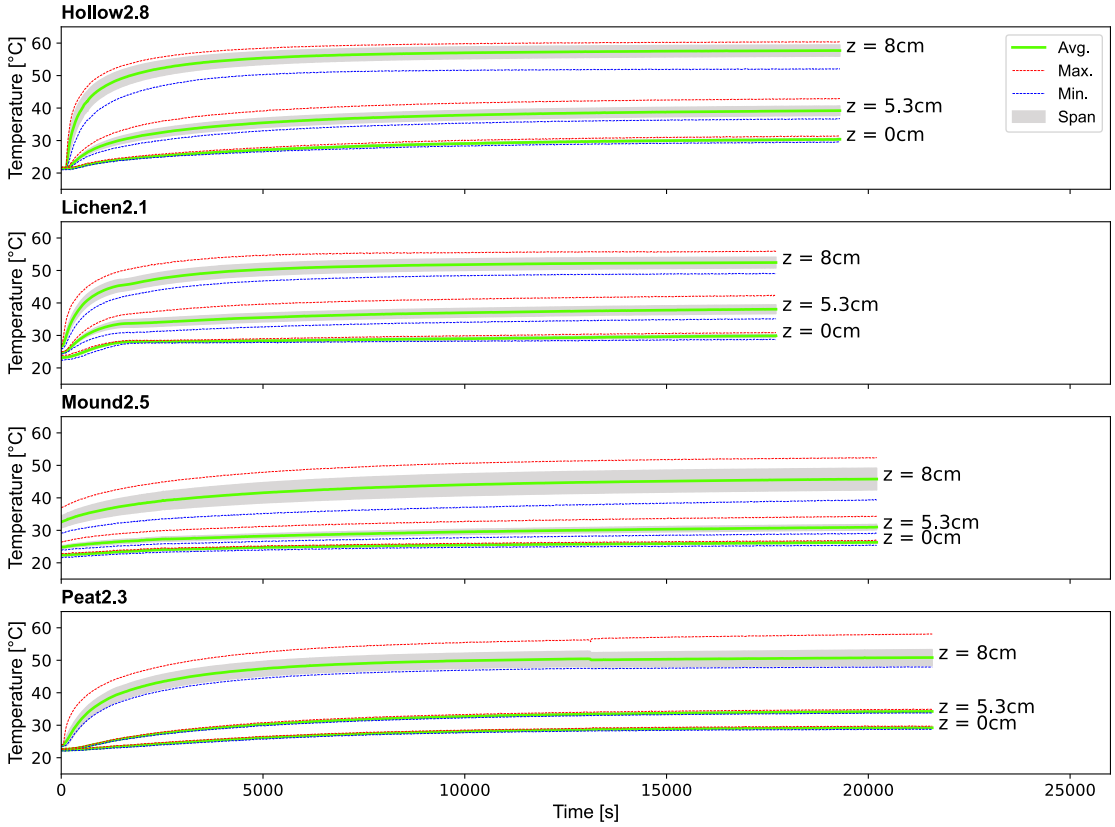

Figure 6.2.13 – Thermal evolution with time for three points located in the profile for each sample type. *Avg.*, *Min.*, *Max.* are respectively the average,minimum and maximum temperatures observed over a line of altitude z from the bottom of the sample. Span corresponds to the thermal envelope observed locally for the three studied points.

As for thermocouple measurements, steady-state heat transfer for all four studied samples is reached after approximately between 20 minutes and 60 minutes of heating from the top. Reached temperatures are consistent for all four samples for the nearest thermocouple (z = 8 cm). Thermal span is reducing with depth. Final thermal equilibrium for all four samples are available in Fig. 6.2.14. One can see that the vertical profiles are not similar between the samples. Peat2.3 is the sample that shows the least oscillation with depth whereas Mound2.5 present the most heterogeneity in the thermal profile.

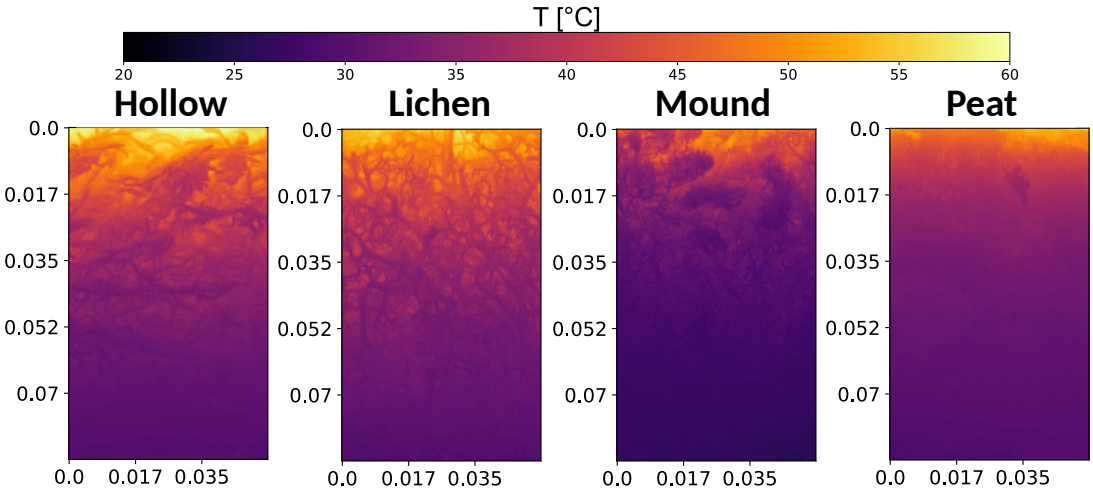

(a) Infrared plots.

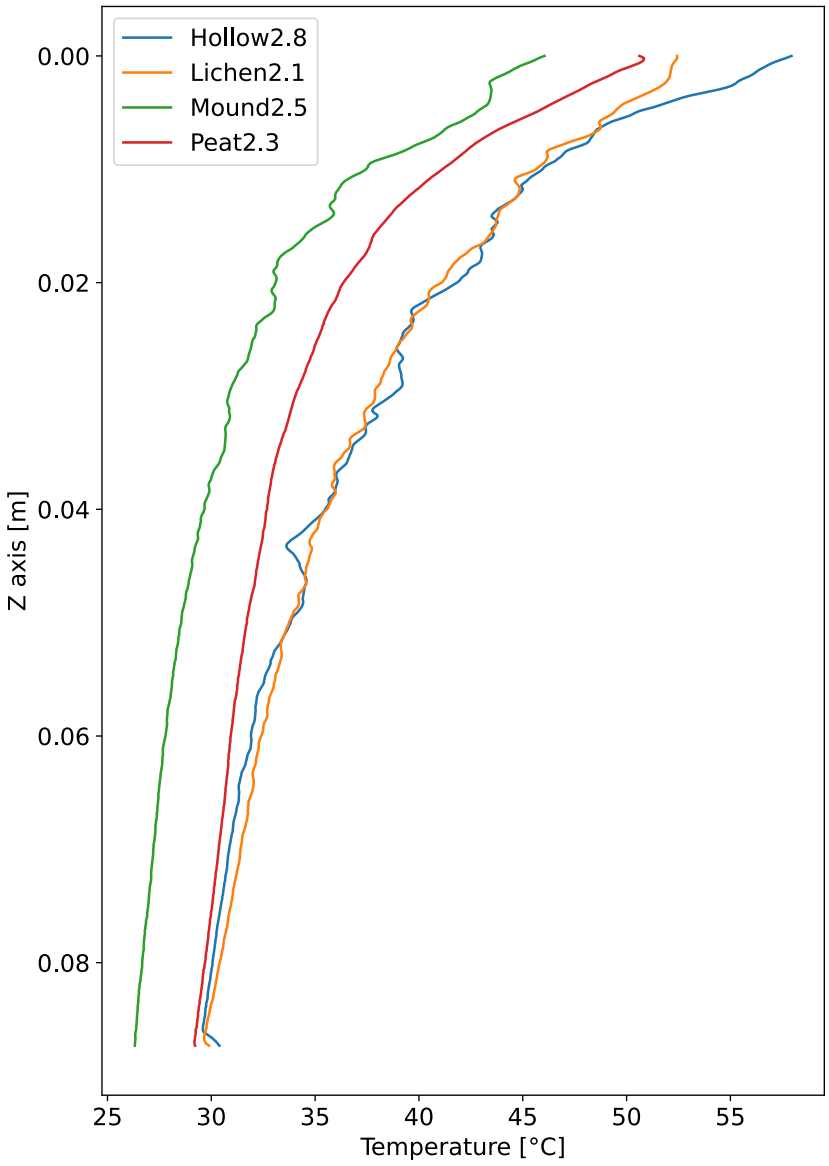

(b) Temperature curves.

Figure 6.2.14 – Infrared image and temperature profile for each sample type after the thermal equilibrium is reached (at t+3600 s).

6.2.3.5 *Interpretations*

In Fig. 6.2.13, one can see that steady-state heat transfer is reached in about one hour of heating and is consistent in time. Hollow2.8 is the sample that shows the fastest steady-state stabilization. Mound2.5 has a distinct thermal behavior in the sense that thermal equilibrium is somehow partial in the first hour and then stabilizes slowly compared to the other samples.

Lichen2.1 have a slightly different behavior for the steady-state heat transfer appearance. In the beginning, all three temperatures rises as for the other samples type. However, a plateau in temperatures appears at t+1500 s. Internal temperatures then continues to rise and reaches steady-state after t+2000 s. This peculiar behavior has been identified in the early stage of the thermal properties of lichen. Indeed, lichen sample tend to shrink in a first instance and dilate in a second phase. As lichens are consisting of a symbiotic association, it is reasonable to assume that the lichen sample has still metabolic activity and hence heating it causes a desiccation phenomenon. Then, dilatation is assumed to be standard thermal expansion. Assessments of this phenomenon is available in Appendix 6.A.1. Thermal expansion is although not visible for other samples, and especially for *Sphagnum* samples. This observation can be put into perspective of the results of conservation against drying (Kämäräinen et al., 2018). It is possible to assume that dry *Sphagnum* does not have significant thermal expansion when it is heated.

One can note that the thermal depth profile at thermal equilibrium for Peat2.3 sample is the most homogeneous among the four samples. This relative homogeneity in the thermal profile can be explained by the fact that Peat2.3 is the most compacted and the least porous sample and moreover the most carbon-rich sample. This composition is assumed to reduce the radiation scattering of the surface. The layered aspect of peat samples can limit the validity of the effective properties in this case and has to be taken into account in real-condition thermal acquisitions.

6.2.4 *Laser-Flash acquisitions*

Among with the experimental setup based on the EN 12667 norm, there are other thermal properties assessment techniques. One of the most common in industry material thermal properties assessment is the Laser-Flash method. In this study, 18 Laser-Flash shots were done using a Netzsch LFA 457 Micro-Flash™device installed at PROMES laboratory (Odeillo, France). The shots were performed in a partial void and a confined argon atmosphere to avoid sample's oxidation. The shots had a duration of 8 s. A summary of the measurements is available in Table 6.2.2. Raw data is available in Appendix 6.A.2.

	$N_{measures}$	$N_{overshoot}$	N_{valid}	κ_{LFA} **[m².s⁻¹]**
Dry Sph.	18	2 (n°7,n°8)	7 (n°11-18)	$8.77 \times 10^{-7} \pm 9.65 \times 10^{-8}$
Living Sph.(a)	11	1 (n°11)	10 (n°1-10)	$8.75 \times 10^{-7} \pm 8.52 \times 10^{-8}$
Living Sph. (b)	9	0	9	$7.71 \times 10^{-7} \pm 6.16 \times 10^{8}$

Table 6.2.2 – Summary table of measurements acquired using Netzsch LFA 457 MicroFlash™ (PROMES laboratory, Odeillo, France).
$N_{measures}$: Total number of measurements done during the experimental campaign;
$N_{overshoot}$: Number of values that failed during the experiments;
N_{valid}: Number of values that are taken into account for κ_{LFA}computation.

Experimental effective thermal diffusivities using the Laser-Flash method are spreading around 8×10^{-7} m².s⁻¹ with a good reproducibility over the shots, which is representative of an insulative material. These effective thermal diffusivities are close to some available literature about *Sphagnum* thermal properties (Beringer et al., 2001; Soudzilovskaia et al., 2013). The values are consistent whether the sample is dry or living, suggesting that volumetric heat capacity and thermal conductivity are compensating each other in this case. The test done with Laser-Flash acquisition allows validating the measurements done with the house-built thermal conductivity measurement system.

6.2.5 *General synthesis on experimental thermal studies*

In this section, an experimental assessment of the effective thermal properties has been done. The experimental methodology mainly relies on the EN 12667 standard to compute effective thermal conductivity of this porous medium. A general synthesis of the effective thermal conductivity for each studied sample is available in Table 6.2.3. The results show a good adequacy with previously published values, which are either field values or analytically assessed values. It is then possible to retrieve volumetric heat capacity from the Laser-Flash experiments done at the PROMES laboratory (subsection 6.2.4) for *Sphagnum* mosses or with previously published data for lichen and peat (Table 6.1.2). One can remark that the computed thermal diffusivities are all in the order of 10^{-7} $m.s^{-1}$, which is representative of an insulative porous medium.

	λ_{eff} [W.m^{-1}.K^{-1}]	α_{eff} [m^2.s^{-1}]	Cw_{eff} [J.m^{-3}.K^{-1}]
Hollow *Sphagnum*	6.817×10^{-2}	8.77×10^{-7}	7.77×10^4
Lichen	5.015×10^{-2}	1.00×10^{-7}	5×10^{5}‡
Mound *Sphagnum*	3.74×10^{-2}	8.77×10^{-7}	4.27×10^4
Peat	4.058×10^{-2}	1.62×10^{-8}	2.5×10^{6}*

Table 6.2.3 – Effective thermal value synthesis using the obtained experimental data available in Table 6.2.1 and the measured thermal diffusivity values acquired using Laser-Flash analysis shown in Table 6.2.2. ‡ Volumetric heat capacity value retrieved from Porada et al. (2016). * Volumetric heat capacity value retrieved from Beringer et al. (2001).

The complementary use of infrared thermography (section 6.2.3) can allow one to precisely observe the propagation of the heat front, giving clues on the nature of the transient heat transfer phase inside this porous medium. However such experimental setup gives the value for a averaged medium accounting for both low vegetation material and air contained in the porous medium.

Many parameters can influence effective thermal properties of such porous media composition (water saturation, porosity and particle size, Farouki, 1981). There are numerous models for thermal conductivity estimation in soils and more widely for porous media. The different models for the computation of an effective thermal conductivity are discussed in section 2.3.2.3. The geometric mean of each material thermal conductivity is currently the most used equation for porous media thermal conductivity. One of the oldest model is the one developed by de Vries (1963), followed by Deardorff (1978) and Ogée and Brunet (2002) One can refer to N. Zhang and Z. Wang (2017) to get a good idea of the variety of existing models.

As it was established for hydraulic properties, field values representativeness can be questionable due to the compressibility factor of the low vegetation layer. The same question raises from thermal properties assessments. The main issue here is that the thermal properties' values obtained either experimentally or with field measurements are dependent of the local thermodynamics at the scale of a study site or even of a specific plot in a study area. These values are to be considered as effective properties of the low vegetation cover due to their dependence to macroscale heterogeneities. In this part, the study aims at retrieving an intrinsic thermal conductivity for *Sphagnum* stems, lichen thallus and peat that can be then used later in a volume averaging solution. This will lead to the definition of a thermal property that is not dependent of any site location nor of a peculiar hydrodynamic condition. Nonetheless, such assessment requires first to thoroughly study the effective thermal conductivity of a set of samples in dry condition in order to have the least different physical phases in the porous media. Numerical fitting

of the *Sphagnum* intrinsic thermal conductivity is possible with thermal simulations on the reconstructed tridimensional samples.

6.3 NUMERICAL THERMAL PROPERTIES INVERSE MODELING

Experimental methods for quantifying heat transfer properties allows, for the techniques presented in section 6.1.2, a quantification of the effective heat transfer properties. However, modeling heat transfer phenomena at a pore-scale requires to know the intrinsic thermal properties of all the phases (fluid and solid) present in the given porous medium. In this section, a inverse modeling is conducted from the experimental effective values obtained in section 6.2.2.3. For this purpose, a modified version of the standard heat diffusion solver implemented in the open-source CFD toolbox *OpenFOAM* is used, named *FourierFoam*. The experimental setup is numerically recreated and the intrinsic thermal conductivity is retrieved by trial-and-error method, as shown in Fig. 6.3.1.

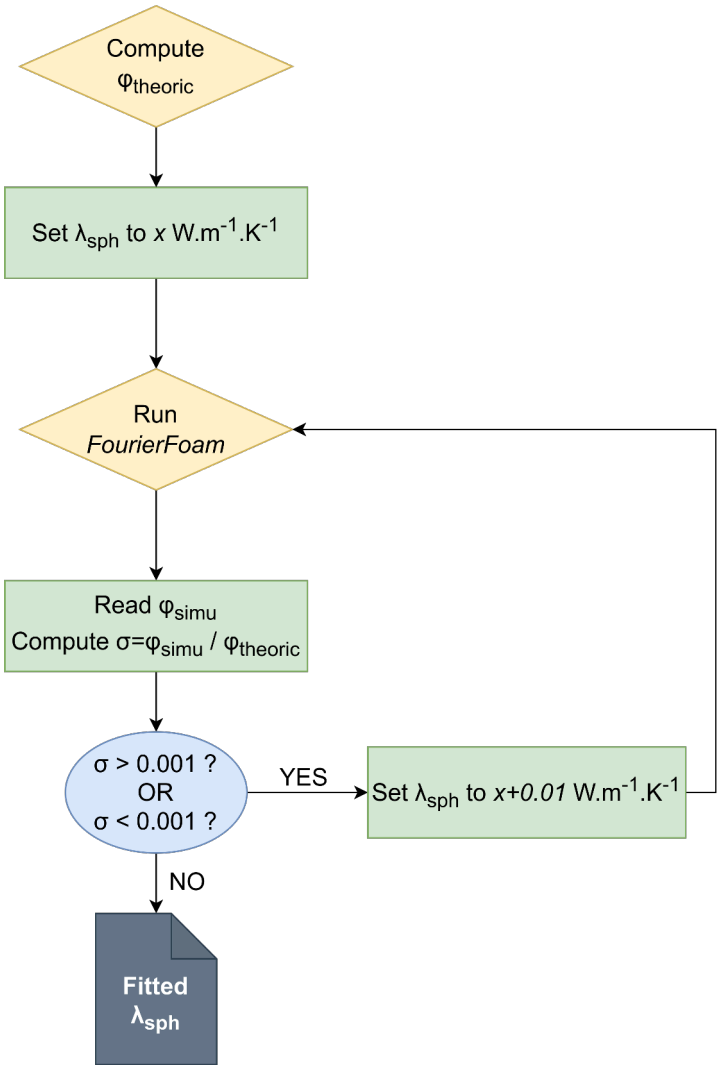

Figure 6.3.1 – Iterative thermal flux fitting workflow.

6.3.1 *Numerical heat transfer case from tomographic data*

One of the key steps in the numerical study of pore-scale heat transfer is to take into account the structural heterogeneities of the porous medium, while maintaining a balance between the accuracy of the representation of the porous medium and the size of the simulation domain. Here, in the case of heat transfer, it is necessary to solve the general heat equation in all the fluid and solid domains making up the porous medium, as opposed to a single-phase flow as presented in Chapter 5. This is all the more true in the case of solving the heat equation by finite volume differences, the standard solving method of OpenFOAM solvers. Two types of mesh are possible when solving an equation on a finite-difference simulation domain: unstructured mesh and structured mesh. The difference between these two mesh types is illustrated by an example of a square mesh, shown in Fig.6.3.2.

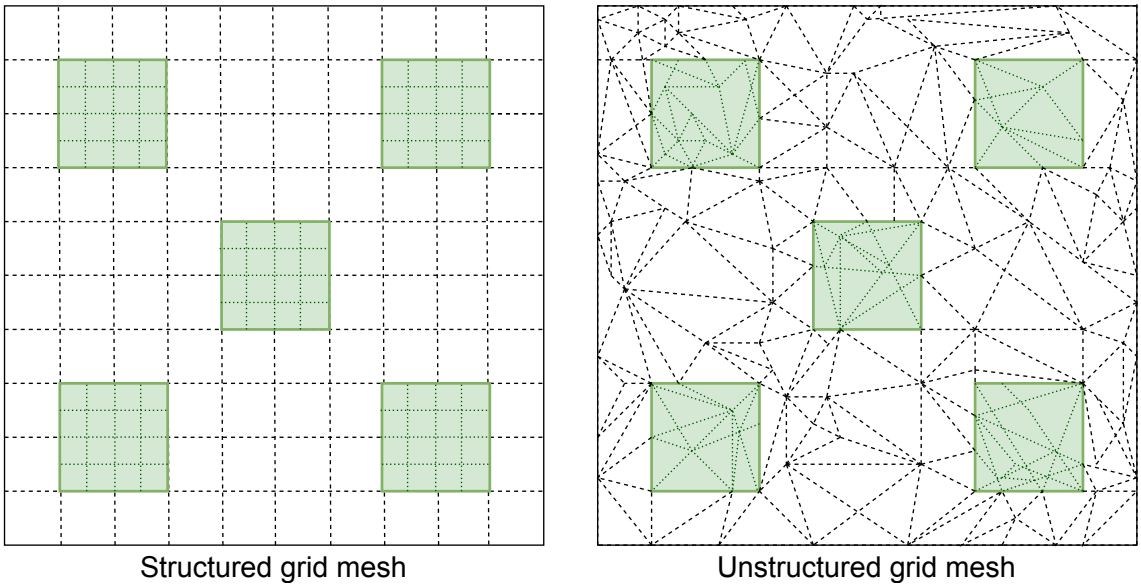

Figure 6.3.2 – *(left side)* Unstructured mesh *(right side)* structured mesh.

The advantage of unstructured meshing is that it allows a finer description of the curves of an object. However, the presence of numerous curves of complex shapes generates a quantity of non-cubic meshes (including triangular or tetrahedral meshes) causing stability problems in solving equations by finite volume difference. Structured meshes, on the other hand, cannot be used to finely define the curves of an object (in which case we observe aliasing of the interface), but the stability of the calculation is guaranteed this time, as the interface between the two domains. When solving a thermal transfer between two phases, the meshes representing the fluid and solid phases must match. Meshing tools for complex shapes are available in *OpenFOAM*, but meshing the exterior and interior of a complex structure often causes problems of representativeness when

solving for the fluid-solid interface. X-ray tomography performed on samples provides a representation of the entire structure of porous media in the form of a cubic mesh (the voxels). In the studied case, the root morphological structural information comes from X-ray tomographies done at a given resolution which is around 90 µm.voxel^{-1} (see section 4.2). This resolution is the minimum size that is reachable in the studied structure.

In this section, a presentation is given of the methodology created specifically for generating a numerical simulation under *OpenFOAM* based on the import of the porous structure. *OpenFOAM* offers various mesh generation tools, some for unstructured meshing (the *snappyHexMesh* tool for importing 3D objects into a *OpenFOAM* case) and for structured meshing (the *blockMesh* meshing tool). Here, the choice of generating a structured mesh directly from the tomographic image has been taken. The main identified advantage for using structured mesh in for studying tomographic samples is that there is no information loss or adding for mesh refining, as the tomographic scans gives a structured representation of an object (voxels). Interfacial phenomena are accurately modeled, although this assumption only works if the sample's resolution is sufficiently small if compared to the actual studied phenomenon. Here, the structured grid mesh generator *blockMesh* is used to create a basic mesh that has the same amount of voxels than the studied sample. Then, a custom-built parallelized cell insertion tool made using Python is used to retrieve the cell coordinates and adapt the syntax of the tomographies to *OpenFOAM* mesh syntax. The code for this Python script is available in Appendix 6.A.4. A comparison between the use of *snappyHexMesh* and the in-house built Python tool is shown in Fig.6.3.3.

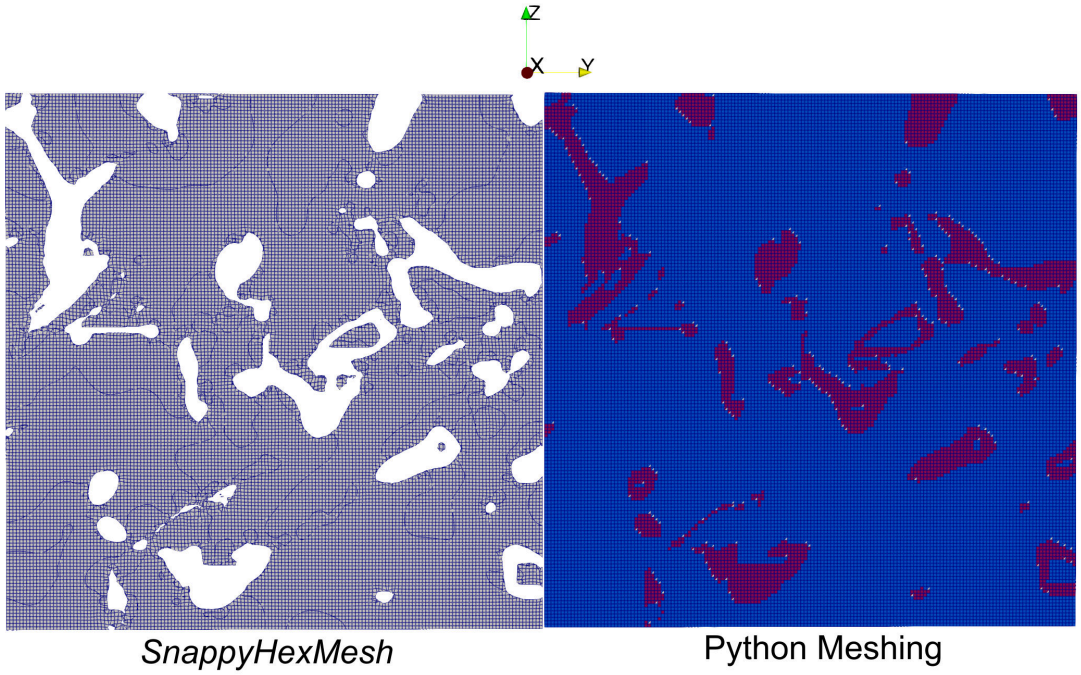

Figure 6.3.3 – *(left)* Structured meshing of a lichen sub-sample using the *SnappyHexMesh automatic meshing* tools from OpenFOAM. Note that the sample is only sampled on the void space (grey) and not inside the lichen thallii (white). *(right)* Lichen subsample meshing using the in-house built Python script for transcribing tiff images to *OpenFOAM* meshes. Edge size is 1.54 cm (160 vx).

Then, phase properties (thermal conductivity, density, specific heat capacity) can be incorporated through the *setFields* dictionary or via a phase-specific structure allowed by the *OpenFOAM* syntax. This methodology allows to create very large structured meshes that can be easily parallelized on a high core number. Also, this facilitates the implementation of as many phases as wanted.

The structured grid is then used for the computation of large heat transfer simulation throughout this study. First, a pure conductive problem is considered with the solving of a diffusion equation in the modeled porous media.

6.3.2 *One-equation heat diffusion model: the* FourierFoam *solver*

Among with the heat transfer algorithm available in *OpenFOAM*, *laplacianFoam* is a purely conductive heat transfer solver. The *laplacianFoam* solver is adapted to this peculiar heat transfer problem by changing the variable type of the thermal diffusivity Some detailed information about the equation implementation of *FourierFoam* is given hereafter. Then, some convergence study results are discussed in subsection 6.3.2.3. Then, the results for some simulations are discussed in section 6.3.2.4.

6.3.2.1 *Algebra basis*

The default implemented *laplacianFoam* in *OpenFOAM* is a finite-volume solver for pure diffusion equation written under the form given in Eq. 6.8:

$$\frac{\partial T}{\partial t} - \nabla \cdot (\kappa \nabla T) = S_T \tag{6.8}$$

In the standard implementation, the *laplacianFoam* solver only uses temperature as spatial scalar input values. The thermal diffusivity is considered constant throughout every part of the mesh, meaning that every node of the mesh has the same thermal conductivity. Another implementation of the heat equation is indeed compulsory to cope with the different phases in our model. To do so, thermal diffusivity is decomposed with thermal conductivity and heat capacity. These values are then parsed in conjunction with temperature information along the mesh. The solved equation becomes then:

$$\rho C_p \frac{\partial T}{\partial t} = \nabla \cdot (\lambda \nabla T) \tag{6.9}$$

One can note that there are no source or sink term in this model. According to Eq. 6.9, the heat flux vector $\overrightarrow{\phi_F}$ can be written as:

$$\overrightarrow{\phi_F} = -\lambda \nabla T \tag{6.10}$$

Thermal conductivity, volumetric mass and thermal capacity are then implemented as scalar field values, depending on the two phases implemented in this structure, namely air (void space) and the sample itself (sample). This allows taking into account the morphological differences that are occurring due to the complex structure of the porous media.

6.3.2.2 *Boundary and initial conditions*

The numerical model's boundary and initial conditions are chosen to be the closest to the ones observed in the experimental setups. Indeed, the topmost surface is set at constant temperature (358 K or 65 °C) and the bottom surface is set constant at 293 K or 20 °C. The side walls are set to a zero Gradient (Neumann) boundary condition on temperature. The time to solve the results are set to 3600 s. A schematic of the boundary conditions is available in Fig. 6.3.4.

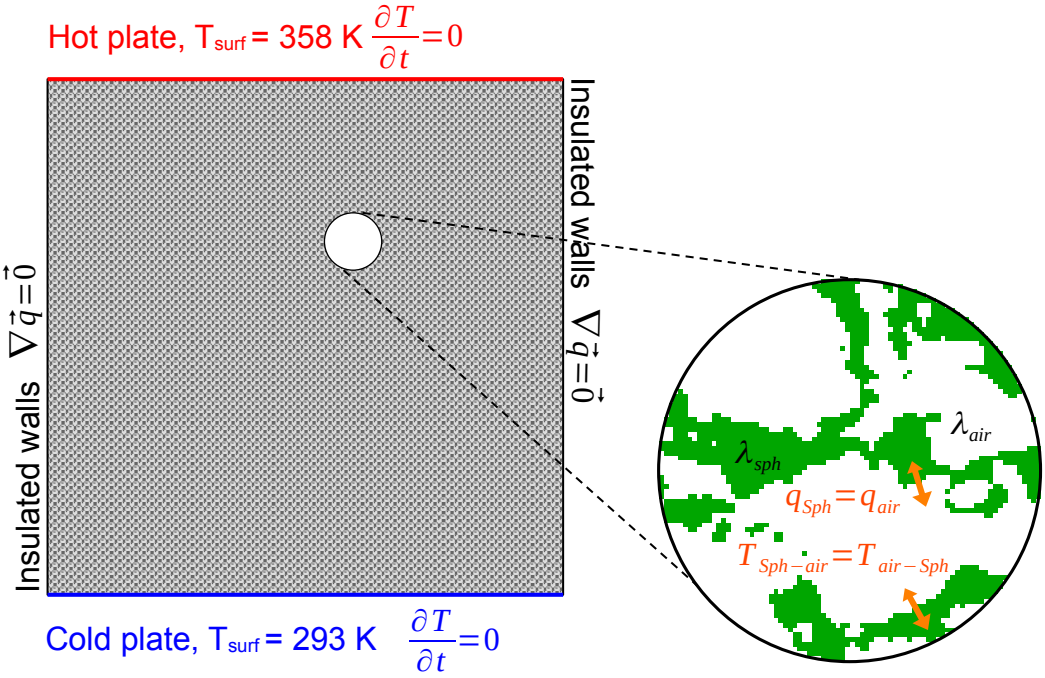

Figure 6.3.4 – Theoretical boundary condition for the inverse modeling of the experiments.

6.3.2.3 *Convergence study*

A convergence study is required to conclude on the representativeness of the results in a finite volume approach. Convergence study is made on the basis of a standardized case, considering a pore space fully occupied by air and thermal properties of wood for the solid phase (in reality *Sphagnum* moss leaf). The thermal properties of these two phases are shown in Table 6.3.1.

Phase	λ **[W.m^{-1}.K^{-1}]**	C_w **[J.m^{-3}.K^{-1}]**
Phase 1 (air at 20°C, 1kPa)	2.62×10^{-2}	1.2×10^{3}
Phase 2 (wood, epicea-type)	3.0×10^{-2}	3.2×10^{5}

Table 6.3.1 – Implemented thermal properties for the convergence study.

The segregation of cells is set according to the tomographic description of Peat2.2 sample in the mesh as shown in Figs 6.3.6-left for a complete block and 6.3.7-left for a slice in the middle section of the sample.

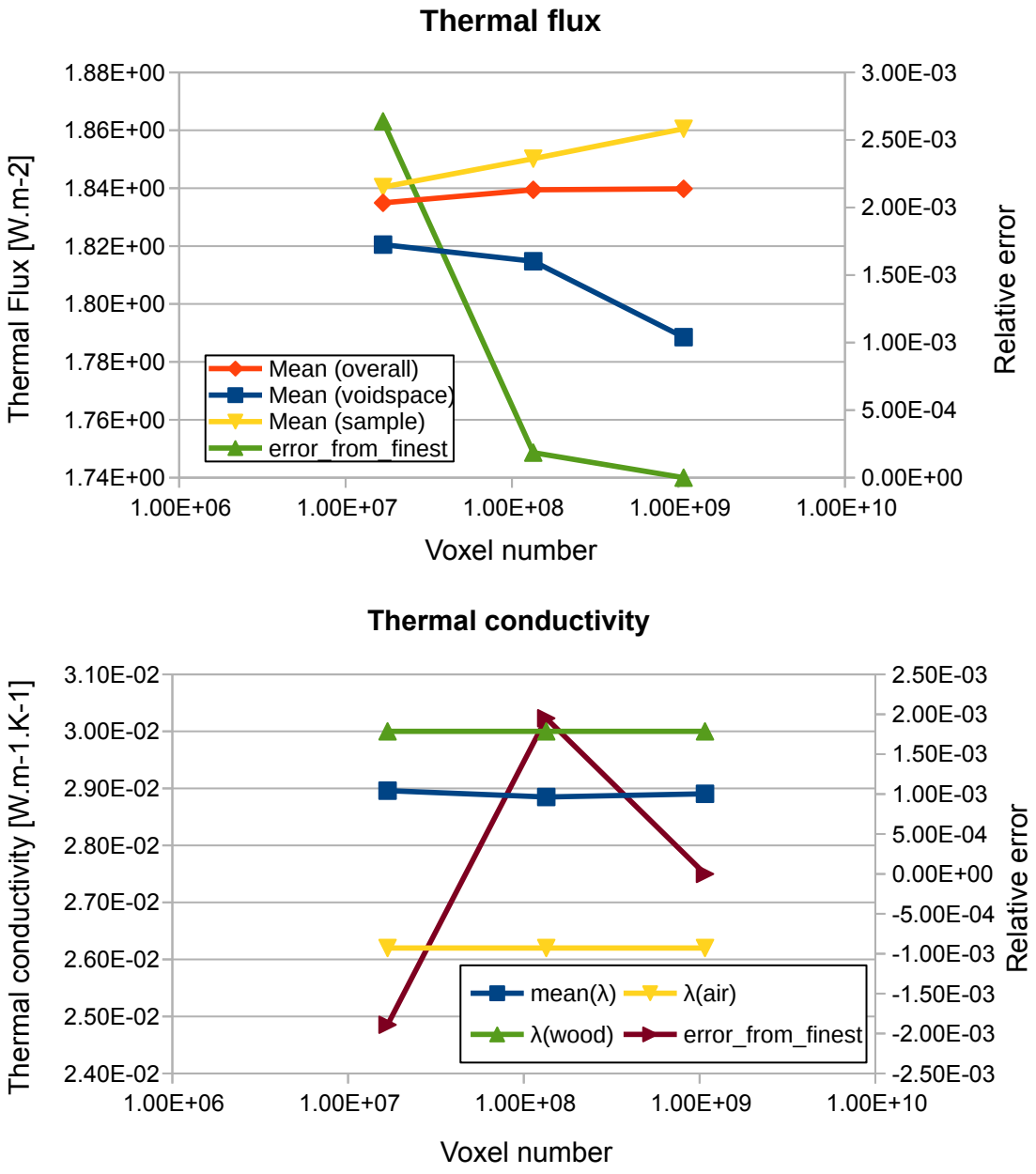

Figure 6.3.5 – *(Upper plot)* Convergence study based on computed thermal flux at the outlet *(Lower plot)* overall thermal conductivity.

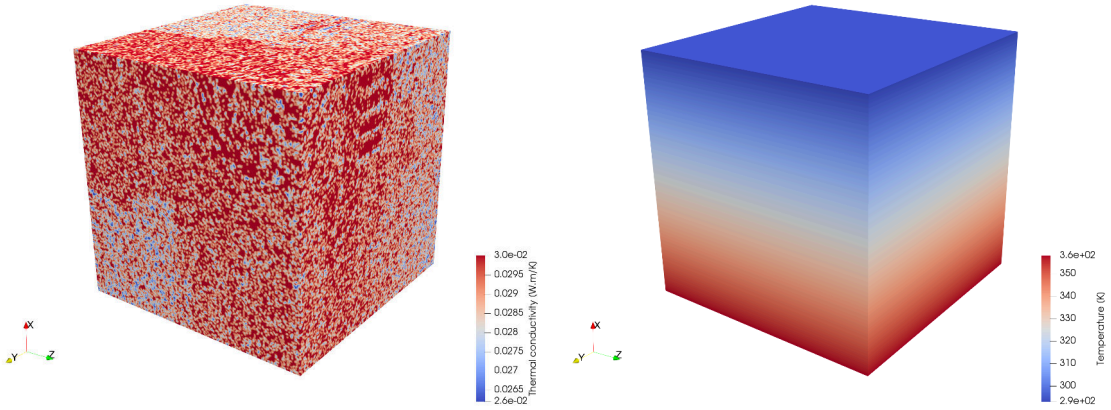

Figure 6.3.6 – *(left)* Thermal conductivity conditions applied on the mesh and *(right)* final thermal equilibrium at t + 32000s.

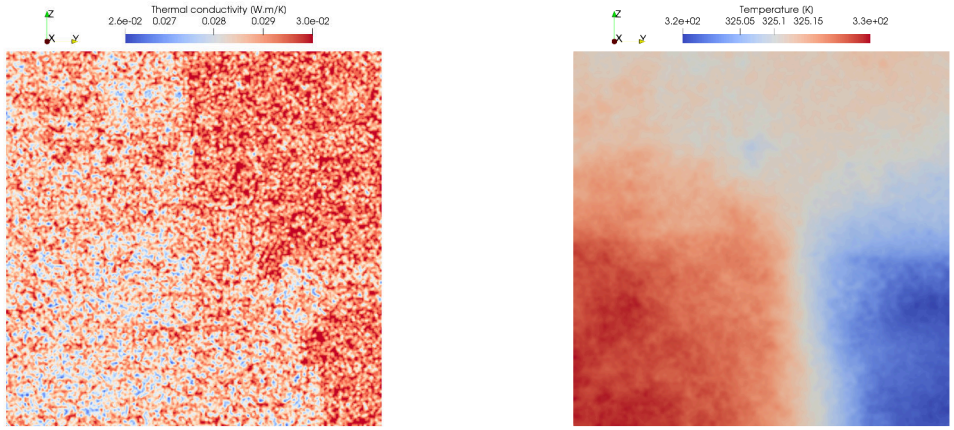

Figure 6.3.7 – *(left)* Slice at half the mesh (z=4.5 cm) with thermal conductivity plotted *(right)* local temperature field at t+32000 s.

A comparison of the relative error from the most refined mesh is done for both effective thermal flux at the outlet and effective thermal conductivity. For effective thermal heat flux, one can see that the error that the mean heat flux value is lowering if the mesh is coarser. There is no such observation for effective thermal conductivity. If comparing per-phase results, it is possible to say that the effective heat flux of the fluid phase at the outlet is decreasing when the mesh becomes coarser, and the contrary for the solid phase. The average value of the overall sample are relatively consistent between all convergence cases. For thermal conductivity, such variations are not visible and each studied refinement show quite good consistency. Such variation in effective heat flux can be explained by the fact that increasing the mesh refinement increases the heat dispersion between the cells as the pores are described with more cells than for coarser meshes. In the contrary, the refining increases heat diffusion capacities. As effective thermal

conductivity is nevertheless consistent, it can be interesting to choose the least refined case to avoid the use of unnecessary amount of computational resources.

6.3.2.4 *Numerical effective thermal flux fitting*

Experiments allows retrieving an effective thermal conductivity that is representative of an averaged value, accounting for the effects of every phase present in the porous medium. The measured heat flux is consequently effective heat flux (see section 2.3.2.3). Then we can compare simulated and measured effective heat fluxes. There is a discrepancy between measured effective heat flux and the one simulated in previous part, and we assume that this difference is due to the fact that we considered arbitrary thermal properties for *Sphagnum* phases. Then we make a fitting of these thermal properties for matching simulated results and measurements, which will give us an estimate of *Sphagnum* thermal properties by inverse modeling. To do so, a dichotomous approach is conducted. A preliminary value for λ_{Sph} of $10^{-2}\,W.m^{-1}.K^{-1}$ is set in the *setFields* dictionary. After the simulation is completed, outlet (bottom patch) heat flux can be computed. The resulting heat flux is compared with the theoretical heat flux obtained with Eq. 6.10. *Sphagnum*'s thermal conductivity is then modified according to the error between the theoretical and the simulated heat flux is significant to a precision of $10^{-2}\,W.m^{-1}.K^{-1}$.
The maximal diffusion time is set to one hour (3600 s) which corresponds to reach thermal equilibrium during the experiments. A visualization of the thermal equilibrium for each sample type are available in Fig. 6.3.8. The obtained thermal flux at the outlet plotted with the equivalent experimentally assessed values are available in Fig. 6.3.9.

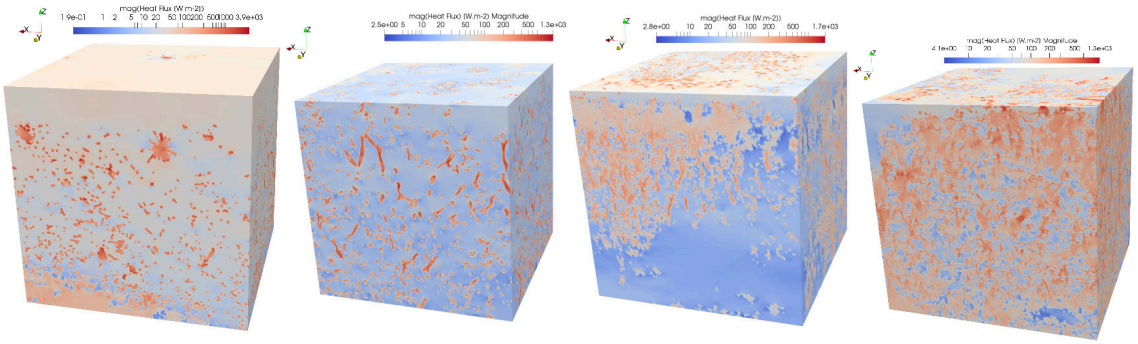

(a) Hollow **(b)** Lichen **(c)** Mound **(d)** Peat

Figure 6.3.8 – Heat flux computations (in $W.m^{-2}$) for each sample type. The tridimensional reconstructions are shown for t+3600 s.

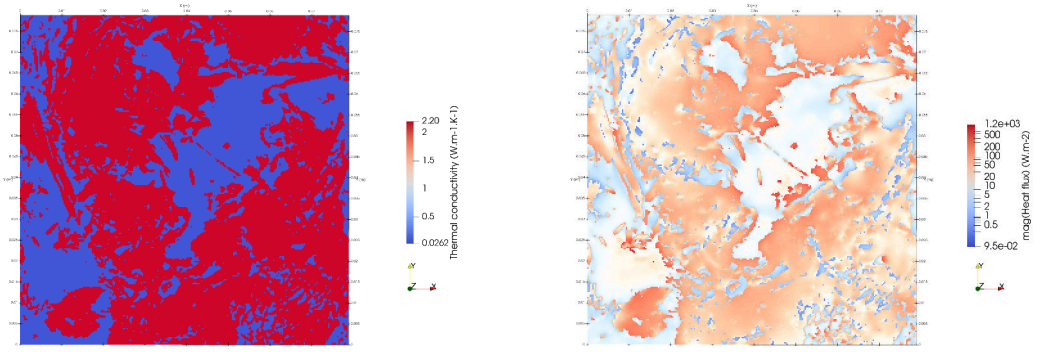

(a) Hollow *Sphagnum* sample

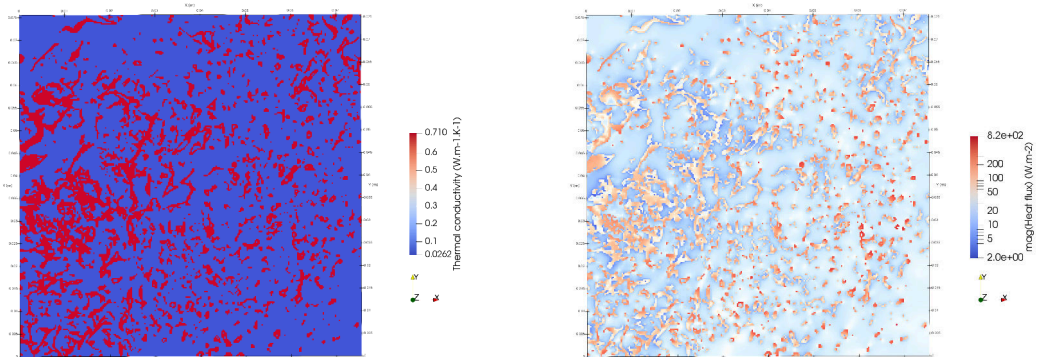

(b) Lichen sample

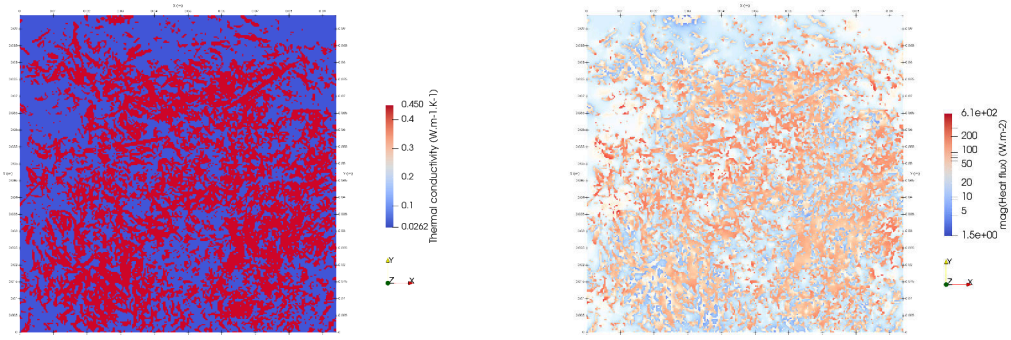

(c) Mound *Sphagnum* sample

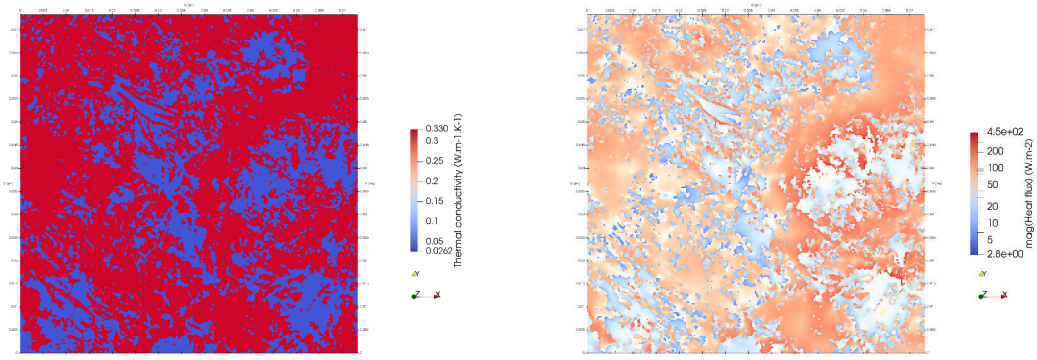

(d) Peat sample

Figure 6.3.9 – (*left*) Thermal conductivity (in $W.m^{-1}.K^{-1}$) and (*right*) computed heat flux (in $W.m^{-2}$) for the outlet wall at t+3600s.

	$\phi_{th}\ [W.m^{-2}]$	$\phi_{simu}\ [W.m^{-2}]$	$\sigma_{err}\ (\%)$	$\lambda_{sphagnum}\ [W.m^{-1}.K^{-1}]$
Hollow *Sph.*	56.06	54.99	1.905	2.2
Lichen	43.05	42.39	1.48	7.1×10^{-2}
Mound *Sph.*	25.60	27.44	−7.18	4.5×10^{-2}
Peat	43.03	41.54	3.48	3.3×10^{-2}

Table 6.3.2 – $\lambda_{Sphagnum}$ (in W.m^{-1}.K^{-1}) fitted according to the experimental thermal flux and the theoretical heat flux ϕ_{th} based on the effective thermal conductivity of Table 6.2.1.

6.3.2.5 *Discussions*

The difference between the thermal conductivities of both studied phases (here air and organic matter for instance) is crucial in the thermal regime setting. It is possible to note that the highest heat flux values are situated on cells that are corresponding to organic matter (Fig. 6.3.8). This behavior is due to the fact that there is a factor of 10 to 100 in thermal conductivities between both phases, as shown in Table 6.3.2. Although the heat flux is still high for the organic matter cells (up to 1000 $W.m^{-2}$), the surface is very small making the heat flux density high. However, one can note that the air phase has a low thermal flux value, with such values matching the effective heat fluxes measured experimentally. One can also note that the heat flux of the peat sample is in average lower than for the hollow sample, although it is less porous, therefore having more highly conductive surfaces.

Some reserves can be emitted on the fact that the *FourierFoam* solver is a one-equation model. Indeed, this means that the only considered heat diffusion mechanism is conduction. Resolving heat transfer omitting convective and radiative transfers is effective in terms of computational costs, however, it is not fully representative of the real world situation.

6.3.3 *Overall conclusion on thermal properties assessment*

In this chapter, effective and intrinsic thermal properties are studied for the Arctic low vegetation cover. In a first section, the experimental study carried out using heat flux measurements and infrared thermography showed that this biological interface is insulative against atmosphere to geosphere heat transfers, especially when the samples are dried ($\lambda_{eff} \approx 10^{-2} W.m^{-1}.K^{-1}$). The obtained effective thermal conductivity values match the values found for field studies available in the literature. The obtained values highlights the insulative potential of the arctic low vegetation cover, at least in the case of dry vegetation cover.

APPENDIX

6.A APPENDICES OF CHAPTER 6.

6.A.1 *Lichen size modification due to temperature*

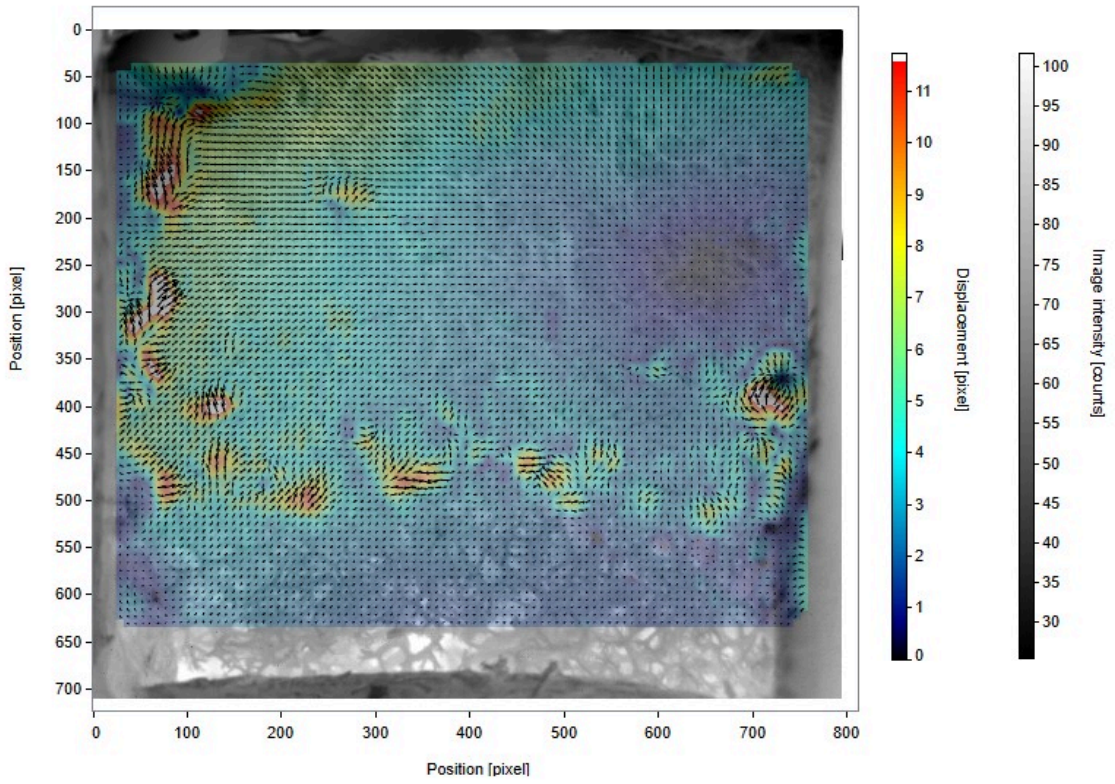

Figure 6.A.1 – Displacement vectors of Lichen structure during heating.

6.A.2 *Raw thermal diffusivity data of Laser-Flash acquisitions (PROMES laboratory, Odeillo, France)*

N° shot	Dry Sph.	Living Sph. (a)	Living Sph. (b)
1	$2.09.10^{-7}$	$8.60.10^{-7}$	$7.40.10^{-7}$
2	$5.08.10^{-7}$	$9.80.10^{-7}$	$7.10.10^{-7}$
3	$4.26.10^{-7}$	$9.70.10^{-7}$	$7.10.10^{-7}$
4	$2.53.10^{-7}$	$9.50.10^{-7}$	$8.60.10^{-7}$
5	$2.68.10^{-7}$	$9.20.10^{-7}$	$7.30.10^{-7}$
6	$1.06.10^{-7}$	$9.10.10^{-7}$	$7.50.10^{-7}$
7	$3.11.10^{-6}$	$8.50.10^{-7}$	$8.50.10^{-7}$
8	$2.05.10^{-5}$	$8.00.10^{-7}$	$8.20.10^{-7}$
9	$1.76.10^{-6}$	$7.80.10^{-7}$	$7.10.10^{-7}$
10	$1.27.10^{-6}$	$7.30.10^{-7}$	
11	$1.08.10^{-7}$	$3.10.10^{-7}$	
12	$8.25.10^{-7}$		
13	$8.15.10^{-7}$		
14	$9.43.10^{-7}$		
15	$8.21.10^{-7}$		
16	$8.96.10^{-7}$		
17	$8.21.10^{-7}$		
18	$8.09.10^{-7}$		

Table 6.A.1 – Raw thermal diffusivity data [in $m^2.s^{-1}$] data from Laser-Flash acquisitions done at PROMES Laboratory (Odeillo, France).

6.A.3 *Pre-processing algorithm for the thermal data of the thermocouples*

```
clear all
close all
clc

%Read the data from the files
d=dlmread('correction_data.csv',',',1,0);
x_data=d(:,1);
err_data=d(:,3);
```

```
%Create a 12-th order polynomial regression of the data
p=polyfit(x_data,err_data,12);
disp(size(p));


err_fit= p(1)*x_data.^12 ...
        +p(2)*x_data.^11 ...
        +p(3)*x_data.^10 ...
        +p(4)*x_data.^9 ...
        +p(5)*x_data.^8 ...
        +p(6)*x_data.^7 ...
        +p(7)*x_data.^6 ...
        +p(8)*x_data.^5 ...
        +p(9)*x_data.^4 ...
        +p(10)*x_data.^3 ...
        +p(11)*x_data.^2 ...
        +p(12)*x_data.^1 ...
        +p(13);


%======== FIGURE 1 : Plotting the error curve ==========
y_corr=d(:,2)+err_fit;
figure(1);
plot(err_fit);

%Open the data to be corrected
data=dlmread('/home/scazaura/Documents/NewDocStructure/Research/Results/
    ThermalK_expe/NF12667/sb2.5_synthesis07122022_k2000.csv',',',1,0);
hotplate_corr=data(:,2)+err_fit;
coldplate_corr=data(:,3)+err_fit;

%Some plots for demonstration...
%======== FIGURE 2 : Data correction on HotPlate ==========
figure(2)
hold on
title("Data correction on HotPlate and ColdPlate")

plot(data(:,1),hotplate_corr,
"linewidth",4);

plot(data(:,1),data(:,2),
"linewidth",4);

plot(data(:,1),data(:,3),"linewidth",4);

plot(data(:,1),coldplate_corr,"linewidth",4);
```

```
set(gca, "linewidth", 1, "fontsize", 14)
l =legend('HotPlate (corrected)', 'HotPlate (original)',
'ColdPlate (corrected)', 'ColdPlate (original)');
set(l, "location", "east",
           "fontsize",14);

ylim([10,80]);
xlabel('Time [s]',"fontsize",16);
ylabel('Temperature [C]',"fontsize",16);
hold off

%======== FIGURE 3 : Data correction on ColdPlate ==========

figure(3)
hold on
title("Data correction on ColdPlate")
plot(data(:,1),data(:,3),"linewidth",4);
plot(data(:,1),coldplate_corr,"linewidth",4);

deltaT_init=data(:,2)-data(:,3);
deltaT_corr=hotplate_corr-coldplate_corr;
errorT = deltaT_init-deltaT_corr;
set(gca, "linewidth", 1, "fontsize", 14)
legend('corrected data', 'original data');
xlabel('Time [s]',"fontsize",16);
ylabel('Temperature [C]',"fontsize",16);
ylim([10,80]);


figure(4)
hold on
plot(x_data,deltaT_init);
set(gca, "linewidth", 1, "fontsize", 14)
plot(x_data,deltaT_corr);

outdata(:,1) =data(:,1);
outdata(:,2) =hotplate_corr;
outdata(:,3) =coldplate_corr;

%Write the corrected data and exit.

dlmwrite('CorrectedData.csv',outdata);
```

6.A.4 *Mesh conversion algorithm for implementing tif stacks as OpenFOAM mesh.*

```
import tifffile as imgio
import numpy as np
import sys
import os
from progress.bar import IncrementalBar
import multiprocessing as mp

__version__ = '1.1'

# How to use :
# python3 StructuMeshing1.py <tif_img> <n_cpus>

def parallel_worker(img_size,coord_arr, ncell_arr):
    name = mp.current_process().name
    pid = mp.current_process().pid
    print("Worker {} (PID : {}) is working on an array of {} values.".format(name,
        pid,coord_arr[2].size))

    sample_arr = np.empty(shape=coord_arr[0,:].size,dtype=int)
    print(coord_arr[0, :].size)


    for index in range(0, coord_arr[0,:].size):
        # Because ncellid upon x is z*(Nx*Ny)+(y*Ny)+x

        sample_arr[index] = int((coord_arr[2, index] * (img_size[0] * img_size[1]))
             + (coord_arr[1, index] * img_size[1]) \
                 + coord_arr[0, index])

        # Write it into an array
        #sample_arr = np.append(sample, sample_arr)

        #voidspace_mask = np.isin(ncell_arr, sample_arr)
        #print("lol",voidspace_mask.size)
        #voidspace_arr = ncell_arr[voidspace_mask]
    return sample_arr

def tif_to_cellzonesandsets_parallel(filepath, n_cpus):
    os.makedirs('PolyMesh/sets',exist_ok=True)
    # Texts for the definitions
    foam_header_zone = ["FoamFile \n",
                        "{ \n",
                        "    version    2.0; \n",
                        "    format     ascii; \n",
```

```
                    "    class       regIOobject; \n",
                    "    location        \"constant/polyMesh\"; \n",
                    "    object      cellZones; \n",
                    "} \n"]
zone_header_voidspace = ["2 \n",
                         "(\n",
                         "voidspace \n",
                         "{ \n",
                         "    type cellZone; \n",
                         "cellLabels     List<label> \n"
                         ]
zone_header_sample = ["sample \n",
                      "{ \n",
                      "    type cellZone; \n",
                      "cellLabels     List<label> \n"
                      ]
cellzone_eof = [") \n",
                "; \n",
                "} \n"]
foam_header_sets_sample = ["FoamFile \n",
                           "{ \n",
                           "    version     2.0; \n",
                           "    format      ascii; \n",
                           "    class       cellSet; \n",
                           "    location        \"constant/polyMesh/sets\"; \n",
                           "    object      sample; \n",
                           "} \n \n"]
foam_header_sets_voidspace = ["FoamFile \n",
                              "{ \n",
                              "    version     2.0; \n",
                              "    format      ascii; \n",
                              "    class       cellSet; \n",
                              "    location        \"constant/polyMesh/sets\"; \n",
                              "    object      voidspace; \n",
                              "} \n \n"]

# Read image and initialize solid matrix
img = imgio.imread(filepath)

# CAREFUL ! array is [stack,x,y] so the first index is actually the stack
print("Image Loaded")
# Get the size of the image and set it into an array
img_size = np.array((img[0,0,:].size,img[0,:,0].size,img[:,0,0].size),dtype=int
    )
print(img_size,img.size)
# Check in the whole stack for Booleans (This is insanely fast !!)
```

```
solid_matrix = np.where(img == 255)

#Concatenate then into x y z array
coordlist = np.vstack([[solid_matrix[2], solid_matrix[1], solid_matrix[0]]])

# Create an array that matches the blockMesh generator
total_ncell = np.arange(start=0, stop=(img[0,0,:].size * img[0,:,0].size * img
    [:,0,0].size), step=1)
ncell_arr = np.empty(shape=0)

# Cut the arrays to comply with parallel processing1
coordlist_cut = np.array_split(coordlist, n_cpus,axis=1)  # Allows inequal
    division of the arrays
total_ncell_cut = np.array_split(total_ncell, n_cpus)

print("Calculating ncells")
results_sample = []
results_voidspace = []
with mp.Pool(processes=n_cpus) as pool:
    for process in range (0,n_cpus):
        results_sample.append(pool.apply_async(parallel_worker, args=(img_size,
            coordlist_cut[process], total_ncell_cut[process])))
    output =np.array([p.get() for p in results_sample],dtype=object)

del results_sample

sample_arr = np.sort(np.concatenate(output))
print("Making difference for voidspace")

voidspace_arr=np.setdiff1d(total_ncell,sample_arr,assume_unique=True)
test_arr = np.in1d(voidspace_arr,sample_arr,assume_unique=True)
print("test",np.where(test_arr==True))
print("Sample cell count is {}".format(sample_arr.size))
print("Voidspace cell count is {}".format(voidspace_arr.size))
print("Control size {}" .format(sample_arr.size + voidspace_arr.size))


# DEBUG
np.savetxt("DEBUGs.csv",sample_arr)
np.savetxt("DEBUGv.csv", voidspace_arr)
np.savetxt("DEBUGt.csv", total_ncell)
# Write to a cellSet file...
cellSetfilesample = 'PolyMesh/sets/sample'
print("Writing cellSets...")
with open(cellSetfilesample, 'w') as thefile:
    thefile.writelines(foam_header_sets_sample)
```

```
        thefile.write(str(sample_arr.size))
        thefile.write("\n")
        thefile.write("(\n")
        for index in range(0, sample_arr.size):
            thefile.write(str(int(sample_arr[index])) + "\n")
        thefile.write(")\n")
    cellSetfilevoidspace = 'PolyMesh/sets/voidspace'
    with open(cellSetfilevoidspace, 'w') as thefile:
        thefile.writelines(foam_header_sets_voidspace)
        thefile.write(str(voidspace_arr.size))
        thefile.write("\n")
        thefile.write("(\n")
        for index in range(0, voidspace_arr.size):
            thefile.write(str(int(voidspace_arr[index])) + "\n")
        thefile.write(")\n")

    # ...And then the same for the cellZones
    cellzonefile = 'PolyMesh/cellZones'

    print("Writing cellSets...DONE")
    print("Writing cellZones...")
    with open(cellzonefile, 'w') as thefile:
        thefile.writelines(foam_header_zone)

        thefile.write("\n")
        thefile.writelines(zone_header_voidspace)
        thefile.write(str(voidspace_arr.size))
        thefile.write("\n")
        thefile.write("(\n")
        for index in range(0, voidspace_arr.size):
            thefile.write(str(int(voidspace_arr[index])) + "\n")
        thefile.writelines(cellzone_eof)
        thefile.writelines(zone_header_sample)
        thefile.write(str(sample_arr.size))
        thefile.write("\n")
        thefile.write("(\n")
        for index in range(0, sample_arr.size):
            thefile.write(str(int(sample_arr[index])) + "\n")
        thefile.writelines(cellzone_eof)
        thefile.write(")\n")
    print("Writing cellZones...DONE, exiting")


if __name__ == '__main__':
    tif_to_cellzonesandsets_parallel(str(sys.argv[1]), int(sys.argv[2]))
```

Part IV

ONGOING WORK AND PERSPECTIVES

7

EXPERIMENTAL ASSESSMENT OF RADIATIVE HEAT TRANSFER INFLUENCE IN THE OVERALL HEAT TRANSFER

In the EN 12667 standard allowing the assessment of effective heat conductivity of a porous medium (section 6.2) as well as in the inverse modeling (section 6.3), the heat source is made of a conductive heat plate. The use of a purely conductive heat transfer means that convective and radiative terms can be neglected in the general heat equation. However, this heat transfer mechanism is not representative of the heat input that can be found in the natural environment. Even though the assumption made of a solely conducive heat transfer is valid for long scale time periods (over a day), this hypothesis cannot be valid anymore if one studies the heat flux on a daily basis where the solar radiative heat flux variation becomes non-negligible. This is particularly the case for dry summers with deep active layer and no snow cover. On a smaller scale, it is also necessary to consider the effect of radiative transfer from solar radiation on one hand, and convection generated by evapotranspiration from vegetation cover on the other. Therefore, a quantification of an effective thermal diffusivity accounting for radiative heat transfer, and hence an effective thermal conductivity is interesting to compare with pure conduction thermal conductivity. The assumption of a radiative transfer is common in the method used for quantitative analyses of field results, such as the ones presented by Kellner (2001) and Kettridge and Baird (2007). In these both studies, a *Triple Probe Heat Pulse Sensor*, (TPHPS) based on the transient heat line thermal properties' assessment methodology initially proposed by Bristow et al. (2001). This method aims at monitoring long-term temperature and thermal conductivity data for site monitoring and water content quantification. This methodology can take into account the effect of daily solar load on the measurement of the thermal conductivity. In the spirit of such work, a small study was carried out to assess the impact of radiative transfer in the overall heat transfer mechanism. In the following section, a presentation of the analytical method for the thermal diffusivity quantification from transient radiative heat transfer is shown. The early results obtained on one dry sample and one living sample are then compared to

conclude over the necessity to include radiative transfer in a future definition of a an effective boundary condition for the arctic low vegetation cover.

7.1 EXPERIMENTAL ASSESSMENT OF RADIATIVE HEAT TRANSFER IMPACTS

7.1.1 *Radiative heat transfer mechanism and assessment techniques*

The use of a periodic thermal regime for quantifying thermal properties is a technique that is well established in the literature. This method has the advantage to contain the three components of heat transfer in the same experiment (heat conduction, heat convection, radiative transfer). This is also the method often used for the quantification of the heat properties of soils. Ångstrom (1862) is the first paper to deal with periodic thermal regime for such purpose. Some more recent papers also deals with this problematic (see Zhu (2016) for an example of such processing). The general workflow used to retrieve thermal properties using a periodic transient approach is based on the methodological description made by Bosanquet and Aris (1954).

From Eq. 2.16, one can write a modified form of the heat equation taking into account radiative transfer as follows:

$$\frac{\partial \theta}{\partial t} = \kappa \frac{\partial^2 \theta}{\partial x^2} - \varepsilon \theta \tag{7.1}$$

with ε the emissivity of the studied material, κ the thermal diffusivity, and θ the dimensionless temperature. In this case, we will consider a perfect black-body ($\varepsilon = 1$). Writing Eq. 7.1 in a dimensionless form requires to introduce dimensionless variables:

$$\begin{aligned} \zeta &= \frac{x}{2\sqrt{\kappa T_{period}}} \\ \tau &= \frac{t}{t_{period}} \\ \eta &= \sqrt{\epsilon t_{period}} \end{aligned} \tag{7.2}$$

with t_{period} being the period duration of a heating and cooling cycle. This lead to the dimensionless equation:

$$\frac{\partial \theta}{\partial \tau} = \frac{\partial^2 \theta}{4 \partial \zeta^2} - \eta^2 \theta \tag{7.3}$$

As a reminder, the Fourier series steady-state solution for such kind of problem is given by the equation:

$$\theta = \sum_{n=1}^{\infty} A_n \exp\left(-\gamma_n \zeta\right) \cos\left(2\pi\tau - \gamma_n^{'}\zeta + \varphi_n\right) \tag{7.4}$$

If we assume that A_1 and A_2 are the amplitude of the first components respectively x_1 and x_2, and B is the phase difference between the two first components, with $l = x_2 – x_1$:

$$\ln \frac{A_1}{A_2} = \frac{\gamma_1 l}{2\sqrt{\kappa t_{period}}} \tag{7.5}$$

$$B = \frac{\gamma_1^{'} l \sqrt{t_{period}}}{4\pi\sqrt{\kappa}} \tag{7.6}$$

Finally, one can retrieve thermal diffusivity κ using the equation:

$$\kappa = \frac{l^2}{2\ln\left(A_1 A_2^{-1}\right)} \cdot B \tag{7.7}$$

This experimental setup is of interest for the studied sample as Lopez-Baeza et al. (1987) showed that using a periodic radiative transfer technique is also suitable for "thermally short" samples. This means that even though the semi-infinite analytical case is not reached because the sample is too short, the method can be applicable. The comparison between this method and the method developed for conduction is discussed in subsection 7.1.5.

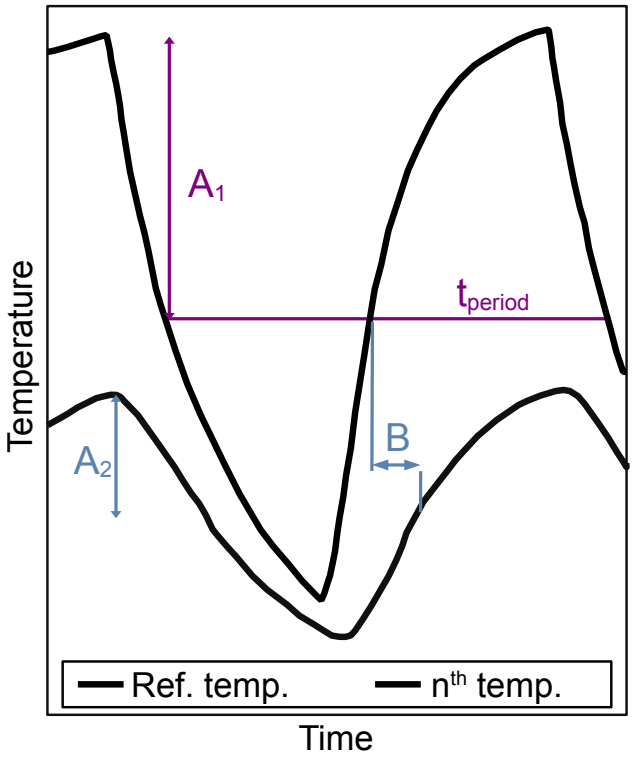

Figure 7.1.1 – Experimental principle and analytical resolution of a periodic thermal regime adapted after Bosanquet and Aris (1954). *Ref. temp.* is the temperature measurement that is the nearest of the heat source. N^{th} is a temperature measurement that is different than the first one. A_1 and A_2 are respectively the first and second amplitude of temperature curves. B is the phase delay between two temperature curves.

7.1.2 *Experimental setup with dry samples*

Therefore, a modified heat source is placed above the same experimental chamber. The previous heating element made of a water-metal heat exchanger is thus replaced by a radiative heat source. In the following experimental setups, a 500 W halogen construction light is used to recreate the standardized radiative solar flux of 350 $W.m^{-2}$ at sample's surface, which corresponds to Sun's mean surface heat flux. The strength of the radiative flux can be then adjusted with the distance between the light and the experimental setup.

The measurement chamber from the conductive heat transfer experiment presented in section 6.2.2.1 is re-used for this assessment. Here, the heating lid is removed to allow the radiative flux to hit sample's surface. Six thermocouples are evenly placed in the middle of the sample, from the top to the bottom, with a 2.5 cm spacing between them. Samples' sides are kept insulated with glass wool. The vertical thermal gradient is monitored in the same way using the fluorine window opening, analogous to the study made for the conductive transfer. A infrared radiation shield is added in front of the camera

to constrain the observation of the infrared thermography to the thermal gradient. A presentation of the experimental setup for dry samples is presented in Fig. 7.1.2.

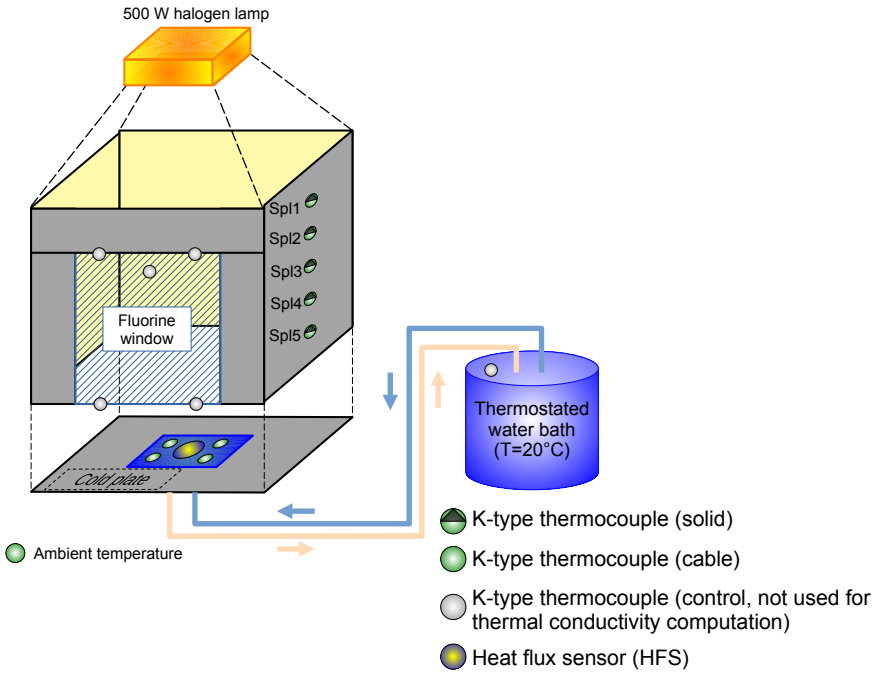

(a) Schematic of the experimental setup.

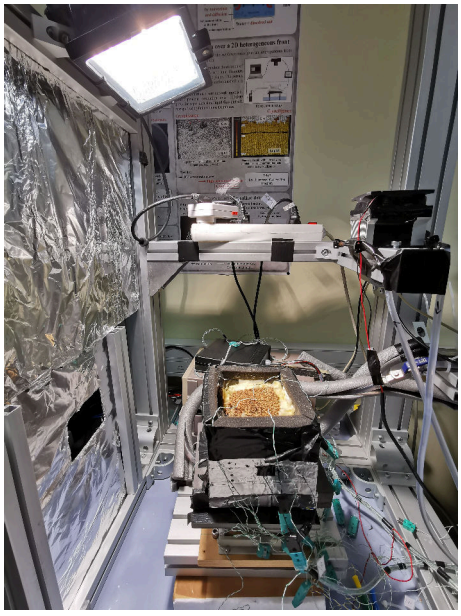

(b) Picture of the transient heat transfer experimental setup.

Figure 7.1.2 – Radiative heat transfer setup. The infrared camera is set behind a reflective surface made of aluminum foliage.

7.1.3 *Experimental setup with wet samples*

Adversely to dry samples, living *Sphagnum* samples are sensitive to intense radiative heat if not placed in a bucket of water. Removing the samples from their containers is also hazardous, since it significantly disturbs the structure and thus the thermal properties' values at the end. Infrared thermography through the fluorine window is also tricky due to the evapotranspiration that would undergo in this case, covering the fluorine window with moisture. In this case, the experimental setup is directly implemented on the sample container itself. Five 2 mm diameter holes are drilled directly in the box to allow the insertion of the thermocouples inside the container. The sample container is placed directly on a regular plate to avoid water leakage. The general experimental setup for living samples is presented in Fig. 7.1.3.

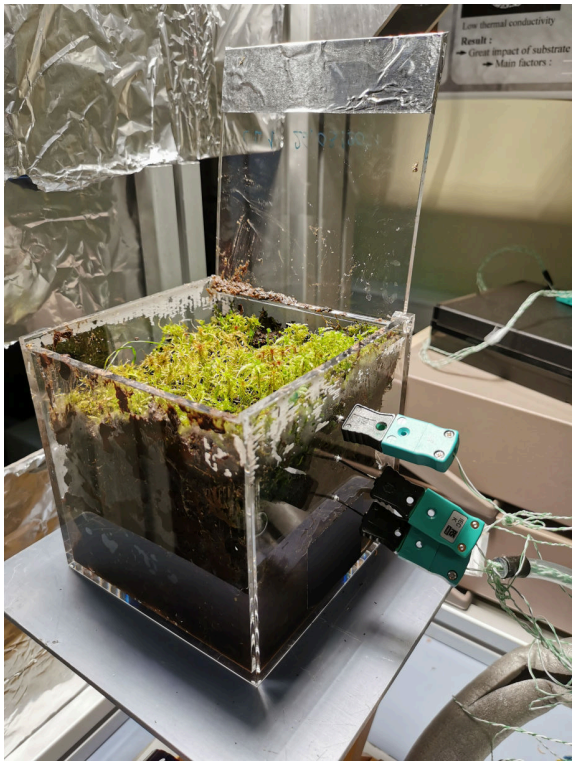

Figure 7.1.3 – Thermocouples inserted in the living sample.

7.1.4 *Heat pulse control and post-processing*

A 30-minutes cycle consisting of a 15-minutes heating (*'light is on'* statement) and a 15-minutes cooling (*'light is off'* statement) is applied using a standard 220 V light temporization module with an accuracy of plus minus two minutes for the state change triggering. This accuracy is assumed to be negligible over other factors playing a role in the heat transfer mechanisms (structural change, evapotranspiration among the most

significant role players). Temperatures as well as thermal flux at the bottom of the sample is measured on a 16-seconds acquisition basis during the whole duration of the experiment.
The algebra basis for retrieving thermal diffusivity from thermocouples situated at different locations has been presented in Eq. 7.4 of section 7.1.1. This equation is valid for any set of thermocouples located inside the sample, provided that the distance between the two thermocouples is accurately known.

First, a manual data cleaning is conducted to fit the exact periods for heating and cooling phases according to the precision of the light temporization module. Then, a Discrete Fourier Transform is computed for each given set of thermocouple data, allowing to retrieve the magnitude of each wave train.
It is then possible to use Eq. 7.7 of section to retrieve the effective radiative thermal diffusivity for a given set of thermocouples inside the sample. Periodic temperature profiles for dry sample and living sample are respectively shown in Fig. 7.1.4 and Fig. 7.1.6. The associated Discrete Fourier Transform plots are presented in Fig. 7.1.5 for a dry sample and in Fig. 7.1.7 for a living sample. The range of available thermocouple combinations and associated effective radiative thermal diffusivity values are shown in Table 7.1.2 for a dry sample and in Table 7.1.4 for a living sample.

7.1.4.1 *Results for a dry sample*

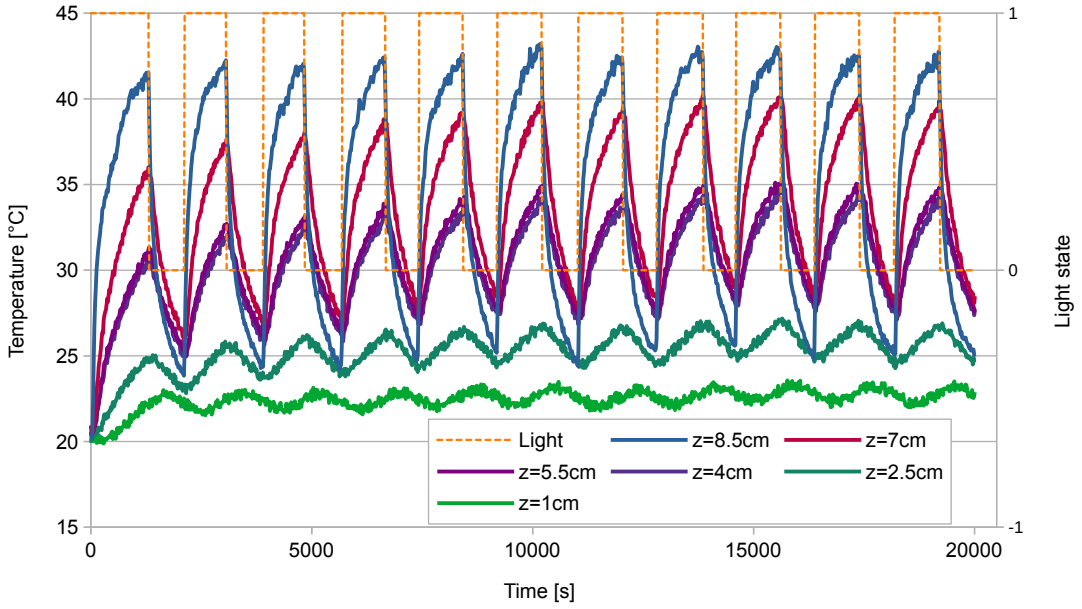

Figure 7.1.4 – Temperature evolution for various locations inside the sample. The light state is depicted with 1: *"the light is on"* and 0: *"the light is off"*.

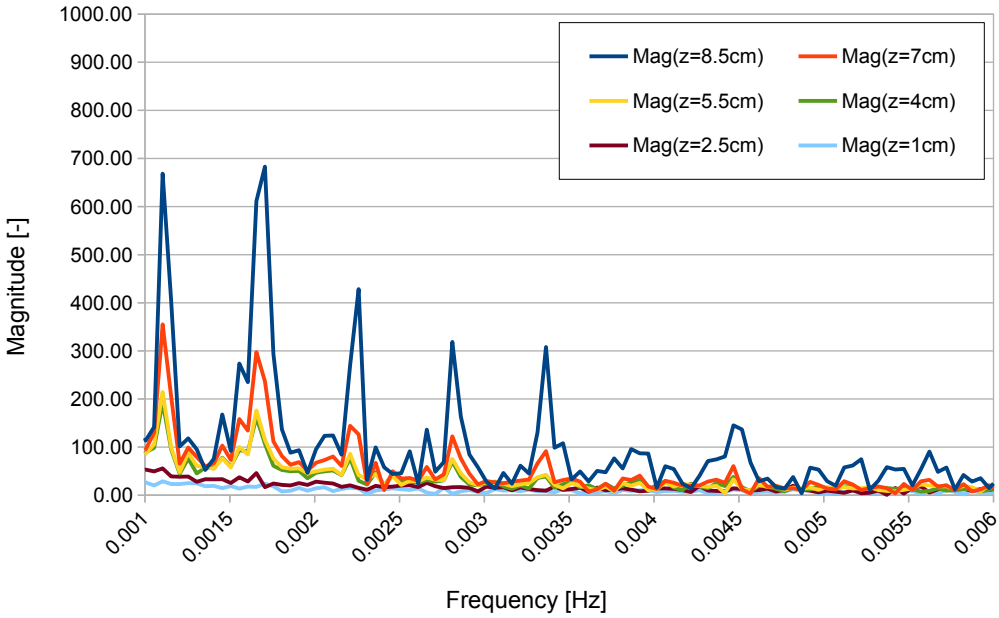

Figure 7.1.5 – Discrete Fourier Transform of the results showed in Fig. 7.1.4.

length [cm]	z=8.5	z=7	z=5.5	z=4	z=2.5	z=1
z=8.5		0.025	0.04	0.055	0.07	0.085
z=7			0.015	0.03	0.045	0.06
z=5.5				0.015	0.03	0.045
z=4					0.015	0.03
z=2.5						0.015
z=1						

Table 7.1.1 – Length associations for the study of effective radiative thermal diffusivity of the dry sample.z is the vertical position (in cm).

$\kappa_{radiative}$ $[m^2.s^{-1}]$	z=8.5	z=7	z=5.5	z=4	z=2.5	z=1
z=8.5		1.87×10^{-5}	1.03×10^{-4}	2.09×10^{-4}	8.31×10^{-5}	9.67×10^{-5}
z=7			1.03×10^{-4}	7.22×10^{-5}	2.56×10^{-5}	4.27×10^{-5}
z=5.5				1.34×10^{-5}	4.62×10^{-5}	6.45×10^{-5}
z=4					1.28×10^{-5}	4.33×10^{-6}
z=2.5						1.12×10^{-5}
z=1						

Table 7.1.2 – Effective radiative thermal diffusivity (in $m^2.s^{-1}$) for dry sample using the length associations of Table 7.1.1. z is the vertical position (in cm).

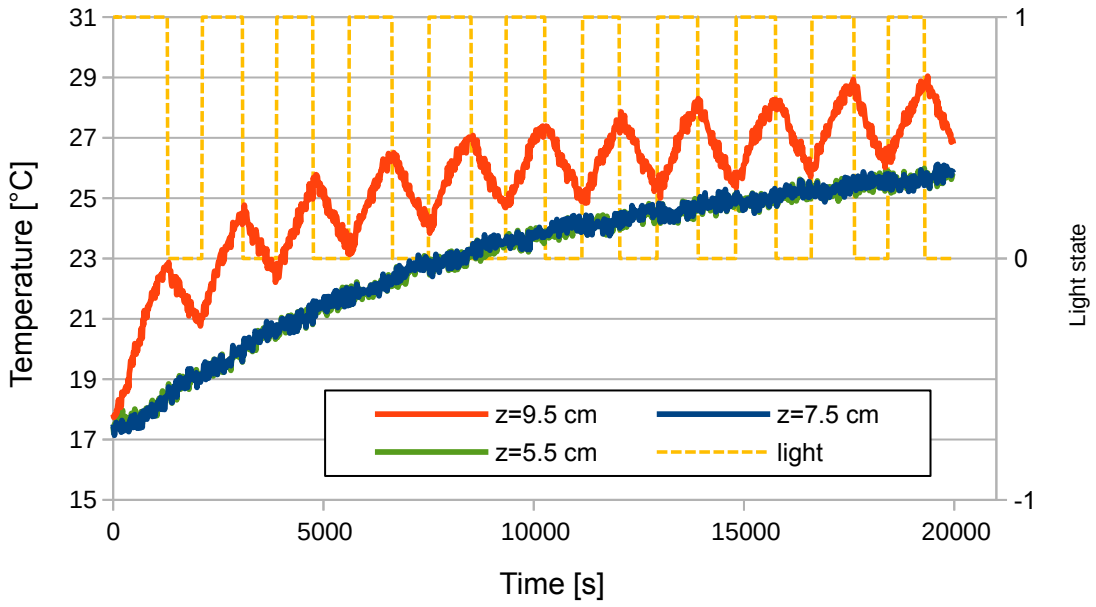

Figure 7.1.6 – Temperature evolution for various locations inside the sample. The light state is depicted with 1: *"the light is on"* and 0: *"the light is off"*.

7.1.4.2 *Results for a living sample*

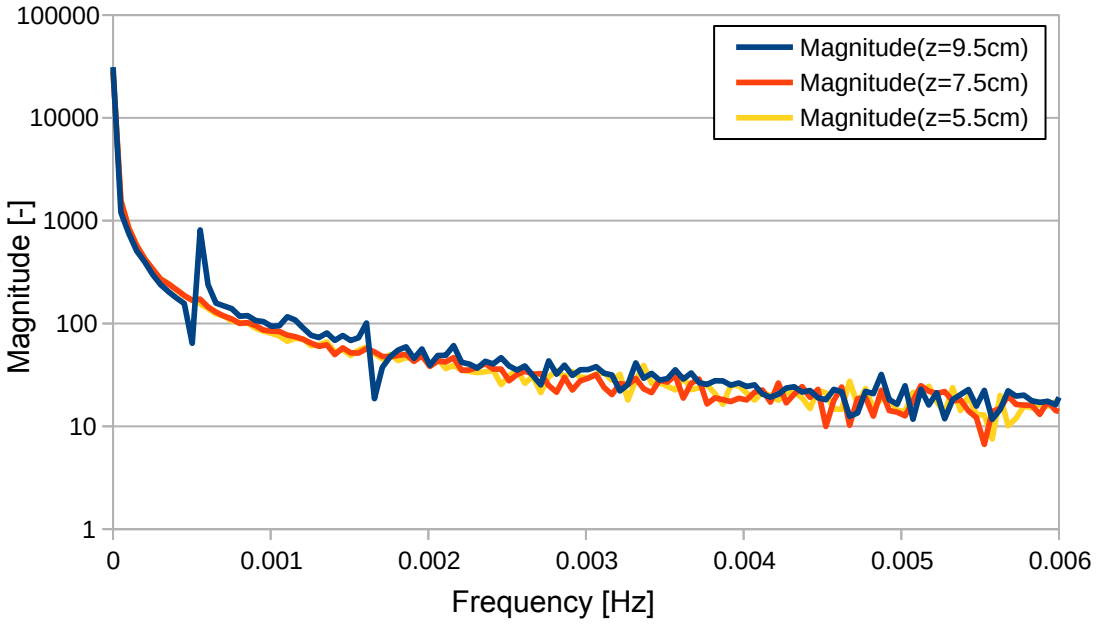

Figure 7.1.7 – Discrete Fourier Transform of the results showed in Fig. 7.1.6.

length [cm]	z=9.5	z=7.5	z=5.5
z=9.5		0.02	0.04
z=7.5			0.02
z=5.5			

Table 7.1.3 – Length associations for the study of radiative transfer thermal diffusivity.z is the vertical position (in cm).

$\kappa_{radiative}\ [m^2.s^{-1}]$	z=9.5	z=7.5	z=5.5
z=9.5		1.77×10^{-5}	7.68×10^{-5}
z=7.5			7.62×10^{-5}
z=5.5			

Table 7.1.4 – Radiative transfer-induced thermal diffusivity for the studied length associations of Table 7.1.3.z is the vertical position (in cm).

Effective radiative thermal diffusivity κ_{rad} ranges from 4.66×10^{-6} m².s⁻¹ to 1.03×10^{-4} m².s⁻¹ depending on the chosen length association. κ_{rad} is higher for small lengths on the upper part of the sample whereas κ_{rad} tends to be lower one large thicknesses and on

deeper horizons. Interestingly, κ_{rad} is quite similar to κ of air in the case of top surface samples.

Such results confirm the high porosity potential on the topmost layers of the samples. The effective radiative thermal conductivity is also higher than the effective thermal conductivity retrieved using pure conduction (section 6.2.2.3) and Laser-Flash method (section 6.2.4). This suggest that in field conditions, the heating surface on the topmost of the moss layer is not a single surface but a volume with an attenuation coefficient for radiative energy. In other words, solar radiative energy will tend to heat the cryptogamic layer deeper than what could be expected for a pure conduction problem. Similar trends can be observed when radiative transfer is implemented in the heat transfer model as shown in the following section.

7.1.5 *Comparison between conductive heat transfer and radiative heat transfer*

A comparison between the heat front propagation between a pure conduction heat transfer and a radiative heat transfer is done using the infrared thermography collected during both experiments. An average thermal profile for each z position is presented on the rightmost graph. The comparison of both heat transfer mechanisms are shown in Fig. 7.1.8. For the radiative heat transfer, the temperature profile for each heat wave is presented for the sake of comparison.

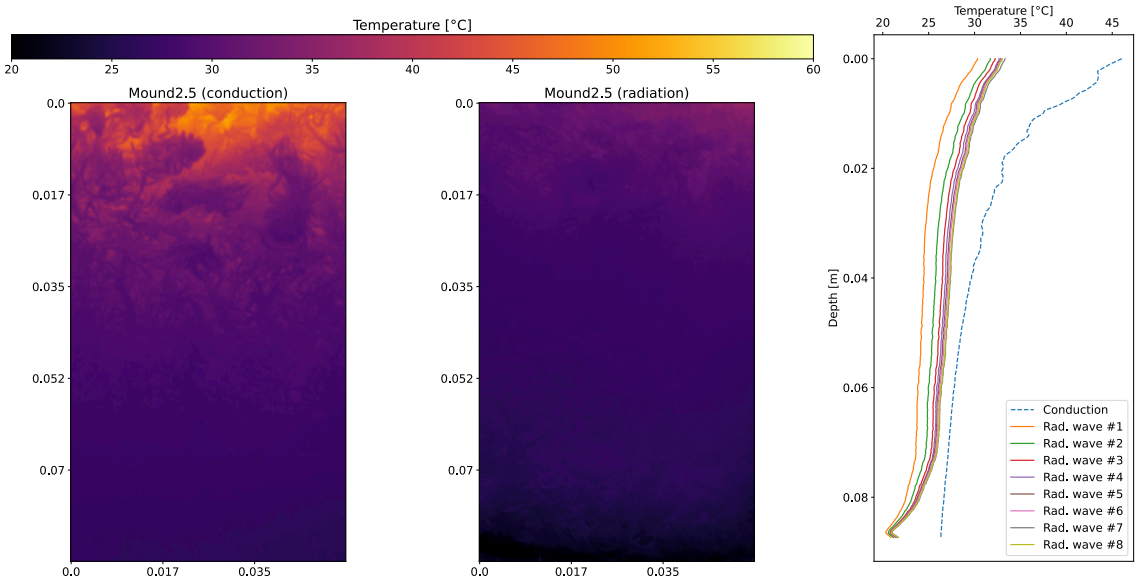

Figure 7.1.8 – Comparison of the heat front propagation by conduction and radiation on Mound2.5 sample.

According to Fig. 7.1.8, the comparative results for conduction and radiation experiments shows that the heat front is visible much deeper in the sample than what has been

observed for the conduction experiments. Indeed, the thermal amplitude is smaller for the radiative heat transfer experiment than for the conductive heat transfer experiment. Heat front propagation dynamic is also very similar for each radiation wave, with a general increase on the first periods and a stabilization trend for higher period numbers. Thermal profiles for radiative heat transfer are smooth and increase constantly as new heat waves are generated. On the other hand, conductive heat transfer profile is heterogeneous and hotter on the surface than for radiative heat transfer.

Such difference between radiative heat transfer and conductive heat transfer shows the capacity of infrared radiation to heat the surface deep in the ground. This deepening of the heat propagation is not clearly visible for living samples were water's latent heat takes the lead over radiative heat transfer.

7.1.6 *Influence of evapotranspiration in infrared thermography acquisitions*

In section 1.2, some clues about the importance of evapotranspiration in peatlands have been given. It is even the most efficient energy vector in arctic and subarctic peatlands (Launiainen et al., 2015), also due to the fact that *Sphagnum* mosses rely on capillary forces to fulfill their water needs. This importance of evapotranspiration is also important for infrared thermography. In section 6.2.3.3, it has been shown that infrared emissivity of dried and living *Sphagnum* are different. Moreover, dense water vapor plumes are visible with infrared thermography due to the lower temperature of water vapor during evaporation. This gives the basis for a potential evapotranspiration observation during living *Sphagnum* sample experiments, and more extensively in arctic wetlands. Evapotranspiration effect on living *Sphagnum* sample is visible in Fig. 7.1.9.

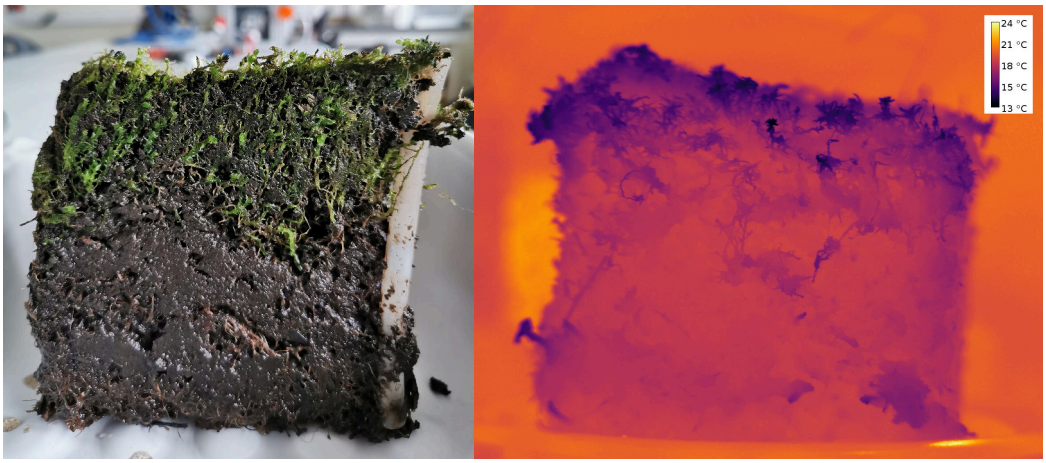

Figure 7.1.9 – *(left)* Picture of a living *Sphagnum* sample. *(right)* Thermal image of a living *Sphagnum* sample one hour after being removed from the sampling box. Note the colder temperature showing on the top of the sample showing occurring evapotranspiration.

During the experiment, the sample is removed from the sampling box thus allowing evapotranspiration to occur. One can see that the topmost layer of the sample is nearly 11 °C colder than the background temperature at 24 °C. This surface layer driven mainly by evapotranspiration can be considered as an energy sink that should be carefully taken into account in a mechanistic model. Therefore, some clues about phase transition between liquid water contained in the film pellicle at the surface of the low vegetation cover can be considered as a non-negligible heat transfer vector as (Launiainen et al., 2015) show for sub-arctic environments.

In a similar way, evapotranspiration can be studied through the drying of a few *Sphagnum* strains. A drying test of one *Sphagnum* stem observed under infrared camera is available in Fig. 7.1.10.

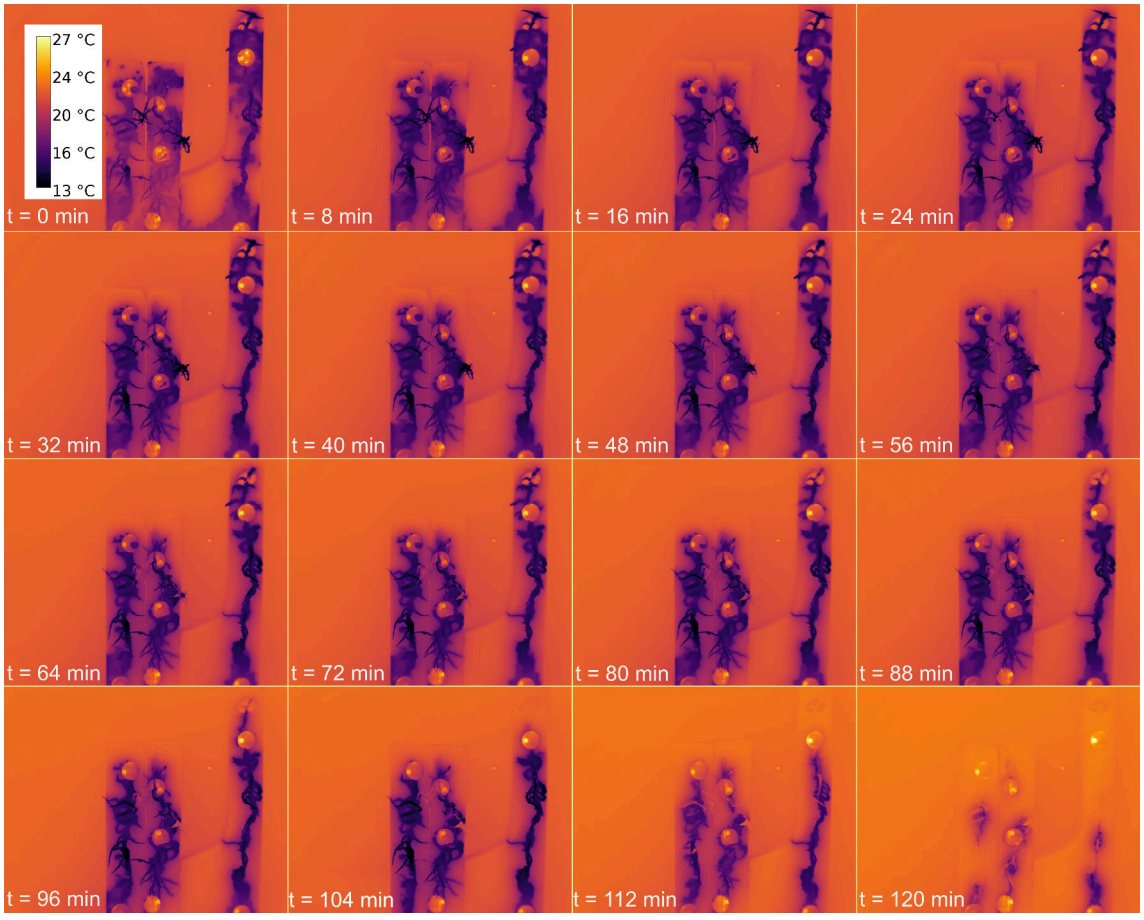

Figure 7.1.10 – Time-lapse of drying *Sphagnum* fiber viewed under infrared thermography.

One can see that during the drying, the temperature of the stem is significantly cooler than the background temperature. This temperature tend to get to the same temperature when the evapotranspiration stops, meaning that the water film over the sample is dried. Although this process is fast is observed for one stem, the drying process takes few days for a *Sphagnum* layer.

The high evapotranspiration occurring at the sample surface could potentially represent a local energy sink that needs to be taken into account in the energy balance between the atmosphere and the geosphere. Thus, the effective thermal conductivity of Arctic vegetation is influenced by the presence of evapotranspiration. The use of infrared thermography in the field could provide means of accurately quantifying the evapotranspiration factor in the local thermal balance.

7.2 EXPERIMENTAL PERSPECTIVES

As shown in section 6.2, thermal heat transfer occurring at the arctic low vegetation cover scale are assumed to be purely conductive in this work. This assumption gave an effective thermal conductivity of the considered porous media. While such hypothesis is acceptable for a supra-diary timescale model, where the radiative solar load is integrated over the course of a day, this is not the case for the study of a daily timescale.

At a daily scale, radiative solar load can vary depending on the cloud cover as well as the Sun's azimuth, depending itself on the day of the year and the location.

The preliminary results presented in this section showed that the heat transfer propagation is not identical between a fully conductive heat transfer and a combined conductive and radiative heat transfer. Indeed, these preliminary experiments give some clues about the solar radiative load attenuation properties in the energy balance of such interface.

Further experiments are required to obtain adequately an exchange coefficient accounting for the radiative heat transfer, ideally taking into account the Sun radiative load variation. Moreover, some further experiments are required to assess the impact of evapotranspiration in the heat transfer energy balance, especially when evapotranspiration is at its maximum at the end of spring.

8

COUPLED SOLID-FLUID MODEL OF THE LOW VEGETATION COVER

8.1 COUPLED HEAT TRANSFER MODEL: THE *chtmultiregionfoam* SOLVER

Sections 6.2.3.3 about the infrared emissivity and chapter 7 on experimental characterization of radiative transfer introduced the necessity to take into account such mechanisms in order to enhance the model's accuracy. Therefore, the following section will lead to a comparison of a one-equation model *FourierFoam* with a coupled heat transfer model for fluid-solid advective and radiative transfers named *chtMultiRegionFoam*. The *chtMultiRegionFoam* which stands for *Coupled Heat Transfer in a Multi-Region mesh* is a *OpenFOAM* solver that enables the simulation of complex heat transfer with solid-fluid coupling for example. This solver is owned by Tonkomo LLC and is distributed with a GPL license, with its source code available in *OpenFOAM* and hosted on GitHub. *chtMultiRegionFoam* has been publicly available in 2017. Whereas *FourierFoam* only solves a diffusion equation in a given domain, *chtMultiRegionFoam* have convective and radiative modules that can be added to it.

8.1.1 *Algebra basis*

In this section, we will briefly present the equation basis of the *chtMultiRegionFoam* solver to get a better perspective to compare with the *FourierFoam* solver. This work will base its roots in the equation description made by (el-Abbassi et al., 2017).

One can also find in the *OpenFOAM* Wiki web page (`https://openfoamwiki.net/index.php/chtMultiRegionFoam`) a more precise description of the theoretical algebra laying behind the *chtMultiRegionFoam* solver. There are three main solving stages for the chtMultiRegionFoam solver:

1. Transport equation solving in the fluid domain
2. Heat transport equation in the solid domain

3. Coupled heat transfer at the solid-fluid boundary

These three stages are solved sequentially to produce a complete algorithm without removing massive parallelization on multiple cores.

8.1.1.1 *Transport equation solving in the fluid domain*

In the first stage of the chtMultiRegionFoam solving, mass, momentum, sensible enthalpy and concentration are solved based on Favre-averaged equations:

$$\begin{cases} \frac{\partial(\bar{\rho})}{\partial t} + \nabla \cdot (\bar{\rho}\tilde{u}) = 0 & (mass) \\ \frac{\partial(\bar{\rho}\tilde{u})}{\partial t} + \nabla \cdot \left(\bar{\rho}\tilde{u}^2\right) = [-\nabla\bar{p} + \nabla \cdot \bar{\tau}] - \nabla \cdot \widetilde{\bar{\rho}u^{*2}} & (momentum) \\ \frac{\partial\left(\bar{\rho}\tilde{h}\right)}{\partial t} + \nabla \cdot \left(\bar{\rho}\tilde{u}\tilde{h}\right) = \frac{D}{D_t}p + \nabla \cdot \left(\frac{\lambda}{C_p}\nabla\tilde{h} - \widetilde{\bar{\rho}u^{*2}}\right) + \tilde{Q} & (enthalpy) \\ \frac{\partial\left(\bar{\rho}\widetilde{Y_\alpha}\right)}{\partial t} + \nabla \cdot \left(\bar{\rho}\tilde{u}\widetilde{Y_\alpha}\right) = \nabla \cdot \rho\Gamma\nabla Y_\alpha + \underbrace{-\nabla \cdot \rho\widetilde{Y_\alpha^* u^*}}_{Reynolds\ stress} & (concentration) \end{cases} \tag{8.1}$$

where:

- ρ is the volumetric mass of the fluid [kg.m^{-3}];
- u the velocity [m.s^{-1}];
- p the pressure [Pa];
- τ the shear stress tensor [Pa];
- h the specific sensible enthalpy [J];
- λ the fluid thermal conductivity [W.m^{-1}.K^{-1}];
- C_p the specific heat capacity at constant pressure [J.kg^{-1}.K^{-1}];
- Q a heat source [W];
- Y_α the species mass fraction of species α [-];
- Γ the species diffusion coefficient [m^2.s^{-1}];
- R the reaction rate of species α [s^{-1}].

˜and ¯represents the averaged values and * marked variables are turbulence-dependent fluctuations.

The solution for the Reynolds stress will not be detailed in this section. One can refer to the resolution presented in (el-Abbassi et al., 2017) for more details.

8.1.1.2 *Heat equation solving in the solid domain*

As there are any convection phenomena in solid, only heat conduction is solved:

$$\frac{\partial(\bar{\rho}h)}{\partial t} = \nabla \cdot (\lambda_s \nabla T) + Q \tag{8.2}$$

In Eq. 8.2, λ_s is the thermal conductivity of the solid.

8.1.1.3 *Conjugate heat transfer at the solid-fluid boundary*

In the *chtMultiRegionFoam* solver, conjugate heat transfer property is computed based on the following relations:

$$T_{f,inter} = T_{s,inter} \tag{8.3}$$

and,

$$\lambda_f \frac{\partial T_f}{\partial y}|_{inter,y+0} = \lambda_s \frac{\partial T_s}{\partial y}|_{inter,y-0} \tag{8.4}$$

A schematic representation of the boundary conditions and the initial state of the numerical model is shown in Fig. 8.1.1. In *OpenFOAM*, conjugate heat transfer is set up with the *turbulentTemperatureCoupledBaffleMixed* boundary condition. This boundary condition gives the user the possibility to add thin layers with different thermal conductivities. In the case shown in following simulations, no peculiar thin layer is added. The interface between *Sphagnum* and air is hence direct.

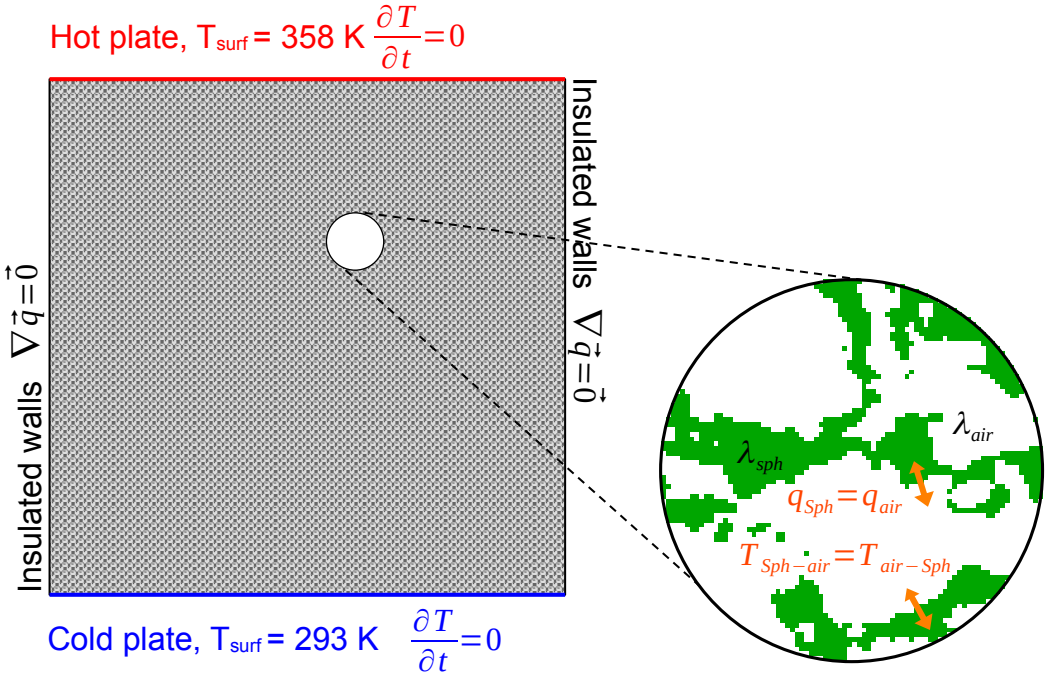

Figure 8.1.1 – Boundary conditions for the coupled heat transfer simulation with the *chtMultiRegionFoam* solver.

Nevertheless, one have to keep in mind that the solving the conjugate heat transfer will require to find a solution for the three heat transfer modes in the fluid domain (conduction, convection and radiative transfer) if the solver implements them. In the case of *chtMultiRegionFoam* solver, the heat transfer mechanisms can be activated or disabled for the simulation. The results shown in subsection 8.1.3 have radiative transfer equation set up but no heat advection ("laminar" flow state in the numerical model).

8.1.2 *Radiative transfer model*

OpenFOAM allows an additional implementation of a radiative transfer model with some transient solvers. There are currently three different radiative transfer models available to be used in the *chtMultiRegionFoam* solver: *NoRadiation*, *fvDOM* (which stands for *finite volume Discrete Ordinates Model* and the *P1* model. The *P1* radiation model is used in the model, and therefore will be presented hereafter. The presentation of the other radiative transfer models are out of the scope of this thesis. In a first paragraph, a brief introduction to the *P1* heat transfer model is presented. The numerical implementation is discussed in the following paragraph. For a theoretical discussion about the *P1* model, one can read Sazhin et al. (1996). An extensive review about the mathematical developments of the *P1*

model is available in Modest (2013). For a more technical report on the implementation of the radiative heat transfer models in *OpenFOAM*, one can consult a detailed workbook made by Vdovin (2009). The *P1* model relies on two main assumptions for the considered study case:

- Linear and isotropic scattering;
- The considered media is optically thick (*i.e.* that means that every radiations is not transmitted through to another media).

In this thesis, a general presentation of the governing equation of the *P1* model will presented hereafter. One may consult the above mentioned literature for more precision about the theoretical developments of such radiative transfer model. Let consider a radiative insensitive field at a given location r around a sphere named s. This intensity field can be written under the form of a Fourier series as follows:

$$I(r,\hat{s}) = \sum_{l=0}^{\infty} \sum_{m=-l}^{l} I_l^m(r) \Gamma_l^m(\hat{s}) \tag{8.5}$$

The *P1* model or *P1* approximation is based on the truncate of Eq. 8.5 if $l > 1$. Then, a second-order elliptic partial differential equation is solved for the incident radiation based on the following equations:

$$\begin{cases} \frac{1}{3\kappa}\nabla \cdot \left(\frac{1}{\beta - \frac{A_1\sigma_S}{3}} \nabla G \right) - G = -4\pi I_b \\ r = r_\omega : (wall) \qquad\qquad -\frac{2-\epsilon}{\epsilon} \frac{2}{3\beta - A_1\sigma_S} \hat{n} \cdot \nabla G + G = 4\pi I_{b\omega} \\ q = -\frac{1}{3\beta - A_1\sigma_S} \nabla G \end{cases} \tag{8.6}$$

with κ the absorption coefficient, β the extinction coefficient, A scattering phase function coefficients, σ_s the scattering coefficient, G the incident radiation, $I_b$and $I_{b\omega}$respectively the black-body radiative intensity field and the black-body radiative intensity at the wall, r the position vector, ϵ the emissivity and q the heat flux.

8.1.3 *Comparison between* FourierFoam *and* ChtMultiRegionFoam

Unlike *FourierFoam* simulations, coupled heat transfer simulations using the *chtMultiRegionFoam* solver are generally more demanding in terms of computational resources. Therefore, the comparison of both solvers will be made on a slice of Mound2.5 sample containing around 7.87 millions cells (30 voxels, which represents around 1.1 mm thick slice). The edge consists of a downscaling of the original X-ray tomography to a resolution of $3.64 \times 10^{-4} m.voxel^{-1}$represented by 512 voxels. A comparison of the temperature field at t+50 s between both models is given in Fig. 8.1.2. A comparison between two surface

plots between the results obtained for *chtMultiRegionFoam* and *FourierFoam* at the outlet with time set at t+50 s is available in Fig. 8.1.3.

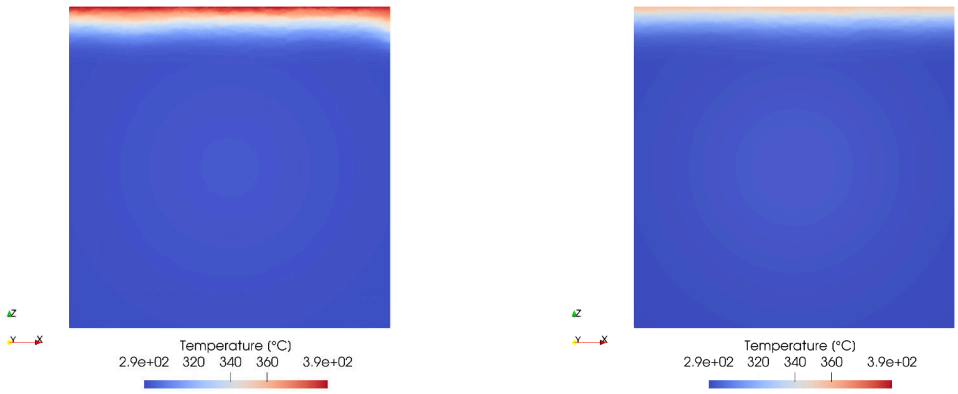

(a) *ChtMultiRegionFoam* **(b)** *FourierFoam*

Figure 8.1.2 – Comparison between a coupled heat flux solver (*ChtMultiRegionFoam*, (a)) and a purely conductive heat transfer solver (*FourierFoam*) for a *Sphagnum* slice at t+50 s.

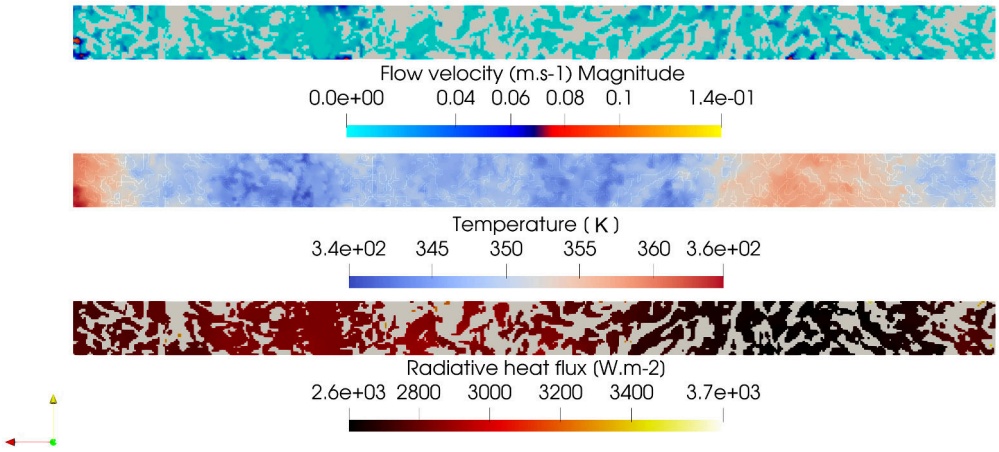

(a) *ChtMultiRegionFoam*

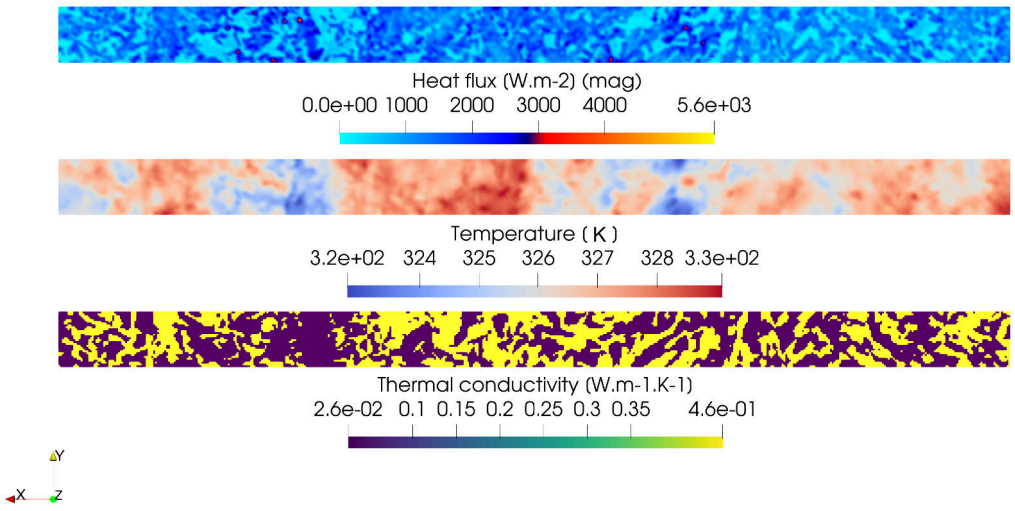

(b) *FourierFoam*

Figure 8.1.3 – Comparison of two heat transfer models, one coupled heat flux solver (*ChtMultiRegionFoam*, (a)) and another purely conductive heat transfer solver (*FourierFoam*) for slice a z+9 cm in a *Sphagnum* sample at t+50 s.

From Fig. 8.1.2 and Fig. 8.1.3, one can see that the temperature plots between the two solvers are not identical. Indeed, the results shown shows the temperatures are more

heterogeneous for *ChtMultiRegionFoam* than for *FourierFoam*. The first solver has a span of 10 °C difference while the latter has a span of more than 20 °C. This difference between both solvers can be explained by the addition of the radiative heat transfer model in the solver that allow radiation to hit the surfaces deeper in the sample compared with a conductive surface. In Fig. 8.1.3, it is possible to note that the consideration of a fluid interface causes some flow velocity, facilitating in the same way the heat transfer from the atmosphere to the geosphere, especially in dry conditions. However, the flow velocity is relatively low, and locally concentrated. The effect of flow in the convective heat transfer is negligible if the heating happens from the top of the sample. However, such assumption has to be studied in the case of bottom-to-top heat transfer where free-convection cells can occur.

8.1.4 *Heat convection phenomena for bottom-up heating*

In previous sections, we considered the heat propagation from the top of the sample to the bottom. This was done throughout the experiments and later the simulations to avoid convection phenomenon inside the measurement chamber and the numerical simulation model. This top-to-bottom heat propagation is valid during summer months, where the most preeminent heat source is the solar radiative load. Still, this is not the case when snow and ice covers the arctic peatlands. Indeed, soil's latent heat and geothermal gradient take the lead in the heat inputs, making the heat flux change direction, from the geosphere to the atmosphere. Yet, this winter heat transfer can be considered as pure conduction due to the fact that ice and packed snow are respectively solids and low-permeability porous medium. However, during spring and autumn when thermal regime can abruptly vary throughout the days, the soil can be warmer than the air, resulting in such situation. This subsection will address the reader with some preliminary simulations about the possible development of an advective heat transfer inside the samples. Some discussions will be given on the potential validity of the Rayleigh numbers presented in section 8.A.

8.2 NUMERICAL PERSPECTIVES

The results obtained for purely conductive heat transfer shows that Arctic low vegetation cover is insulating cover. Inverse modeling done on such layer showed that the intrinsic thermal properties of *Sphagnum*, lichen and peat are of the same order of magnitude than for the thermal properties of air, and thereby effective thermal properties of such porous medium. If seen in a purely conductive heat transfer, the peculiarities of a porous medium are not straightforward.

However, it has been possible to demonstrate in the preliminary works developed in the previous section that the addition of a radiative heat transfer source facilitates the overall heat transfer. Therefore, it is mandatory to account for radiative heat transfer in a subdiary time-scale study. Moreover, some clues about the influence of density-driven flows (advection) in such porous media has to be studied carefully. The potential influence of advection in the heat transfer is discussed in Appendix 8.A. One other perspective in the computationally-efficient modeling of the low arctic vegetation cover transfer properties is the addition of a local sink term accounting for the evapotranspiration of the vegetation, correcting the laboratory energy balance for living samples.

APPENDIX

8.A CONVECTION INFLUENCE ASSESSMENT ON HEAT TRANSFER

In the previous section of this study, a brief recall of the simplified unidimensional heat transfer has been discussed. However, it is possible to argue that the considered fibrous porous media does not only imply heat conduction mechanisms because of its composite nature. Indeed, convective mechanisms cannot be forgotten when there is a fluid-phase heat transfer, although it heavily depends on the considered porous media. Such mechanisms are extensively discussed in notable monographs such as Kaviany (1995) and Nield and Bejan (2013).

Some dimensionless numbers are available to evaluate the prevalence of convective mechanisms over conductive mechanisms. One of the most common dimensionless number used in heat transfer science is the Rayleigh number Ra. Ra is the product of the Grashof Gr number accounting for free internal convection in a fluid with the Prandtl number Pr accounting for thermal diffusive transfer. For a bottom up heat transfer, the Grashof number is defined as in Eq. 8.7:

$$Gr = \frac{g\beta\Delta T l_c^3 \rho^2}{\mu^2} \tag{8.7}$$

with g the gravity acceleration (in $m.s^{-2}$), β the thermal expansion coefficient (in K^{-1}), ΔT the temperature difference between the uniform temperature and the perturbation (in K), l_c the characteristic length scale of the studied system (in m), ρ the volumetric mass (in $kg.m^{-3}$) and μ the dynamic viscosity (in Pa.s). On the other hand, the Prandtl number can be written as in Eq. 8.8:

$$Pr = \frac{\mu C_p}{\lambda} \tag{8.8}$$

with C_p the specific heat capacity (in $J.kg^{-1}.K^{-1}$) and λ the thermal conductivity (in $W.m^{-1}.K^{-1}$). Then, Rayleigh number is equal to:

$$Ra = GrPr = \frac{g\beta\Delta T l_c^3 \rho^2 C_p}{\mu\lambda} \tag{8.9}$$

which can be simplified by replacing in Eq. 8.9 the kinematic viscosity $\nu = \frac{\mu}{\rho}$ (in $m^2.s^{-1}$) and the thermal diffusivity κ in ($m^2.s^{-1}$). Ra number becomes then:

$$Ra = \frac{g\beta\Delta T l_c^3}{\kappa \upsilon} \tag{8.10}$$

In a porous medium in which convection cells can be observed, Rayleigh number must take into account the properties of the considered fluid but also the intrinsic properties of the porous media. This is done by multiplying the Rayleigh number with the Darcy number $Da = \frac{k}{d^2}$ with k^* the effective intrinsic permeability of the porous medium (in m^2) and d^* the effective pore size diameter (in m) leading to the Rayleigh-Darcy number Ra_D:

$$Ra_D = \frac{g\beta\Delta T k d}{\kappa \upsilon} \tag{8.11}$$

The Rayleigh-Darcy number is an important clue to study whether convective mechanisms have a significant impact on heat transfer mechanisms. Critical Ra_D values are different for a given porous structure. Therefore, identifying Rayleigh number bounds is compulsory. Some preliminary values of critical Rayleigh values have been given in Sutton (1950) synthesizing some of the work done by Rayleigh (1916).
In the peculiar case developed here for the thesis, the Rayleigh-Darcy number will be evaluated as a function of permeability for liquid water at 4 °C, and standard atmospheric air. ΔT is set to 40 °C, g equals to 9.81 $m.s^{-2}$ and d^* is 10^{-3} m (corresponding to the mean size of the space between each pseudoleaf of *Sphagnum*). Thermophysical data for this assessment is based on the parametric study available in Tsilingiris (2008). A synthesis is available in Table 8.A.1.

	Liquid water (4 °C)	**Moist air (25 °C)**	**Dry air (25 °C)**
$\beta\ [K^{-1}]$	2.1×10^{-4}	3.4×10^{-3}	3.4×10^{-3}
$\upsilon\ [m^2.s^{-1}]$	1.6×10^{-6}	1.8×10^{-5}	1.8×10^{-5}
$\kappa\ [m^2.s^{-1}]$	1.3×10^{-7}	2×10^{-5}	1.8×10^{-5}

Table 8.A.1 – Data for Rayleigh number estimation from the data gathered in Tsilingiris (2008).

We can find respective equations for Rayleigh number assuming a Rayleigh-Bénard boundary condition[1] in conjunction with the studied fluid detailed in Eq. 8.12 to Eq. 8.14:

$$Ra_D^{water} = 3.84 \times 10^8 k \tag{8.12}$$

$$Ra_D^{dry} = 4.12 \times 10^7 k \tag{8.13}$$

1 A Rayleigh-Bénard condition is an abrupt heating from the bottom of the sample, allowing natural convection to occur.

$$Ra_D^{moist} = 3.71 \times 10^6 k \tag{8.14}$$

This set of equation shows that water has the most potential to create convective cells in a porous medium whereas moist air does the least. The occurrence of turbulence through the porous medium is dependent on the critical Rayleigh number, thus establishing a boundary between a purely conductive regime and a hybrid conductive-convective regime.

Critical Rayleigh values are extensively discussed in the literature for various situations. The a classical assessment of a critical Rayleigh value for free surfaces is given in Heitz and Westwater (1971) is $Ra \approx 1708$. On the other hand, some critical Rayleigh values for porous media are also known and is set with $Ra \approx 4\pi^2 \approx 40$ (Lapwood, 1948), obtained based on linear stability.

At this point, it might be useful to recall that the obtained intrinsic permeabilities obtained using Direct Numerical Simulations (see section 5.3.3) are situated between 10^{-8} to 10^{-9} m². This means that the Ra_D number are to be mostly equal or less than 1. This value is therefore far from the critical Rayleigh values mentioned above. Indeed, this means that the convective heat transfer phenomena can be neglected in the study of heat transfer phenomena. Although internal convection can be neglected when the porous medium is saturated with air, convection can occur in the case of water-unsaturated medium. Moreover, convection happens also in larger bodies such as lakes or sea at larger scale in arctic ecosystems.

GENERAL CONCLUSION

Rising mean annual temperatures and precipitation increase are two of the main expected consequences of global climate change on arctic environments. The hypothesis of an arctic lower vegetation cover assimilated to a porous medium is the guiding thread of this thesis. This approach has led to a complete experimental and numerical procedure, from sampling to numerical reconstruction and characterization of transfer properties.

In this work, the numerical reconstruction done through X-ray tomography gives new insights in the study of such complex patchwork of vegetation (*Sphagnum* mosses) and composite organisms (lichens). The morphological properties study of the low vegetation layer shows that this layer can be assumed to be highly porous, with porosities often exceeding 80%. A representative elementary volume of porosity is defined for most of the samples, and the computation of specific surface area shows significant water and nutrient exchange potential of such low vegetation cover.

The numerical hydraulic properties study, done through volume averaging on a representative elementary volume, denoted high hydraulic conductivities for all samples type studied in the Khanymey sample lot collection. These results can also be obtained using a mesoscale model, such as a pore network model made of throats and spheres. Both direct numerical simulations and pore-network model converge on analogous values of 10^{-8} $m.s^{-1}$, which agrees partly with field and previous numerical models. One of the main advantage of doing a numerical study of hydraulic properties is the reproducibility of the numerical protocol, allowing for statistically robust results. This method also avoids some compressibility biases of *Sphagnum* moss, which is common in field studies.

In terms of thermal properties, experimental assessments and numerical inverse modeling both allowed to quantify the effective thermal conductivity on one hand and intrinsic thermal conductivity of the low vegetation samples from Khanymey on the other hand. Using some porous medium established standards for such quantification showed an effective thermal conductivity of about $10^{-2} W.m^{-1}.K^{-1}$ which is in good agreement with both in-field studies and previous numerical models. Inverse modeling of effective heat transfer enable to quantify the intrinsic thermal properties of *Sphagnum*, lichen and peat, with thermal conductivities 10 to 100 times higher than the effective thermal conductivity. Such difference shows the insulating properties of the low vegetation layer as a porous media.

The work presented in this thesis shows some aspects of the complex physics that occur in the arctic low vegetation cover. The remoteness of the study sites and the fragile nature of the samples lead to samples in both tundra environments for the result production and in nearby mires for the experimental setting and preliminary work. At the same time, scans and numerical models of such complex porous structure gave the opportunity to foster the full potential of high performance computing for properties assessment. The coupled experimental and numerical approach gives some positive inputs on the validity of such methods compared to experimental studies.

Yet, experimental and numerical methods' setup complexity lead to the deep study of few samples concentrated on one study site (Khanymey). However, this workflow is applicable to any low vegetation sample collected and scanned in the same way. Therefore, the study of other scanned samples (from other Siberian research stations, Kajbasovo and Kulingdakan) and samples from Abisko could bring more information for the transfer properties assessments. Indeed, such large scale quantification opens the possibility to establish an effective computationally-efficient boundary condition representative of the complexity of arctic low vegetation cover.

Some peculiar studies on the impact of radiative transfer and the mapping of the solar radiative load on this complex patchwork of low vegetation is yet to be conducted in a near future. Finding a non-destructive contrast agent for X-ray tomography in ice condition is also part of a near future perspective, allowing to quantify transfer properties on unsaturated porous media.

Finally, some upscaling has to be made in order to fed Earth System Models with the obtained morphological and transfer properties. This upscaling will require a strong topographical description of the vegetation cover based on remote sensing, first at catchment-scale and further at continental scale.

These steps will enable the description of a future computationally-efficient effective boundary condition of the low vegetation cover in arctic environments for land surface models in a mechanistic point of view such as the *permaFoam* solver, a numerical twin of permafrost-driven dynamics at the watershed scale.

BIBLIOGRAPHY

Aalto, J. et al. (May 28, 2018). "Statistical Forecasting of Current and Future Circum-Arctic Ground Temperatures and Active Layer Thickness." en. In: *Geophysical Research Letters* 45.10, pp. 4889–4898. ISSN: 00948276. DOI: 10.1029/2018GL078007. URL: http://doi.wiley.com/10.1029/2018GL078007 (visited on 03/17/2021).

Adamo, P. et al. (Mar. 2007). "Lichen and Moss Bags as Monitoring Devices in Urban Areas.Part II: Trace Element Content in Living and Dead Biomonitors and Comparison with Synthetic Materials." en. In: *Environmental Pollution* 146.2, pp. 392–399. ISSN: 02697491. DOI: 10.1016/j.envpol.2006.03.047. URL: https://linkinghub.elsevier.com/retrieve/pii/S0269749106002272 (visited on 11/03/2021).

Adon, Rashidah et al. (Feb. 2013). "Overview of the Sustainable Uses of Peat Soil in Malaysia with Some Relevant Geotechnical Assessments." In: *International Journal of Integrated Engineering* 4.4. URL: https://penerbit.uthm.edu.my/ojs/index.php/ijie/article/view/584.

AFNOR (2001). "Thermal Insulation — Determination of Steady-State Thermal Resistance and Related Properties — Heat Flow Meter Apparatus." Pat. EN 12667:2001 F (France).

Agaesse, Tristan et al. (Nov. 2016). "Validation of Pore Network Simulations of Ex-Situ Water Distributions in a Gas Diffusion Layer of Proton Exchange Membrane Fuel Cells with X-ray Tomographic Images." en. In: *Journal of Power Sources* 331, pp. 462–474. ISSN: 03787753. DOI: 10.1016/j.jpowsour.2016.09.076. URL: https://linkinghub.elsevier.com/retrieve/pii/S0378775316312381 (visited on 10/21/2020).

Åkerman, H. Jonas and Margareta Johansson (July 2008). "Thawing Permafrost and Thicker Active Layers in Sub-Arctic Sweden." en. In: *Permafrost and Periglacial Processes* 19.3, pp. 279–292. ISSN: 10456740, 10991530. DOI: 10.1002/ppp.626. URL: https://onlinelibrary.wiley.com/doi/10.1002/ppp.626 (visited on 08/28/2023).

Alempic, Jean-Marie et al. (Feb. 18, 2023). "An Update on Eukaryotic Viruses Revived from Ancient Permafrost." en. In: *Viruses* 15.2, p. 564. ISSN: 1999-4915. DOI: 10.3390/v15020564. URL: https://www.mdpi.com/1999-4915/15/2/564 (visited on 09/14/2023).

Al-Ameen, Zohair et al. (2015). "Latest Methods of Image Enhancement and Restoration for Computed Tomography: A Concise Review." In: *Applied Medical Informatics* 36.1, pp. 1–12. URL: https://ami.info.umfcluj.ro/index.php/AMI/article/view/510.

Andersson, N. Å et al. (1996). "The Abisko Scientific Research Station." In: *Ecological Bulletin* 45, pp. 11–14. URL: https://gorgone.univ-toulouse.fr/login?url=https://www.jstor.org/stable/20113179.

Ångstrom, A. J. (1862). "Neue Methode, das Wärmeleitungsvermögen der Körper zu bestimmen." de. In: *Annalen der Physik und Chemie* 190.12, pp. 513–530. ISSN: 00033804, 15213889. DOI: 10.1002/andp.18621901202. URL: https://onlinelibrary.wiley.com/doi/10.1002/andp.18621901202 (visited on 03/29/2023).

Auda, Yves et al. (Sept. 19, 2023). "A New Land Cover Map of Two Watersheds under Long-Term Environmental Monitoring in the Swedish Arctic Using Sentinel-2 Data." en. In: *Water* 15.18, p. 3311. ISSN: 2073-4441. DOI: 10.3390/w15183311. URL: https://www.mdpi.com/2073-4441/15/18/3311 (visited on 10/06/2023).

Bachmat, Yehuda and Jacob Bear (1987). "On the Concept and Size of a Representative Elementary Volume (Rev)." In: *Advances in Transport Phenomena in Porous Media*. Ed. by Jacob Bear and M. Yavuz Corapcioglu. Dordrecht: Springer Netherlands, pp. 3–20. ISBN: 978-94-010-8121-4 978-94-009-3625-6. DOI: 10.1007/978-94-009-3625-6_1. URL: http://link.springer.com/10.1007/978-94-009-3625-6_1 (visited on 03/16/2022).

Baird, A. (1997). "Field Estimation of Macropore Functioning and Surface Hydraulic Conductivity in a Fen Peat." In: *Hydrological Processes* 3.11, pp. 287–295. DOI: 10.1002/(SICI)1099-1085(19970315)11:3<287::AID-HYP443>3.0.CO;2-L.

Bakatovich, Aliaksandr and Florindo Gaspar (Dec. 2019). "Composite Material for Thermal Insulation Based on Moss Raw Material." en. In: *Construction and Building Materials* 228, p. 116699. ISSN: 09500618. DOI: 10.1016/j.conbuildmat.2019.116699. URL: https://linkinghub.elsevier.com/retrieve/pii/S0950061819321178 (visited on 01/30/2023).

Banfield, J. F. et al. (Mar. 30, 1999). "Biological Impact on Mineral Dissolution: Application of the Lichen Model to Understanding Mineral Weathering in the Rhizosphere." en. In: *Proceedings of the National Academy of Sciences* 96.7, pp. 3404–3411. ISSN: 0027-8424, 1091-6490. DOI: 10.1073/pnas.96.7.3404. URL: http://www.pnas.org/cgi/doi/10.1073/pnas.96.7.3404 (visited on 11/24/2020).

Bear, Jacob (1972). *Dynamics of Fluids in Porous Media*. Dynamics of fluids in porous media. Dover Books on Physics and Chemistry. New York: Dover Publications. 764 pp. ISBN: 978-0-486-65675-5.

Bense, V. F. et al. (Sept. 2012). "Permafrost Degradation as a Control on Hydrogeological Regime Shifts in a Warming Climate: Groundwater and Degrading Permafrost." en. In: *Journal of Geophysical Research: Earth Surface* 117.F03036. ISSN: 01480227. DOI: 10.1029/2011JF002143. URL: http://doi.wiley.com/10.1029/2011JF002143 (visited on 11/10/2021).

Beringer, Jason et al. (2001). "The Representation of Arctic Soils in the Land Surface Model: The Importance of Mosses." In: *Journal of Climate* 14.15, pp. 3324–3335. DOI: 10.1175/1520-0442(2001)014%3C3324:TROASI%3E2.0.CO;2.

Bernard-Jannin, Léonard et al. (Sept. 20, 2018). "Hydrological Control of Dissolved Organic Carbon Dynamics in a Rehabilitated Sphagnum Dominated Peatland: A Water-Table Based Modelling Approach." en. In: *Hydrology and Earth System Sciences*

22.9, pp. 4907–4920. ISSN: 1607-7938. DOI: 10.5194/hess-22-4907-2018. URL: https://hess.copernicus.org/articles/22/4907/2018/ (visited on 11/10/2021).

Bernier, P.Y. et al. (Apr. 2011). "Boreal Lichen Woodlands: A Possible Negative Feedback to Climate Change in Eastern North America." en. In: *Agricultural and Forest Meteorology* 151.4, pp. 521–528. ISSN: 01681923. DOI: 10.1016/j.agrformet.2010.12.013. URL: https://linkinghub.elsevier.com/retrieve/pii/S0168192311000050 (visited on 11/10/2021).

Berteaux, Dominique et al. (June 2017). "Effects of Changing Permafrost and Snow Conditions on Tundra Wildlife: Critical Places and Times." In: *ARCTIC SCIENCE* 3 (2, SI), pp. 65–90. DOI: 10.1139/as-2016-0023.

Bird, R. Byron et al. (2002). *Transport Phenomena*. 2nd, Wiley international ed. New York: J. Wiley. 895 pp. ISBN: 978-0-471-41077-5.

Biskaborn, Boris K. et al. (Dec. 2019). "Permafrost Is Warming at a Global Scale." en. In: *Nature Communications* 10.1 (1), p. 264. ISSN: 2041-1723. DOI: 10.1038/s41467-018-08240-4. URL: http://www.nature.com/articles/s41467-018-08240-4 (visited on 08/28/2020).

Blok, D. et al. (Nov. 2011). "The Cooling Capacity of Mosses: Controls on Water and Energy Fluxes in a Siberian Tundra Site." en. In: *Ecosystems* 14.7, pp. 1055–1065. ISSN: 1432-9840, 1435-0629. DOI: 10.1007/s10021-011-9463-5. URL: http://link.springer.com/10.1007/s10021-011-9463-5 (visited on 01/27/2023).

Blunt, Martin J. (2017). *Multiphase Flow in Permeable Media: A Pore-Scale Perspective*. Cambridge, United Kingdom ; New York, NY: Cambridge University Press. 482 pp. ISBN: 978-1-107-09346-1.

Boelter, D. H. (1968). "Important Physical Properties of Peat Materials." In: 3rd International Peat Congress. Quebec, Cananada: Department of Energy, Mines and Ressources, Nationam Research Council of Canada, pp. 150–154. URL: https://www.nrs.fs.usda.gov/pubs/jrnl/1968/nc_1968_boelter_001.pdf.

Bosanquet, C H and R Aris (July 1954). "On the Application of Angstr m's Method of Measuring Thermal Conductivity." In: *British Journal of Applied Physics* 5.7, pp. 252–255. ISSN: 0508-3443. DOI: 10.1088/0508-3443/5/7/304. URL: https://iopscience.iop.org/article/10.1088/0508-3443/5/7/304 (visited on 03/27/2023).

Bousquet, Gwenaëlle et al. (2016). *Étude de Fonctionnement et Du Comportement de La Tourbière de Clarens*. Toulouse: Université Toulouse III - Paul Sabatier, p. 96.

Bristow, Keith L. et al. (May 2001). "A Small Multi-Needle Probe for Measuring Soil Thermal Properties, Water Content and Electrical Conductivity." en. In: *Computers and Electronics in Agriculture* 31.3, pp. 265–280. ISSN: 01681699. DOI: 10.1016/S0168-1699(00)00186-1. URL: https://linkinghub.elsevier.com/retrieve/pii/S0168169900001861 (visited on 03/10/2023).

Brooks, R A and G Di Chiro (May 1, 1976). "Beam Hardening in X-ray Reconstructive Tomography." In: *Physics in Medicine and Biology* 21.3, pp. 390–398. ISSN: 00319155. DOI:

10.1088/0031-9155/21/3/004. URL: https://iopscience.iop.org/article/10.1088/0031-9155/21/3/004 (visited on 10/14/2023).

Brovkin, Victor et al. (Apr. 16, 2009). "Global Biogeophysical Interactions between Forest and Climate: FOREST-CLIMATE INTERACTIONS." en. In: *Geophysical Research Letters* 36.7, n/a–n/a. ISSN: 00948276. DOI: 10.1029/2009GL037543. URL: http://doi.wiley.com/10.1029/2009GL037543 (visited on 10/11/2023).

Brown, G. O. and H. T. Hsieh (May 2000). "Evaluation of Laboratory Dolomite Core Sample Size Using Representative Elementary Volume Concepts." EN. In: *Water Resources Research* 36.5 (5), pp. 1199–1207. DOI: 10.1029/2000WR900017.

Buades, A. et al. (Jan. 2005). "A Review of Image Denoising Algorithms, with a New One." en. In: *Multiscale Modeling & Simulation* 4.2, pp. 490–530. ISSN: 1540-3459, 1540-3467. DOI: 10.1137/040616024. URL: http://epubs.siam.org/doi/10.1137/040616024 (visited on 08/29/2023).

Buades, Antoni et al. (Sept. 13, 2011). "Non-Local Means Denoising." In: *Image Processing On Line* 1, pp. 208–212. ISSN: 2105-1232. DOI: 10.5201/ipol.2011.bcm_nlm. URL: https://www.ipol.im/pub/art/2011/bcm_nlm/?utm_source=doi (visited on 08/29/2023).

Burke, Eleanor J. et al. (Sept. 16, 2020). "Evaluating Permafrost Physics in the Coupled Model Intercomparison Project 6 (CMIP6) Models and Their Sensitivity to Climate Change." en. In: *The Cryosphere* 14.9, pp. 3155–3174. ISSN: 1994-0424. DOI: 10.5194/tc-14-3155-2020. URL: https://tc.copernicus.org/articles/14/3155/2020/ (visited on 04/20/2022).

Cazaurang, Simon (2023). "Caractérisation Des Propriétés de Transfert de La Couverture Végétale Inférieure Arctique - Approche Expérimentale et Numérique Couplée." Thèse de doctorat de dynamique des Fluides. Toulouse, France: Toulouse INP - ENSEEIHT.

Cazaurang, Simon et al. (Jan. 19, 2023). "Numerical Assessment of Morphological and Hydraulic Properties of Moss, Lichen and Peat from a Permafrost Peatland." en. In: *Hydrology and Earth System Sciences* 27.2, pp. 431–451. ISSN: 1607-7938. DOI: 10.5194/hess-27-431-2023. URL: https://hess.copernicus.org/articles/27/431/2023/ (visited on 04/05/2023).

Circum-Arctic Map of Permafrost and Ground-Ice Conditions (1997). In collab. with J. Brown et al. USGS.

Claisse, Peter A. (2016). "Transport of Fluids in Solids." en. In: *Civil Engineering Materials*. Elsevier, pp. 83–90. ISBN: 978-0-08-100275-9. DOI: 10.1016/B978-0-08-100275-9.00009-7. URL: https://linkinghub.elsevier.com/retrieve/pii/B9780081002759000097 (visited on 03/16/2022).

Clayton, Leah K et al. (May 1, 2021). "Active Layer Thickness as a Function of Soil Water Content." In: *Environmental Research Letters* 16.5, p. 055028. ISSN: 1748-9326. DOI: 10.1088/1748-9326/abfa4c. URL: https://iopscience.iop.org/article/10.1088/1748-9326/abfa4c (visited on 03/15/2022).

Cnudde, V. and M.N. Boone (Aug. 2013). "High-Resolution X-ray Computed Tomography in Geosciences: A Review of the Current Technology and Applications." en. In: *Earth-*

Science Reviews 123, pp. 1–17. ISSN: 00128252. DOI: 10.1016/j.earscirev.2013.04.003. URL: https://linkinghub.elsevier.com/retrieve/pii/S001282521300069X (visited on 01/15/2020).

Company, Chemical Rubber and David R. Lide, eds. (2004). *CRC Handbook of Chemistry and Physics: A Ready-Reference Book of Chemical and Physical Data*. eng. 85. ed. Boca Raton: CRC Press. ISBN: 978-0-8493-0485-9.

Copernicus (2021). *Arctic Wildfires*. Copernicus climate change Service. URL: https://climate.copernicus.eu/esotc/2021/arctic-wildfires.

Corriol, Gilles (2009). "Pyrrhoglossum Moliniophilum Sp. Nov.(Basidiomycota, Cortinariales), a New Species and First Record of the Genus in Europe." In: *Cryptogamie* 30.2, pp. 141–152.

Costanza-Robinson, Molly S. et al. (July 2011). "Representative Elementary Volume Estimation for Porosity, Moisture Saturation, and Air-Water Interfacial Areas in Unsaturated Porous Media: Data Quality Implications." en. In: *Water Resources Research* 47.7 (7). ISSN: 00431397. DOI: 10.1029/2010WR009655. URL: http://doi.wiley.com/10.1029/2010WR009655 (visited on 02/28/2020).

Crockett, Audrey C. et al. (Sept. 2016). "Relationships between Vegetation Type, Peat Hydraulic Conductivity, and Water Table Dynamics in Mountain Fens: Relating Vegetation Type and Peat Hydraulic Conductivity in Mountain Fens." en. In: *Ecohydrology* 9.6, pp. 1028–1038. ISSN: 19360584. DOI: 10.1002/eco.1706. URL: http://doi.wiley.com/10.1002/eco.1706 (visited on 12/03/2020).

Cunliffe, Andrew M. et al. (May 27, 2019). "Rapid Retreat of Permafrost Coastline Observed with Aerial Drone Photogrammetry." en. In: *The Cryosphere* 13.5, pp. 1513–1528. ISSN: 1994-0424. DOI: 10.5194/tc-13-1513-2019. URL: https://tc.copernicus.org/articles/13/1513/2019/ (visited on 10/11/2023).

Darbon, Jerome et al. (May 2008). "Fast Nonlocal Filtering Applied to Electron Cryomicroscopy." In: *2008 5th IEEE International Symposium on Biomedical Imaging: From Nano to Macro*. 2008 5th IEEE International Symposium on Biomedical Imaging (ISBI 2008). Paris, France: IEEE, pp. 1331–1334. ISBN: 978-1-4244-2002-5. DOI: 10.1109/ISBI.2008.4541250. URL: http://ieeexplore.ieee.org/document/4541250/ (visited on 08/29/2023).

Darcy, Henry (1856). *Les Fontaines Publiques de La Ville de Dijon: Exposition et Application Des Principes à Suivre et Des Formules à Employer Dans Les Questions de Distributions d'eau.* Victor Dalmont.

Davarzani, Hossein (2010). "Détermination Théorique et Expérimentale Des Coefficients de Diffusion Er de Thermodiffusion En Milieu Poreux." Université de Toulouse.

Davy, Richard, Linling Chen, et al. (Oct. 2018). "Arctic Amplification Metrics." en. In: *International Journal of Climatology* 38.12, pp. 4384–4394. ISSN: 08998418. DOI: 10.1002/joc.5675. URL: https://onlinelibrary.wiley.com/doi/10.1002/joc.5675 (visited on 09/12/2023).

Davy, Richard and Philipp Griewank (Aug. 1, 2023). "Arctic Amplification Has Already Peaked." In: *Environmental Research Letters* 18.8, p. 084003. ISSN: 1748-9326. DOI: 10.1088/1748-9326/ace273. URL: https://iopscience.iop.org/article/10.1088/1748-9326/ace273 (visited on 09/12/2023).

Dawson-Haggerty et al. (Dec. 8, 2019). *Trimesh*. Version 3.2.0. URL: https://trimsh.org/.

De Guzman, Earl Marvin B. and Marolo C. Alfaro (July 2018). "Geotechnical Properties of Fibrous and Amorphous Peats for the Construction of Road Embankments." en. In: *Journal of Materials in Civil Engineering* 30.7, p. 04018149. ISSN: 0899-1561, 1943-5533. DOI: 10.1061/(ASCE)MT.1943-5533.0002325. URL: https://ascelibrary.org/doi/10.1061/%28ASCE%29MT.1943-5533.0002325 (visited on 01/30/2023).

Deardorff, J. W. (1978). "Efficient Prediction of Ground Surface Temperature and Moisture, with Inclusion of a Layer of Vegetation." en. In: *Journal of Geophysical Research* 83.C4, p. 1889. ISSN: 0148-0227. DOI: 10.1029/JC083iC04p01889. URL: http://doi.wiley.com/10.1029/JC083iC04p01889 (visited on 04/26/2023).

Degiovanni, Alain (1994). "Conductivité et Diffusivité Thermique Des Solides." In: *Techniques de l'ingénieur* 1.R2850.

Delwiche, Charles F. and Ruth E. Timme (June 2011). "Plants." en. In: *Current Biology* 21.11, R417–R422. ISSN: 09609822. DOI: 10.1016/j.cub.2011.04.021. URL: https://linkinghub.elsevier.com/retrieve/pii/S0960982211004374 (visited on 01/27/2023).

De Vries, D. (1963). "Thermal Properties of Soils." In: van Wijk, W. *Physics of Plant Environment*. Amsterdam: North-Holland Publ. Co., pp. 210–235.

Dimitrov, Dimitre D. et al. (July 2010). "Modeling Peat Thermal Regime of an Ombrotrophic Peatland with Hummock-Hollow Microtopography." en. In: *Soil Science Society of America Journal* 74.4, pp. 1406–1425. ISSN: 03615995. DOI: 10.2136/sssaj2009.0288. URL: http://doi.wiley.com/10.2136/sssaj2009.0288 (visited on 01/30/2023).

Dong, Hu and Martin J. Blunt (Sept. 14, 2009). "Pore-Network Extraction from Micro-Computerized-Tomography Images." en. In: *Physical Review E* 80.3 (3), p. 036307. ISSN: 1539-3755, 1550-2376. DOI: 10.1103/PhysRevE.80.036307. URL: https://link.aps.org/doi/10.1103/PhysRevE.80.036307 (visited on 01/16/2020).

Du, Xinzhong et al. (May 2020). "Hydro-Climate and Biogeochemical Processes Control Watershed Organic Carbon Inflows: Development of an in-Stream Organic Carbon Module Coupled with a Process-Based Hydrologic Model." en. In: *Science of The Total Environment* 718, p. 137281. ISSN: 00489697. DOI: 10.1016/j.scitotenv.2020.137281. URL: https://linkinghub.elsevier.com/retrieve/pii/S0048969720307919 (visited on 10/19/2021).

Durantez, Pilar et al. (2014). *Étude hydrogéologique sur la tourbière de Clarens*. FR. Toulouse: Université Toulouse III - Paul Sabatier, p. 92.

Durlofsky, Louis J. (May 1991). "Numerical Calculation of Equivalent Grid Block Permeability Tensors for Heterogeneous Porous Media." en. In: *Water Resources Research* 27.5,

pp. 699–708. ISSN: 00431397. DOI: 10.1029/91WR00107. URL: http://doi.wiley.com/10.1029/91WR00107 (visited on 11/25/2020).

El-Abbassi, M. et al. (Sept. 2017). "Modelling Turbulent Combustion Coupled with Conjugate Heat Transfer in OpenFOAM." In: Tenth Mediterranean Combustion Symposium. Napoli, Italy.

Elliott, James and Jonathan Price (Mar. 2020). "Comparison of Soil Hydraulic Properties Estimated from Steady-State Experiments and Transient Field Observations through Simulating Soil Moisture in Regenerated Sphagnum Moss." en. In: *Journal of Hydrology* 582, p. 124489. ISSN: 00221694. DOI: 10.1016/j.jhydrol.2019.124489. URL: https://linkinghub.elsevier.com/retrieve/pii/S0022169419312247 (visited on 11/10/2021).

Eyring, Veronika et al. (May 26, 2016). "Overview of the Coupled Model Intercomparison Project Phase 6 (CMIP6) Experimental Design and Organization." en. In: *Geoscientific Model Development* 9.5, pp. 1937–1958. ISSN: 1991-9603. DOI: 10.5194/gmd-9-1937-2016. URL: https://gmd.copernicus.org/articles/9/1937/2016/ (visited on 10/11/2023).

Fabre, Clément et al. (June 10, 2017). "Using Modeling Tools to Better Understand Permafrost Hydrology." en. In: *Water* 9.6, p. 418. ISSN: 2073-4441. DOI: 10.3390/w9060418. URL: http://www.mdpi.com/2073-4441/9/6/418 (visited on 10/19/2021).

Faggioni, Lorenzo and Michela Gabelloni (Dec. 2016). "Iodine Concentration and Optimization in Computed Tomography Angiography: Current Issues." en. In: *Investigative Radiology* 51.12, pp. 816–822. ISSN: 1536-0210, 0020-9996. DOI: 10.1097/RLI.0000000000000283. URL: https://journals.lww.com/00004424-201612000-00009 (visited on 10/14/2023).

Farouki, Omar T. (Dec. 1981). *Thermal Properties of Soils*. Monograph CRREL Monograph 81-1. Hanover, NH, USA: Cold Regions Research and Engineering Laboratory. URL: https://apps.dtic.mil/sti/citations/ADA111734.

Fatehnia, Milad (2015). "Automated Method for Determining Infiltration Rate in Soils." en. In: DOI: 10.13140/RG.2.1.2295.3682. URL: http://rgdoi.net/10.13140/RG.2.1.2295.3682 (visited on 01/10/2024).

Fatt, I. (Dec. 1, 1956). "The Network Model of Porous Media." en. In: *Transactions of the AIME* 207.01, pp. 144–181. ISSN: 0081-1696. DOI: 10.2118/574-G. URL: http://www.onepetro.org/doi/10.2118/574-G (visited on 11/23/2020).

Fourier, Joseph (1822). *Théorie analytique de la chaleur*. fr. Paris: Firmin Didot, père et fils. 687 pp. URL: https://gallica.bnf.fr/ark:/12148/bpt6k1045508v/f9.item.

Fox-Kemper, B. et al. (2023). "Ocean, Cryosphere and Sea Level Change." In: *Climate Change 2021: The Physical Science Basis. Contribution of Working Group I to the Sixth Assessment Report of the Intergovernmental Panel on Climate Change*. Ed. by V. Masson-Delmotte et al. Cambridge University Press. URL: https://www.ipcc.ch/report/ar6/wg1/chapter/chapter-9/.

Frost, Gerald V. and Howard E. Epstein (Apr. 2014). "Tall Shrub and Tree Expansion in Siberian Tundra Ecotones since the 1960s." en. In: *Global Change Biology* 20.4, pp. 1264–

1277. ISSN: 13541013. DOI: 10.1111/gcb.12406. URL: https://onlinelibrary.wiley.com/doi/10.1111/gcb.12406 (visited on 09/18/2023).

Galvin, LF (1976). "Physical Properties of Irish Peats." In: *Irish Journal of Agricultural Research*, pp. 207–221. JSTOR: 25555820. URL: https://www.jstor.org/stable/25555820.

Ge, Nan et al. (Mar. 1, 2016). "Calibrating the X-ray Attenuation of Liquid Water and Correcting Sample Movement Artefacts during *in Operando* Synchrotron X-ray Radiographic Imaging of Polymer Electrolyte Membrane Fuel Cells." In: *Journal of Synchrotron Radiation* 23.2, pp. 590–599. ISSN: 1600-5775. DOI: 10.1107/S1600577515023899. URL: https://scripts.iucr.org/cgi-bin/paper?S1600577515023899 (visited on 08/30/2023).

Genxu, Wang et al. (July 2017). "Processes of Runoff Generation Operating during the Spring and Autumn Seasons in a Permafrost Catchment on Semi-Arid Plateaus." en. In: *Journal of Hydrology* 550, pp. 307–317. ISSN: 00221694. DOI: 10.1016/j.jhydrol.2017.05.020. URL: https://linkinghub.elsevier.com/retrieve/pii/S0022169417303098 (visited on 10/19/2021).

Gerrienne, Philippe et al. (2020). "Earliest Evidence of Land Plants in Brazil." en. In: *Brazilian Paleofloras*. Ed. by Roberto Iannuzzi et al. Cham: Springer International Publishing, pp. 1–39. ISBN: 978-3-319-90913-4. DOI: 10.1007/978-3-319-90913-4_2-1. URL: http://link.springer.com/10.1007/978-3-319-90913-4_2-1 (visited on 06/13/2023).

Giovannini, André and Benoît Bédat (2012). *Transfert de chaleur*. fre. Toulouse: Cépaduès éd. ISBN: 978-2-36493-024-7.

Golubev, V., C. McCarter, et al. (Dec. 2021). "Ecohydrological Implications of the Variability of Soil Hydrophysical Properties between Two Sphagnum Moss Microforms and the Impact of Different Sample Heights." en. In: *Journal of Hydrology* 603, p. 126956. ISSN: 00221694. DOI: 10.1016/j.jhydrol.2021.126956. URL: https://linkinghub.elsevier.com/retrieve/pii/S0022169421010064 (visited on 11/10/2021).

Golubev, V. and P. Whittington (Apr. 2018). "Effects of Volume Change on the Unsaturated Hydraulic Conductivity of Sphagnum Moss." en. In: *Journal of Hydrology* 559, pp. 884–894. ISSN: 00221694. DOI: 10.1016/j.jhydrol.2018.02.083. URL: https://linkinghub.elsevier.com/retrieve/pii/S0022169418301653 (visited on 11/26/2020).

Gong, Jinnan et al. (Nov. 23, 2020). "Modelling the Habitat Preference of Two Key Sphagnum Species in a Poor Fen as Controlled by Capitulum Water Content." en. In: *Biogeosciences* 17.22, pp. 5693–5719. ISSN: 1726-4189. DOI: 10.5194/bg-17-5693-2020. URL: https://bg.copernicus.org/articles/17/5693/2020/ (visited on 07/29/2021).

Gonzalez, Aridane G. et al. (Jan. 2016). "Metal and Proton Adsorption Capacities of Natural and Cloned Sphagnum Mosses." en. In: *Journal of Colloid and Interface Science* 461, pp. 326–334. ISSN: 00219797. DOI: 10.1016/j.jcis.2015.09.012. URL: https://linkinghub.elsevier.com/retrieve/pii/S0021979715301831 (visited on 11/03/2021).

Gordon, J. et al. (Sept. 30, 2016). "Mercury and Methylmercury Biogeochemistry in a Thawing Permafrost Wetland Complex, Northwest Territories, Canada: Northwest Territories, Canada." en. In: *Hydrological Processes* 30.20, pp. 3627–3638. ISSN: 08856087. DOI: 10.1002/hyp.10911. URL: https://onlinelibrary.wiley.com/doi/10.1002/hyp.10911 (visited on 09/15/2023).

Goremykin, V. V. and F. H. Hellwig (July 2005). "Evidence for the Most Basal Split in Land Plants Dividing Bryophyte and Tracheophyte Lineages." en. In: *Plant Systematics and Evolution* 254.1-2, pp. 93–103. ISSN: 0378-2697, 1615-6110. DOI: 10.1007/s00606-005-0337-1. URL: http://link.springer.com/10.1007/s00606-005-0337-1 (visited on 01/27/2023).

Gostick, Jeff et al. (Aug. 3, 2019). *PMEAL/Porespy: New Features and Bug Fixes*. Version v1.2.0. DOI: 10.5281/ZENODO.2633284. URL: https://zenodo.org/record/2633284 (visited on 06/22/2020).

Gostick, Jeff T. (Aug. 16, 2017). "Versatile and Efficient Pore Network Extraction Method Using Marker-Based Watershed Segmentation." en. In: *Physical Review E* 96.2 (2), p. 023307. ISSN: 2470-0045, 2470-0053. DOI: 10.1103/PhysRevE.96.023307. URL: https://link.aps.org/doi/10.1103/PhysRevE.96.023307 (visited on 07/06/2020).

Goubet, Manon et al. (Aug. 2021). "3D Multi-Scale Study on Metal/Polymer Nano-Composites." en. In: *Microscopy and Microanalysis* 27.S1, pp. 1766–1768. ISSN: 1431-9276, 1435-8115. DOI: 10.1017/S1431927621006462. URL: https://www.cambridge.org/core/product/identifier/S1431927621006462/type/journal_article (visited on 11/10/2021).

Grenier, Christophe et al. (Apr. 2018). "Groundwater Flow and Heat Transport for Systems Undergoing Freeze-Thaw: Intercomparison of Numerical Simulators for 2D Test Cases." en. In: *Advances in Water Resources* 114, pp. 196–218. ISSN: 03091708. DOI: 10.1016/j.advwatres.2018.02.001. URL: https://linkinghub.elsevier.com/retrieve/pii/S0309170817307510 (visited on 11/10/2021).

Gruber, S. (Feb. 17, 2012). "Derivation and Analysis of a High-Resolution Estimate of Global Permafrost Zonation." en. In: *The Cryosphere* 6.1, pp. 221–233. ISSN: 1994-0424. DOI: 10.5194/tc-6-221-2012. URL: https://tc.copernicus.org/articles/6/221/2012/ (visited on 07/27/2023).

Guo, Donglin and Huijun Wang (Nov. 27, 2017). "Simulated Historical (1901-2010) Changes in the Permafrost Extent and Active Layer Thickness in the Northern Hemisphere: Historical Permafrost Change." en. In: *Journal of Geophysical Research: Atmospheres* 122.22, pp. 12, 285–12, 295. ISSN: 2169897X. DOI: 10.1002/2017JD027691. URL: http://doi.wiley.com/10.1002/2017JD027691 (visited on 03/15/2022).

Hamamoto, S. et al. (Jan. 2016). "Transport Properties and Pore-Network Structure in Variably-Saturated *Sphagnum* Peat Soil: Mass Transport Properties for Peat Soil." en. In: *European Journal of Soil Science* 67.1 (1), pp. 121–131. ISSN: 13510754. DOI: 10.1111/ejss.12312. URL: http://doi.wiley.com/10.1111/ejss.12312 (visited on 01/14/2020).

Harlan, R. L. and J.F. Nixon (1978). "Ground Thermal Regime." In: *Geotechnical Engineering for Cold Regions*. Ed. by Orlando B. Andersland and Duwayne M. Anderson. New York: McGraw-Hill, pp. 103–163. ISBN: 978-0-07-001615-6.

Harrap, Michael J. M., Natalie Hempel De Ibarra, et al. (Dec. 2018). "Reporting of Thermography Parameters in Biology: A Systematic Review of Thermal Imaging Literature." en. In: *Royal Society Open Science* 5.12, p. 181281. ISSN: 2054-5703. DOI: 10.1098/rsos.181281. URL: https://royalsocietypublishing.org/doi/10.1098/rsos.181281 (visited on 04/26/2023).

Harrap, Michael J. M. and Sean A. Rands (Dec. 2021). "Floral Infrared Emissivity Estimates Using Simple Tools." en. In: *Plant Methods* 17.1, p. 23. ISSN: 1746-4811. DOI: 10.1186/s13007-021-00721-w. URL: https://plantmethods.biomedcentral.com/articles/10.1186/s13007-021-00721-w (visited on 04/26/2023).

Harris, Brogan J. et al. (June 2020). "Phylogenomic Evidence for the Monophyly of Bryophytes and the Reductive Evolution of Stomata." en. In: *Current Biology* 30.11, 2001–2012.e2. ISSN: 09609822. DOI: 10.1016/j.cub.2020.03.048. URL: https://linkinghub.elsevier.com/retrieve/pii/S0960982220304188 (visited on 01/27/2023).

Hayward, P. M. and R. S. Clymo (June 22, 1982). "Profiles of Water Content and Pore Size in *Sphagnum* and Peat, and Their Relation to Peat Bog Ecology." en. In: *Proceedings of the Royal Society of London. Series B. Biological Sciences* 215.1200, pp. 299–325. ISSN: 0080-4649, 2053-9193. DOI: 10.1098/rspb.1982.0044. URL: https://royalsocietypublishing.org/doi/10.1098/rspb.1982.0044 (visited on 11/24/2020).

Heck, Melanie A. et al. (Jan. 2021). "Axenic *in Vitro* Cultivation of 19 Peat Moss (*Sphagnum* L.) Species as a Resource for Basic Biology, Biotechnology, and Paludiculture." en. In: *New Phytologist* 229.2, pp. 861–876. ISSN: 0028-646X, 1469-8137. DOI: 10.1111/nph.16922. URL: https://onlinelibrary.wiley.com/doi/10.1111/nph.16922 (visited on 08/10/2023).

Heikurainen, Leo (1963). "On Using Ground Water Table Fluctuations for Measuring Evapotranspiration." In: *Acta Forestalia Fennica* 76.5, pp. 5–16. ISSN: 0001-5636. URL: http://hdl.handle.net/10138/17653.

Heitz, W. L. and J. W. Westwater (May 1, 1971). "Critical Rayleigh Numbers for Natural Convection of Water Confined in Square Cells With L/D From 0.5 to 8." en. In: *Journal of Heat Transfer* 93.2, pp. 188–195. ISSN: 0022-1481, 1528-8943. DOI: 10.1115/1.3449783. URL: https://asmedigitalcollection.asme.org/heattransfer/article/93/2/188/429624/Critical-Rayleigh-Numbers-for-Natural-Convection (visited on 04/20/2023).

Hill, R. (Sept. 1963). "Elastic Properties of Reinforced Solids: Some Theoretical Principles." en. In: *Journal of the Mechanics and Physics of Solids* 11.5, pp. 357–372. ISSN: 00225096. DOI: 10.1016/0022-5096(63)90036-X. URL: https://linkinghub.elsevier.com/retrieve/pii/002250966390036X (visited on 10/11/2023).

Hinzman, Larry D. and Douglas L. Kane (1992). "Potential Response of an Arctic Watershed during a Period of Global Warming." en. In: *Journal of Geophysical Research* 97.D3,

p. 2811. ISSN: 0148-0227. DOI: 10.1029/91JD01752. URL: http://doi.wiley.com/10.1029/91JD01752 (visited on 01/26/2021).

Hjort, Jan, Olli Karjalainen, et al. (Dec. 11, 2018). "Degrading Permafrost Puts Arctic Infrastructure at Risk by Mid-Century." en. In: *Nature Communications* 9.1, p. 5147. ISSN: 2041-1723. DOI: 10.1038/s41467-018-07557-4. URL: https://www.nature.com/articles/s41467-018-07557-4 (visited on 09/16/2023).

Hjort, Jan, Dmitry Streletskiy, et al. (Jan. 11, 2022). "Impacts of Permafrost Degradation on Infrastructure." en. In: *Nature Reviews Earth & Environment* 3.1, pp. 24–38. ISSN: 2662-138X. DOI: 10.1038/s43017-021-00247-8. URL: https://www.nature.com/articles/s43017-021-00247-8 (visited on 10/11/2023).

Hobbie, Sarah E. and F. Stuart Chapin (June 1998). "An Experimental Test of Limits to Tree Establishment in Arctic Tundra." en. In: *Journal of Ecology* 86.3, pp. 449–461. ISSN: 0022-0477, 1365-2745. DOI: 10.1046/j.1365-2745.1998.00278.x. URL: https://besjournals.onlinelibrary.wiley.com/doi/10.1046/j.1365-2745.1998.00278.x (visited on 09/18/2023).

Hofmeister, Anne M. et al. (Mar. 16, 2021). "Possible Roles of Permafrost Melting, Atmospheric Transport, and Solar Irradiance in the Development of Major Coronavirus and Influenza Pandemics." en. In: *International Journal of Environmental Research and Public Health* 18.6, p. 3055. ISSN: 1660-4601. DOI: 10.3390/ijerph18063055. URL: https://www.mdpi.com/1660-4601/18/6/3055 (visited on 09/14/2023).

Holdridge, L. R. (Apr. 4, 1947). "Determination of World Plant Formations From Simple Climatic Data." en. In: *Science* 105.2727, pp. 367–368. ISSN: 0036-8075, 1095-9203. DOI: 10.1126/science.105.2727.367. URL: https://www.science.org/doi/10.1126/science.105.2727.367 (visited on 06/13/2023).

Hong, Seongwon et al. (Jan. 2, 2018). "Porosimetric Features of Calcium Sulfoaluminate and Portland Cement Pastes: Testing Protocols and Data Analysis." en. In: *Journal of Structural Integrity and Maintenance* 3.1, pp. 52–66. ISSN: 2470-5314, 2470-5322. DOI: 10.1080/24705314.2018.1426168. URL: https://www.tandfonline.com/doi/full/10.1080/24705314.2018.1426168 (visited on 10/06/2023).

Howie, Sarah A. and Richard J. Hebda (May 30, 2018). "Bog Surface Oscillation (Mire Breathing): A Useful Measure in Raised Bog Restoration." en. In: *Hydrological Processes* 32.11, pp. 1518–1530. ISSN: 08856087. DOI: 10.1002/hyp.11622. URL: http://doi.wiley.com/10.1002/hyp.11622 (visited on 01/26/2021).

Hueffer, Karsten et al. (Mar. 2020). "Factors Contributing to Anthrax Outbreaks in the Circumpolar North." en. In: *EcoHealth* 17.1, pp. 174–180. ISSN: 1612-9202, 1612-9210. DOI: 10.1007/s10393-020-01474-z. URL: https://link.springer.com/10.1007/s10393-020-01474-z (visited on 09/14/2023).

Huntley, B and W Cramer (1997). "Arctic Ecosystems and Environmental Change." In: Crawford, R. M. M. and North Atlantic Treaty Organization. *Disturbance and Recovery in Arctic Lands: An Ecological Perspective*. NATO ASI Series vol. 25. Dordrecht ; Boston: Kluwer Academic Publishers. ISBN: 978-0-7923-4418-6.

Intergovernmental Panel on Climate Change (IPCC) (May 19, 2022). *The Ocean and Cryosphere in a Changing Climate: Special Report of the Intergovernmental Panel on Climate Change*. 1st ed. Cambridge University Press. ISBN: 978-1-00-915796-4 978-1-00-915797-1. DOI: 10.1017/9781009157964. URL: https://www.cambridge.org/core/product/identifier/9781009157964/type/book (visited on 01/16/2023).

International Permafrost Association (2015). "What Is Permafrost ?" In: URL: https://ipa.arcticportal.org/publications/occasional-publications/what-is-permafrost (visited on 06/11/2020).

International Union of Soil Sciences (2022). *World Reference Base for Soil Resources. International Soil Classification System for Naming Soils and Creating Legends for Soil Maps. 4th Edition.* Vienna, Austria: International Union of Soil Sciences. URL: https://wrb.isric.org/files/WRB_fourth_edition_2022-12-18.pdf.

Ishikawa, M (May 30, 2003). "Thermal Regimes at the Snow-Ground Interface and Their Implications for Permafrost Investigation." In: *Geomorphology* 52.1-2, pp. 105–120. ISSN: 0169-555X. DOI: 10.1016/S0169-555X(02)00251-9.

Jackowicz-Korczyński, Marcin et al. (June 2010). "Annual Cycle of Methane Emission from a Subarctic Peatland: CH4 Fluxes from a Subarctic Peatland." en. In: *Journal of Geophysical Research: Biogeosciences* 115.G2, n/a–n/a. ISSN: 01480227. DOI: 10.1029/2008JG000913. URL: http://doi.wiley.com/10.1029/2008JG000913 (visited on 05/03/2021).

Jungclaus, J. H. et al. (Apr. 2022). "The ICON Earth System Model Version 1.0." en. In: *Journal of Advances in Modeling Earth Systems* 14.4, e2021MS002813. ISSN: 1942-2466, 1942-2466. DOI: 10.1029/2021MS002813. URL: https://agupubs.onlinelibrary.wiley.com/doi/10.1029/2021MS002813 (visited on 10/11/2023).

Kain, Günther et al. (Nov. 2, 2021). "Production and Physical–Mechanical Characterization of Peat Moss (Sphagnum) Insulation Panels." en. In: *Materials* 14.21, p. 6601. ISSN: 1996-1944. DOI: 10.3390/ma14216601. URL: https://www.mdpi.com/1996-1944/14/21/6601 (visited on 01/30/2023).

Kämäräinen, A. et al. (Aug. 15, 2018). "Physical Growing Media Characteristics of Sphagnum Biomass Dominated by Sphagnum Fuscum (Schimp.) Klinggr." eng. In: *Mires and Peat* 1.21, pp. 1–16. ISSN: 1819-754X. DOI: 10.19189/MaP.2017.OMB.278. URL: https://doi.org/10.19189/MaP.2017.OMB.278 (visited on 09/22/2021).

Kåresdotter, Elisie et al. (May 2021). "Mapping the Vulnerability of Arctic Wetlands to Global Warming." en. In: *Earth's Future* 9.5, e2020EF001858. ISSN: 2328-4277, 2328-4277. DOI: 10.1029/2020EF001858. URL: https://agupubs.onlinelibrary.wiley.com/doi/10.1029/2020EF001858 (visited on 10/10/2023).

Karlsson, Johanna Mard et al. (Oct. 2015). "Hydro-Climatic and Lake Change Patterns in Arctic Permafrost and Non-Permafrost Areas." In: *Journal of Hydrology* 529.1, pp. 134–145. ISSN: 0022-1694. DOI: 10.1016/j.jhydrol.2015.07.005.

Kaviany, M (1995). *Principles of Heat Transfer in Porous Media*. English. ISBN: 978-1-4612-4254-3. URL: https://doi.org/10.1007/978-1-4612-4254-3 (visited on 05/28/2021).

Kellner, Erik (Dec. 2001). "Surface Energy Fluxes and Control of Evapotranspiration from a Swedish Sphagnum Mire." en. In: *Agricultural and Forest Meteorology* 110.2, pp. 101–123. ISSN: 01681923. DOI: 10.1016/S0168-1923(01)00283-0. URL: https://linkinghub.elsevier.com/retrieve/pii/S0168192301002830 (visited on 01/30/2023).

Kettridge, N. and A. Baird (May 22, 2007). "In Situ Measurements of the Thermal Properties of a Northern Peatland: Implications for Peatland Temperature Models." en. In: *Journal of Geophysical Research* 112.F2, F02019. ISSN: 0148-0227. DOI: 10.1029/2006JF000655. URL: http://doi.wiley.com/10.1029/2006JF000655 (visited on 06/24/2021).

Khan, Zohaib Atiq et al. (Nov. 2020). "Efficient Extraction of Pore Networks from Massive Tomograms via Geometric Domain Decomposition." en. In: *Advances in Water Resources* 145, p. 103734. ISSN: 03091708. DOI: 10.1016/j.advwatres.2020.103734. URL: https://linkinghub.elsevier.com/retrieve/pii/S0309170820304814 (visited on 07/26/2021).

Kharuk, Viacheslav I. et al. (May 30, 2023). "Lightning-Ignited Wildfires beyond the Polar Circle." en. In: *Atmosphere* 14.6, p. 957. ISSN: 2073-4433. DOI: 10.3390/atmos14060957. URL: https://www.mdpi.com/2073-4433/14/6/957 (visited on 09/18/2023).

Kim, Jin-Soo et al. (Jan. 10, 2020). "Extensive Fires in Southeastern Siberian Permafrost Linked to Preceding Arctic Oscillation." en. In: *Science Advances* 6.2, eaax3308. ISSN: 2375-2548. DOI: 10.1126/sciadv.aax3308. URL: https://www.science.org/doi/10.1126/sciadv.aax3308 (visited on 10/10/2023).

Klaminder, Jonatan et al. (Dec. 2008). "An Explorative Study of Mercury Export from a Thawing Palsa Mire: Mercury Export from a Palsa Mire." en. In: *Journal of Geophysical Research: Biogeosciences* 113.G4. ISSN: 01480227. DOI: 10.1029/2008JG000776. URL: http://doi.wiley.com/10.1029/2008JG000776 (visited on 08/28/2023).

Klinova, E. A. et al. (2012). "State geological map of the Russian Federation." Ru. In:

Kohler, Jack et al. (2006). "A Long Term Arctic Snow Depth Record from Abisko, Northern Sweden, 1913-2004." In: *Polar Research* 2.25, pp. 91–113. DOI: 10.3402/polar.v25i2.6240.

Koponen, A. et al. (July 1, 1996). "Tortuous Flow in Porous Media." en. In: *Physical Review E* 54.1, pp. 406–410. ISSN: 1063-651X, 1095-3787. DOI: 10.1103/PhysRevE.54.406. URL: https://link.aps.org/doi/10.1103/PhysRevE.54.406 (visited on 03/16/2022).

– (Sept. 1997). "Permeability and Effective Porosity of Porous Media." en. In: *Physical Review E* 56.3, pp. 3319–3325. ISSN: 1063-651X, 1095-3787. DOI: 10.1103/PhysRevE.56.3319. URL: https://link.aps.org/doi/10.1103/PhysRevE.56.3319 (visited on 03/15/2022).

Kuklina, Vera et al. (Feb. 23, 2022). "Fires on Ice: Emerging Permafrost Peatlands Fire Regimes in Russia's Subarctic Taiga." en. In: *Land* 11.3, p. 322. ISSN: 2073-445X. DOI: 10.3390/land11030322. URL: https://www.mdpi.com/2073-445X/11/3/322 (visited on 09/18/2023).

Kuva, J. et al. (2018). "Imaging Connected Porosity of Crystalline Rock by Contrast Agent-Aided X-ray Microtomography and Scanning Electron Microscopy." In: *Journal of Microscopy* 270.1, pp. 98–109. DOI: 10.1111/jmi.12661. URL: https://onlinelibrary.wiley.com/doi/abs/10.1111/jmi.12661.

Lahiri, B. B. et al. (2012). "Medical Applications of Infrared Thermography: A Review." In: *Infrared Physics & Technology* 1.55, pp. 221–235. DOI: http://dx.doi.org/10.1016/j.infrared.2012.03.007.

Laine, Jukka et al. (2018). *Sphagnum Mosses: The Stars of European Mires*. eng. Helsinki: Department of Forest Sciences, University of Helsinki. 326 pp. ISBN: 978-951-51-3143-0.

Lapwood, E. R. (Oct. 1948). "Convection of a Fluid in a Porous Medium." en. In: *Mathematical Proceedings of the Cambridge Philosophical Society* 44.4, pp. 508–521. ISSN: 0305-0041, 1469-8064. DOI: 10.1017/S030500410002452X. URL: https://www.cambridge.org/core/product/identifier/S030500410002452X/type/journal_article (visited on 05/02/2023).

Launiainen, Samuli et al. (Sept. 2015). "Coupling Boreal Forest CO2, H2O and Energy Flows by a Vertically Structured Forest Canopy – Soil Model with Separate Bryophyte Layer." en. In: *Ecological Modelling* 312, pp. 385–405. ISSN: 03043800. DOI: 10.1016/j.ecolmodel.2015.06.007. URL: https://linkinghub.elsevier.com/retrieve/pii/S0304380015002562 (visited on 01/16/2020).

Laurén, A. and J. Heiskanen (Nov. 1, 1997). "Physical Properties of the Mor Layer in a Scots Pine Stand I. Hydraulic Conductivity." en. In: *Canadian Journal of Soil Science* 77.4 (4), pp. 627–634. ISSN: 0008-4271, 1918-1841. DOI: 10.4141/S95-002. URL: http://www.nrcresearchpress.com/doi/10.4141/S95-002 (visited on 06/25/2020).

Le, Kieu Hiep et al. (Sept. 2016). "Pore Network Simulations of Heat and Mass Transfer inside an Unsaturated Capillary Porous Wick in the Dry-out Regime." en. In: *Transport in Porous Media* 114.3, pp. 623–648. ISSN: 0169-3913, 1573-1634. DOI: 10.1007/s11242-016-0737-4. URL: http://link.springer.com/10.1007/s11242-016-0737-4 (visited on 09/20/2023).

Leroy, P. et al. (May 2008). "Complex Conductivity of Water-Saturated Packs of Glass Beads." en. In: *Journal of Colloid and Interface Science* 321.1, pp. 103–117. ISSN: 00219797. DOI: 10.1016/j.jcis.2007.12.031. URL: https://linkinghub.elsevier.com/retrieve/pii/S0021979707018279 (visited on 11/25/2020).

Li, Mingyang et al. (July 14, 2019). "The Scale Effect of Double-Ring Infiltration and Soil Infiltration Zoning in a Semi-Arid Steppe." en. In: *Water* 11.7, p. 1457. ISSN: 2073-4441. DOI: 10.3390/w11071457. URL: https://www.mdpi.com/2073-4441/11/7/1457 (visited on 01/10/2024).

Liljedahl, Anna K. et al. (Apr. 2016). "Pan-Arctic Ice-Wedge Degradation in Warming Permafrost and Its Influence on Tundra Hydrology." en. In: *Nature Geoscience* 9.4, pp. 312–318. ISSN: 1752-0894, 1752-0908. DOI: 10.1038/ngeo2674. URL: http://www.nature.com/articles/ngeo2674 (visited on 01/16/2020).

Lim, A. G. et al. (2017). "Structural-Functional Features of Landscapes with Active Thermocarst in the Northern Taiga of Western Siberia." In: *Ukrainian Journal of Ecology* 7.4, pp. 414–423. ISSN: 2520-2138.

Limpens, Juul et al. (Mar. 2021). "Shrubs and Degraded Permafrost Pave the Way for Tree Establishment in Subarctic Peatlands." en. In: *Ecosystems* 24.2, pp. 370–383. ISSN: 1432-9840, 1435-0629. DOI: 10.1007/s10021-020-00523-6. URL: https://link.springer.com/10.1007/s10021-020-00523-6 (visited on 09/18/2023).

Liskova, Elena A. et al. (June 24, 2021). "Reindeer Anthrax in the Russian Arctic, 2016: Climatic Determinants of the Outbreak and Vaccination Effectiveness." In: *Frontiers in Veterinary Science* 8, p. 668420. ISSN: 2297-1769. DOI: 10.3389/fvets.2021.668420. URL: https://www.frontiersin.org/articles/10.3389/fvets.2021.668420/full (visited on 09/14/2023).

Loiko, S. V. et al. (June 30, 2019). "Microtopography Controls of Carbon and Related Elements Distribution in the West Siberian Frozen Bogs." en. In: *Geosciences* 9.7, p. 291. ISSN: 2076-3263. DOI: 10.3390/geosciences9070291. URL: https://www.mdpi.com/2076-3263/9/7/291 (visited on 08/25/2023).

Lopez-Baeza, E et al. (Sept. 14, 1987). "Angstrom's Thermal Diffusivity Method for Short Samples." In: *Journal of Physics D: Applied Physics* 20.9, pp. 1156–1158. ISSN: 0022-3727, 1361-6463. DOI: 10.1088/0022-3727/20/9/011. URL: https://iopscience.iop.org/article/10.1088/0022-3727/20/9/011 (visited on 03/21/2023).

Loranty, Michael M. et al. (Aug. 31, 2018). "Reviews and Syntheses: Changing Ecosystem Influences on Soil Thermal Regimes in Northern High-Latitude Permafrost Regions." en. In: *Biogeosciences* 15.17, pp. 5287–5313. ISSN: 1726-4189. DOI: 10.5194/bg-15-5287-2018. URL: https://bg.copernicus.org/articles/15/5287/2018/ (visited on 04/20/2022).

Lupascu, M. et al. (Nov. 2012). "Temperature Sensitivity of Methane Production in the Permafrost Active Layer at Stordalen, Sweden: A Comparison with Non-permafrost Northern Wetlands." en. In: *Arctic, Antarctic, and Alpine Research* 44.4, pp. 469–482. ISSN: 1523-0430, 1938-4246. DOI: 10.1657/1938-4246-44.4.469. URL: https://www.tandfonline.com/doi/full/10.1657/1938-4246-44.4.469 (visited on 05/03/2021).

Lutzoni, François and Jolanta Miadlikowska (July 2009). "Lichens." en. In: *Current Biology* 19.13, R502–R503. ISSN: 09609822. DOI: 10.1016/j.cub.2009.04.034. URL: https://linkinghub.elsevier.com/retrieve/pii/S0960982209010331 (visited on 01/27/2023).

Lyon, Steve W. et al. (Jan. 1, 2018). "Lessons Learned from Monitoring the Stable Water Isotopic Variability in Precipitation and Streamflow across a Snow-Dominated Subarctic Catchment." en. In: *Arctic, Antarctic, and Alpine Research* 50.1, e1454778. ISSN: 1523-0430, 1938-4246. DOI: 10.1080/15230430.2018.1454778. URL: https://www.tandfonline.com/doi/full/10.1080/15230430.2018.1454778 (visited on 04/16/2021).

Maalal, Otman et al. (Feb. 9, 2021). "Determination of the Throat Size Distribution of a Porous Medium as an Inverse Optimization Problem Combining Pore Network

Modeling and Genetic and Hill Climbing Algorithms." en. In: *Physical Review E* 103.2, p. 023303. ISSN: 2470-0045, 2470-0053. DOI: 10.1103/PhysRevE.103.023303. URL: https://link.aps.org/doi/10.1103/PhysRevE.103.023303 (visited on 07/29/2021).

Malmer, Nils et al. (Oct. 6, 2005). "Vegetation, Climatic Changes and Net Carbon Sequestration in a North-Scandinavian Subarctic Mire over 30 Years." en. In: *Global Change Biology* 0.0, 051006062331004–??? ISSN: 1354-1013, 1365-2486. DOI: 10.1111/j.1365-2486.2005.01042.x. URL: https://onlinelibrary.wiley.com/doi/10.1111/j.1365-2486.2005.01042.x (visited on 08/10/2023).

Malmström, C (1925). "Some Pointers for the Drainage of Peat Soils in Noorland." In: *Skogliga Ron* 4.

Manabe, Syukuro and Ronald J. Stouffer (1980). "Sensitivity of a Global Climate Model to an Increase of CO_2 Concentration in the Atmosphere." en. In: *Journal of Geophysical Research* 85.C10, p. 5529. ISSN: 0148-0227. DOI: 10.1029/JC085iC10p05529. URL: http://doi.wiley.com/10.1029/JC085iC10p05529 (visited on 09/11/2023).

Marschall, Mariann and Michael C. F. Proctor (Oct. 2004). "Are Bryophytes Shade Plants? Photosynthetic Light Responses and Proportions of Chlorophyll a, Chlorophyll b and Total Carotenoids." en. In: *Annals of Botany* 94.4, pp. 593–603. ISSN: 1095-8290, 0305-7364. DOI: 10.1093/aob/mch178. URL: https://academic.oup.com/aob/article-lookup/doi/10.1093/aob/mch178 (visited on 09/25/2023).

Maschenko, E. N. et al. (Dec. 2021). "Morphology, Individual Age, DNA and Sex of the Yuka Mammoth (Mammuthus Primigenius) from Northern Yakutia, Russia." en. In: *Paleontological Journal* 55.11, pp. 1230–1259. ISSN: 0031-0301, 1555-6174. DOI: 10.1134/S003103012111006X. URL: https://link.springer.com/10.1134/S003103012111006X (visited on 09/13/2023).

McCarter, C. and J. Price (Feb. 2014). "Ecohydrology of *Sphagnum* Moss Hummocks: Mechanisms of Capitula Water Supply and Simulated Effects of Evaporation: Ecohydrology of Sphagnum Moss Hummocks." en. In: *Ecohydrology* 7.1, pp. 33–44. ISSN: 19360584. DOI: 10.1002/eco.1313. URL: https://onlinelibrary.wiley.com/doi/10.1002/eco.1313 (visited on 11/10/2021).

McCarter, C., F. Rezanezhad, et al. (Aug. 2020). "Pore-Scale Controls on Hydrological and Geochemical Processes in Peat: Implications on Interacting Processes." en. In: *Earth-Science Reviews* 207, p. 103227. ISSN: 00128252. DOI: 10.1016/j.earscirev.2020.103227. URL: https://linkinghub.elsevier.com/retrieve/pii/S0012825220302737 (visited on 03/09/2021).

Meredith, Michael et al. (2019). *IPCC Special Report on the Ocean and Cryosphere in a Changing Climate*. URL: https://doi.org/10.1017/9781009157964.005..

Minayeva, Tatiana et al. (2016). "Arctic Peatlands." en. In: *The Wetland Book*. Ed. by C. Max Finlayson et al. Dordrecht: Springer Netherlands, pp. 1–15. ISBN: 978-94-007-6173-5. DOI: 10.1007/978-94-007-6173-5_109-2. URL: http://link.springer.com/10.1007/978-94-007-6173-5_109-2 (visited on 01/19/2023).

Modest, M. F. (2013). *Radiative Heat Transfer*. Third Edition. New York: Academic Press. 882 pp. ISBN: 978-0-12-386944-9.

Mohammadmoradi, Peyman and Apostolos Kantzas (Oct. 2016). "Pore-Scale Permeability Calculation Using CFD and DSMC Techniques." en. In: *Journal of Petroleum Science and Engineering* 146, pp. 515–525. ISSN: 09204105. DOI: 10.1016/j.petrol.2016.07.010. URL: https://linkinghub.elsevier.com/retrieve/pii/S0920410516302698 (visited on 10/19/2021).

Mojtabi, A. et al. (Jan. 10, 2019). "Transferts de chaleur dans les milieux poreux - Conduction, convection, rayonnnement." FR. In: *Techniques de l'ingénieur*. Énergie | Physique énergétique. URL: https://www.techniques-ingenieur.fr/res/pdf/encyclopedia/42214210-be8250.pdf.

Morgalev, Sergey Yu et al. (Jan. 2023). "Fractionation of Organic C, Nutrients, Metals and Bacteria in Peat Porewater and Ice after Freezing and Thawing." en. In: *Environmental Science and Pollution Research* 30.1, pp. 823–836. ISSN: 0944-1344, 1614-7499. DOI: 10.1007/s11356-022-22219-1. URL: https://link.springer.com/10.1007/s11356-022-22219-1 (visited on 10/12/2023).

Morgalev, Y. N. et al. (Aug. 2017). "Bacteria Primarily Metabolize at the Active Layer/Permafrost Border in the Peat Core from a Permafrost Region in Western Siberia." en. In: *Polar Biology* 40.8, pp. 1645–1659. ISSN: 0722-4060, 1432-2056. DOI: 10.1007/s00300-017-2088-1. URL: http://link.springer.com/10.1007/s00300-017-2088-1 (visited on 04/01/2021).

Nagare, R. M. et al. (Feb. 15, 2012). "Effects of Freezing on Soil Temperature, Freezing Front Propagation and Moisture Redistribution in Peat: Laboratory Investigations." en. In: *Hydrology and Earth System Sciences* 16.2, pp. 501–515. ISSN: 1607-7938. DOI: 10.5194/hess-16-501-2012. URL: https://hess.copernicus.org/articles/16/501/2012/ (visited on 10/10/2023).

Näslund, L.-Å. et al. (July 1, 2005). "X-Ray Absorption Spectroscopy Measurements of Liquid Water." en. In: *The Journal of Physical Chemistry B* 109.28, pp. 13835–13839. ISSN: 1520-6106, 1520-5207. DOI: 10.1021/jp052046q. URL: https://pubs.acs.org/doi/10.1021/jp052046q (visited on 08/30/2023).

Nield, Donald A. and Adrian Bejan (2013). *Convection in Porous Media*. en. New York, NY: Springer New York. ISBN: 978-1-4614-5540-0 978-1-4614-5541-7. DOI: 10.1007/978-1-4614-5541-7. URL: https://link.springer.com/10.1007/978-1-4614-5541-7 (visited on 04/07/2023).

Nijp, Jelmer J. et al. (2017). "A Modification of the Constant-Head Permeameter to Measure Saturated Hydraulic Conductivity of Highly Permeable Media." en. In: *MethodsX* 4, pp. 134–142. ISSN: 22150161. DOI: 10.1016/j.mex.2017.02.002. URL: https://linkinghub.elsevier.com/retrieve/pii/S2215016117300080 (visited on 10/27/2020).

Noiriel, Catherine and Cyprien Soulaine (Oct. 2021). "Pore-Scale Imaging and Modelling of Reactive Flow in Evolving Porous Media: Tracking the Dynamics of the Fluid–Rock

Interface." en. In: *Transport in Porous Media* 140.1, pp. 181–213. ISSN: 0169-3913, 1573-1634. DOI: 10.1007/s11242-021-01613-2. URL: https://link.springer.com/10.1007/s11242-021-01613-2 (visited on 10/14/2023).

O'Connor, Michael T. et al. (June 16, 2020). "Empirical Models for Predicting Water and Heat Flow Properties of Permafrost Soils." en. In: *Geophysical Research Letters* 47.11, e2020GL087646. ISSN: 0094-8276, 1944-8007. DOI: 10.1029/2020GL087646. URL: https://onlinelibrary.wiley.com/doi/10.1029/2020GL087646 (visited on 10/19/2021).

O'Donnell, Jonathan A et al. (2009). "The Effect of Moisture Content on the Thermal Conductivity of Moss and Organic Soil Horizons from Black Spruce Ecosystems in Interior Alaska." In: *Soil Science* 174.12, pp. 646–651.

Obu, Jaroslav et al. (June 2019). "Northern Hemisphere Permafrost Map Based on TTOP Modelling for 2000–2016 at 1 Km2 Scale." en. In: *Earth-Science Reviews* 193, pp. 299–316. ISSN: 00128252. DOI: 10.1016/j.earscirev.2019.04.023. URL: https://linkinghub.elsevier.com/retrieve/pii/S0012825218305907 (visited on 09/13/2023).

Oehri, Jacqueline et al. (Oct. 31, 2022). "Vegetation Type Is an Important Predictor of the Arctic Summer Land Surface Energy Budget." en. In: *Nature Communications* 13.1, p. 6379. ISSN: 2041-1723. DOI: 10.1038/s41467-022-34049-3. URL: https://www.nature.com/articles/s41467-022-34049-3 (visited on 10/10/2023).

Ogée, J. and Y. Brunet (Jan. 2002). "A Forest Floor Model for Heat and Moisture Including a Litter Layer." en. In: *Journal of Hydrology* 255.1-4, pp. 212–233. ISSN: 00221694. DOI: 10.1016/S0022-1694(01)00515-7. URL: https://linkinghub.elsevier.com/retrieve/pii/S0022169401005157 (visited on 04/26/2023).

Olefeldt, David and Nigel T. Roulet (Oct. 2014). "Permafrost Conditions in Peatlands Regulate Magnitude, Timing, and Chemical Composition of Catchment Dissolved Organic Carbon Export." en. In: *Global Change Biology* 20.10, pp. 3122–3136. ISSN: 13541013. DOI: 10.1111/gcb.12607. URL: https://onlinelibrary.wiley.com/doi/10.1111/gcb.12607 (visited on 11/10/2021).

Orgogozo, Laurent (Jan. 2022). "RichardsFoam3: A New Version of RichardsFoam for Continental Surfaces Hydrogeology Modelling." en. In: *Computer Physics Communications* 270, p. 108182. ISSN: 00104655. DOI: 10.1016/j.cpc.2021.108182. URL: https://linkinghub.elsevier.com/retrieve/pii/S0010465521002940 (visited on 12/15/2021).

Orgogozo, Laurent, Anatoly S. Prokushkin, et al. (Apr. 2019). "Water and Energy Transfer Modeling in a Permafrost-dominated, Forested Catchment of Central Siberia: The Key Role of Rooting Depth." en. In: *Permafrost and Periglacial Processes* 30.2, pp. 75–89. ISSN: 1045-6740, 1099-1530. DOI: 10.1002/ppp.1995. URL: https://onlinelibrary.wiley.com/doi/abs/10.1002/ppp.1995 (visited on 01/17/2020).

Orgogozo, Laurent, Nicolas Renon, et al. (Dec. 2014). "An Open Source Massively Parallel Solver for Richards Equation: Mechanistic Modelling of Water Fluxes at the Watershed Scale." en. In: *Computer Physics Communications* 185.12 (12), pp. 3358–3371. ISSN:

00104655. DOI: 10.1016/j.cpc.2014.08.004. URL: https://linkinghub.elsevier.com/retrieve/pii/S0010465514002719 (visited on 01/17/2020).

Orgogozo, Laurent, Thibault Xavier, et al. (Jan. 2023). "Permafrost Modelling with OpenFOAM®: New Advancements of the permaFoam Solver." en. In: *Computer Physics Communications* 282, p. 108541. ISSN: 00104655. DOI: 10.1016/j.cpc.2022.108541. URL: https://linkinghub.elsevier.com/retrieve/pii/S0010465522002600 (visited on 06/06/2023).

Otsu, Nobuyuki (Jan. 1979). "A Threshold Selection Method from Gray-Level Histograms." In: *IEEE Transactions on Systems, Man, and Cybernetics* 9.1 (1), pp. 62–66. ISSN: 0018-9472, 2168-2909. DOI: 10.1109/TSMC.1979.4310076. URL: http://ieeexplore.ieee.org/document/4310076/ (visited on 01/15/2020).

Päivänen, Juhani (1973). "Hydraulic Conductivity and Water Retention in Peat Soils." In: *Acta Forestalia Fennica* 0.129. ISSN: 00015636. DOI: 10.14214/aff.7563. URL: http://www.silvafennica.fi/article/7563 (visited on 01/16/2020).

Park, Hotaek, Alexander N. Fedorov, Pavel Konstantinov, et al. (Sept. 22, 2021). "Numerical Assessments of Excess Ice Impacts on Permafrost and Greenhouse Gases in a Siberian Tundra Site Under a Warming Climate." In: *Frontiers in Earth Science* 9, p. 704447. ISSN: 2296-6463. DOI: 10.3389/feart.2021.704447. URL: https://www.frontiersin.org/articles/10.3389/feart.2021.704447/full (visited on 10/10/2023).

Park, Hotaek, Alexander N. Fedorov, Mikhail N. Zheleznyak, et al. (May 2015). "Effect of Snow Cover on Pan-Arctic Permafrost Thermal Regimes." In: *CLIMATE DYNAMICS* 44.9-10, pp. 2873–2895. ISSN: 0930-7575. DOI: 10.1007/s00382-014-2356-5.

Park, Hotaek, Samuli Launiainen, et al. (Sept. 2018). "Modeling the Effect of Moss Cover on Soil Temperature and Carbon Fluxes at a Tundra Site in Northeastern Siberia." en. In: *Journal of Geophysical Research: Biogeosciences* 123.9 (9), pp. 3028–3044. ISSN: 21698953. DOI: 10.1029/2018JG004491. URL: http://doi.wiley.com/10.1029/2018JG004491 (visited on 01/16/2020).

Parker, W. J. et al. (Sept. 1961). "Flash Method of Determining Thermal Diffusivity, Heat Capacity, and Thermal Conductivity." en. In: *Journal of Applied Physics* 32.9, pp. 1679–1684. ISSN: 0021-8979, 1089-7550. DOI: 10.1063/1.1728417. URL: http://aip.scitation.org/doi/10.1063/1.1728417 (visited on 03/16/2023).

Patankar, Suhas V. (1980). *Numerical Heat Transfer and Fluid Flow*. eng. Series in Computational Methods in Mechanics and Thermal Sciences. New York: Hemisphere Publ. Co. 197 pp. ISBN: 978-0-89116-522-4.

Pavelsky, Tamlin M. and Laurence C. Smith (Nov. 10, 2006). "Intercomparison of Four Global Precipitation Data Sets and Their Correlation with Increased Eurasian River Discharge to the Arctic Ocean." en. In: *Journal of Geophysical Research* 111.D21, p. D21112. ISSN: 0148-0227. DOI: 10.1029/2006JD007230. URL: http://doi.wiley.com/10.1029/2006JD007230 (visited on 09/14/2023).

Payandi-Rolland, Dahédrey, L.S. Shirokova, Paty Nakhle, et al. (Mar. 2020). "Aerobic Release and Biodegradation of Dissolved Organic Matter from Frozen Peat: Effects of Temperature and Heterotrophic Bacteria." en. In: *Chemical Geology* 536, p. 119448. ISSN: 00092541. DOI: 10.1016/j.chemgeo.2019.119448. URL: https://linkinghub.elsevier.com/retrieve/pii/S0009254119305777 (visited on 04/13/2021).

Payandi-Rolland, Dahédrey, L.S. Shirokova, M. Tesfa, et al. (Dec. 2020). "Dissolved Organic Matter Biodegradation along a Hydrological Continuum in Permafrost Peatlands." en. In: *Science of The Total Environment* 749, p. 141463. ISSN: 00489697. DOI: 10.1016/j.scitotenv.2020.141463. URL: https://linkinghub.elsevier.com/retrieve/pii/S0048969720349925 (visited on 11/03/2022).

Petrescu, A. M. R. et al. (Jan. 30, 2008). "Modelling CH4 Emissions from Arctic Wetlands: Effects of Hydrological Parameterization." en. In: *Biogeosciences* 5.1, pp. 111–121. ISSN: 1726-4189. DOI: 10.5194/bg-5-111-2008. URL: https://bg.copernicus.org/articles/5/111/2008/ (visited on 08/28/2023).

Piskova, K. and M. Sacha (2023). *Brmlab. BioOSM - Cladonia Stellaris*. URL: https://brmlab.s0c4.net/bioosm/det/01e764352ff43569b93e4e49fed20f5d.htm.

Pitard, F. F. (1994). "Exploration of the "Nugget Effect"." In: *Geostatistics for the Next Century*. Ed. by Roussos Dimitrakopoulos. Vol. 6. Dordrecht: Springer Netherlands, pp. 124–136. ISBN: 978-94-010-4354-0 978-94-011-0824-9. DOI: 10.1007/978-94-011-0824-9_16. URL: http://link.springer.com/10.1007/978-94-011-0824-9_16 (visited on 10/14/2023).

Pokrovsky, Oleg S. et al. (2014). *Biogeochemistry of Thermokarst Lakes of Western Siberia*. Biochemistry Research Trends. New York: Nova Publishers. 163 pp. ISBN: 978-1-62948-567-6.

Porada, Philipp et al. (Sept. 30, 2016). "Effects of Bryophyte and Lichen Cover on Permafrost Soil Temperature at Large Scale." en. In: *The Cryosphere* 10.5 (5), pp. 2291–2315. ISSN: 1994-0424. DOI: 10.5194/tc-10-2291-2016. URL: https://www.the-cryosphere.net/10/2291/2016/ (visited on 06/11/2020).

Potkay, Aaron et al. (Apr. 2020). "Water and Vapor Transport in Algal-fungal Lichen: Modeling Constrained by Laboratory Experiments, an Application for *Flavoparmelia Caperata*." en. In: *Plant, Cell & Environment* 43.4, pp. 945–964. ISSN: 0140-7791, 1365-3040. DOI: 10.1111/pce.13690. URL: https://onlinelibrary.wiley.com/doi/10.1111/pce.13690 (visited on 11/02/2022).

Price, Jonathan S. and P. Whittington (Feb. 2010). "Water Flow in Sphagnum Hummocks: Mesocosm Measurements and Modelling." en. In: *Journal of Hydrology* 381.3-4, pp. 333–340. ISSN: 00221694. DOI: 10.1016/j.jhydrol.2009.12.006. URL: https://linkinghub.elsevier.com/retrieve/pii/S0022169409007847 (visited on 01/14/2021).

Price, Jonathan S., P. Whittington, et al. (Mar. 2008). "A Method to Determine Unsaturated Hydraulic Conductivity in Living and Undecomposed *Sphagnum* Moss." en. In: *Soil Science Society of America Journal* 72.2, pp. 487–491. ISSN: 03615995. DOI: 10.2136/

sssaj2007.0111N. URL: http://doi.wiley.com/10.2136/sssaj2007.0111N (visited on 08/18/2020).

Puustjärvi, Viljo (1977). *Peat and its use in horticulture*. engfin. Publication - Turveteollisuusliitto ; 3. Helsinki: Turveteollisuusliitto. 160 pp. ISBN: 978-951-95397-0-6.

Quintard, Michel (2015). "Transfers in Porous Media." en. In: *Special Topics & Reviews in Porous Media: An International Journal* 6.2, pp. 91–108. ISSN: 2151-4798. DOI: 10.1615/SpecialTopicsRevPorousMedia.2015013158. URL: http://www.dl.begellhouse.com/journals/3d21681c18f5b5e7,09dfc75d18d3a6ca,148b9c94371359eb.html (visited on 01/17/2020).

Quintard, Michel and Stephen Whitaker (1989). "Ecoulement Monophasique En Milieux Poreux : Effet Des Hétérogénéités." In: *Journal de Mécanique Théorique et Appliquée* 6 (6), pp. 691–726. ISSN: 0750-7240. URL: https://www.researchgate.net/profile/Stephen-Whitaker-3/publication/230704130_Ecoulement_monophasique_en_milieu_poreux_Effet_des_heterogeneites_locales/links/0912f50f75a59771b7000000/Ecoulement-monophasique-en-milieu-poreux-Effet-des-heterogeneites-locales.pdf.

– (Feb. 1994). "Transport in Ordered and Disordered Porous Media II: Generalized Volume Averaging." en. In: *Transport in Porous Media* 14.2, pp. 179–206. ISSN: 0169-3913, 1573-1634. DOI: 10.1007/BF00615200. URL: http://link.springer.com/10.1007/BF00615200 (visited on 01/15/2020).

Quinton, W.L., T. Elliot, et al. (Oct. 2009). "Measuring Physical and Hydraulic Properties of Peat from X-ray Tomography." en. In: *Geoderma* 153.1-2, pp. 269–277. ISSN: 00167061. DOI: 10.1016/j.geoderma.2009.08.010. URL: https://linkinghub.elsevier.com/retrieve/pii/S0016706109002638 (visited on 10/14/2023).

Quinton, W.L., D.M. Gray, et al. (Oct. 2000). "Subsurface Drainage from Hummock-Covered Hillslopes in the Arctic Tundra." en. In: *Journal of Hydrology* 237.1-2, pp. 113–125. ISSN: 00221694. DOI: 10.1016/S0022-1694(00)00304-8. URL: https://linkinghub.elsevier.com/retrieve/pii/S0022169400003048 (visited on 11/25/2020).

Raudina, T.V. et al. (Sept. 2018). "Permafrost Thaw and Climate Warming May Decrease the CO2, Carbon, and Metal Concentration in Peat Soil Waters of the Western Siberia Lowland." en. In: *Science of The Total Environment* 634, pp. 1004–1023. ISSN: 00489697. DOI: 10.1016/j.scitotenv.2018.04.059. URL: https://linkinghub.elsevier.com/retrieve/pii/S0048969718312233 (visited on 04/02/2020).

Rawlins, M. A. et al. (Sept. 24, 2009). "Divergence in Seasonal Hydrology across Northern Eurasia: Emerging Trends and Water Cycle Linkages." en. In: *Journal of Geophysical Research* 114.D18, p. D18119. ISSN: 0148-0227. DOI: 10.1029/2009JD011747. URL: http://doi.wiley.com/10.1029/2009JD011747 (visited on 09/14/2023).

Rayleigh, Lord (Dec. 1916). "On Convection Currents in a Horizontal Layer of Fluid, When the Higher Temperature Is on the under Side." en. In: *The London, Edinburgh, and Dublin Philosophical Magazine and Journal of Science* 32.192, pp. 529–546. ISSN: 1941-5982, 1941-5990. DOI: 10.1080/14786441608635602. URL: https://www.tandfonline.com/doi/full/10.1080/14786441608635602 (visited on 04/25/2023).

Reick, Christian H. et al. (Feb. 2021). "JSBACH 3 - The Land Component of the MPI Earth System Model: Documentation of Version 3.2." en. Version 1. In: p. 4990986. DOI: 10.17617/2.3279802. URL: https://pure.mpg.de/pubman/item/item_3279802 (visited on 10/11/2023).

Revich, Boris A. et al. (Mar. 28, 2022). "Risks for Public Health and Social Infrastructure in Russian Arctic under Climate Change and Permafrost Degradation." en. In: *Atmosphere* 13.4, p. 532. ISSN: 2073-4433. DOI: 10.3390/atmos13040532. URL: https://www.mdpi.com/2073-4433/13/4/532 (visited on 09/14/2023).

Rezanezhad, Fereidoun et al. (July 2016). "Structure of Peat Soils and Implications for Water Storage, Flow and Solute Transport: A Review Update for Geochemists." en. In: *Chemical Geology* 429, pp. 75–84. ISSN: 00092541. DOI: 10.1016/j.chemgeo.2016.03.010. URL: https://linkinghub.elsevier.com/retrieve/pii/S0009254116301243 (visited on 01/14/2020).

Richards, L. A. (Nov. 1931). "Capillary Conduction of Liquids Throught Porous Medium." en. In: *Physics* 1.5, pp. 318–333. ISSN: 0148-6349, 2163-5102. DOI: 10.1063/1.1745010. URL: http://aip.scitation.org/doi/10.1063/1.1745010 (visited on 04/21/2021).

Robinson, P.J. and J. A. Davies (1972). "Laboratory Determinations of Water Surface Emissivity." In: *Journal of Applied Meteorology (1962-1982)*, pp. 1391–1393.

Roustaei, Mahya et al. (Oct. 2022). "Estimating Ice and Unfrozen Water in Permafrost Samples Using Industrial Computed Tomography Scanning." In:

Roux, Nicolas et al. (Apr. 2017). "Laboratory and Numerical Simulation of the Evolution of a River's Talik: Laboratory and Numerical Simulations of River's Talik Evolution." en. In: *Permafrost and Periglacial Processes* 28.2, pp. 460–469. ISSN: 10456740. DOI: 10.1002/ppp.1929. URL: https://onlinelibrary.wiley.com/doi/10.1002/ppp.1929 (visited on 04/20/2022).

Sadeghi, Amin and Jeff Gostick (Mar. 12, 2020). *Berea Sandstone Simulation Using PoreSpy and OpenPNM*. Berea Sandstone Simulation Using PoreSpy and OpenPNM. URL: https://github.com/PMEAL/OpenPNM/blob/dev/examples/applications/relative_permeability.ipynb (visited on 10/30/2020).

Sarasto, Juhani (1963). "Tutkimuksia rahka- ja saraturpeiden vedenläpäisevyydestä | A study of the permeability to water of different kind of peat." fi. In: *Suo* 3, pp. 32–36. URL: http://www.suo.fi/pdf/article9305.pdf.

Sazhin, S.S. et al. (Feb. 1996). "The P-1 Model for Thermal Radiation Transfer: Advantages and Limitations." en. In: *Fuel* 75.3, pp. 289–294. ISSN: 00162361. DOI: 10.1016/0016-2361(95)00269-3. URL: https://linkinghub.elsevier.com/retrieve/pii/0016236195002693 (visited on 07/20/2023).

Schaepman-Strub, Gabriela and Jin-Soo Kim (Dec. 2, 2022). "What Set Siberia Ablaze?" en. In: *Science* 378.6623, pp. 944–945. ISSN: 0036-8075, 1095-9203. DOI: 10.1126/science.ade8673. URL: https://www.science.org/doi/10.1126/science.ade8673 (visited on 10/10/2023).

Schindelin, Johannes et al. (July 2012). "Fiji: An Open-Source Platform for Biological-Image Analysis." en. In: *Nature Methods* 9.7 (7), pp. 676–682. ISSN: 1548-7091, 1548-7105. DOI: 10.1038/nmeth.2019. URL: http://www.nature.com/articles/nmeth.2019 (visited on 02/25/2020).

Schlesinger, Michael E. and John F. B. Mitchell (1987). "Climate Model Simulations of the Equilibrium Climatic Response to Increased Carbon Dioxide." en. In: *Reviews of Geophysics* 25.4, p. 760. ISSN: 8755-1209. DOI: 10.1029/RG025i004p00760. URL: http://doi.wiley.com/10.1029/RG025i004p00760 (visited on 09/11/2023).

Schuur, E. A. G et al. (Apr. 2015). "Climate Change and the Permafrost Carbon Feedback." en. In: *Nature* 520.7546, pp. 171–179. ISSN: 0028-0836, 1476-4687. DOI: 10.1038/nature14338. URL: http://www.nature.com/articles/nature14338 (visited on 02/23/2021).

Schuur, Edward A. G et al. (Sept. 1, 2008). "Vulnerability of Permafrost Carbon to Climate Change: Implications for the Global Carbon Cycle." en. In: *BioScience* 58.8, pp. 701–714. ISSN: 1525-3244, 0006-3568. DOI: 10.1641/B580807. URL: https://academic.oup.com/bioscience/article/58/8/701/380621 (visited on 09/11/2023).

Serreze, Mark C. and Jennifer A. Francis (June 2006). "The Arctic Amplification Debate." en. In: *Climatic Change* 76.3-4, pp. 241–264. ISSN: 0165-0009, 1573-1480. DOI: 10.1007/s10584-005-9017-y. URL: http://link.springer.com/10.1007/s10584-005-9017-y (visited on 09/12/2023).

Shi, Xiaoying et al. (Jan. 20, 2021). "Extending a Land-Surface Model with Sphagnum Moss to Simulate Responses of a Northern Temperate Bog to Whole Ecosystem Warming and Elevated CO2." en. In: *Biogeosciences* 18.2, pp. 467–486. ISSN: 1726-4189. DOI: 10.5194/bg-18-467-2021. URL: https://bg.copernicus.org/articles/18/467/2021/ (visited on 07/29/2021).

Shiklomanov, Nikolay I. and Marlene Laruelle (Oct. 2, 2017). "A Truly Arctic City: An Introduction to the Special Issue on the City of Norilsk, Russia." en. In: *Polar Geography* 40.4, pp. 251–256. ISSN: 1088-937X, 1939-0513. DOI: 10.1080/1088937X.2017.1387823. URL: https://www.tandfonline.com/doi/full/10.1080/1088937X.2017.1387823 (visited on 10/11/2023).

Shiklomanov, Nikolay I., Dmitry A. Streletskiy, et al. (Jan. 1, 2017). "Climate Change and Stability of Urban Infrastructure in Russian Permafrost Regions: Prognostic Assessment Based on GCM Climate Projections." en. In: *Geographical Review* 107.1, pp. 125–142. ISSN: 0016-7428, 1931-0846. DOI: 10.1111/gere.12214. URL: https://www.tandfonline.com/doi/full/10.1111/gere.12214 (visited on 10/11/2023).

Shirokova, L. S. et al. (May 2013). "Biogeochemistry of Organic Carbon, CO2, CH4, and Trace Elements in Thermokarst Water Bodies in Discontinuous Permafrost Zones of Western Siberia." en. In: *Biogeochemistry* 113.1-3 (1-3), pp. 573–593. ISSN: 0168-2563, 1573-515X. DOI: 10.1007/s10533-012-9790-4. URL: http://link.springer.com/10.1007/s10533-012-9790-4 (visited on 01/16/2020).

Shirokova, L.S. et al. (Mar. 2021). "Lichen, Moss and Peat Control of C, Nutrient and Trace Metal Regime in Lakes of Permafrost Peatlands." en. In: *Science of The Total Environment* 782.146737. ISSN: 00489697. DOI: 10.1016/j.scitotenv.2021.146737. URL: https://linkinghub.elsevier.com/retrieve/pii/S0048969721018052 (visited on 04/01/2021).

Shuster, W.D. et al. (June 2021). "*K* in an Urban World: New Contexts for Hydraulic Conductivity." en. In: *JAWRA Journal of the American Water Resources Association* 57.3, pp. 493–504. ISSN: 1093-474X, 1752-1688. DOI: 10.1111/1752-1688.12918. URL: https://onlinelibrary.wiley.com/doi/10.1111/1752-1688.12918 (visited on 01/10/2024).

Sidiras, N. and C.H. Roth (Feb. 1987). "Infiltration Measurements with Double-Ring Infiltrometers and a Rainfall Simulator under Different Surface Conditions on an Oxisol." en. In: *Soil and Tillage Research* 9.2, pp. 161–168. ISSN: 01671987. DOI: 10.1016/0167-1987(87)90082-1. URL: https://linkinghub.elsevier.com/retrieve/pii/0167198787900821 (visited on 01/10/2024).

Silin, Dmitriy and Tad Patzek (Nov. 2006). "Pore Space Morphology Analysis Using Maximal Inscribed Spheres." en. In: *Physica A: Statistical Mechanics and its Applications* 371.2, pp. 336–360. ISSN: 03784371. DOI: 10.1016/j.physa.2006.04.048. URL: https://linkinghub.elsevier.com/retrieve/pii/S037843710600464X (visited on 11/23/2020).

Soudzilovskaia, N.A et al. (Dec. 2013). "Dominant Bryophyte Control over High-Latitude Soil Temperature Fluctuations Predicted by Heat Transfer Traits, Field Moisture Regime and Laws of Thermal Insulation." en. In: *Functional Ecology* 27.6 (6). Ed. by J. Schweitzer, pp. 1442–1454. ISSN: 02698463. DOI: 10.1111/1365-2435.12127. URL: http://doi.wiley.com/10.1111/1365-2435.12127 (visited on 01/16/2020).

Soulaine, Cyprien et al. (May 2016). "The Impact of Sub-Resolution Porosity of X-ray Microtomography Images on the Permeability." en. In: *Transport in Porous Media* 113.1, pp. 227–243. ISSN: 0169-3913, 1573-1634. DOI: 10.1007/s11242-016-0690-2. URL: http://link.springer.com/10.1007/s11242-016-0690-2 (visited on 11/10/2021).

Sousa, Filipe et al. (Apr. 2019). "Nuclear Protein Phylogenies Support the Monophyly of the Three Bryophyte Groups (Bryophyta Schimp.)" en. In: *New Phytologist* 222.1, pp. 565–575. ISSN: 0028-646X, 1469-8137. DOI: 10.1111/nph.15587. URL: https://onlinelibrary.wiley.com/doi/10.1111/nph.15587 (visited on 01/27/2023).

Stepanenko, V. M. et al. (Mar. 2020). "An Overview of Parameterezations of Heat Transfer over Moss-Covered Surfaces in the Earth System Models." en. In: *Izvestiya, Atmospheric and Oceanic Physics* 56.2 (2), pp. 101–111. ISSN: 0001-4338, 1555-628X. DOI: 10.1134/S0001433820020139. URL: http://link.springer.com/10.1134/S0001433820020139 (visited on 06/02/2020).

Strack, M. et al. (Dec. 2009). "Moisture Controls on CO $_2$ Exchange in a *Sphagnum* - Dominated Peatland: Results from an Extreme Drought Field Experiment." en. In: *Ecohydrology* 2.4, pp. 454–461. ISSN: 19360584, 19360592. DOI: 10.1002/eco.68. URL: http://doi.wiley.com/10.1002/eco.68 (visited on 11/12/2020).

Streletskiy, Dmitry A, Luis J Suter, et al. (Feb. 1, 2019). "Assessment of Climate Change Impacts on Buildings, Structures and Infrastructure in the Russian Regions on Permafrost." In: *Environmental Research Letters* 14.2, p. 025003. ISSN: 1748-9326. DOI: 10.1088/1748-9326/aaf5e6. URL: https://iopscience.iop.org/article/10.1088/1748-9326/aaf5e6 (visited on 10/11/2023).

Streletskiy, Dmitry A, Nikita I Tananaev, et al. (Sept. 1, 2015). "Permafrost Hydrology in Changing Climatic Conditions: Seasonal Variability of Stable Isotope Composition in Rivers in Discontinuous Permafrost." In: *Environmental Research Letters* 10.9, p. 095003. ISSN: 1748-9326. DOI: 10.1088/1748-9326/10/9/095003. URL: https://iopscience.iop.org/article/10.1088/1748-9326/10/9/095003 (visited on 11/10/2021).

Stuefer, Svetlana L. et al. (Nov. 2017). "Recent Extreme Runoff Observations From Coastal Arctic Watersheds in Alaska." en. In: *Water Resources Research* 53.11, pp. 9145–9163. ISSN: 0043-1397, 1944-7973. DOI: 10.1002/2017WR020567. URL: https://agupubs.onlinelibrary.wiley.com/doi/10.1002/2017WR020567 (visited on 10/05/2023).

Sutton, O. S (Dec. 22, 1950). "On the Stability of a Fluid Heated from Below." en. In: *Proceedings of the Royal Society of London. Series A. Mathematical and Physical Sciences* 204.1078, pp. 297–309. ISSN: 0080-4630, 2053-9169. DOI: 10.1098/rspa.1950.0175. URL: https://royalsocietypublishing.org/doi/10.1098/rspa.1950.0175 (visited on 04/07/2023).

Takata, Kumiko and Masahide Kimoto (2000). "A Numerical Study on the Impact of Soil Freezing on the Continental-Scale Cycle." In: *Journal of the Meteorological Society of Japan* 78.3 (3), pp. 199–201.

Tananaev, Nikita et al. (Jan. 7, 2020). "Permafrost Hydrology Research Domain: Process-Based Adjustment." en. In: *Hydrology* 7.1, p. 6. ISSN: 2306-5338. DOI: 10.3390/hydrology7010006. URL: https://www.mdpi.com/2306-5338/7/1/6 (visited on 10/19/2021).

Tanguy, Rodrigue et al. (Aug. 2023). "Permafrost Degradation in the Ice-Wedge Tundra Terrace of Paulatuk Peninsula (Darnley Bay, Canada)." en. In: *Geomorphology* 435, p. 108754. ISSN: 0169555X. DOI: 10.1016/j.geomorph.2023.108754. URL: https://linkinghub.elsevier.com/retrieve/pii/S0169555X23001745 (visited on 10/10/2023).

Tarhanen, S et al. (Jan. 1999). "Membrane Permeability Response of Lichen Bryoria Fuscescens to Wet Deposited Heavy Metals and Acid Rain." en. In: *Environmental Pollution* 104.1, pp. 121–129. ISSN: 02697491. DOI: 10.1016/S0269-7491(98)00157-2. URL: https://linkinghub.elsevier.com/retrieve/pii/S0269749198001572 (visited on 11/24/2020).

Tarnocai, C. et al. (June 2009). "Soil Organic Carbon Pools in the Northern Circumpolar Permafrost Region: Soil Organic Carbon Pools." en. In: *Global Biogeochemical Cycles* 23.2, n/a–n/a. ISSN: 08866236. DOI: 10.1029/2008GB003327. URL: http://doi.wiley.com/10.1029/2008GB003327 (visited on 09/11/2023).

Taud, H. et al. (2005). "Porosity Estimation Method by X-ray Computed Tomography." In: *Journal of Petroleum Science and Engineering* 47.3, pp. 209–217. ISSN: 0920-4105. DOI:

10.1016/j.petrol.2005.03.009. URL: https://www.sciencedirect.com/science/article/pii/S0920410505000586.

Taylor, Karl E. et al. (Apr. 1, 2012). "An Overview of CMIP5 and the Experiment Design." en. In: *Bulletin of the American Meteorological Society* 93.4 (4), pp. 485–498. ISSN: 1520-0477. DOI: 10.1175/BAMS-D-11-00094.1. URL: https://journals.ametsoc.org/bams/article/93/4/485/60085/An-Overview-of-CMIP5-and-the-Experiment-Design (visited on 06/29/2020).

Thai, Vu Hong et al. (Oct. 2018). "A Comparison between the Use of Continuous and Pore Network Approach in the Simulation of the Drying Process of Porous Media with Different Pore Size Distributions." en. In: *Vietnam Journal of Chemistry* 56.5, pp. 564–569. ISSN: 08667144. DOI: 10.1002/vjch.201800048. URL: https://onlinelibrary.wiley.com/doi/10.1002/vjch.201800048 (visited on 09/20/2023).

Throckmorton, Heather M. et al. (Dec. 30, 2016). "Active Layer Hydrology in an Arctic Tundra Ecosystem: Quantifying Water Sources and Cycling Using Water Stable Isotopes: Active Layer Hydrology in the Arctic Coastal Plain." en. In: *Hydrological Processes* 30.26, pp. 4972–4986. ISSN: 08856087. DOI: 10.1002/hyp.10883. URL: https://onlinelibrary.wiley.com/doi/10.1002/hyp.10883 (visited on 10/19/2021).

Tifafi, Marwa et al. (Jan. 2018). "Large Differences in Global and Regional Total Soil Carbon Stock Estimates Based on SoilGrids, HWSD, and NCSCD: Intercomparison and Evaluation Based on Field Data From USA, England, Wales, and France." en. In: *Global Biogeochemical Cycles* 32.1, pp. 42–56. ISSN: 0886-6236, 1944-9224. DOI: 10.1002/2017GB005678. URL: https://agupubs.onlinelibrary.wiley.com/doi/10.1002/2017GB005678 (visited on 10/11/2023).

Triska, Frank J and LWG Bert Higler (2009). "Biogeochemical Processes in River Systems." In: *Fresh Surface Water* 2, p. 175.

Troitsky, A. V. et al. (Dec. 2007). "Contribution of Genosystematics to Current Concepts of Phylogeny and Classification of Bryophytes." en. In: *Biochemistry (Moscow)* 72.12, pp. 1368–1376. ISSN: 0006-2979, 1608-3040. DOI: 10.1134/S0006297907120115. URL: http://link.springer.com/10.1134/S0006297907120115 (visited on 04/06/2021).

Tsilingiris, P.T. (May 2008). "Thermophysical and Transport Properties of Humid Air at Temperature Range between 0 and 100°C." en. In: *Energy Conversion and Management* 49.5, pp. 1098–1110. ISSN: 01968904. DOI: 10.1016/j.enconman.2007.09.015. URL: https://linkinghub.elsevier.com/retrieve/pii/S0196890407003329 (visited on 04/07/2023).

Turberg, P. et al. (July 2014). "Characterization of Structural Disturbances in Peats by X-ray CT-based Density Determinations: Characterization of Structural Disturbances in Peats." en. In: *European Journal of Soil Science* 65.4 (4), pp. 613–624. ISSN: 13510754. DOI: 10.1111/ejss.12148. URL: http://doi.wiley.com/10.1111/ejss.12148 (visited on 01/15/2020).

Turetsky, Merritt et al. (2019). "Permafrost Collapse Is Accelerating Carbon Release." In: *Nature* 569, pp. 32–34.

van der Molen and Wijmstra, T.A (Dec. 1994). "The Thermal Regime of Hummock-Hollow Complexes on Clara Bog, Co. Offaly." In: *Biology and Environment*. Proceedings of the Royal Irish Academy 94B, p. 3. JSTOR: 20499939. URL: https://www.jstor.org/stable/20499939.

Van Wijk, W. and D. de Vries (1963). *Physics of Plant Environment*. Amsterdam: North-Holland Publ. Co. 382 pp.

Vdovin, Alexey (2009). *Radiation Heat Transfer in OpenFOAM*. Göteborg: Chalmers University of Technology. URL: https://www.tfd.chalmers.se/~hani/kurser/OS_CFD_2009/AlexeyVdovin/Radiation_in_OpenFoam_final.pdf.

Vedie, E. et al. (Mar. 15, 2011). "Physical Modelling of Rainfall- and Snowmelt-Induced Erosion of Stony Slope Underlain by Permafrost." en. In: *Earth Surface Processes and Landforms* 36.3, pp. 395–407. ISSN: 01979337. DOI: 10.1002/esp.2054. URL: https://onlinelibrary.wiley.com/doi/10.1002/esp.2054 (visited on 11/10/2021).

Vellvehi, M. et al. (Nov. 2011). "Irradiance-Based Emissivity Correction in Infrared Thermography for Electronic Applications." en. In: *Review of Scientific Instruments* 82.11, p. 114901. ISSN: 0034-6748, 1089-7623. DOI: 10.1063/1.3657154. URL: http://aip.scitation.org/doi/10.1063/1.3657154 (visited on 02/16/2023).

Vidal, Daniele and Rui Pitarma (July 15, 2019). "Infrared Thermography Applied to Tree Health Assessment: A Review." en. In: *Agriculture* 9.7, p. 156. ISSN: 2077-0472. DOI: 10.3390/agriculture9070156. URL: https://www.mdpi.com/2077-0472/9/7/156 (visited on 03/21/2023).

Virta, J. (1962). "Suohydrologisista tutkimuksista Lapissa ja Pohjanmaalla | On the research of peat land hydrology in Lapland and Ostrobothnia." fi. In: *Suo* 3, pp. 30–35. URL: http://www.suo.fi/pdf/article9289.pdf.

Volkova, I. I. et al. (2018). "Peat Forming Mosses as a Key Component of Peat Deposits and Mire Vegetation of the West Siberian Taiga." en. In: *Mosses: Ecology, Life Cycle and Significance*. Ed. by Oleg S. Pokrovsky et al. Environmental Science, Engineering and Technology. New York: Nova Science Publishers, Incorporated, pp. 175–189. ISBN: 978-1-5361-4330-0.

Voortman, Bernard R. et al. (Dec. 30, 2014). "Unsaturated Hydraulic Properties of Xerophilous Mosses: Towards Implementation of Moss Covered Soils in Hydrological Models: Unsaturated Hydraulic Properties of Xerophious Mosses." en. In: *Hydrological Processes* 28.26, pp. 6251–6264. ISSN: 08856087. DOI: 10.1002/hyp.10111. URL: https://onlinelibrary.wiley.com/doi/10.1002/hyp.10111 (visited on 11/10/2021).

Wagner, Anna M. et al. (Dec. 2018). "Permafrost Degradation and Subsidence Observations during a Controlled Warming Experiment." en. In: *Scientific Reports* 8.1, p. 10908. ISSN: 2045-2322. DOI: 10.1038/s41598-018-29292-y. URL: http://www.nature.com/articles/s41598-018-29292-y (visited on 11/10/2021).

Walvoord, Michelle A. and Barret L. Kurylyk (June 2016). "Hydrologic Impacts of Thawing Permafrost-A Review." en. In: *Vadose Zone Journal* 15.6 (6), vzj2016.01.0010. ISSN:

15391663. DOI: 10.2136/vzj2016.01.0010. URL: http://doi.wiley.com/10.2136/vzj2016.01.0010 (visited on 06/11/2020).

Weber, Tobias K. D. et al. (Jan. 2017). "Unsaturated Hydraulic Properties of *Sphagnum* Moss and Peat Reveal Trimodal Pore-Size Distributions: Trimodal Hydraulic Properties of Sphagnum Moss." en. In: *Water Resources Research* 53.1, pp. 415–434. ISSN: 00431397. DOI: 10.1002/2016WR019707. URL: http://doi.wiley.com/10.1002/2016WR019707 (visited on 11/12/2020).

Weller, H.G. et al. (1998). "A Tensorial Approach to Computational Continuum Mechanics Using Object-Oriented Techniques." In: *Computers in Physics* 12.6 (6), pp. 620–631.

Weston, David J. et al. (Sept. 2015). "*S Phagnum* Physiology in the Context of Changing Climate: Emergent Influences of Genomics, Modelling and Host–Microbiome Interactions on Understanding Ecosystem Function." en. In: *Plant, Cell & Environment* 38.9, pp. 1737–1751. ISSN: 0140-7791, 1365-3040. DOI: 10.1111/pce.12458. URL: https://onlinelibrary.wiley.com/doi/10.1111/pce.12458 (visited on 06/15/2023).

Whitaker, Stephen (1999). *The Method of Volume Averaging*. English. Vol. 13. Theory and Applications of Transport in Porous Media. Dordrecht: Springer. ISBN: 978-94-017-3389-2. URL: http://public.ebookcentral.proquest.com/choice/publicfullrecord.aspx?p=3106854 (visited on 01/14/2020).

Whittaker, Robert Harding (1975). *Communities and Ecosystems*. 2d ed. New York: Macmillan. 385 pp. ISBN: 978-0-02-427390-1.

Williams, G. P. (1968). "The Thermal Regime of Sphagnum Peat Bog." In: Third International Peat Congress. Quebec, Canada: National Research Counsil of Canada, pp. 195–200.

Woo, Ming-ko (2012). *Permafrost Hydrology*. en. Berlin, Heidelberg: Springer Berlin Heidelberg. ISBN: 978-3-642-23461-3 978-3-642-23462-0. DOI: 10.1007/978-3-642-23462-0. URL: https://link.springer.com/10.1007/978-3-642-23462-0 (visited on 06/26/2023).

Wu, Ruonan, Eric M. Bottos, et al. (2022). "RNA Viruses Linked to Eukaryotic Hosts in Thawed Permafrost." en. In: *mSystems* 7.6. Ed. by Haiyan Chu, e00582–22. ISSN: 2379-5077. DOI: 10.1128/msystems.00582-22. URL: https://journals.asm.org/doi/10.1128/msystems.00582-22 (visited on 09/14/2023).

Wu, Ruonan, Gareth Trubl, et al. (2022). "Permafrost as a Potential Pathogen Reservoir." en. In: *One Earth* 5.4, pp. 351–360. ISSN: 25903322. DOI: 10.1016/j.oneear.2022.03.010. URL: https://linkinghub.elsevier.com/retrieve/pii/S2590332222001439 (visited on 09/14/2023).

Xie, Yongkun et al. (Mar. 1, 2023). "Enhanced Asian Warming Increases Arctic Amplification." In: *Environmental Research Letters* 18.3, p. 034041. ISSN: 1748-9326. DOI: 10.1088/1748-9326/acbdb1. URL: https://iopscience.iop.org/article/10.1088/1748-9326/acbdb1 (visited on 09/12/2023).

Yadav, Juhi et al. (Sept. 2020). "Dramatic Decline of Arctic Sea Ice Linked to Global Warming." en. In: *Natural Hazards* 103.2, pp. 2617–2621. ISSN: 0921-030X, 1573-0840. DOI:

10.1007/s11069-020-04064-y. URL: https://link.springer.com/10.1007/s11069-020-04064-y (visited on 09/11/2023).

Ye, Hengchun et al. (2004). "The Impact of Climatic Conditions on Seasonal River Discharges in Siberia." In: *Journal of Hydrometeorology* 5.2, pp. 286–295. DOI: 10.1175/1525-7541(2004)005<0286:TIOCCO>2.0.CO;2. URL: https://journals.ametsoc.org/view/journals/hydr/5/2/1525-7541_2004_005_0286_tiocco_2_0_co_2.xml.

Yi, Shuhua et al. (Mar. 6, 2009). "Characteristics of Organic Soil in Black Spruce Forests: Implications for the Application of Land Surface and Ecosystem Models in Cold Regions." en. In: *Geophysical Research Letters* 36.5, p. L05501. ISSN: 0094-8276. DOI: 10.1029/2008GL037014. URL: http://doi.wiley.com/10.1029/2008GL037014 (visited on 09/20/2021).

Yun, Tae Sup et al. (2013). "Evaluation of Rock Anisotropy Using 3D X-ray Computed Tomography." In: *Engineering Geology* 163, pp. 11–19. ISSN: 0013-7952. DOI: 10.1016/j.enggeo.2013.05.017. URL: https://www.sciencedirect.com/science/article/pii/S0013795213001804.

Záveská Drábková, Lenka et al. (May 14, 2015). "Phytohormone Profiling across the Bryophytes." en. In: *PLOS ONE* 10.5. Ed. by Ive De Smet, e0125411. ISSN: 1932-6203. DOI: 10.1371/journal.pone.0125411. URL: https://dx.plos.org/10.1371/journal.pone.0125411 (visited on 06/13/2023).

Zhang, Dongxiao et al. (Apr. 15, 2000). "Pore Scale Study of Flow in Porous Media: Scale Dependency, REV, and Statistical REV." en. In: *Geophysical Research Letters* 27.8 (8), pp. 1195–1198. ISSN: 00948276. DOI: 10.1029/1999GL011101. URL: http://doi.wiley.com/10.1029/1999GL011101 (visited on 02/26/2020).

Zhang, Liping et al. (2009). "Heat Transfer Performance of Porous Copper Fabricated by Lost Carbonate Sintering Process." en. In: *MRS Proceedings* 1188, pp. 1188-LL04–07. ISSN: 0272-9172, 1946-4274. DOI: 10.1557/PROC-1188-LL04-07. URL: http://link.springer.com/10.1557/PROC-1188-LL04-07 (visited on 03/30/2023).

Zhang, Nan and Zhaoyu Wang (July 2017). "Review of Soil Thermal Conductivity and Predictive Models." en. In: *International Journal of Thermal Sciences* 117, pp. 172–183. ISSN: 12900729. DOI: 10.1016/j.ijthermalsci.2017.03.013. URL: https://linkinghub.elsevier.com/retrieve/pii/S1290072916315228 (visited on 02/21/2023).

Zhang, Zhongyang et al. (Sept. 2023). "Response Mechanism of Soil Structural Heterogeneity in Permafrost Active Layer to Freeze–Thaw Action and Vegetation Degradation." en. In: *CATENA* 230, p. 107250. ISSN: 03418162. DOI: 10.1016/j.catena.2023.107250. URL: https://linkinghub.elsevier.com/retrieve/pii/S0341816223003417 (visited on 12/21/2023).

Zheng, Xiuqing et al. (2013). "Improving Spatial Adaptivity of Nonlocal Means in Low-Dosed CT Imaging Using Pointwise Fractal Dimension." en. In: *Computational and Mathematical Methods in Medicine* 2013, pp. 1–8. ISSN: 1748-670X, 1748-6718. DOI: 10.1155/2013/902143. URL: http://www.hindawi.com/journals/cmmm/2013/902143/ (visited on 08/29/2023).

Zhu, Yuan (Jan. 2016). "Heat-Loss Modified Angstrom Method for Simultaneous Measurements of Thermal Diffusivity and Conductivity of Graphite Sheets: The Origins of Heat Loss in Angstrom Method." en. In: *International Journal of Heat and Mass Transfer* 92, pp. 784–791. ISSN: 00179310. DOI: 10.1016/j.ijheatmasstransfer.2015.09.032. URL: https://linkinghub.elsevier.com/retrieve/pii/S0017931015009710 (visited on 03/29/2023).

Simon Cazaurang (2023). “Caractérisation Des Propriétés de Transfert de La Couverture Végétale Inférieure Arctique - Approche Expérimentale et Numérique Couplée.” Thèse de doctorat de dynamique des Fluides. Toulouse, France: Toulouse INP - ENSEEIHT